Developing an electrochemical tissue perfusion sensor

Severin Luc Ramses Harvey

A thesis submitted for the degree of Doctor of Philosophy and the Diploma of Imperial College

Department of Bioengineering
Imperial College London
SW7 2AZ

I hereby declare that the work presented in this thesis is my own.

Severin L. R. Harvey

Abstract

This thesis focuses on the development of an electrochemical tissue perfusion sensor. Tissue perfusion is the cellular level mass transport mechanism which describes the movement of nutrients and metabolites within in tissue and is a measure of tissue health. Our understanding of tissue perfusion is still limited because current measurement tools are inadequate.

The tissue perfusion measurement technique developed overcomes the limitation of current methods in that continuous and cellular level measurements are possible. This is achieved using a platinum ring-disc microelectrode operated in the collector-generator mode. This electrode pair is placed in tissue where one electrode generates hydrogen whilst the other collects it. Tissue perfusion will strongly influence the movement of H_2 between the two closely spaced electrodes. The ratio of collector to generator current can thus be used to quantify tissue perfusion.

To make the micron size ring-disc electrodes, a novel fabrication method was used. It relies on hollow cylindrical sputter coating and produces sensors with diameter as small as 28 μm. A number of numerical models of the sensor under diffusion and convection mass transport modes were constructed to assist the design process and to further our understanding of the behaviour of the electrodes in different situations. Experimental characterisation of the sensor was also carried out under diffusion and convection mass transport modes. These experiments also improved the design of the sensor and often agreed with numerical predictions. Finally the sensor was tested in a number of animal and human tissues as well as perfusion models. These were used as a proof of principle to confirming the capability of the sensor to continuously measure changes in tissue perfusion at the cellular level.

à ma maman

Acknowledgements

I would like to thank Kim Parker and Danny O'Hare for their supervision. Thank you for always suggesting rather than imposing guidance and for broadening my horizons with countless facts, stories, ideas and jokes. It was a true delight.
I would like to thank Torr Scientific Ltd. for a great year in Portslade. Dave Bates, Des Sheham and Peter Coxon thank you for introducing me to PVD techniques, BBC Radio 4, 6 am starts and above all a down to earth approach to complex engineering and manufacturing.
Thanks to Ipso Bio Ltd. for the funding.

To my lovely girlfriend Nuria Roque Rosell for everything and more. Merci, maca.

Many thanks also to Ivan Cheung and Suzanne Cawley for there help as project students and the perfused friendship we now share.

To all the good friends I have made at Imperial College and in the PFSU in particular. The chats, the laughs, the late nights and weekends in the office or in the pub were all inspiring and exhilarating aspects of my PhD. I would like to mention in particular: Arun Arora, Costas Anastassiou, Martin Arundell, Eleni Bitziou, Emma Corcoles, Stephanie Cremers, Delphine Feuerstein, Parry Hashemi, Yoko Kikuchi, Pei Ling Leow, Alexandra Lindsay, Luca Marcelli, Nina Nier, Bhavik Patel, Ohm Seelanan, and Hong Zhao. Thank you for the good times.

Above all I would like to thank my family, my brother, Tristan, sister, Raffaella, and mother, Odile, for their unconditional support, love and encouragement.
To my father for all that he did and who unfortunately never got to see this work.

Finally I would like to thank all my electrodes for three years of challenging interaction.

Content

List of Figures

List of Tables

Citations to previously published work

Parts of this thesis have appeared (or will soon appear) in patents and scientific publications:

Chapter 2: Metallic ring-disc microelectrode fabrication using inverted hollow cylindrical sputter coater. *Sensors and Actuators B: Chemical*, *Available online 15 September 2007.* S.L.R. Harvey, P. Coxon, D. Bates, K.H. Parker and D. O'Hare

Chapter 3: Theoretical evaluation of the collection efficiency at ring-disc microelectrodes. *Journal of Electroanalytical Chemistry*, *Volume 610, Issue 2*, *1 December 2007*, *Pages 122-130.* S.L.R. Harvey, K.H. Parker and D. O'Hare

Chapter 3,5: MA Ghanem, M Thompson, RG Compton, BA Coles, S Harvey, KH Parker, D O'Hare, F Marken: Microwave induced jet boiling investigated via voltammetry at ring-disk microelectrodes. Journal of Physical Chemistry B 110 (2006) 17589-94.

A US patent (Ref 11/565083) has been filed and covers the method of operation, geometry and operating mode of the tissue perfusion sensor developed in this thesis.

A European patent is now being drafted and will cover the use of the sensor to distinguish between different types of tissue. This relates to the transient current response at the electrode **(Chapter 3 and Chapter 6).**

1

Introduction

1.1 Tissue perfusion

Tissue perfusion describes the movement of respiratory gases, nutrients and metabolites within tissue. Tissue perfusion is the microscopic mass transport mechanism that cells rely upon to exchange nutrients and metabolites or waste products. It has two components, a diffusive and a convective one. The convection term is predominant in the capillary blood vessels, whilst the diffusive term is predominant outside the capillaries. To illustrate this, we can consider a single cell in tissue. The nutrients it relies upon such as oxygen or glucose, will be transported by convection in the capillaries, then by diffusion from the capillaries to the cell. Similarly the metabolites or waste products of the cell such as carbon dioxide or lactate, will be transported away from the cells by diffusion until they reach the capillaries where they will be convected away. This combination of diffusion and convection mass transport is what tissue perfusion describes.

Understanding tissue perfusion, or microcirculation as it is also known, began with the work of August Krogh, a Swedish physiologist who was awarded the Nobel prise in 1920 for his work on microcirculation. He demonstrated that blood flow in tissue is regulated by capillary vessels opening and closing to meet the tissue oxygen needs. He published "The Anatomy and Physiology of Capillaries", a book in which his observations and measurement of the mass transport mechanisms in tissue are further developed (1). One of the key observations is that in muscles, capillary vessels are ordered in such a way that they all supply a comparable cylindrical volume of cells. Based on this observation, Krogh and Erlang proposed a model for the diffusion of oxygen from the capillaries and into the tissue. This model is called the cylinder model illustrated in Figure 1.1 and described by the following equation:

$$U(r,y) = P(y) - \frac{m}{D\alpha}\left[\frac{R_t^2}{2}\ln\left(\frac{r}{R_c}\right) - \frac{r^2 - R_c^2}{4}\right] \tag{1.1}$$

Where U (r, y) is the partial pressure of oxygen PO_2 (mmHg) located at point (r, y); $P(y)$ is the PO_2 at a the point y on the capillary wall where $r = R_c$; R_c and R_t are the radii of the capillary and tissue cylinder, respectively; D and α are the diffusion (cm^2/s) and solubility

coefficients for O_2 (mlO_2/g.mmHg) respectively; and *m* is an the O_2 consumption rate (mlO_2/g.s).

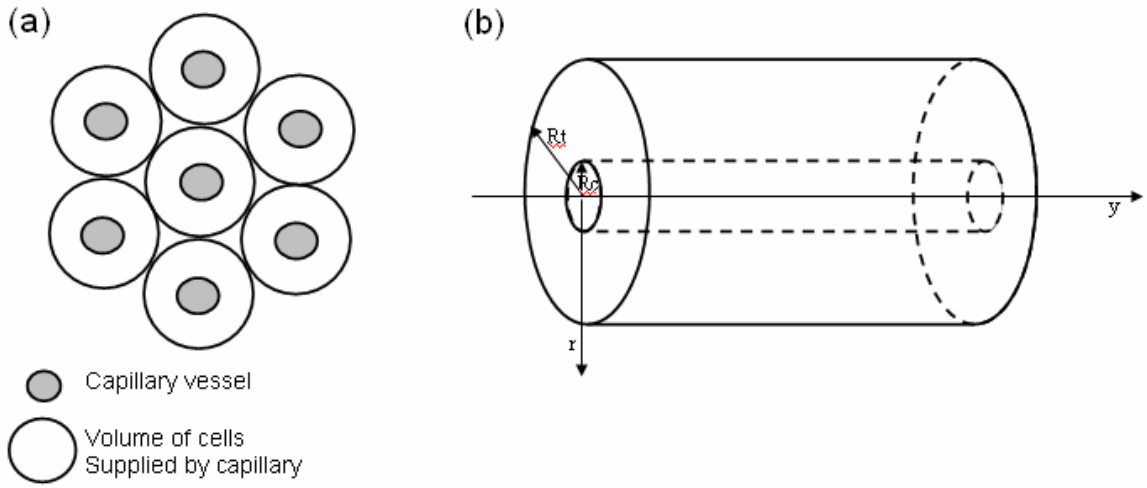

Figure 1.1: (a) Schematic of the cross section through a muscle. (b) Diagram of the Krogh-Erlang model for the diffusion of oxygen from a capillary towards the tissue. The internal cylinder with radius Rc represents the capillary, The outer cylinder with radius Rt represents the volume of cells supplied by the capillary.

The work of Krogh helps describe tissue perfusion as a cellular level mass transport mechanism that maintains the cell activity. The levels of perfusion in a tissue often change, when it drops severely or for a prolonged periods of time the cells will suffer and their survival will become compromised. This is referred to as poor perfusion and when it occurs in vital organs such as the heart or brain it can have fatal consequences. In general, tissue perfusion drops because of a blockage in the vascular network, this occurs for instance in wounds, during heart attacks (myocardial infarction or coronary thrombosis), strokes, venous ulcers, arthritis and in many other serious health problems.

Today tissue perfusion is studied for two main reasons; the first is to gain a fundamental understanding of cellular level mass transport in the body. The work of Michel and of Levick highlight the advances done over the past forty years (2-8). Michel and Curry provide a good review of the microcirculation along with the books by Charm

and Kurland or Wiedeman et al. (9-11). The second reason tissue perfusion is studied is to develop responses to the health problems associated with extreme levels of perfusion. Work in this area focuses, for instance, on finding ways of reperfusing hearts following ischemia (12) or improving wound healing (13-15); in these events the damage is caused by a drop in perfusion levels. Other cases include limiting angiogenesis and blood supply to tumours (16), in these events it is high levels of perfusion which are damaging.

1.2 Existing perfusion measurement techniques

There is a growing number of techniques that can be used to measure tissue perfusion:

- Functional magnetic resonance imaging (fMRI).
- Laser Doppler flowmetry (LDF)
- Radioactive or fluorescent microparticules injection
- Hydrogen clearance
- Heat clearance
- Ultasound
- Visual reflectance
- Pressure, velocity sensors

Although they are reported to measure tissue perfusion, most of these techniques measure blood flow not tissue perfusion. The misunderstanding comes from the loose interpretation made of tissue perfusion, which tends to include any flow or mass transport measurement in tissue. In fact, tissue perfusion occurs on a much smaller scale. In this thesis we will refer to tissue perfusion when dealing with cellular level mass transport mechanisms. Of the techniques listed above, the ones that actually measure tissue perfusion as we define it are:

- Radioactive or fluorescent microparticules injection
- Laser Doppler flowmetry
- Heat clearance
- Hydrogen clearance

The other techniques do not yet have the spatial resolution to measure on the micron level. Most of these reach their measurement limit around 2 mm^3; this is notably the case of fMRI and the ultrasound techniques, which are otherwise great tools for performing blood flow measurements.

We will now describe the basis of these four techniques and explain why they too lack key features needed to study perfusion. The inadequacy of the current measurement techniques has motivated our work towards developing a new technique.

In the radioactive or fluorescent micro-particles technique, micro-balls are injected into blood vessels upstream of the tissue being investigated. These micro-balls are either fluorescently or radioactively labelled and they will be transported by the blood through the tissue. When the particles reach the capillary level, they will get lodged in the capillaries because they are slightly larger than the capillary diameter. This is generaly done in animals because the tissue then has to be excised and slices prepared so that the micro-balls that have become lodged can be counted under the microscope. Blood flow is estimated by considering the number of capillary vessels that were open and active and extrapolating the volume flow rate in that slab of tissue (17,18). In bone blood flow, this method is considered to be the "gold standard" (19,20). The problems with this technique are that it is destructive, which makes it unsuitable for humans. Also the assumptions made about calculating blood flow from the number of open capillaries is debatable and there is no consideration of alternative mass transport routes, such as diffusion and the lymphatic flow as pointed out by Fluck et al. (21). As a result, blood flow is generally underestimated using this method. Despite this, it is often used as a benchmark against which to compare other tissue perfusion measurement techniques (22,23).

Laser Doppler flowmetry uses a monochromatic laser beam that is shone at the skin surface. The light that is reflected from moving objects such as blood cell and vessel wall, will undergo a Doppler shift. The amount of shift is related to the speed of the object. The detection of the reflected laser light is made by photodetectors. Blood flow is then correlated to the speed of the red blood cells (24,25). This technique is now well established and has been well reviewed (26,27). One of the key application of Laser Doppler flowmetry is the monitoring of burns (28,29). This method only gives relative values and not real blood flow because the volume probed varies due to the nature of the

technique. Another disadvantage is that the penetration of the laser into tissue is limited, thus the technique is mostly restricted to surface blood flow measurements, although recently it has been used endoscopically (30).

Thermal clearance is one of the oldest techniques used for measuring tissue perfusion and is still in use today (31-35). It involves a heating source and a thermocouple both of which are placed in tissue. The heating source heats the tissue and monitors the time needed for the tissue to return to the original temperature after the heating source is turned off. The understanding is that the circulating blood will cool the tissue back to normal levels that is 37 ° C. There are two problems with this method. The first is that the temperature resolution has to be very accurate because the amount of heating that can be administered is limited because of risks of burning the tissue with too much heating. The other problem is that the response of the body to over-heating often involves vasodilatation and blood flow alterations which lead to unnatural or stimulated tissue responses. It is thus difficult to be certain of the validity of the mass transport measurement made using this method.

The hydrogen clearance techniques, also called the hydrogen wash in / wash out technique, was developed by Aukland et al in 1963 (36) and was further developed by Lubbers and Stosseck in the seventies (37,38). In this technique, a known quantity of hydrogen gas (H_2) is introduced into the breathing air or injected into the artery of an animal or patient. The surgeon positions a platinum electrode in the tissue of interest. This electrode is held at a potential such that it detects all dissolved hydrogen gas that comes in contact with its surface. Once the amount of H_2 detected reaches a steady state, the tissue is assumed to be saturated and the supply of H_2 is turned off. The clearance of H_2 is then monitored. H_2 is removed from the tissue in very much the same way as the metabolites of a cell. Through monitoring the H_2 clearance, blood flow can be estimated by approximating the volume of the blood vessels in the tissue in which the measurement is made. This method is also considered to be one of the “gold standard” of tissue perfusion measurements and has been well reviewed in the past by Young as well as by Harrison and Kessler (39,40). It is used for heart perfusion measurements (41,42), brain measurements (43-45), or to compare and calibrate other measurement techniques (32,46-49). There are however problems with this method in that it only provides one

measurement for each clearance. Repeated measurements are possible but the time required to saturate then clear the tissue is rather long; usually 15-20 minutes are required and this can double or triple in poorly perfused tissue (39,50). This poor temporal resolution was somewhat improved by measuring the arrival of hydrogen rather than its departure from a tissue, this allows for measurements every 5 min (51). Still this poor temporal resolution is a significant limitation of the technique. Other types of gases have also been used for clearance measurements such as Nitrous oxide; the technique and its limitations remain the same however (52-54).

Current tissue perfusion measurement techniques have some clear disadvantages and limitations. The main drawbacks are the poor spatial resolution, poor temporal resolution and poor choice of marker for monitoring perfusion. These limitations have motivated our work in developing a novel perfusion measurement technique which combines high spatial and temporal resolution and provides physiologically accurate measurements of the mass transport mechanisms involved in tissue perfusion.

1.3 The ring-disc, collector-generator microelectrode method

We have developed a method of measuring tissue perfusion that overcomes the limitations of the established techniques by enabling cellular level measurements, continuous monitoring and use of diffusible and inert tracer. The technique we have developed is an electrochemical technique which involves implanting two platinum electrodes into the tissue of interest. The two platinum electrodes are used in the collector-generator assembly. In this technique one electrode generates hydrogen gas by electrolysis of water whilst the other, placed a distance away, collects the generated hydrogen gas. The mass transport mechanism that allows the dissolved H_2 to move from the generator to the collector electrode is tissue perfusion. The transport of CO_2 in tissue from a cell where it is generated to the capillary where it is removed is very much analogous to the movement of H_2 in our technique. In a tissue where perfusion levels are high, most of the H_2 generated will be washed away by the capillaries before it can reach the collector electrode. As a result, the level of collected H_2 will be low. In a tissue where perfusion levels are low, the H_2 generated will not be washed away and a large portion of

it will be collected. The collection efficiency (CE) is defined as the percentage ratio of the collector to generator current and is often used to describe these measurements. This is the basis of the technique which was pioneered by Stossek and Lubbers in 1972 (38). In their work, they presented the use of two disc shaped Pt electrodes for the measurement of tissue perfusion in the brain. Their approach was successful although it still relied on pulse generation rather than continuous generation of H_2. This was because of the large size of the electrodes used (i.e. 200 μm diameter), which would produce too much hydrogen if used continuously. Another problem with the approach was the shape of the electrodes, both discs. This implies that the sensor has a preferred orientation, or that not all directions in which perfusion is acting will be measured by the sensor. In our approach the problems associated with the size and orientation of the sensor are overcome by using micron sized ring-disc electrode as the collector-generator. Figure 1.2 shows a schematic view of the sensor in tissue and the way it works.

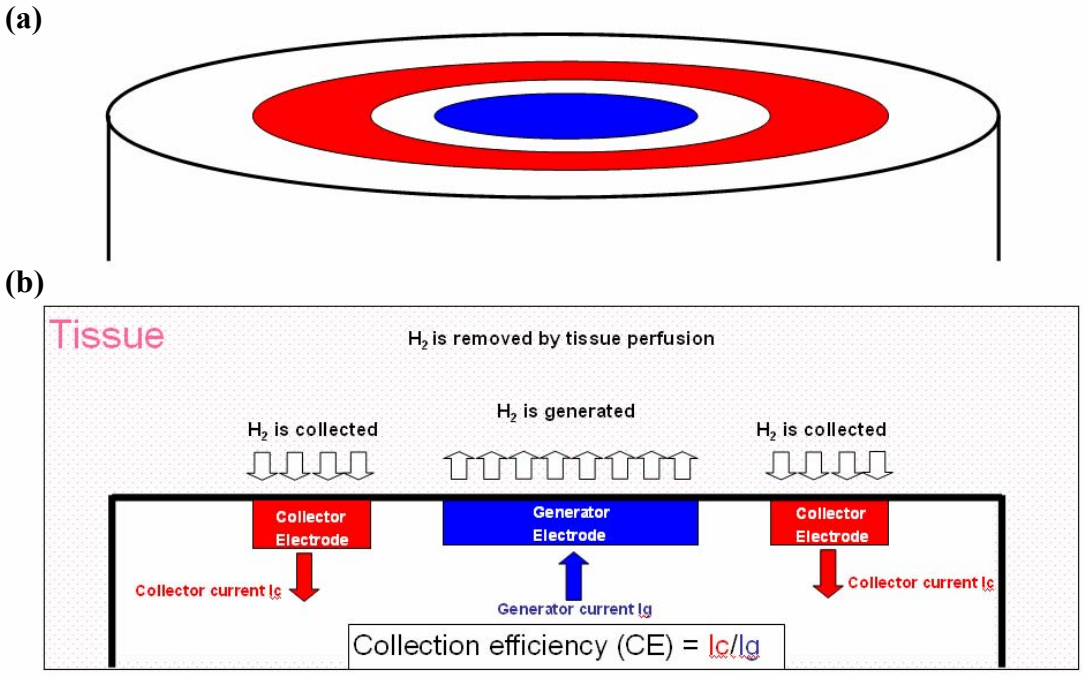

Figure 1.2: (a) Three dimensional view of the sensor, the ring is shown in red and the disc in blue. (b) Section view of the sensor inserted into tissue. Again the disc is in blue and the ring in red. This illustration shows a disc generating case, with hydrogen being generated at the disc and then being either collected at the ring or removed by tissue perfusion.

1.4 Electrochemical methods

The sensor used relies on electrochemical methods which will now be described briefly. Electrochemistry is concerned with the events that take place at the interface between an electrical conductor and an ionic conductor through which a current is flowing. In our case we use these techniques to quantify the movement of H_2 from one electrode to another. The collector and generator electrodes both made of platinum perform different reactions. The generator produces H_2, the tracer molecule, by electrolysis of the water found in tissue, whilst the collector detect H_2 which reaches its surface. The steps involved in either reaction are described in Figure 1.3 where we see the link between the mass transport and the electron transfer. One of the advantages of using electrochemical techniques is that there is a direct relationship between the number of tracer molecules that have reacted at the surface of an electrode and the current that is measured. This imparts great resolution to the measurements made.

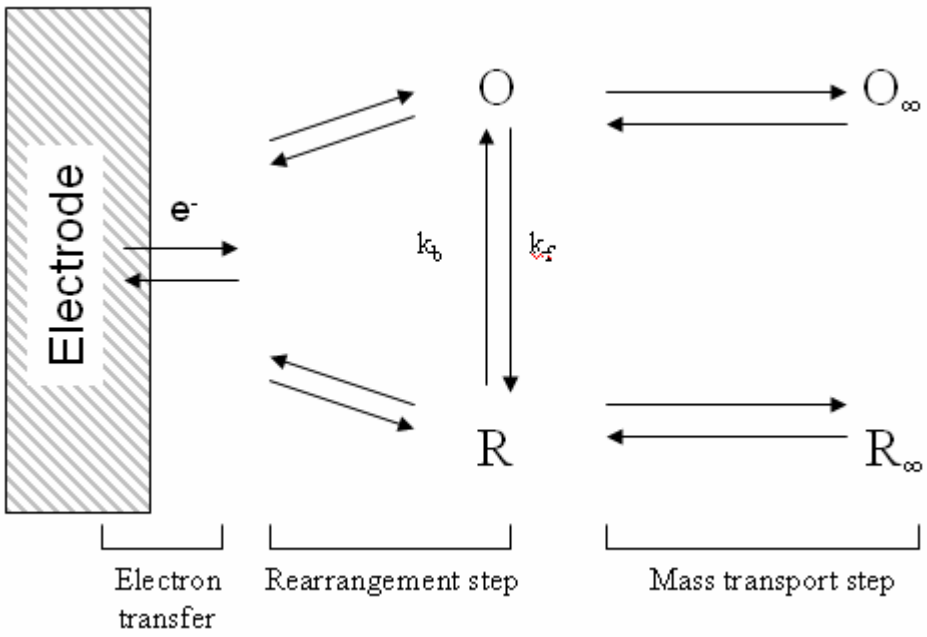

Figure 1.3: Scheme of electron transfer at an electrode. The first step is the mass transport which brings the species close to the electrode. The rearrangement of the species and the space around it occurs before and after the electron transfer.

There are two ways of forcing a reaction at the surface of an electrode either by imposing a voltage and monitoring the current or imposeing a current and monitoring the voltage. The first is done through a potentiostat (i.e. a constant voltage source) and the second through a galvanostat (i.e. a constant current source). Potentiostats are more commonly used as they allow for more selectivity of the reaction that takes place at the electrode surface. Galvanostats provide a control of the flux at an electrode, which is useful to control the concentration of products of a reaction because of the direct link between current and the number of electrons passed. In this thesis both instruments have used. The potentiostat is used for three techniques; cyclic voltammetry, chronoamperometry and constant voltage amperometry recordings. Cyclic voltammetry was used to identify precisely the potentials and current levels that were required to collect and generate H_2. Constant voltage amperometry was always used to collect the hydrogen, because the levels collected changed throughout the course of an experiment. Often the generation of H_2 was also done using constant voltage amperometry. The galvanostat was used exclusively to generate a fixed flux of H_2. The reason for generating fixed flux of hydrogen is that is makes the interpretation of the results simpler but also it eliminates any variations in the production of hydrogen. These variations could be due to changes in the mass transport of water in tissue or degradation of the surface of the generator electrode, for instance through fouling.

1.4.1 Microelectrodes

The electrodes used in this work are microelectrodes. Microelectrodes are electrodes which have at least one characteristic dimension on the micron scale (i.e. radius of the disc, thickness of a band etc.). When this is the case, the behaviour of the electrode departs from that of a macroelectrode. The main difference in the behaviour comes from the changes in mass transport to and from a microelectrode. As a result of their small size microelectrodes have a number of advantages such as, improved mass transport, high signal to noise ratios, increased temporal resolution, low charging currents and reduced solution resistance artefacts (55,56).

Microelectrodes have been used extensively and their advantages have made them the number one choice for electrochemical investigation. Microelectrodes come in a

variety of different shapes; ring, wire, band, tubes, arrays, but most commonly the disc. Disc microelectrodes are predominant mainly due to their ease of fabrication and as a result the breadth of knowledge regarding them is significant. In this thesis both disc and ring microelectrodes are used. Ring microelectrodes and especially thin ring microelectrodes are used because they benefit from further improved mass transport properties. This is because the ratio of electrode edge to electrode area is far greater than for other disc or even band microelectrodes. This is important because the edge of an electrode benefits from radial mass transport, whereas at the centre of the electrode the mass transport is mostly normal. Consequently the current density at the edge is higher than at the centre of an electrode. This effect is known as the edge effect and is described in Figure 1.4.

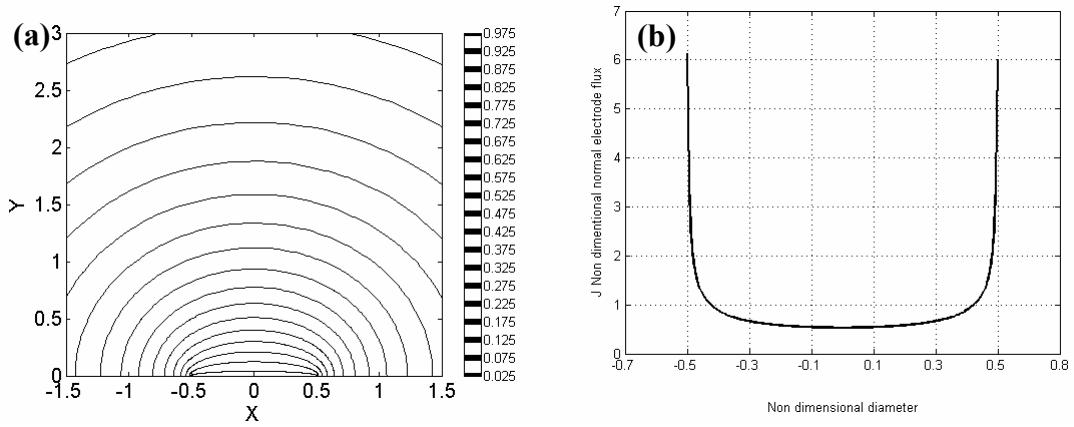

Figure 1.4: Two dimensional view of the edge effect at a disc microelectrode. **(a)** Concentration contour. **(b)** Flux over the surface of the electrode. The edge of the electrode is clearly passing more current than the centre, which is representative of the edge effect. The electrode has dimentions -0.5<X<0.5. (Plots taken from simulations presented in Chapter 3)

The diffusion limiting current at a disc electrode set in an insulating plane is defined by Equation 1.2 (57):

$$I_D = 4nFDcr \tag{1.2}$$

Where n is the number of electrons exchanged, F is Faraday's constant, D is the diffusion coefficient of the species, c its bulk concentration and r the radius of the disc. Typical currents at the disc are between 6 and 1 μA depending on whether hydrogen was generated or collected.

Whilst the diffusion limiting current for a thin ring set in an insulating plane is defined by Equation 1.3 (58):

$$I_R = nFDc\frac{\pi^2(a+b)}{\ln[16(b+a)/(a-b)]} \tag{1.3}$$

Where a and b are the inner and outer radii of the ring respectively. A thin ring is defined as having a/b >0.91. Our ring electrodes have a/b ratios between 0.92-0.95. Typical currents at the ring are between 10 and 1 μA again depending on whether it generates or collects H_2.

The main motivation for using microelectrodes is their small size which brings our measurement tool within the range of capillary and cellular length scales. The other reason is their unparalleled ability to detect changes in mass transport.

1.4.2 Ring-disc microelectrode

Ring-disc microelectrodes are a type of dual electrode detector that are becoming popular for electroanalytical measurements. Other types of dual electrode detectors such as the disc–disc and the band–band have featured more predominantly in recent publications (59-63) although this is probably due to their ease of fabrication rather than their properties as sensors. Indeed, the ring-disc microelectrode has advantages over other dual electrode detectors in that the two electrodes are radially symmetric and of different shapes. The radial symmetry of the electrodes simplifies the positioning of the sensor

experimentally as the sensor has no preferred axis. The different shape of the electrodes is useful because very versatile measurements are possible owing to the significant difference in the edge to area ratios between the ring and the disc. These features make the ring-disc microelectrode, a powerful dual electrode detector particularly when used as a collector-generator for the study of mass transport effects.

1.4.3 Hydrogen evolution on platinum

Hydrogen generation or hydrogen evolution on electrodes is one of the most studied processes in electrochemical history. A wide range of electrode materials and solution conditions have been used to study this process, which have greatly contributed to our fundamental understanding of electrode reactions (64-66). In acidic solutions, the overall reaction is

$2H^+ + 2e^- \rightleftharpoons H_2$

Or

$2\ H_3O^+ + 2e^- \rightleftharpoons H_2 + 2H_2O$

whilst in neutral and basic solutions the following reaction prevails:

$2H_2O + 2\ e^- \rightleftharpoons H_2 + 2OH^-$

Hydrogen evolution is a reaction that involves an absorbed intermediate. Cyclic voltammetry provides a way of showing the presence of absorbed intermediates (see Fig 1.5). The absorption occurs at potential slightly positive of the H_2 evolution potential. The two peaks denoted Hs and Hw in Fig 1.5 are characteristic and indicate the presence of strongly and weakly absorbed hydrogen respectively (M-H bonds). As the level of over-potential is increased the bonds between the metal and the H atoms will be broken to form the H_2. There are two possible mechanisms that can lead to the breaking of the M-H bond, either a chemical or an electrochemical mechanism. In ether case the strength of the M-H bond bears significancantly on the rate of the hydrogen evolution. The rate limiting step can either be the formation of the H-M intermediate or the breaking of the

H-M bond. Volcano plots are useful at illustrating the relationship between hydrogen generation and bond strength for different materials. Figure 1.6 show one such plot taken from Krishtalik (67) and further discussed by Trasatti (68). From these we see clearly that platinum along with rhodium, rhenium and iridium display the highest current densities, meaning they posses the right bond strength to yield maximum H_2 generation.

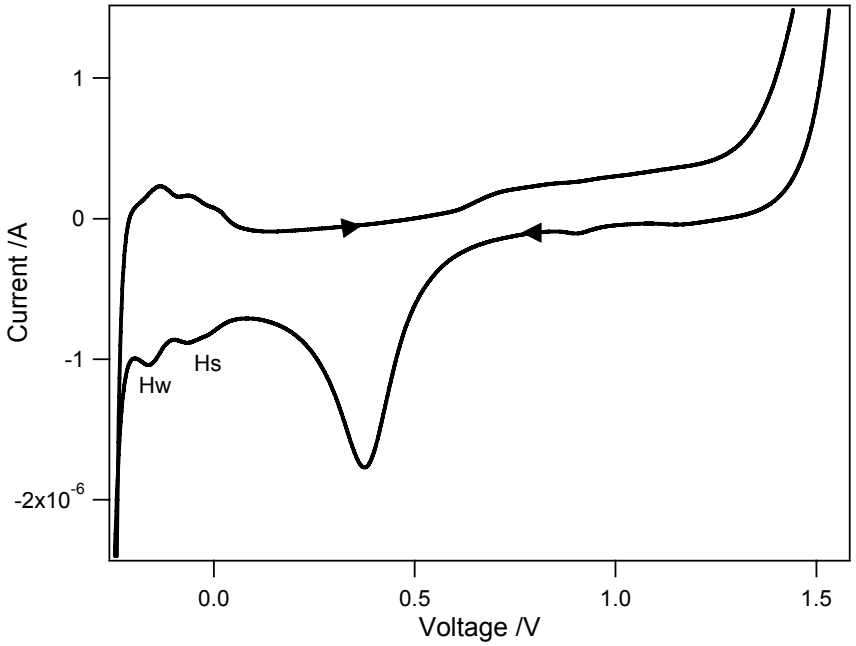

Figure 1.5: Current voltage plot for a 125 μm Pt disc electrode in 0.5 M H_2SO_4 with scan rate of 0.1 mV/s (Ag/AgCl reference electrode). Arrows indicate the direction of the scan, which shows all of the characteristic features of hydrogen evolution on polycrystalline Pt. Hw and Hs refer to the peaks that represent the weakly and strongly absorbed hydrogen. The large peak that occurs around 0.4 V is due to the stripping of the platinum oxide.

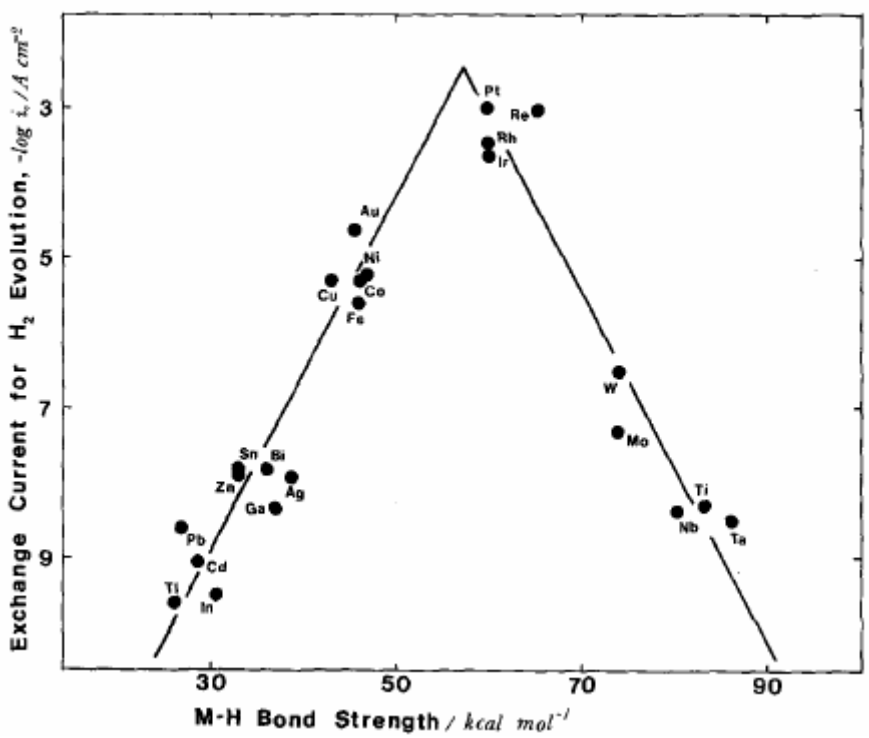

Figure 1.6: Exchange current for electrolytic hydrogen evolution vs. strength of intermediate metal-hydrogen bond formed during electrochemical reaction (from Krishtalik (67)).

The H_2 formed is in a dissolved form in the solution surrounding the electrode (in tissue this is the extra-cellular fluids). If the rate of H_2 generation is too great; it can lead to the formation of bubbles, which is unwanted both because it complicates the measurements of current but also because it may be harmful to the tissue. The classical view of bubble nucleation was first proposed by Volmer and Weber (69), this process has been well reviewed by Jones et al. and will only briefly be discussed here((70) and references therein). As H_2 is being generated, it will saturate the solution surrounding the electrode. As the level of saturation increases, the molecular attraction energy increases, the dissolved H_2 is said to be in a bound state and has a net negative energy (relative to a free molecule at rest). This state is favourable for phase transfer. Yet for a bubble to grow, the pressure within the bubble has to overcome the surface tension of the solution on its wall. Initially the surface to volume ratio is very high, which means extremely high levels of saturation are needed. For a container free of defects on its walls, bubble

nucleation is typically initiated at 100 times super-saturation. When defects are present on the walls of the container or in the solution, bubbles appear at 10 times super-saturation.

In our case the electrodes producing the hydrogen may have defects on the surface or at the interface between the electrode and the insulator. However, we attempt to minimise this by careful polishing and electrode cleaning. Furthermore, the reduced size of our electrode means the probability for bubble formation is further reduced (i.e. the most likely place for bubble formation has to be the surface of the electrode because of the high concentration). Both these points suggest that we will be able to generate supersaturated H_2 before bubbles will form. Macpherson and Unwin reported H_2 super-saturation up to 3-4 times using a 25 μm disc diameter electrode in 0.1 M KNO_3 before bubbles were seen (71). This is particularly useful as it will significantly improve the time resolution of our measurement technique and mean we can probe larger volumes with smaller electrodes.

1.5 Numerical modelling of electrochemical processes

Numerical modelling in electrochemistry has been used for over thirty years. It is mainly concerned with solving concentration profiles over time and space in order to explain the processes occurring at the electrode and within its vicinity. Feldberg is credited as being the first to use numerical simulation to solve electrochemical problems back in 1964 (72-74). Since then the subject has been greatly advanced by the work of Bard and Britz for instance (56,75). Numerical modeling in electrochemistry is today well established and routinely used. Solving the governing mass transport and kinetic equations can be done in a number of ways. In the past finite difference was the only viable discretisation method; today more methods are available, namely finite element, finite volume and boundary element methods. The choice of solver was motivated by the computational power needed and the ease with which it could be programmed. Advances in hardware and software means one can now run electrochemical simulations on a personal computer through commercially available, user friendly software. It thus makes sense to use discretisation techniques that are more flexible and powerful. In this thesis, the finite element software Comsol was used to run the simulations. The main advantages

is that non-uniform mesh elements can be constructed, which makes the modeling of complex geometries possible. The robustness of this package has been well demonstrated in electrochemical publications and elsewhere (76-81).

1.6 Aims and outline of the present work.

The aim of this work is to develop an electrochemical tissue perfusion sensor. The sensor should overcome the limitations of existing tissue perfusion measurement techniques and be capable of measuring on the cellular level in a continuous fashion using a diffusible and inert tracer.

This aim can be broken down into four specific objectives:

- Develop a production protocol for the fabrication of a collector-generator electrode assembly. The electrochemical sensor selected is the ring-disc microelectrode which combines small size and multi-directional mass transport measurement capacities.
- Develop a numerical model of the electrochemical processes occurring at the ring-disc microelectrode to aid the design and further our understanding of the sensor behaviour.
- Test the sensor under different mass transport modes to identify the mass transport measurement capacities of the sensor in environments that are relevant to tissue. Tissue perfusion involves a diffusive and convective term acting in a medium with complex geometry; all of these will have to be investigated.
- Test the sensor *in vitro* in a variety of tissue environments as a proof of principle for the operation of the sensor.

In Chapter 2 a novel ring-disc microelectrode fabrication method based on cylindrical sputter coating is described. The machine built for this purpose is characterised and optimised to produce ring-disc electrodes ranging from 28 to 150 μm in diameter and with ring thicknesses from 0.5 μm to 3 μm. The electrodes made display an electrochemical behaviour that agrees well with theoretical predictions and the fabrication method developed produces electrodes on a large scale.

Chapter 3 discusses theoretical aspects of the ring-disc microelectrode and its use in different mass transport modes. To this effect a number of finite element models are presented, they cover amongst other things investigations into the influence of electrode

size, operating mode and mass transport on the measurement made with the ring-disc sensor.

Chapter 4 pertains to diffusion and the use of the sensor to detect changes in this mass transport mode. This chapter also serves to introduce the experimental techniques that are used in subsequent chapters.

In Chapter 5 the effects of convection mass transport are considered. The ring-disc microelectrode is used to measure changes in flow through tubes, porous media, pulsatile and jet flow. These provide a way of characterising the behaviour of the sensor in environments that are close to those observed in tissue as well as validate some of the numerical predictions and display the measurement potential of the sensor.

Finally Chapter 6 describes the steps taken to prepare the sensor for use *in-vivo* as well as some proof of concept perfusion measurements using the ring-disc microelectrode in different types of tissue and animal models.

2

Ring-disc microelectrode fabrication

The development of a novel fabrication process for making ring-disc microelectrode is presented. The new method relies on the use of an inverted cylindrical sputter coater, which coats micron size layers of platinum onto polyimide insulated wires. The construction and optimisation of the machine is presented along with the electrodes produced using this process.

2.1 Introduction

Ring-disc microelectrodes are made up of two electrodes, the ring and the disc. Disc microelectrodes are well established electrodes, the most popular fabrication methods have been covered in a book by Bard and Mirkin (82) and reviews by Wightman and Wipf (83). Perhaps the simplest method of making a disc electrode is to seal a micron sized wire into an insulator, often by sealing the wire into a pulled glass capillary. The complexity in making ring-disc microelectrodes lies in the fabrication of the ring. Currently there are four ways of making micro-ring electrodes, all of which can be adapted to make micro ring-disc electrodes. These methods are micro-lithography, electroless deposition, conductive paint deposition and vapour deposition and they will be briefly described in the following paragraphs. Because none of the current methods of fabricating ring-disc microelectrodes suited our requirements, a novel method was developed based on the use of a special type of physical vapour deposition. The design, construction and characterisation of this coater is described in the latter part of this chapter.

2.1.1 Micro-lithography

Although micro-lithography was not used in this work it is worth describing the technique and some of its advantages and disadvantages. Microlithography is a popular and well established method of making microelectrodes of varying sizes and shapes; the technique has been well described in a number of books and reviews (84-86). It is basically the same method that is used in integrated circuit fabrication. The process starts with a metal substrate being coated with a photosensitive material (photoresist). Selective areas are then exposed to UV light through a mask. A developing process leaves resist on the chosen areas. The metal substrate areas not covered by the photoresist are then etched away. Once the photoresist is removed the patterned metal electrodes are revealed.

Two types of photoresists exist; positive or negative resist. Positive resists are initially marginally soluble. Upon exposure to UV light, they become highly soluble. A positive image of the mask is thus retained. Negative resists have the opposite properties as they become less soluble after exposure to radiation. It is therefore the negative image of the mask that is retained.

One of the main drawbacks of microlithography is that the electrodes produced are either recessed or protruding. Protruding electrodes occur when no insulator is used to seal the electrodes. When an insulator is used, a recess is almost always present. Both of these geometries are non-ideal and they require more complex interpretation especially when the electrodes are used as collector-generators. Theoretical and experimental studies of single electrodes have shown that a recess or a protrusion will significantly disrupt the current density at an electrode; a recess will decrease the current whilst a protrusion will increase it. (87,88).

Another drawback of this method is that ring-disc electrodes cannot be fabricated using lithography, this is because the connection to the disc must pass through the ring. As a result the ring is not continuous, which again means that the electrodes are not ideal. Figure 2.1 shows what can be achieved by lithography; such designs have been used by many authors for collector-generator applications (89-91).

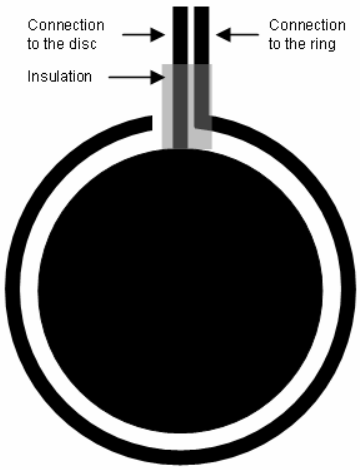

Figure 2.1: Typical ring-disc electrode produced by micro-lithography. The ring is incomplete and one or both electrodes are either protruding or recessed.

2.1.2 Electroless deposition

Electroless deposition is a process by which an insulating material can be coated with a conducting material. Its name differentiates it from the more classical electrode deposition where the deposition is driven by an electron flux occurring at the surface of a conducting material (i.e. an electrode). In electroless deposition, the flux of electrons is

not provided by a conducting surface, instead it is provided by a chemical reductant in solution. Not all conducting materials can be deposited in this way, there is however, a process for platinum black deposition which was investigated.

The first step is to make a solution containing Pt, this is done by mixing 0.3 g chloroplatinic acid ($H_2PtCl_66H_2O$) with 10 g of deionised water. This constitutes a 3% solution. To initiate the reaction a few drops of a 5% solution of lead acetate ($Pb(C_2H_30_2)_2$) are added to the solution. Platinum black will then form on any surface placed in solution. This process was used to coat insulated Pt wires by simple immersion.

The rate of the deposition is controlled by the amount of lead acetate that is added to the chloroplatinic acid solution. (Method taken from Rosebury (92)).

This deposition technique was rather unsatisfactory in our hands. Very limited deposition was observed even on the walls of the glass beaker containing the platinising solution. Moreover we later discovered that the solutions used are also the basis for the constant current deposition of Pt (93). This further casts a doubt on the validity of the method proposed by Rosebury, if current is being used by others to force the reaction then it is unlikely that the reaction can proceed by itself. The limited success achieved with this method meant we did not proceed with it.

2.1.3 Conductive paint deposition

Conductive paint deposition was used in this work to fabricate Pt rings and carbon rings. The first step is to make a disc electrode. In our case the size of the insulator surrounding the disc must be small and controllable. The only reliable method in this case is to use a capillary puller to make the disc electrode. This method is well described by Wightman and Wipf (83) and Miller and Pelling (94) and involves sealing a fine wire into a glass capillary by means of a capillary puller. Careful polishing of the tip reveals a disc surrounded by a uniform layer of glass.

To make ring-disc microelectrodes, a 50 μm Pt wire (99.99% Advent) was first sealed into a 1.5 mm borosilicate glass capillary (World Precision Instruments Inc., Sarasota Florida) using a Narishige (Tokyo, Japan) PB7 vertical puller. The next step was to deposit a layer of conducting paint onto the outside of the glass. Initially a carbon paint (Spi 05006AB West Chester USA) was used because it was cheap and dried in air.

Subsequently a platinum paint was used (Harovia Liquid gold). Applying the paint to the glass was done by dip coating or by rotating the capillary in a lathe and using a paintbrush to deposit the paint on the capillary.

For the platinum paint, multiple coatings were often required. To improve the deposition each layer was cured in the oven at 70°C for 15min. This removed the bulk of the solvent in the paint. Once the desired number of layers had been applied the capillary was placed in the oven at 700°C for 15min to pyrolyse the paint.

Connections were made to the wire (disc) and paint layer (ring) using silver epoxy and silver wires. The entire assembly was then cast in epoxy. Figure 2.2 summarises the process and Figure 2.3 shows some typical SEM pictures of the ring-disc microelectrodes produced in this manner. Achieving uniform paint deposition was the biggest problem with this method. Another problem encountered was that it was hard to have both ring and disc concentric (see Figure 2.3). The electrochemical behaviour of the carbon ring sensors is good as can been seen in Figure 2.4. The limiting currents for the disc are consistent with theoretical solutions, those from the ring less consistent (probably due to the recess or protrusion of the carbon ring). Only partial success was achieved with the Pt paint deposition. Getting the Pt to stick to the glass was a problem as well as achieving uniform and reproducible rings. Some of these problems were alluded to by MacPherson and Unwin (95). It seems the cleanliness of the glass and the freshness of the solution are paramount to achieving satisfactory rings. For making Pt ring-disc microelectrodes this fabrication process proved too inconsistent and time consuming so it was abandoned.

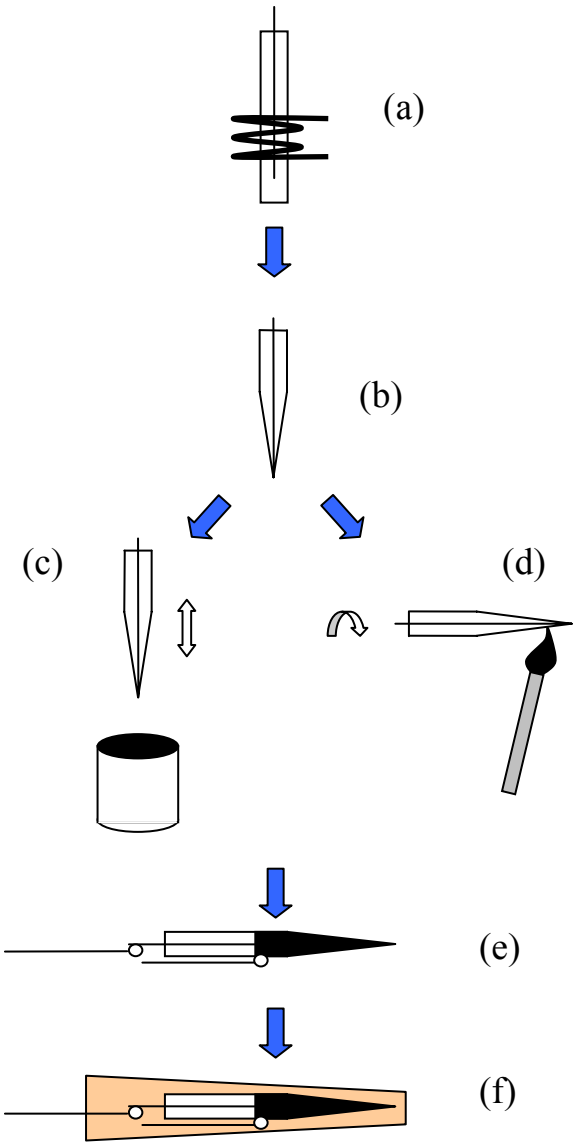

Figure 2.2: Steps involved in the ring-disc microelectrode conductive paint deposition fabrication technique. **(a)** A platinum wire is inserted into a glass capillary which is heated in a capillary puller. **(b)** The capillary has been pulled and the wire is sealed into the glass. **(c)** The capillary is dip coated repeatedly with a conductive paint (Pt or C). **(d)** Alternatively the conducting paint can be applied to a rotating capillary using a paintbrush. **(e)** Once the paint has dried (air drying for C, oven curing for Pt) connections are made to the ring and disc. **(f)** The entire assembly is sealed in epoxy resin.

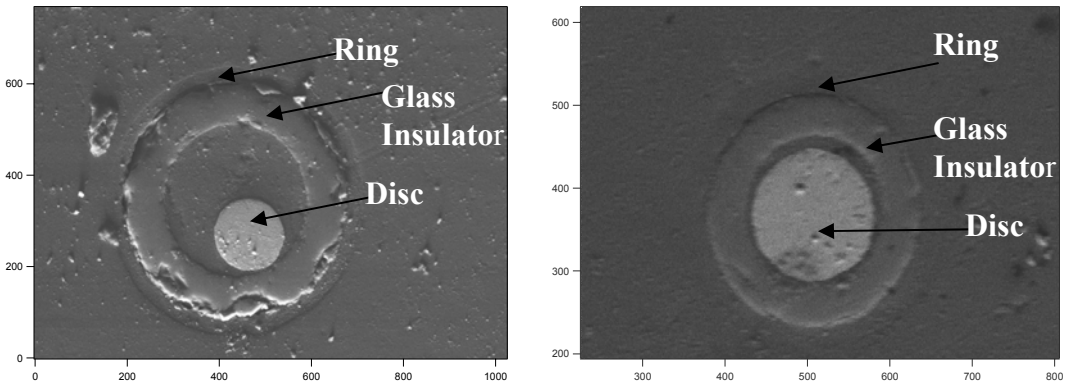

Figure 2.3: Scanning electron micrographs of ring-disc microelectrodes produced by the conductive paint deposition technique. The discs are 50 μm in diameter, the rings are seen only faintly as a small recess on the outside of the glass insulator. The rings shown here are made of carbon, a material less distinguishable under SEM. Left hand image shows a sensor with an eccentric disc. The right hand image shows a uniform and concentric electrode.

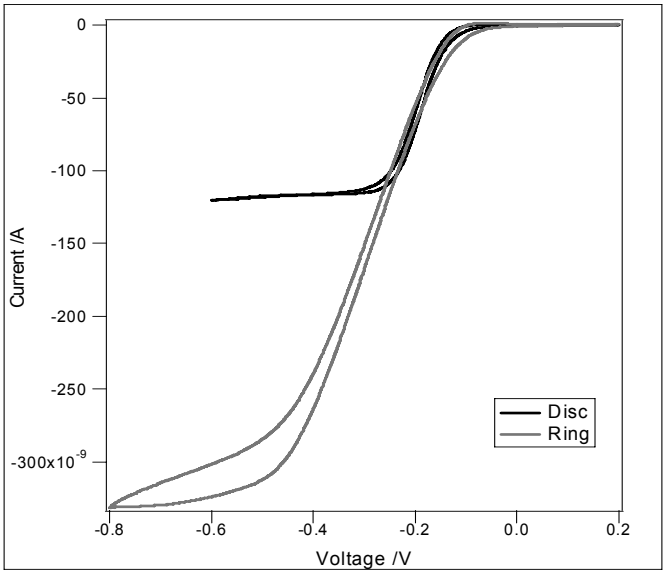

Figure 2.4: Typical cyclic voltammogram for an electrode produce by dip coating. The carbon ring (grey) and Pt disc (black) responses are shown in a 10mM solution of $Ru(NH_3)_6^{3+/2+}$ in 1M KCl.

2.1.4 Vapour deposition

Vapour deposition is an established technique that is used routinely in science and engineering for the fabrication of thin films. Rossnagel (96) and Swann (97) provide good reviews of the subject whilst Rosebury (92) and Roth (98) have written some very useful books on the subject in which most practical and theoretical problems are answered. Two types of vapour deposition exist, chemical and physical vapour deposition. Both of which have been used to make ring-disc microelectrodes.

In chemical vapour deposition (CVD), a gas mixture is made to react at a given temperature and pressure to produce the desired deposit within a vacuum chamber. CVD was first used by Zhao et al. to make carbon/carbon ring-disc microelectrodes (99). In their method, a carbon fibre is first coated with silica, then with carbon by introducing different gas mixtures at high temperature into the vacuum chamber. The deposition of silicon and carbon can be repeated to produce multiple coatings. A cut perpendicular to the carbon fibre axis reveals a carbon ring separated from the carbon fibre disc by a layer of silica. This method is elegant with the advantage that the insulator and then the carbon film deposits uniformly and from all sides onto the surface of the carbon fibre. As a result the ring and disc are radially symmetrical and uniform. The application of these electrodes has been demonstrated for dual analyte detection as well as for HPLC end column detection (100,101). Kovalcik et al. also used a similar CVD method coupled with electrode modification to fabricate different metallic ring-disc electrodes (102). The first stage involved the use of the CVD method to fabricate a tungsten/tungsten ring-disc microelectrode sealed in silica. In the subsequent step the tungsten electrodes were partially etched away followed by electroplating of the chosen metal into the voids. They illustrated this technique by making a Cu/Cu ring-disc microelectrode. This complex fabrication process, however, highlights one of the main drawbacks of using CVD in that not all materials can be deposited. Moreover, for those materials that can be deposited the operating procedures required are often quite complicated; this is especially true for metal deposition. Finally it must be said that achieving reproducible metallic microelectrodes appears difficult and the potential for mass production seems limited.

In physical vapour deposition (PVD), the material to be deposited is eroded away from a target surface by the bombardment of argon ions in a plasma. The bombardment of the target surface leads to the formation of a cloud/vapour of particles which will deposit onto any surface they come in contact with. This process is also referred to as sputter coating. In most cases to make a ring-disc microelectrode using PVD, a pulled capillary electrode is placed above the planar target of a sputter coater so that a layer of material is deposited onto all sides of the glass insulation to form the ring. Liljeroth et al. have perfected this technique, often rotating the capillary above the target to achieve more uniform ring thickness (77,103). The clear advantage of this method is that any conducting material can be sputtered to form a ring. There are, however, some disadvantages. The location of the capillary electrode above the target will significantly influence the uniformity of the ring as well as its radial symmetry about the disc. This is because the sputtered particles will only reach the surfaces facing the target (i.e. line of sight deposition). Rotating the pulled capillary electrode above the target helps to overcome this problem but it does not totally eradicate it, especially when thin rings are being deposited (i.e. $\leq$1 μm). Having a ring that is slightly eccentric or of non-uniform thickness is not so problematic if the sensor is used for dual analyte detection. It is, however, a problem when the ring-disc is used as a collector-generator because eccentric and non-uniform electrodes will complicate the interpretation of the measurements (77). Another disadvantage of using classical PVD targets to coat micron sized pulled capillary electrodes is that most of the sputtered target material is wasted as it never reaches the capillary electrode. This makes the process expensive, especially when precious metals are being deposited.

2.2 Design, building and characterisation of an inverted cylindrical sputter coater

To overcome the limitations of the existing fabrication techniques, a novel method for the fabrication of metallic ring-disc microelectrodes was developed. In this method an inverted cylindrical sputter coater is used to continuously coat micron sized insulated wires. The cylindrical target used in the sputter coater ensures a uniform and

symmetrical coating of the wire and its small size improves the deposition rate as well as minimising the cost and waste of the target. Design features such as the ability of the coater to deposit all conducting materials, its small dimensions and ease of assembly are presented. Following the optimisation of the operating parameters of the coater, namely the cathode voltage and chamber pressure, the deposition rate achieved for platinum is just below 1 nm/s. The smallest sensors produced have outer diameters less than 28 μm and rings as thin as 0.5 μm.

The method used is a PVD technique that overcomes the limitations associated with the previous use of this method, namely the non-uniform ring deposition and the waste of target material. As a result, the cost of the process is reduced and the electrode reproducibility is improved. This is achieved by using a cylindrical target rather than the classical planar target in an arrangement called the inverted cylindrical sputter coater. Inverted cylindrical sputter coaters were developed in 1935 by Penning (104) and have been well reviewed (105,106). Rather than sputtering from a flat target the sputtering occurs from the inside surface of a cylindrical target. This focuses the sputtered material towards the centre of the cylinder, which increases the deposition rates and improves the uniformity of the coating and has been shown to be well suited for the continuous coating of fibres or ribbons. Because the wires are passed through the target using a simple spooling mechanism, significant length of wires can be coated at once without having to break the vacuum or stop the sputtering process.

In our application, we have to consider the fact that the size of the wires to be coated rarely exceeds a couple of hundreds of microns, well below the typical size of fibres coated previously using inverted cylindrical sputter coaters (107,108). Another important consideration is the volume of the target. Most electrodes are made from precious metals of extremely high purity and are therefore expensive. If the size of the target can be reduced the overall coating process will be cheaper. By using a small cylinder target we are able to reduce the target volume as well as reducing the distance between the target and the wire to be coated. As a result the uniformity of the coating is improved, the deposition rates are greatly enhanced and the price associated with the coating is reduced.

2.2.1 Materials, methods and instrumentation

Coater

Figure 2.5a shows a detailed drawing of the coater and Fig 2.5b shows the cross sectional view of the sputter coater designed Figure 2.6 shows a picture of the coater and some of its components. All of the chamber components are standard vacuum components apart from the target holder. The evacuation of the chamber is first done by a rotary vane pump (1.5 Two Stage Edwards), then a turbo-molecular pump (Pfieffer TPH 190) is used to reach the lower pressures. The pressure in the chamber is monitored using either Pirani or Penning gages (Edwards) depending on the value of the pressure ($1\text{-}10^{-4}$ mbar for the Pirani and $10^{-2}\text{-}10^{-6}$ mbar for the Penning). All connectors, fittings and valves were purchased from Edwards, Crawley UK. The target holder was machined out of MACOR and houses the cathode (i.e. the target), and two copper cylinder anodes one above and one below the cathode. The target holder is removable, which makes changing the target easy as well as simplifying the cleaning and maintenance. The cathode is connected to a high voltage source (Brandenburg), whilst the anodes are connected to ground (not shown in drawing). The current passing between the cathode and the anodes during the sputtering is monitored and controlled as it gives a good representation of the amount of sputtering that is taking place and is indicative of the deposition rate (109).

Pt/Pt Ring-Disc microelectrode fabrication using a hollow cylinder sputter coater

Insulated wires are available from most precious metal suppliers and come in different sizes and with the advantage that the insulation thickness is known and consistent. We found that the best insulator was polyimide, because of its heat resistance and the apparent ease with which the sputtered particles stuck to it. This cannot be said for polyester insulated wires which are affected by heat.

Before coating, the polyimide insulated wire is cleaned in ethanol, then water and dried. The wire is then mounted onto spools; one above and one below the target holder. The speed at which the wire passes through the target is controlled by an electric motor fitted with a set of gears. To coat the wire, the chamber is first evacuated to a low pressure ($<10^{-5}$ mbar). The process of sputter coating occurs when a glow discharge is initiated between an anode and the cathode (- target). This is done by applying a negative voltage to the target (2.5 kV applied

across a ballast resistance 100 kΩ), and introducing argon, at a pressure of 0.3 mbar into the chamber. In the glow discharge process a free electron is accelerated toward the substrate by the applied electric field (voltage) and collides with Ar atoms causing positive Ar^+ ions to be formed. The argon ions are in turn accelerated by the field but in the opposite direction toward the cathode, and in doing so acquire significant energy from the field. When they strike the target at high velocity target atoms or molecules are 'sputtered' from the surface and being mostly neutral drift at random with their initial kinetic energy toward the substrate where they condense into dense solid films of the target material.

Once this process has stabilised, the insulated wire is passed through the cloud of sputtered target material at the centre of the cylinder. The thickness of the deposition is controlled by the rate at which the wire is fed past the target. Polyester-insulated Pt wires of different core diameter, 25, 50 and 125 μm (99.99% Goodfellow), were coated with Pt using this process. Once coated, the wires are cut into 3 cm long sections. Separate connections are made to the inner metal core and the outer metal sputtered layer using silver wires (99.99% Goodfellow) and conducting epoxy (Circuit Works). The entire assembly is then potted in epoxy resin (CY13GI+HY1300, Robnor Resins, Swindon). To reveal the ring-disc, the epoxy assembly is cut perpendicular to the wire using a diamond saw. The electrodes are then polished using aqueous slurries of 1, 0.3 and 0.05 μm alumina with rinsing and sonication between each polish. Finally the electrodes are cleaned by cycling the potential from -1.5 V to 1.5 V for 15 min at 2.5 V/s, then holding the potential at -1.5 V for 15min in 0.5 M H_2SO_4.

Chemical Reagents

Chemical reagents $Ru(NH_3)_6Cl_3$, KCl, (Aldrich) were used to make a solution of 10mM $Ru(NH_3)_6Cl_3$ in 1M KCl. The solutions were deoxygenated by bubbling with nitrogen for 20 min prior to use. Demineralised and filtered water was taken from a Purite Select system (resistivity of ≥14 MΩ cm).

Instrumentation

An eight channel potentiostat CHI 1030 (CH Instruments Inc. Texas) was used to control the voltage at the ring and disc microelectrodes which were placed in a glass

electrochemical cell also containing a large Pt mesh counter and Ag|AgCl (3 mol dm^{-3} KCl) reference electrodes. Visual reflectance thickness monitoring was carried out using a Filmetric F20. Scanning electron microscopy (SEM) imaging was carried out using a Jeol S610 system.

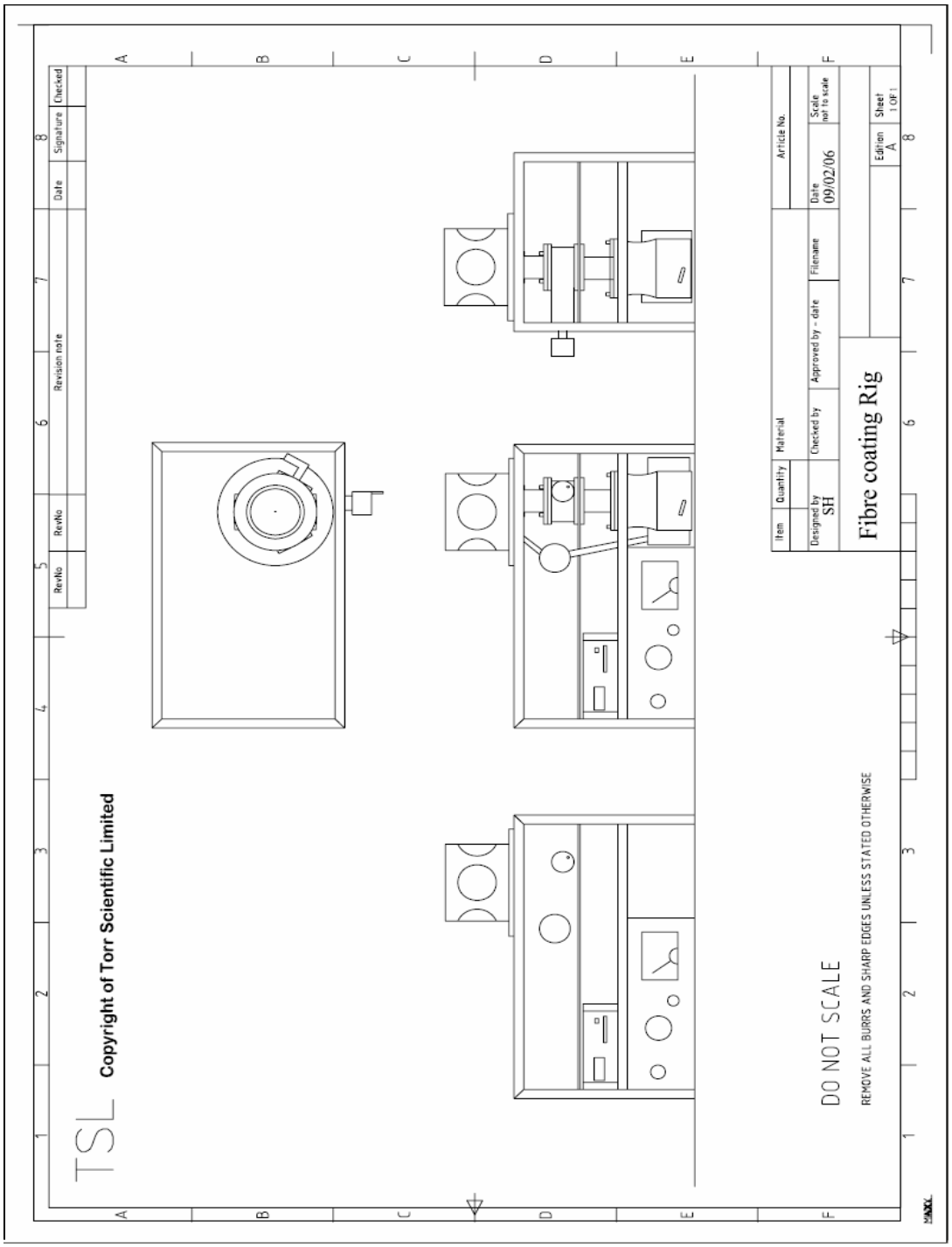

(a)

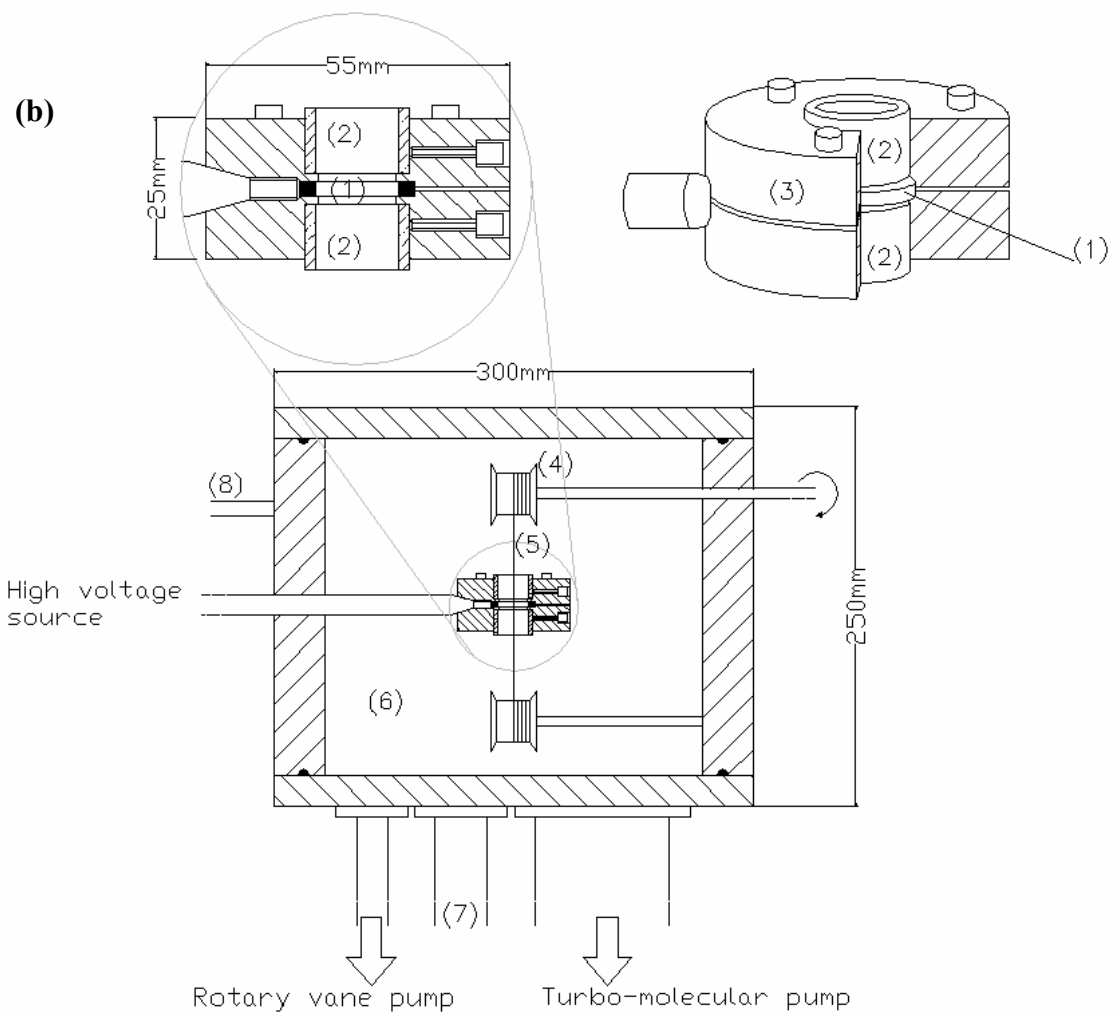

Figure 2.5: (a) Drawing of the coater (additional drawings used are in Appendix 1). **(b)** Cross section view of the inverted cylindrical sputter coater and detailed view of the target holder. (1) Cathode ring, metal target (2) Anodes, copper (3) Target holder, MACOR (4) Wire spooling mechanism (5) Insulated wire (6) Vacuum chamber, Aluminium (7) Pressure sensor (8) Argon inlet.

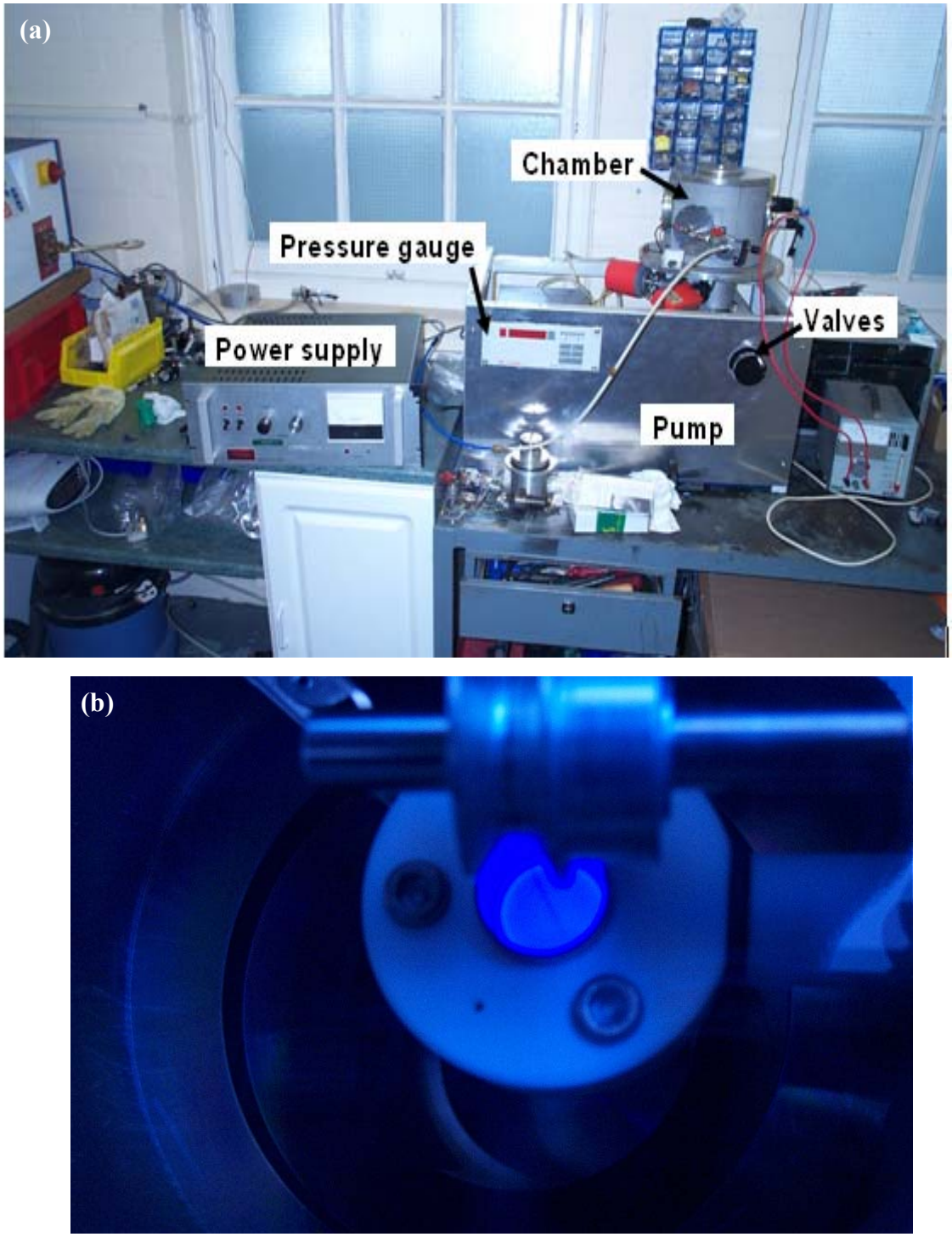

Figure 2.6: (a) Picture of the coating rig. **(b)** View inside the chamber whilst it is in operation.

2.2.2 Coater characterisation and optimisation

Of the many parameters involved in the sputtering process the cathode voltage and argon chamber pressure are the most influential in determining the rate of deposition and the quality of the metal coating on the wire.

We consider first the influence of the applied voltage on the current between the cathode and the anodes for different argon chamber pressures. The current-voltage relationship describes the way in which the argon molecules are ionised in the plasma. Figure 2.7 shows a simulation of the voltage distribution between the anode and the cathode. These simulations were only used to help visualise the voltage profile, they were not used to assist the design of the coater.

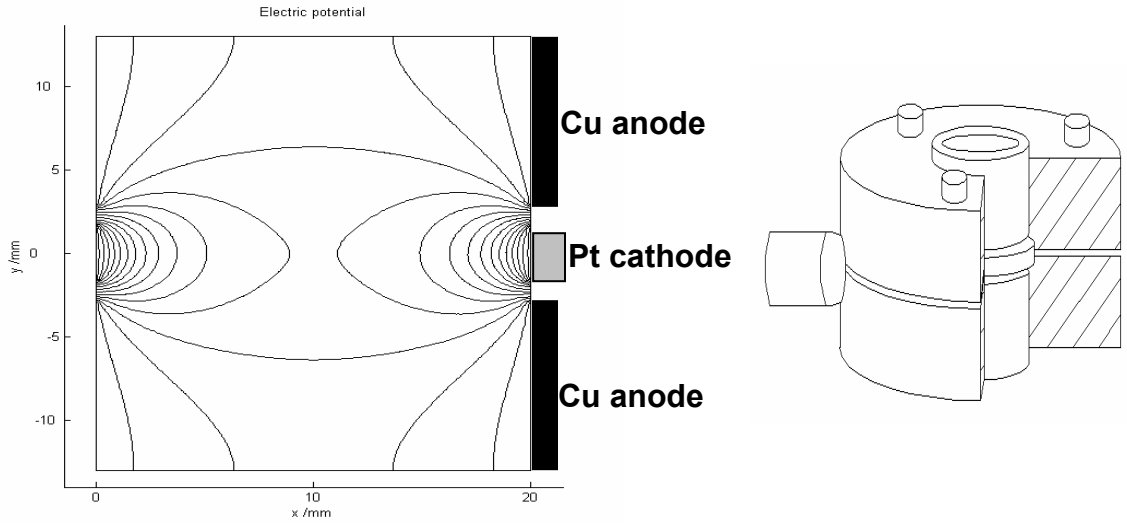

Figure 2.7: The graph on the left hand side shows the simulated voltage profile through a section of the chamber. The location of the anode and cathodes on the graph are depicted schematically. On the right is a three dimensional view of the anode and cathode arrangement.

The I-V plots in Figure 2.8 will differ from coater to coater due to the large number of parameters involved in the ionisation process (110). It has been demonstrated that inverted cylindrical sputter coaters operating with no or low magnetic enhancement can display a current plateau as the voltage applied to the cathode increases. Such a plateau behaviour was not observed in our system, which could be due to the overheating

of the gas in the plasma (111). The variation in the slope with argon pressure highlights the change in the number of ionisation events that are taking place (Fig 2.8). Except for the lowest applied voltage 0.5 kV, as the pressure increases the current response increases for a given voltage. This is also seen by the change in colour and brightness of the plasma which becomes more intense as the pressure increases. The measurements in Figure 2.8 were limited by the 8 mA current cut off limit of the power source, which was reached above 0.2 mBar (circle, square and diamond marked lines) when the applied voltage was beyond 1.5 kV. When the coatings were carried out, a different wiring arrangement was used which made it possible to bypass this cut off and reach higher current values.

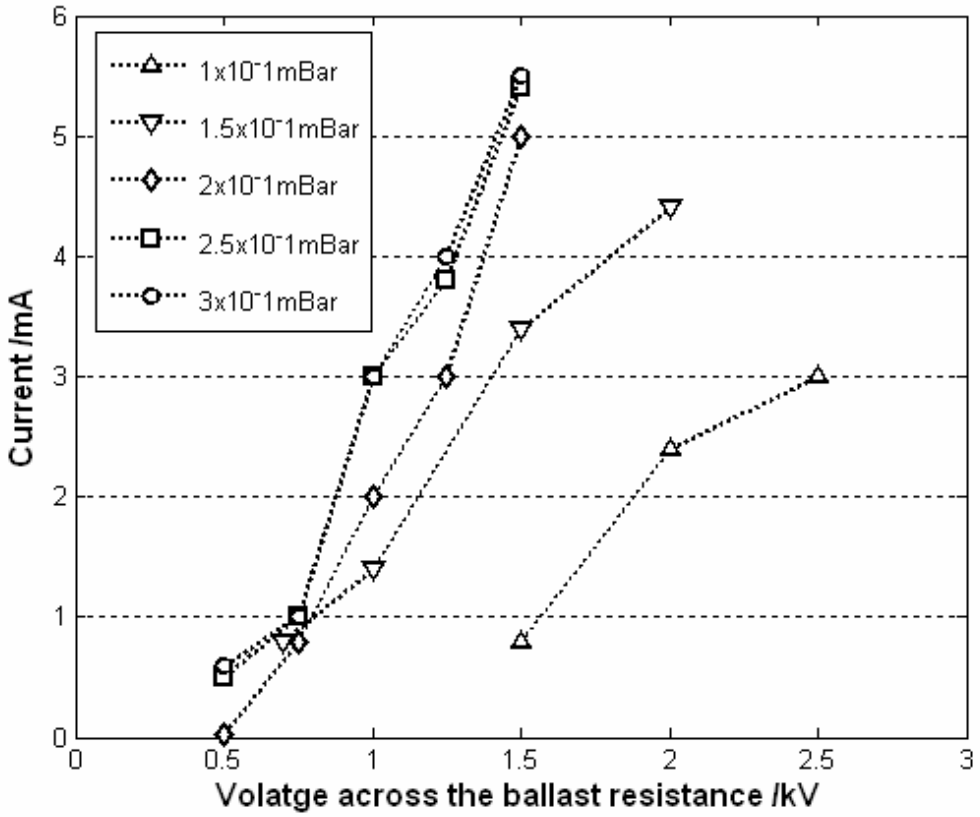

Figure 2.8: Current voltage characteristics of the coater for different chamber argon pressures.

In Figure 2.8 the effects of increasing the argon pressure appear beneficial and rather straightforward; however this is not entirely true. Changing the argon pressure in

the chamber will have two effects. The first is to influence the amount of target bombardment that is taking place. This is seen clearly in Figure 2.8 where the current between the electrodes is up to 4 times higher as the pressure goes from 0.1 to 0.3 mBar for a given cathode voltage. The second effect will be to influence the mean free path of the target material that has been sputtered away by the bombardment. A low chamber pressure will increase the mean free path of the sputtered material and ultimately lead to more deposition, a high chamber pressure will have the opposite effect. To investigate the antagonistic effects of chamber pressure on the deposition rate, a series of glass slides were placed at the centre cylinder coater. Pt was deposited onto each slide for 30 s with a constant cathode voltage of 2.5 kV across the ballast resistance but for varying argon chamber pressures. The thickness of the deposition was then measured using an optical thickness monitor by correlating the transmittance with thickness. We found that the thickness increased steadily from 20 to 30 nm as the pressure increased from 0.15 to 0.35 mBar. Beyond 0.35 mBar the thickness dropped rapidly to less than 10 nm. The steady increase followed by the sharp decrease in the deposition as the pressure goes up is characteristic and has been reported previously for many types of sputter coaters (108). It suggests that there is an optimum pressure at which the system should be run to achieve the highest deposition rate, in our case 0.3 to 0.35 mBar. This optimum chamber pressure is specific to platinum deposition. A different optimal pressure is likely and the characterisation described would have to be repeated if other materials are to be deposited.

Having established the optimum voltage and pressure at which to operate the coater, it is now possible to investigate the deposition profile onto wires. This was done again by placing a glass slide in front of the target onto which platinum was deposited for 15 s at a constant voltage of 2.5 kV and chamber pressure of 0.3 mBar. Figure 2.9 shows the distribution profile measured along the vertical axis of the slide. The Gaussian distribution of the thickness along the glass plate is almost perfect. The maximum values are directly in front of the target and correspond to a deposition of 1nm/s which is high for diode sputtering (109). To achieve different coating thicknesses, a spooling mechanism is used which allows the wire to be moved through the cylinder at different speeds.

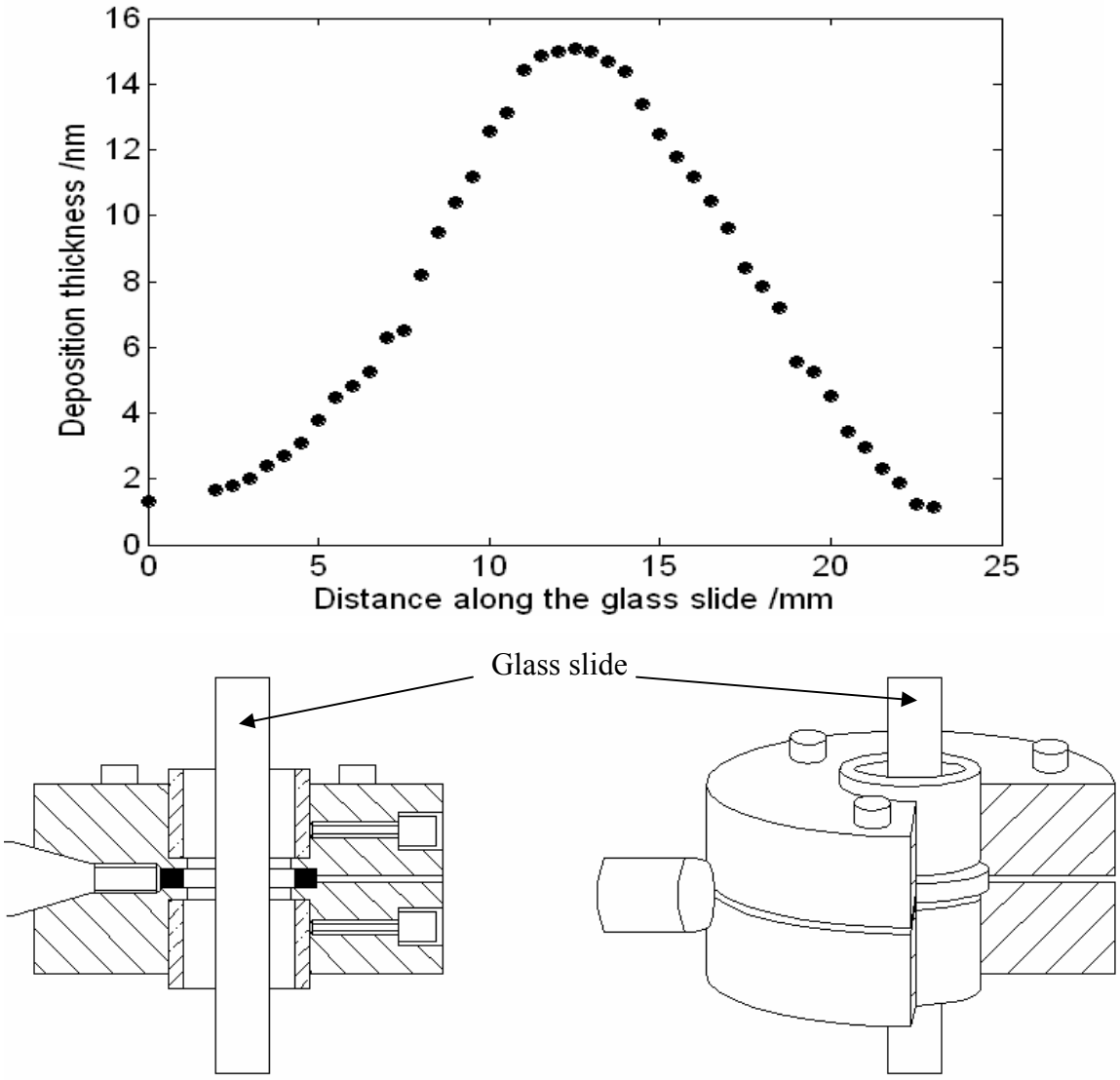

Figure 2.9: Thickness distribution of Pt along the vertical axis of the Pt deposited onto a glass slide placed in the cylinder coater. Schematics below the graph show the location of the glass slide in the coater. The thickness measurements were made at the centre of the glass slide, this was identified at the start of the slide as the point with the highest thickness.

2.2.3 Electrochemical sensors

To illustrate the application of this coating process for electrochemical electrodes Pt/Pt ring-disc microelectrodes of three different dimensions were fabricated using different sized insulated wires, 25, 50 and 125 μm (see Figure 2.10). It is clear that the rings are very uniform and centred about the discs. Figure 2.10(c) shows a vertical cross section through a coated wire (i.e. perpendicular to the plane of the ring-disc). The thickness of the deposition along this wire was measured to be 6.01±0.31 μm, this highlights the consistent nature of the deposition along the wire.

Figure 2.11(a) shows the cyclic voltammograms for all three ring-disc electrodes in 10 mM $Ru(NH_3)_6^{3+/2+}$ in 1M KCl. Each electrode was scanned alone so as not to induce any feedback or shielding effects. The limiting currents observed for each microelectrode agree well with theoretical predictions for a microdisc (57) and microring (58). This is especially relevant to the ring currents as it implies that the entire surface of the ring is electroactive thus confirming the integrity of the coating observed under SEM. Figure 2.11(b),(c) show collector-generator type response of the electrodes where one electrode is reducing $Ru(NH_3)_6^{3+}$ to $Ru(NH_3)_6^{2+}$ and the other is oxidising $Ru(NH_3)_6^{2+}$ back to $Ru(NH_3)_6^{3+}$. For a disc generating case Fig 2.11(b) the collection efficiency for the 25, 50 and 125 μm electrodes is 13.5, 42.5 and 31 % respectively. When the ring is generating (Fig 2.11(c)) the collection efficiency is 61, 46.5 and 47%. These differences in collection efficiency are due to the subtle differences in the electrode dimensions. The collection efficiency of a ring-disc electrode depends on the dimensions of the disc and ring electrodes as well as the size of the spacing between them. Predicting the collection efficiency of a ring-disc electrode is not possible a priori, the only reliable method is numerical modelling. Such models have been developed by ourselves (112) and by others in the past for macro ring-disc electrodes (113).

The difference in the limiting currents observed between the cyclic voltammograms in Figure 2.11(a) and the amperometric traces in 2.11(b),(c) are characteristic of feedback mechanisms. Feedback occurs when the collector and generator electrodes are close enough that their diffusion profiles overlap. In this event the products of the reaction at the collector diffuse back to the generator. This is also called redox cyclic and has an effect to increase the current at both electrodes. The

increase in generator current due to feedback for ring generating cases is 49%, 22% and 7% for the 25, 50 and 125 μm electrodes respectively. When the disc is generating the increase in current due to feedback is 87%, 1% and 17%. These effects are considerable and often provide valuable current amplification when noise is significant or when low redox concentrations are being used. The large variability in the amount of feedback achieved from one electrode to the other is somewhat concerning. Comparing the experimental current with those predicted by the numerical model does show a mismatch (see Fig 2.11., dotted lines are simulated, solid lines are empirical recodings). The discrepancy between the experimental and numerical current values is probably due to non-planar electrode surfaces. A full description of the numerical model is presented in the following chapter along with an investigation of the effects of recessed and protruding electrodes.

The large majority of measurements made with these electrodes were stable for weeks. The electrodes that did deteriorate were brought back to their original condition with a light polish.

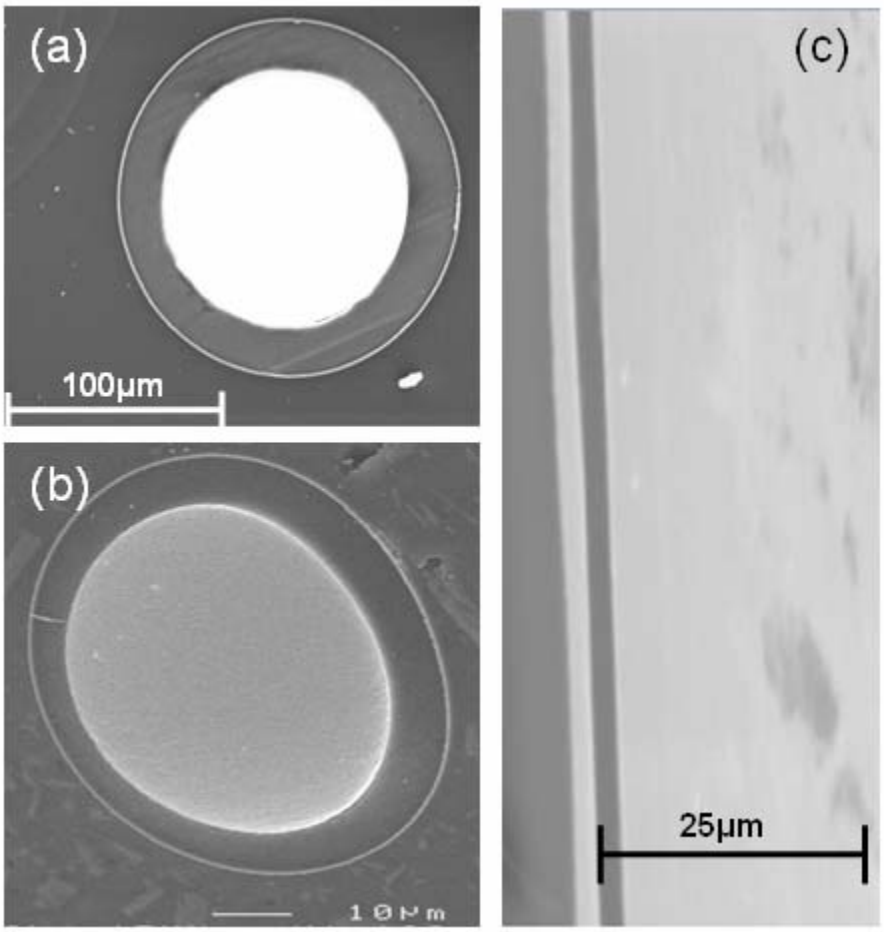

Figure 2.10: SEM pictures of the ring-disc microelectrodes. (a) 125 micron core insulated wire, (b) 50 micron core insulted wire. (c) Transverse slice through a wire to reveal the uniform coating achieved along the length of the wire. More pictures of the electrodes are given in Appendix 2.

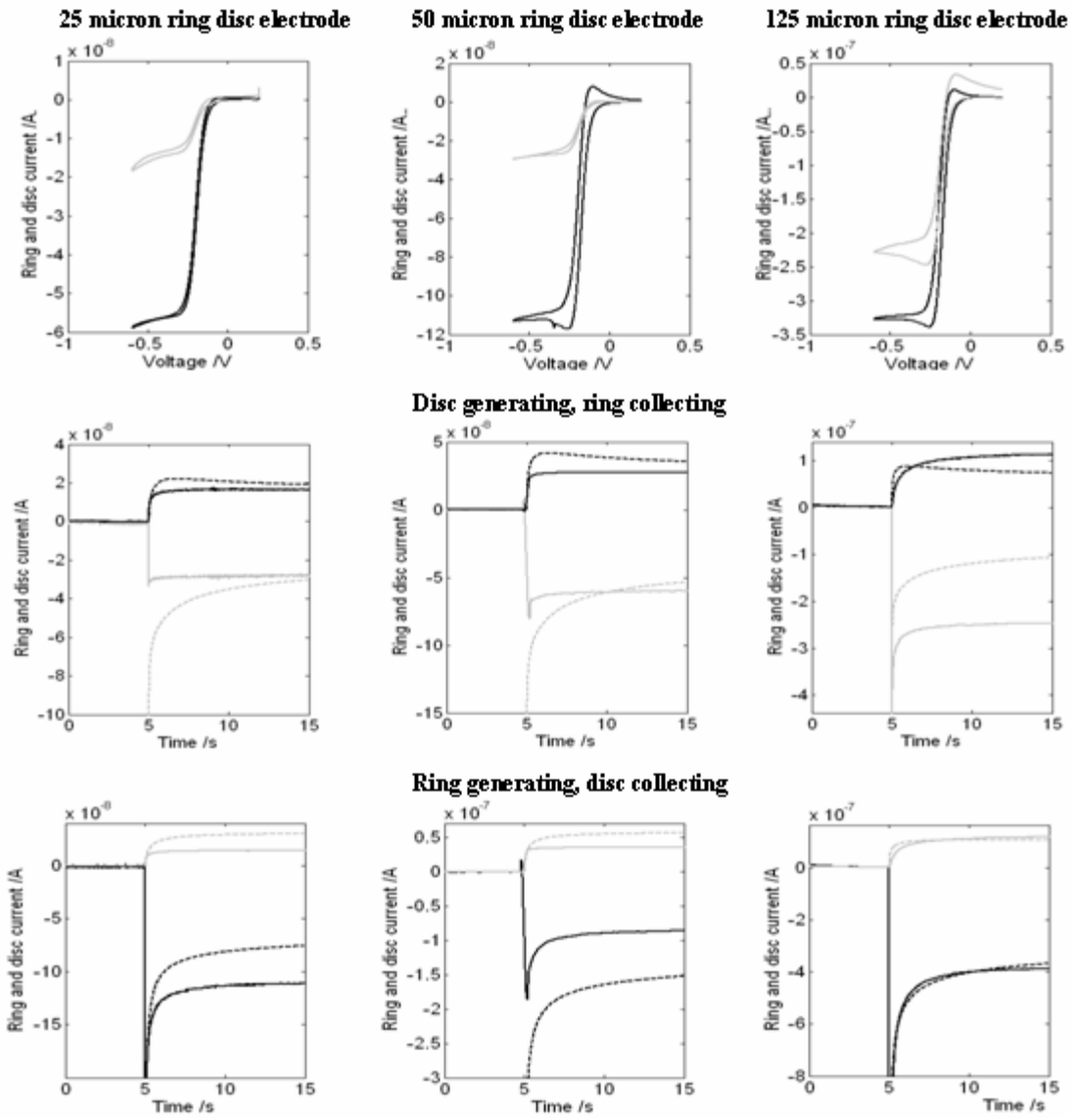

Figure 2.11: (a) Cyclic voltammograms for all three Pt/Pt ring-disc microelectrodes **(b)** Disc generating ring collecting for three electrodes of different geometry. The generation step is switched on after 5 s. **(c)** Ring generating disc collecting. The redox couple used is $Ru(NH_3)_6^{3+/2+}$ 10 mM concentrations and the scan rate was 0.05 V. Ring electrodes current are represented in grey lines, disc electrodes currents are in black. In (b) and (c) the dotted lines represent simulated current responses, whilst solid lines show experimental recordings.

To showcase the possibilities that arise from this new fabrication method, a number of miscellaneous electrodes were made. These electrodes were not used directly

for the work that is reported in this thesis, but they are interesting and have many applications in other fields of electrochemistry. These electrodes are a ring-ring-disc microelectrode and an iridium-gold electrode.

The ring-ring-disc or double ring-disc microelectrode was made by first coating an insulated wire in platinum (as described above), then coating a hollow silicon fibre with platinum. Placing the ring-disc fibre into the hollow fibre and insulating the entire assembly produces a double ring-disc electrode. Figure 2.12 shows an SEM picture of the electrode. Figure 2.13 (a) show typical cyclic voltamograms (b) and collector-generator type responses, where the disc is generating (ring generating modes were also investigated). The main feature of this electrode is the close proximity of the three electrodes and their radial symmetry (although this is not the case in Fig 12 subsequent cuts revealed radially symmetrical electrodes). Possible application would be in multi-analyte detection or a self-contained sensor. By self-contained we mean a sensor that has reference and counter electrodes as part of the same assembly. Plating of the inner ring with silver was investigated but resulted in some cross talk with the other electrodes (more control of the plating should solve the problem).

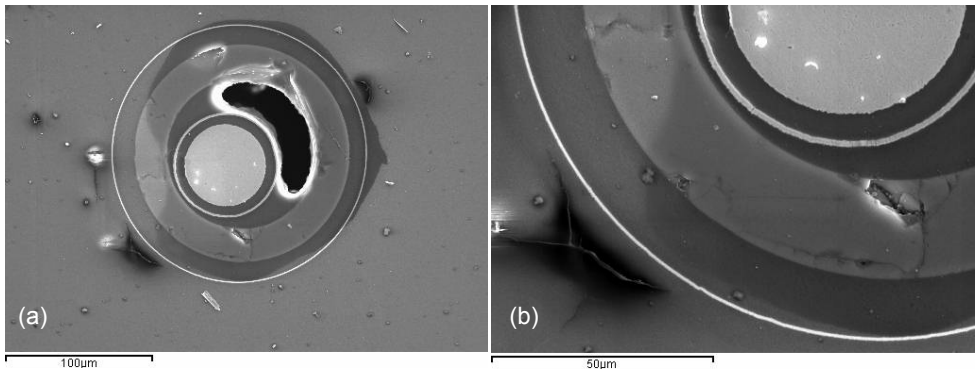

Figure 2.12: (a) SEM picture of the double ring-disc electrode, the insulation appears not to have filled a volume between the tube and ring-disc wire, this was not the case further up the electrode, at which point the radial symmetry of the electrodes was also improved (i.e. observed under light microscope after cutting the electrode tip). Pt areas appear in white, both rings are clearly visible.

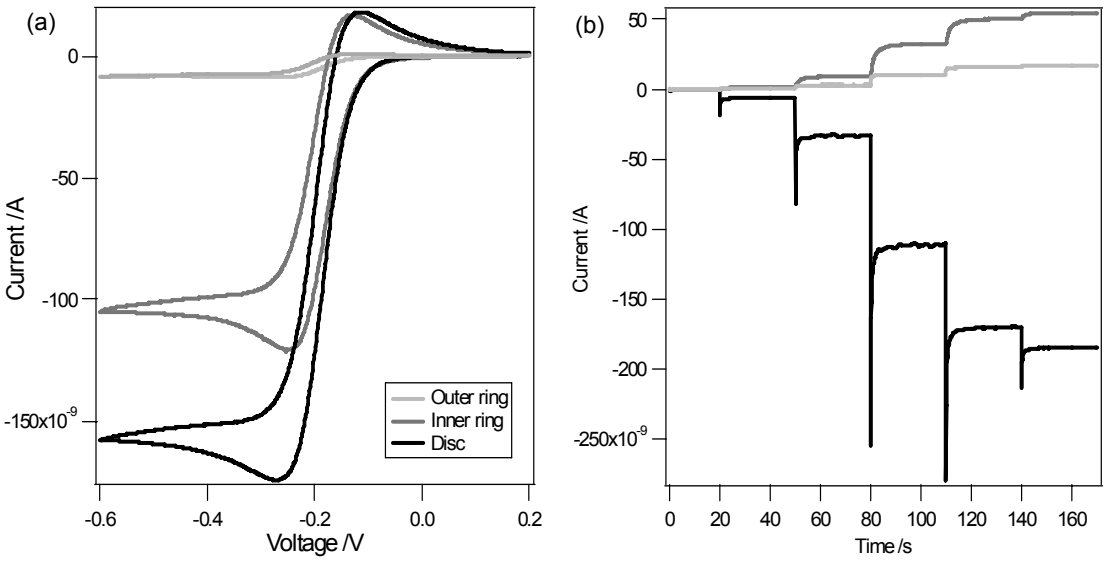

Figure 2.13: (a) Cyclic voltammograms in 20 mM $Ru(NH_3)_6^{3+/2+}$ in 1M KCl of the disc (black), inner ring (dark grey) and outer ring electrodes (light grey). **(b)** Collector-generator response, where the disc is generating $Ru(NH_3)_6^{3+}$ and the inner and outer ring are collecting $Ru(NH_3)_6^{2+}$. The generator voltage was decreased every 30 s in increments of 0.1 V from 0V to -0.6 V vs Ag/AgCl.

The iridium-gold ring-disc electrode was made with the view of developing a pH and oxygen sensor; the oxygen being detected ameperometricaly at the gold disc and the pH being measured from open circuit potential at the ring. To coat iridium the pressure and voltage characteristics of the coater had to be altered slightly to achieve the best deposition rate. Other than that, the process was the same as for the Pt coating of the Pt insulated wires. For the iridium ring to detect pH changes it has to be oxidised. This is done by anodisation in 0.5 M H_2SO_4 following the method of O'Hare et al. (114). Figure 2.14 shows the calibration of the iridium vs a commercial pH meter, the slope is below the Nernstian predictions (i.e 30mV rather than 60-70mV) which could be due to incomplete Ir oxidation. Figure 2.15 shows the response of the Au disc when the voltage is scanned from -0.4 to 1V vs Ag/AgCl. and the change in pH as measured with the Ir ring. The pH drops as electrolysis of water occurs (i.e. oxygen is generated which leaves a surplus of protons), these are consistent with our expectations. When hydrogen was generated the opposite pH shift was measured at the ring.

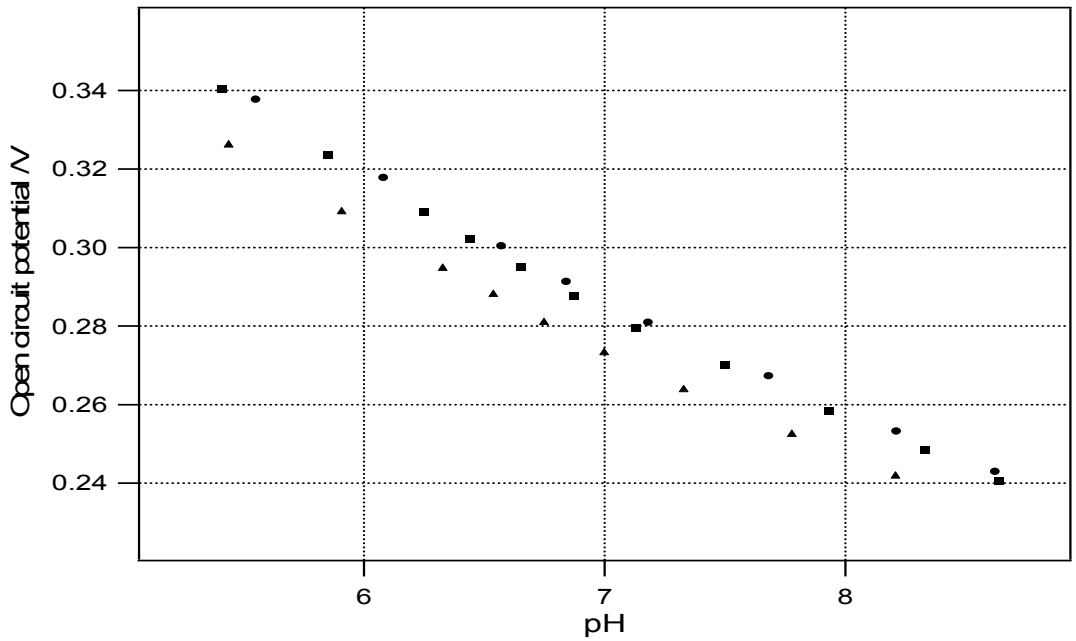

Figure 2.14: Open circuit potential recorded by the iridium ring vs pH recorded by a commercial pH meter. Circle, square and dimond markers show three trials.

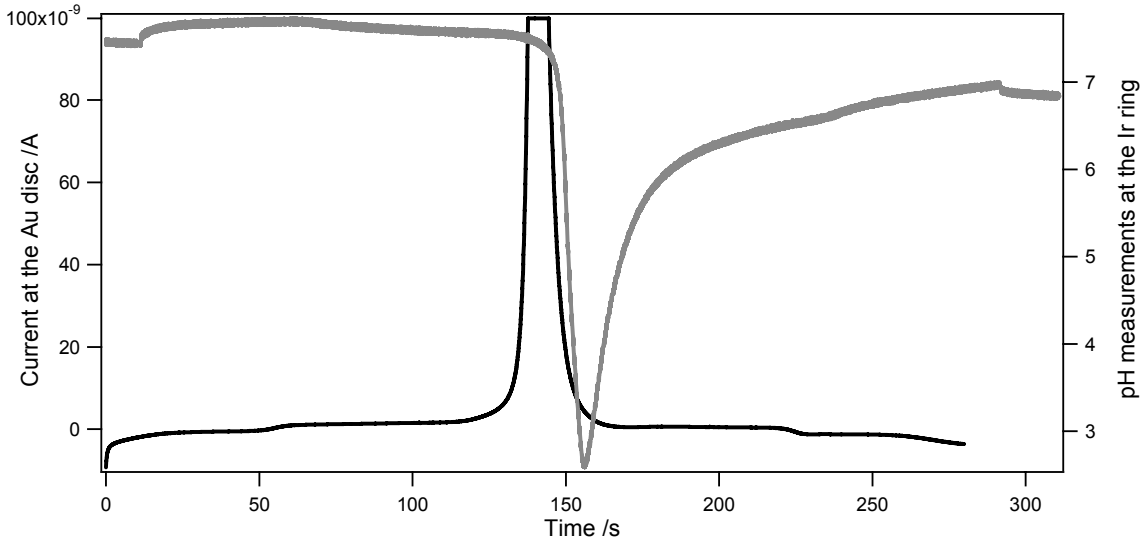

Figure 2.15: In black is the current recorded at the gold disc, left axis. In grey is the pH shift recorded at the ring over the same time interval, right axis. For the current measurement the bottom axis can be turned into voltage by multiplying by the scan rate (v = 0.01 V/s)

2.3 Conclusion

A novel method for the fabrication of ring-disc microelectrodes has been presented. The novelty of the fabrication technique involves the use of an inverted hollow cylindrical sputter coater to deposit metal films continuously onto insulated wires from all sides. The systematic study of the parameters pertaining to the coater has identified the optimum cathode voltage for Pt depositionto be 2.5 kV across a 100 Ω ballast resistance and the argon chamber pressure as 0.3 mbar which results in a deposition rate of 1 nm/s. The consistency and uniformity of the metal deposition along the wire is a notable feature of this method. This is achieved by the ring shape and small size of the target, which has the added advantage of reducing the cost associated with the coating. Future developments of the coater could include the use of several sequential targets of different material through which the wire could be passed to achieve multiple material coatings or alternate metal and insulator coatings.

The electrodes produced exhibit excellent electrochemical behaviour, which agree with theoretical predictions for thin rings and ring-disc interations. The smallest sensor produced had an outer diameter less than 28 μm, although we believe this is far from the lower limit achievable with the present coater. Reducing the size of the target should enable the fabrication of extremely small ring-disc microelectrodes.

Although used for the fabrication of ring-disc microelectrodes, this method is equally well suited for the fabrication of micro-ring electrodes and micro-optical ring electrodes.

3

Numerical modelling of the ring-disc electrode

A detailed numerical analysis of the behaviour of the ring-disc microelectrode is presented. In the first part of this chapter the effect of diffusion mass transport on the sensor behaviour is considered. In the second part convection mass transport is added to the models. In both mass transport modes the influence of electrode size, flux distribution and operating mode on the measurement made are investigated. Some of the models described relate to experiments presented in subsequent chapters, in most cases the correlation between experimental results and numerical predictions are good.

3.1 Introduction

Numerical modelling in electrochemistry is primarily concerned with solving concentration profiles through space and over a period of time. These can arise from electrochemical reactions at the surface of electrodes, chemical reactions in solution or mass transports of depolarised electrolyte. The reasons for numerically modelling electrochemical problems are of course varied and numerous especially as the practice is becoming more widespread. Some of the more popular reasons are:

- To validate experimental observations, in cases where no analytical solutions exist or because limited experimental recordings are available.
- To attribute experimental measurements to physical phenomena.
- To carry out a systematic study of the parameters affecting the electrode reactions. These could be electrode geometry, mass transport effects such as diffusion or convection, electrochemical reaction rates and many others.
- To investigate cases that are currently impossible or hard to achieve experimentally. For instance where dangerous reactions are concerned or for systems of very small size.

In this thesis the main purpose of the numerical modelling has been to assist in the sensor design process. To this effect a systematic study of the parameters influencing the measurements capacities of the sensor was undertaken. These are the electrode geometry, the mass transport in the vicinity of the sensor and the volume probed by the sensor. The modelling work highlighted important features of the sensors such as the significance of having both electrodes on the same plane or the use of the transient profile to assess the level of diffusion within the medium surrounding the sensor. It also helped solve some key problems that arose through the experimental work. Overall, a greater understanding of the processes occurring at the electrode and within its vicinity was achieved through the use of numerical modelling and this significantly contributed to the outcome of this work.

3.1.1 Governing equations

The basic equation solved in electrochemical modelling is the diffusion equation, known as Fick's second law:

$$\frac{\partial c}{\partial t} = D\nabla^2 c \tag{3.1}$$

Where c is the concentration, t the time, D the diffusion coefficient and ∇^2 is the Laplacian operator in space. This is a second order partial differential equation, and when solved will describe the concentration profile of a species through space and over time. The different forms of the Laplacian used in this chapter are listed below:

In Cartesian coordinates:

Two dimensional $$\nabla^2 c = \frac{\partial^2 c}{\partial x^2} + \frac{\partial^2 c}{\partial y^2} \tag{3.2}$$

In axisymmetric cylindrical coordinates:

Two dimensional $$\nabla^2 c = \frac{\partial^2 c}{\partial r^2} + \frac{1}{r}\frac{\partial c}{\partial r} + \frac{\partial^2 c}{\partial z^2} \tag{3.3}$$

In addition to increasing the number of dimensions considered, the equation system is made more complicated by the addition of more than one chemical species. In this work the concentration profile of up to two species was modelled.

Finally and probably most significantly the governing equations can be made more complex by considering additional mass transport modes, namely convection and migration in solution. The complete mass transport equation known as the Nernst-Planck equation then becomes:

$$\frac{\partial c}{\partial t} = +D\nabla^2 c - u\nabla c + \frac{zF}{\Re T} D\nabla c \tag{3.4}$$

Where **u** is the fluid velocity, ∇ is the gradient, **z** is the charge, **F** Faraday's constant, $\Re$ the universal gas constant and **T** the temperature.

3.1.2 Static vs Dynamic

Electrochemical problems can be solved in a static (i.e. steady state) or dynamic (i.e. time dependent) way. Dynamic model are more complex as they involve solving for the variation of concentration over time and space. Dynamic models are required when modelling cyclic voltammetry for instance. Static models are more common and simpler in that the concentration is only a function of space. In this case left hand side of the mass transport equations Eq. 3.1, 3.4 are set equal to zero. In electrochemistry, however the time dependency of the static model is implied because the time constants are small. We refer to these as quasi steady state models. Such models are used, for instance, to establish diffusion limiting currents as well as in most cases where convection is considered. In this thesis both quasi steady state and dynamic models were used in order to probe the relationship between the sensor and its environment.

3.1.3 Discretisation methods

Before the model can be solved it has to be discretised, this is the process of replacing a continuous system of differential equations by a finite discrete approximation. There are a number of different descretisation methods. The following list highlights the ones used in electrochemical modelling:

- Finite difference
- Finite element
- Boundary element
- Finite volume

Finite difference discretisation

Finite difference currently dominates the electrochemical modelling scene (75). This is because it is relatively straightforward to implement, it is cheap computationally and it has been very successful. This discretisation method works by dividing the model space into a series of equidistant points, known as nodes. The derivatives in the mass transport equation are then approximated as finite difference in concentration between adjacent nodes. In a two dimensional system the concentration at each node will be described with respect to its four neighbours by a set of linear equations. Initial and boundary conditions provide the limits for the solution iteration, these will end when the variation in successive solutions at each node is below a set threshold.

Finite difference has its limitations, for instance in very non-linear systems or when non-uniform boundary conditions are applied as well as when complex model geometries are being considered. As the problems in electrochemistry become more elaborate and computer power less of an issue, choosing more sophisticated discretisation techniques becomes pertinent.

Finite element discretisation

Finite element discretisation has become the standard in engineering modelling. It is also becoming popular with electrochemists because the problems considered are getting more complicated and the geometries less ideal. Finite elements methods (FEM) were first developed in 1943 by Richard Courant to solve vibration systems (115). A broader definition was then presented by Turner et al in 1956 (116).

FEM works by dividing a body into smaller elements of finite dimensions called finite elements, these are connected by a finite number of joints called nodes. The properties of the elements are formulated and combined to obtain the properties of the entire body. The governing differential equations are solved approximately over the finite element. The solutions of each element are then combined to obtain the solution for the entire body. This is possible because continuity is ensured at each node. Initial and boundary conditions provide the limits for the solution iteration; these will end when the variation in successive solutions is below a set threshold.

FEM allows for non-uniform boundary conditions and complex geometries both of which are used in our models. As a result we chose to use finite element methods as our discretisation technique.

3.1.4 Numerical solvers

The commercial numerical modelling package used in this work has a number of built in solvers (UMFPACK, GMRES, Conjugate gradients, Geometric multigrid ect.). In general the UMFPACK solver was used as it is COMSOL's most robust and complete solver. These solvers also enable multiphysics problem solving, for our application this is useful as we will often combine mass transports with fluid flow simulations.

3.1.5 Assumptions and simplifications

When using numerical modelling it is essential to establish whether the physical conditions encountered experimentally are well represented by the equations in the model. This is the first requirement the model has to fulfil in order for its results to be compared to the experimental findings. In most cases the experimental measurement environment is subject to too many physical processes for them all to be accounted for in a model. As a result the first stage often involves simplification of the processes being modelled. In this thesis a number of simplifications and assumptions are made:

- Geometrical simplification of the sensor and its environment. This work almost entirely focuses on solving the mass transport between two electrodes that are coupled electrochemically. The nature of this couple requires that a species is generated at one electrode and collected at another. For any quantitative information to be extracted from the model, the mass transport problem has to be solved in three dimensions. This is unfortunately quite expensive computationally. However the geometrical symmetry of the ring-disc electrode makes it possible to use axial symmetry about the centre of the disc to simplify the three dimensional model into a less computationally demanding two dimensional model (see Fig 3.1) This simplification was almost always used.
- The environment in which the sensor is evolving is assumed homogeneous. This is not the case experimentally especially when in biological tissue. Yet to try and

address the non-uniform nature of tissue in our models would have been limiting and in all cases except for Section 3.2.4, the space surrounding the electrodes was assume to be uniform.

- Migration mass transport is not significant. This assumption is true experimentally because the solutions used contained large amounts of background electrolyte. Physiologically this assumption also holds again, due to the large concentration of ions in the body. The presence of an excess amount of ions will effectively limit the effects of migration to within few bond lengths of the surface of the electrode (56).
- The entire surface of the electrode is assumed to be active electrochemically. That is to say that the electrochemical reaction taking place at the electrode is possible over its entire surface. Moreover we did not account for non-ideal geometries of the electrodes (i.e. distorted discs, incomplete rings etc.)
- The chemical reaction taking place at the electrode surface is assumed to be a first order reaction of the kind $A \pm e^- \rightleftharpoons B$
- The diffusion coefficients are constant throughout the experiment.
- For the steady state mass transport limiting conditions, the concentration of reactant at the electrode surface reaches 0. This does not necessarily imply that the concentration of product will equal 1.

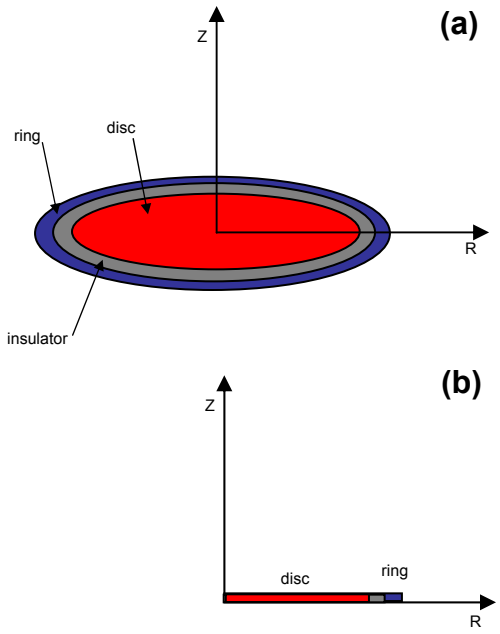

Figure 3.1: (a) View of a ring-disc microelectrode in three dimensions and **(b)** the subsequent simplification of the geometry by taking advantage of the axial symmetry about z.

3.2 Pure diffusion

The following sections describe a number of models and simulation results in which only diffusion mass transport is considered. Diffusion plays a key role in tissue perfusion as it is the mass transport that bridges the gap between the areas where convection is occurring and the areas too distant from a blood vessel to benefit from convection. Most cells are not directly in contact with the capillary vessels, they therefore rely heavily on diffusion for their survival.

There is also evidence that diffusion plays a significant role when the flow to a region of tissue has been impaired. A number of studies have investigated this, confirming that at the cellular level diffusion of gases, nutrient and metabolite is paramount (11). Studying diffusion with the sensor is therefore key to its application to monitor tissue perfusion. The models described in this section have helped design the most efficient sensor geometry as well as investigating the significance of membranes, reaction rates, diffusion coefficient and analyte concentration on the measurement capacity of the sensor.

3.2.1 Investigation of the parameters affecting the collection efficiency of ring-disc microelectrodes

The parameters affecting the collection efficiency of a ring-disc microelectrode operating in the collector-generator mode are numerous. The first parameters considered pertain to electrode geometry; the disc radius and the inner and outer ring radii (see Section 3.2.1.a). We investigate the way in which the collection efficiency changes for different sensor dimensions. The influence of recess and protrusion of the electrodes is also studied over a reasonable range of distances (Section 3.2.1.b). The other parameters considered pertain to the flux distribution at the surface of the ring and disc electrodes, focusing on the generator electrode (Section 3.2.1.c). The flux distribution at the generator is influenced by the voltage applied and the relative rates of mass transport or electron transfer of the species used.

(a) Effect of electrode geometry on the collection efficiency

A semi-analytical solution for the collection efficiency of ring-disc microelectrodes was proposed by Phillips and Stone (113) although practically achievable devices lie off their graph. Moreover the semi analytical solution still requires a numerical modelling step before the analytical step can be realised. As a result, this approach has found little application. More recently a purely numerical approach was taken by Liljeroth et al (77) and produced solutions that were in good agreement with experiments. This method, a finite element approach, is the one we have chosen to pursue as it allows non-uniform meshes to be constructed. This becomes useful when complex geometries are being modelled or when non-uniform boundary conditions are applied; both of which are relevant to our case.

Theory

We consider a system consisting of a ring-disc microelectrode set in an insulating plane. The model is in cylindrical polar coordinates (r,z) with rotational symmetry about the z axis as described in Fig. 3.2a. The solution within the model boundary contains an electro-active species, A, which is assumed to undergo a simple one electron transfer leading to species B.

$$A \pm e^{-} \rightleftharpoons B \tag{3.5}$$

The forwards reaction occurs at the generator electrode whilst the backwards reaction occurs at the collector. The collection reaction is always assumed to be diffusion limited. Species A and B are assumed to diffuse freely in solution and have equal diffusion coefficients, D. The model geometry, parameters and equation system were non-dimensionalised with respect to the radius of the disc, R_1, the bulk concentration of species A, $C_{A,\infty,}$ and the diffusion coefficient, D (75) in the following way:

$$c_A = \frac{C_A}{C_{A,\infty}} \qquad c_B = \frac{C_B}{C_{A,\infty}} \qquad r = \frac{R}{R_1} \qquad z = \frac{Z}{R_1} \qquad \tau = \frac{tD}{R_1^{\,2}}$$

Note that the non-dimensional diffusion coefficient equals one and that dimensionless parameters are in lower case, whilst dimensional ones are in upper case. For a still solution with high background electrolyte concentrations, the mathematical model describing the mass transport of species A and B is given by:

$$\nabla^2 c_A = 0 \tag{3.6}$$

$$\nabla^2 c_B = 0 \tag{3.7}$$

Where ∇^2 is the Laplacian operator in cylindrical coordinates (see Section 3.1.1 Eq. 3.3). The boundary conditions used in these sections are sumarised in Table 3.1. The flux at the electrodes is given by:

$$J = 2\pi \int_{\rho_1}^{\rho_2} \nabla_n c r dr \tag{3.8}$$

The integration limits ρ_1 and ρ_2 are respectively 0 and r_1 for the disc and r_2 and r_3 for the ring. Where ∇_n is the normal gradient operator.

The collection efficiency is defined as:

$$CE = \left| \frac{J_c}{J_g} \right| \times 100 \tag{3.9}$$

Where J_c and J_g are the collector and generator fluxed respectively.

The model boundaries, r_{max} and z_{max} were twenty times greater than r_3. Simulations with larger limits did not significantly change the flux measured at the electrodes (i.e. <1%). The mesh was refined at the electrodes (minimum element size $0.01 \times r_1$) and allowed to grow towards the boundaries. Doubling the number of mesh elements did not noticeably enhance the solution. The current at a 50 μm diameter disc electrode as evaluated by our model is 1.1% lower than that found using the analytical solution for a microdisc (57). Simulations were carried out using the finite element solver Comsol 3.2 in Matlab 6.5.

The model was meshed with unstructured triangular elements. The mesh density was high on the disc, ring and ring-disc spacing boundaries (minimum element size 0.01). The mesh was then allowed to grow towards the edges of the model (growth rate 1.2). With these settings the models had upwards of 3000 mesh elements. Figure 3.2 shows a typical meshed model.

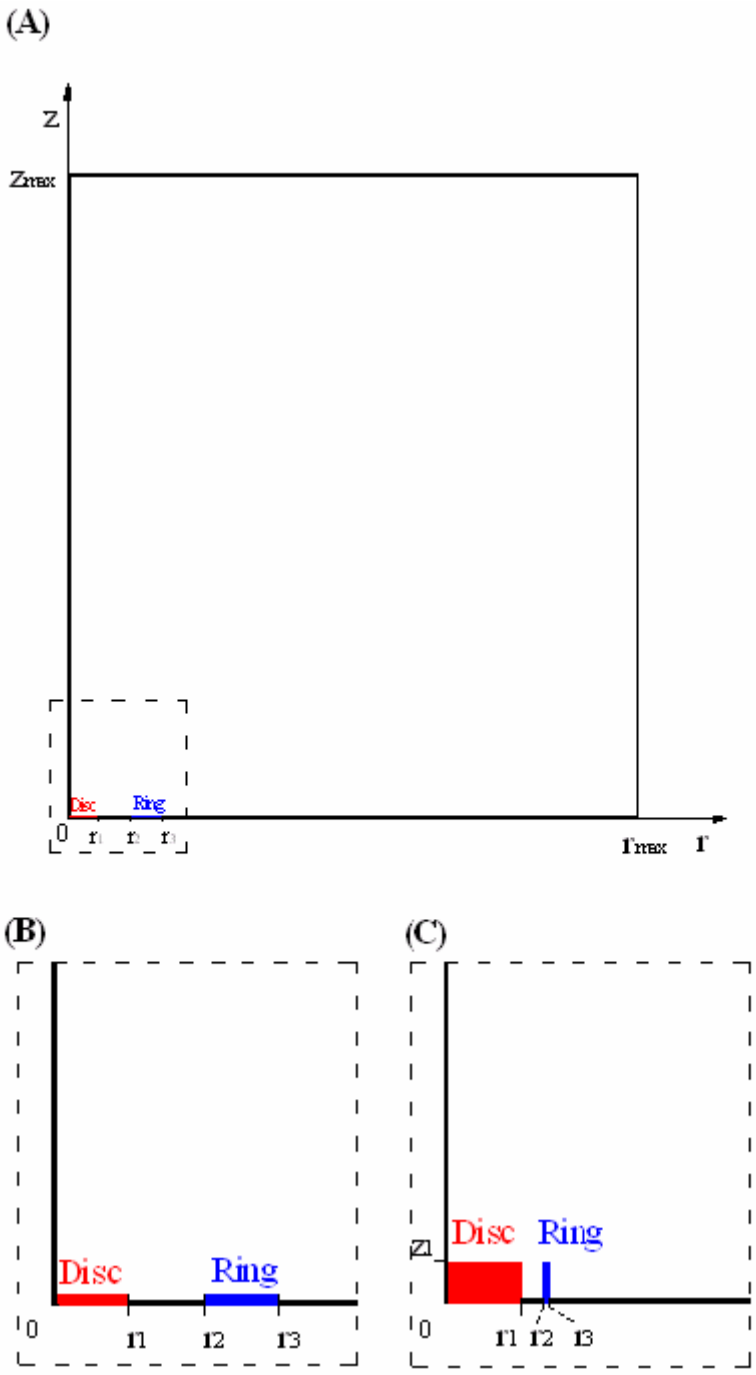

Figure 3.2: Model geometry used **(a)**. Close up of the ring disc area for the planar **(b)** and the protruding case (used in section 3.2.1b) **(c)**. z_1 is the height of the protrusion whether it is for both ring and disc, just disc or just ring protruding. For the recessed model z_1 is negative. The model is a two dimensional model with axisymmetry about z.

Table 3.1. Boundary conditions for both ring and disc generating cases.

	Disc generating	Ring generating
Boundary conditions		
$z=0 \quad 0<r\leq r_1$ $z=0 \quad r_2<r\leq r_3$ $z=0 \quad r_1<r\leq r_2;\ r_3<r\leq r_{max}$ $r=0 \quad 0<z\leq z_{max}$ $r=r_{max} \quad 0<z\leq z_{max}$ $z=z_{max} \quad 0<r\leq r_{max}$	$c_A = 0;\ \nabla_n c_B = -\nabla_n c_A$ $\nabla_n c_A = -\nabla_n c_B;\ c_B = 0$ $\nabla_n c_A = \nabla_n c_B = 0$ Axial symmetry $c_A = 1;\ c_B = 0$ $c_A = 1;\ c_B = 0$	$\nabla_n c_A = -\nabla_n c_B\ ;\ c_B = 0$ $c_A = 0;\nabla_n c_B = -\nabla_n c_A$ $\nabla_n c_A = \nabla_n c_B = 0$ Axial symmetry $c_A = 1;\ c_B = 0$ $c_A = 1;\ c_B = 0$

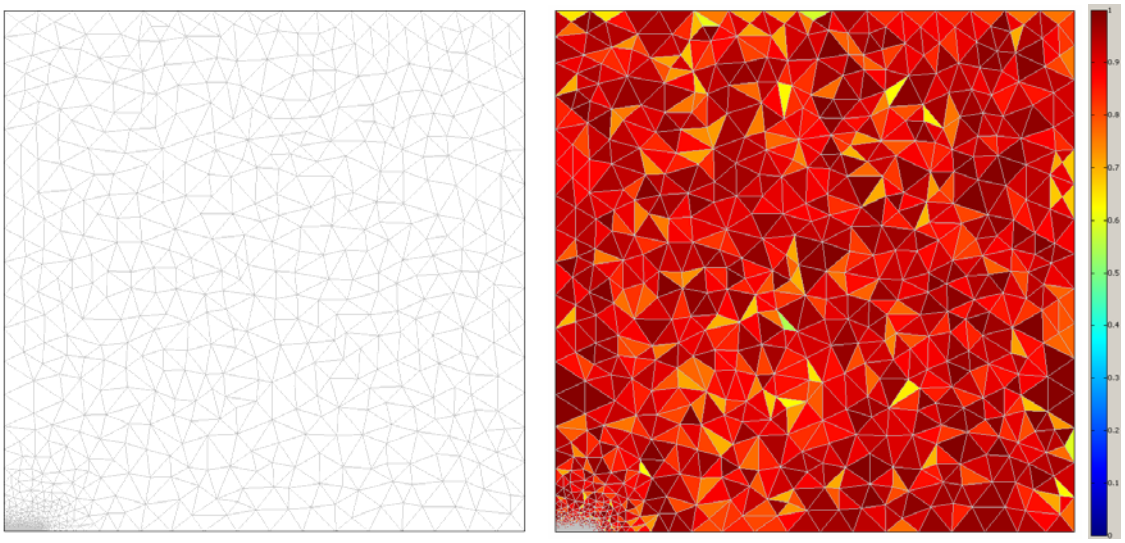

Figure 3.3: Model mesh elements, note the increased mesh density around the electrodes. Left hand image shows mesh quality on a scale of 0 to 1, 1 being the highest.

Results and discussion

Electrochemical coupling occurs between two electrodes when an electroactive species is produced at one electrode (the generator) and reacts at the other electrode (the collector). In a still solution, the generated species diffuses away, some eventually reaching the appropriately polarised surface of the collector electrode where it will react. The redox couples used is $Ru(NH_3)_6^{3+/2+}$ in 10mM concentrations. Comparing the current drawn by the generator and the collector provides information about the diffusion of the species from one electrode to the other and is usually described in terms of the collection efficiency (CE) Eq. 3.9.

The effects of varying the size of the disc, inner ring radius and outer ring radius are investigated for the diffusion limited case, with $Ru(NH_3)_6^{3+/2+}$ as the redox couple. The simulated collection efficiency results are presented in Fig 3.4 where both the disc and ring generators are considered. When the disc is generating (Fig 3.4a,c) the collection efficiency is seen to increase as the outer ring radius, r_3 is increased and decrease with increasing inner ring radius, r_2. Large inner ring radii are often required to maximise the volume probed by the sensor and if the disc is generating then one would recommend having a large ring in order to retain high CE values. When the ring is generating (Fig 3.4b,d) the collection efficiency drops both as the inner ring radius and outer ring radius are increased. The higher CE values in Fig 3.4d illustrate the benefits of using thin rings, where the edge effects are more predominant. The significant difference between the values for CE for the disc and the ring generating cases highlights the advantage of having two different geometries that can be used in alternation to probe different aspects of the mass transport problem being investigated. A compromise has to be reached however on the outer ring radius to ensure that both modes can yield high CE.

If other mass transport modes are to be investigated using ring-disc microelectrodes, then having a high collection efficiency will ensure a wide detection range. It is worth noting that the CE values obtained for the steady state diffusion case are not necessarily the maximum values that can be achieved, under forced convection (117) and in scanning electrochemical microscopy (SECM) experiments (77,103) higher collection efficiencies are possible. Nevertheless the values obtained under diffusion mass transport provide a starting point for selecting the optimal geometry for the electrodes.

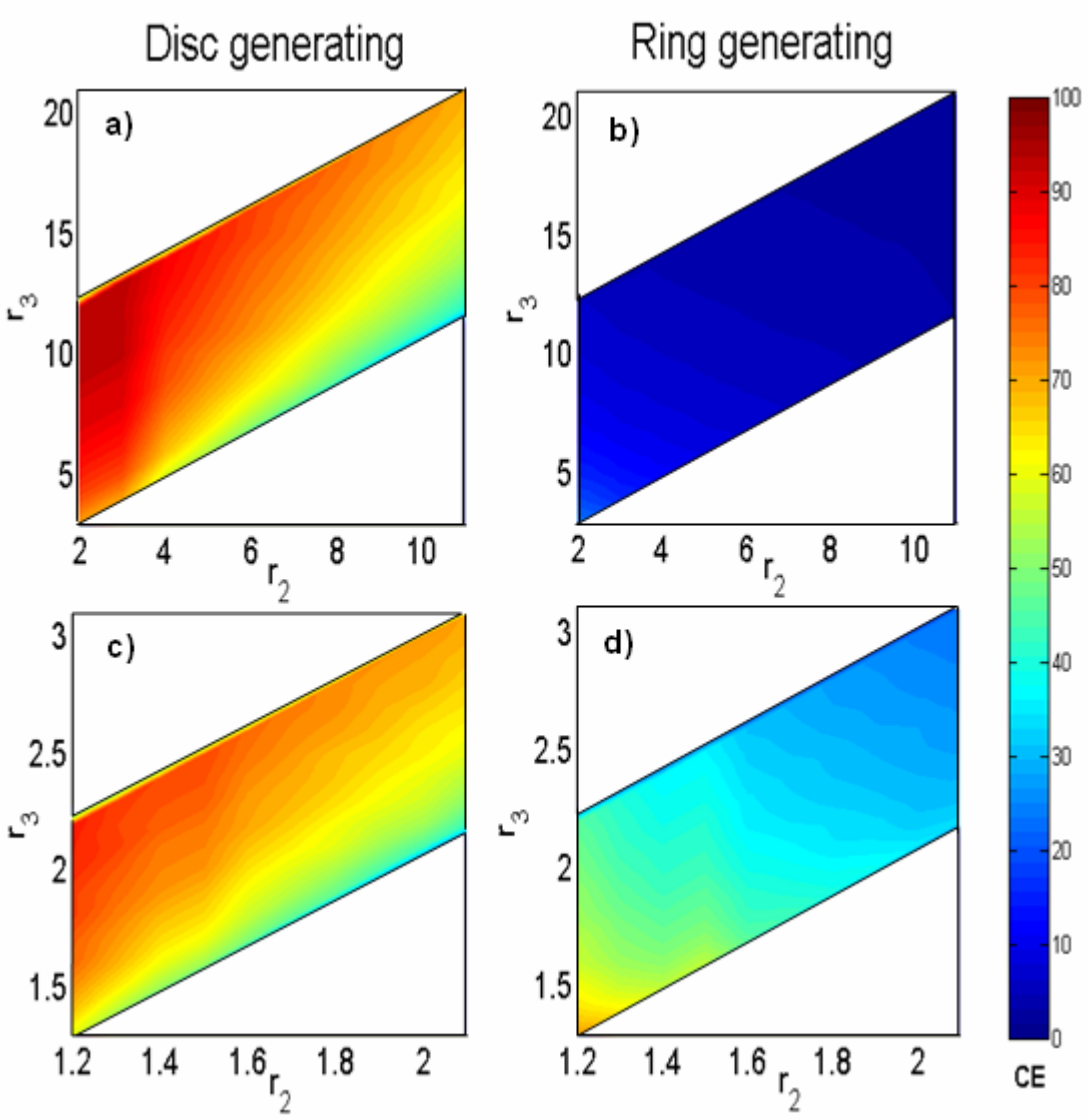
Disc generating
Ring generating
a)
b)
c)
d)
r3
r2
CE
20
15
10
5
2
4
6
8
10
3
2.5
2
1.5
1.2
1.4
1.6
1.8
100
90
80
70
60
50
40
30
20
10
0

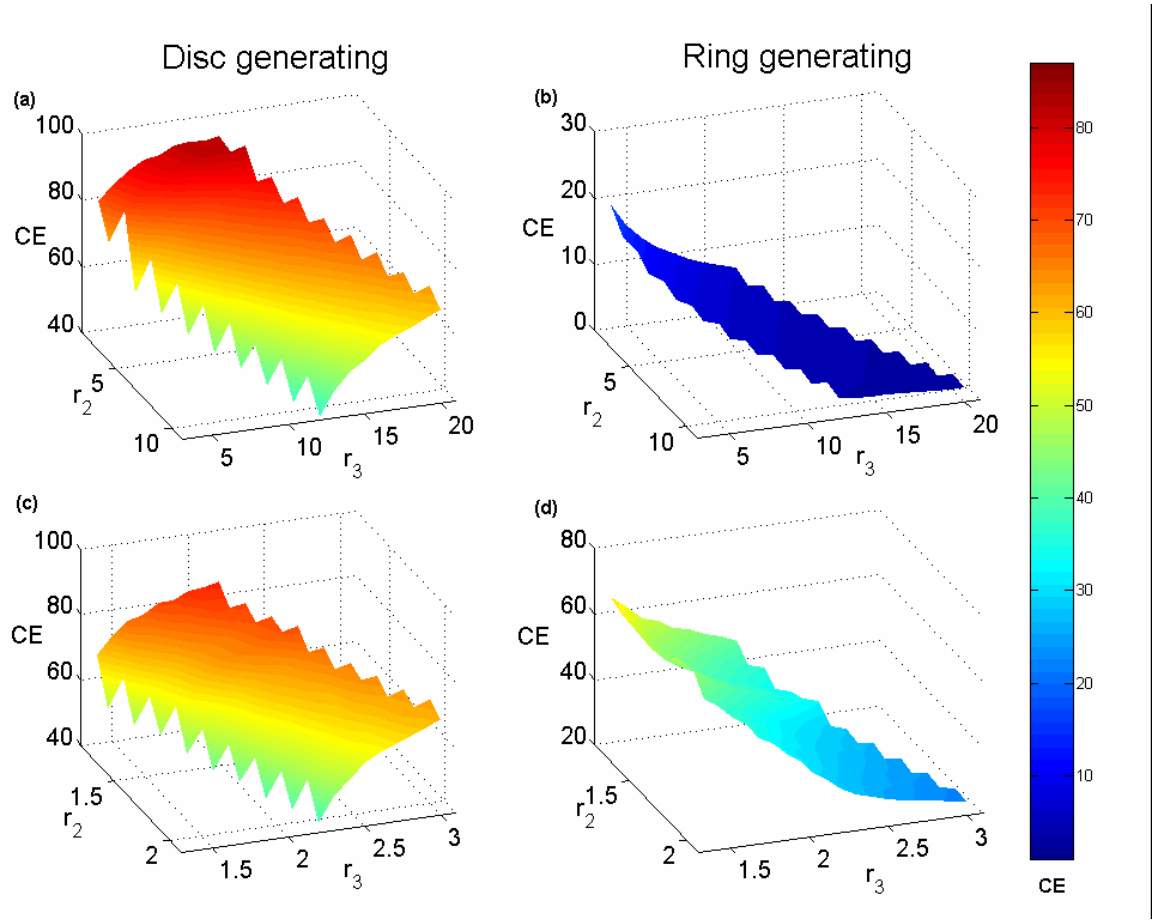

Figure 3.4: Effect of varying the electrode geometry on the collection efficiency. Outer ring radius,r_3, is plotted against inner ring radius,r_2. All lengths are normalised with respect to the disc radius, the electroactive species used is $Ru(NH_3)_6^{3+/2+}$, $D_{Ru} = 7.6x10^{-10}\ m^2s^{-1}$. The changes in collection efficiency (CE) are shown by the colour scale. **(a)** and **(c)** are for disc generating cases, **(b)**, **(d)** are for ring generating cases. Both sets of four plots show the same data only in different presentations.

(b) Recessed and protruding electrodes

When comparing CE values obtained with our model and those obtained experimentally, by ourselves and others, some discrepancies appear (see Table 3.2) The values obtained by us for Electrode A and Electrode B are for the redox couple $Ru(NH_3)_6^{3+/2+}$. The inconsistent nature of the discrepancy between the modelled CE and the experimental values would tend to suggest that the cause is experimental rather than numerical. SEM observation of the surface of our electrodes often revealed minor geometrical imperfections which seem to stem from the polishing process. We found that polishing sometimes produced protruding or recessed electrodes as a result of the differences between the hardness of electrode and the insulating material. This observation motivated our numerical investigation of these effects which incidentally is relevant to electrodes produced by lithographic techniques which also result in protrusions or recesses being formed.

Authors	Redox couple	Electrode dimensions			Disc Generating Collection Efficiency %		
					Experimental	Modeled	Difference % vs Model
		r1	r2	r3			
Kovalcik et al [102]	$MV^{2+/1+}$	1.25E-05	2.25E-05	2.35E-05	38	38.1	-0.3
Ghanem et al.[121]	$Fe(CN)_6^{4-/3-}$	2.50E-05	3.20E-05	3.24E-05	30	26.0	15.4
Liljeroth et al.[103]	$FcMeOH^{/1+}$	1.25E-05	1.24E-04	1.25E-04	33	19.4	70.1
Liljeroth et al.[77]	$Ru(NH_3)_6^{3+/2+}$	5.00E-06	3.47E-05	3.50E-05	26	23.0	13.0
Electrode A	$Ru(NH_3)_6^{3+/2+}$	2.50E-05	3.12E-05	3.37E-05	49.5	49.5	0.0
Electrode B	$Ru(NH_3)_6^{3+/2+}$	6.60E-05	8.90E-05	9.04E-05	34.7	26.2	32.4

Authors	Redox couple	Electrode dimensions			Ring Generating Collection Efficiency %		
					Experimental	Modelled	Difference % vs Model
		r1	r2	r3			
Kovalcik et al [102]	$MV^{2+/1+}$	1.25E-05	2.25E-05	2.35E-05	28	32	-12.5
Ghanem et al.[121]	$Fe(CN)_6^{4-/3-}$	2.50E-05	3.20E-05	3.24E-05	84	50.3	67
Liljeroth et al.[103]	$FcMeOH^{/1+}$	1.25E-05	1.24E-04	1.25E-04	-	3.9	-
Liljeroth et al.[77]	$Ru(NH_3)_6^{3+/2+}$	5.00E-06	3.47E-05	3.50E-05	-	6.2	-
Electrode A	$Ru(NH_3)_6^{3+/2+}$	2.50E-05	3.12E-05	3.37E-05	56.3	50.1	12.4
Electrode B	$Ru(NH_3)_6^{3+/2+}$	6.60E-05	8.90E-05	9.04E-05	37.2	46.6	-20.2

An analytical solution for the current at a deeply recessed micro-disc was established by Bond et al.(88) More recently an analytical solution for coupled electrochemical and chemical (EC') mechanism at a recessed micro-disc electrode was presented.(118) Recessed and protruding disc and band electrodes have also been studied numerically.(87,119,120) To our knowledge, however, there has been no investigation of the effects of protruding or recessed collector-generator assemblies.

The model used is essentially the same as in the previous section only additional boundaries are present because of the recess and protrusion. The changes made to the geometry of the model are seen in Figure 3.2c, and the additional boundary conditions are given in Table 3.3. The flux at the electrodes also changes, for a recessed case, the walls surrounding the electrodes are assumed insulating so flux is given by:

$$J = 2\pi \int_{\rho_1}^{\rho_2} \nabla_n c r dr \tag{3.10}$$

The integration limits ρ_1 and ρ_2 are respectively 0 and r_1 for the disc and r_2 and r_3 for the ring. For the protruding case the protruding walls are considered active electrochemically so the flux at the electrodes must include these boundaries:
For the protruding disc:

$$J = 2\pi \left(\int_0^{r_1} \nabla_n c r dr + r_1 \int_0^{z_1} \nabla_n c dz \right) \tag{3.11}$$

For the protruding ring:

$$J = 2\pi\left(\int_{r_2}^{r_3} \nabla_n c r dr + r_2 \int_0^{z_1} \nabla_n c dz + r_3 \int_0^{z_1} \nabla_n c dz \right) \quad (3.12)$$

Table 3.3. Boundary conditions for both ring and disc generating cases.

	Disc generating	Ring generating
Boundary conditions		
z=0 $0<r\leq r_1$	$c_A = 0$; $\nabla_n c_B = -\nabla_n c_A$	$\nabla_n c_A = -\nabla_n c_B$; $c_B = 0$
z=0 $r_2<r\leq r_3$	$\nabla_n c_A = -\nabla_n c_B$; $c_B = 0$	$c_A = 0$; $\nabla_n c_B = -\nabla_n c_A$
z=0 $r_1<r\leq r_2$; $r_3<r\leq r_{max}$	$\nabla_n c_A = \nabla_n c_B = 0$	$\nabla_n c_A = \nabla_n c_B = 0$
r=0 $0<z\leq z_{max}$	Axial symmetry	Axial symmetry
$r= r_{max}$ $0<z\leq z_{max}$	$c_A = 1$; $c_B = 0$	$c_A = 1$; $c_B = 0$
$z= z_{max}$ $0<r\leq r_{max}$	$c_A = 1$; $c_B = 0$	$c_A = 1$; $c_B = 0$
Recessed electrodes $r= r_1$; $r= r_2$; $r= r_3$ $0<z\leq z_1$	$\nabla_n c_A = \nabla_n c_B = 0$	$\nabla_n c_A = \nabla_n c_B = 0$
Protruding electrodes $r= r_1$ $0<z\leq z_1$ $r= r_2$; $r= r_3$ $0<z\leq z_1$	$c_A = 0$; $\nabla_n c_B = -\nabla_n c_A$ $\nabla_n c_A = -\nabla_n c_B$; $c_B = 0$	$\nabla_n c_A = -\nabla_n c_B$; $c_B = 0$ $c_A = 0$; $\nabla_n c_B = -\nabla_n c_A$

Results and discussion

For a given electrode geometry (r_1= 25 μm, r_2= 31.2 μm and r_3= 33.7 μm) three cases are considered with ring and disc as generators, (i) both ring and disc protruding or recessed (circle marker), (ii) only disc protruding or recessed (square marker), (iii) only ring protruding or recessed (diamond marker). Fig 3.5 summarises the results obtained, the solid symbols represent disc generating cases and the open symbols ring generating cases. There is a clear indication that the CE drops with increasing recess and rises with increasing protrusion of the electrodes. The only times this is not the case is when the generator alone is recessed or protruding, then both protrusion and recesses result in a slight drop in the CE value. It seems therefore that altering the mass transport to the collector is the critical factor in altering the CE of the ring-disc microelectrodes. This observation is true regardless of the shape of the collector but is more marked when the ring is collecting than when the disc is collecting. This is because radial diffusion to a micro-ring electrode is even more predominant than to a micro-disc electrode. Further simulations were carried out to assess the influence of electrode geometry on these

results. For different electrode geometries the trends described in Fig 3.5 stay unchanged, except that as the separation between the electrodes increases, the effects of protrusion and recess on the CE decrease. Similarly as the outer ring radius is increased, a recess or protrusion will have less of an effect. From the trends described in Fig 3.5 it is possible to infer that Electrode A has a slight protrusion of the disc (≈1 μm), similarly the electrode used by Ghanem et al.(121) which has comparable geometries could have a protruding disc or both a protruding ring and disc.

In practice, the size of the recess or protrusion that occurs as a result of polishing is small (≤1 μm). Unfortunately the changes in CE appear steepest at low z_1 values. For electrodes produced by micro-lithography the recesses or protrusions are larger but their value is known and controllable, which is advantageous. If lithography is to be used, one would recommend not using an insulator to produce protruding electrodes which benefit from the increase in CE values.

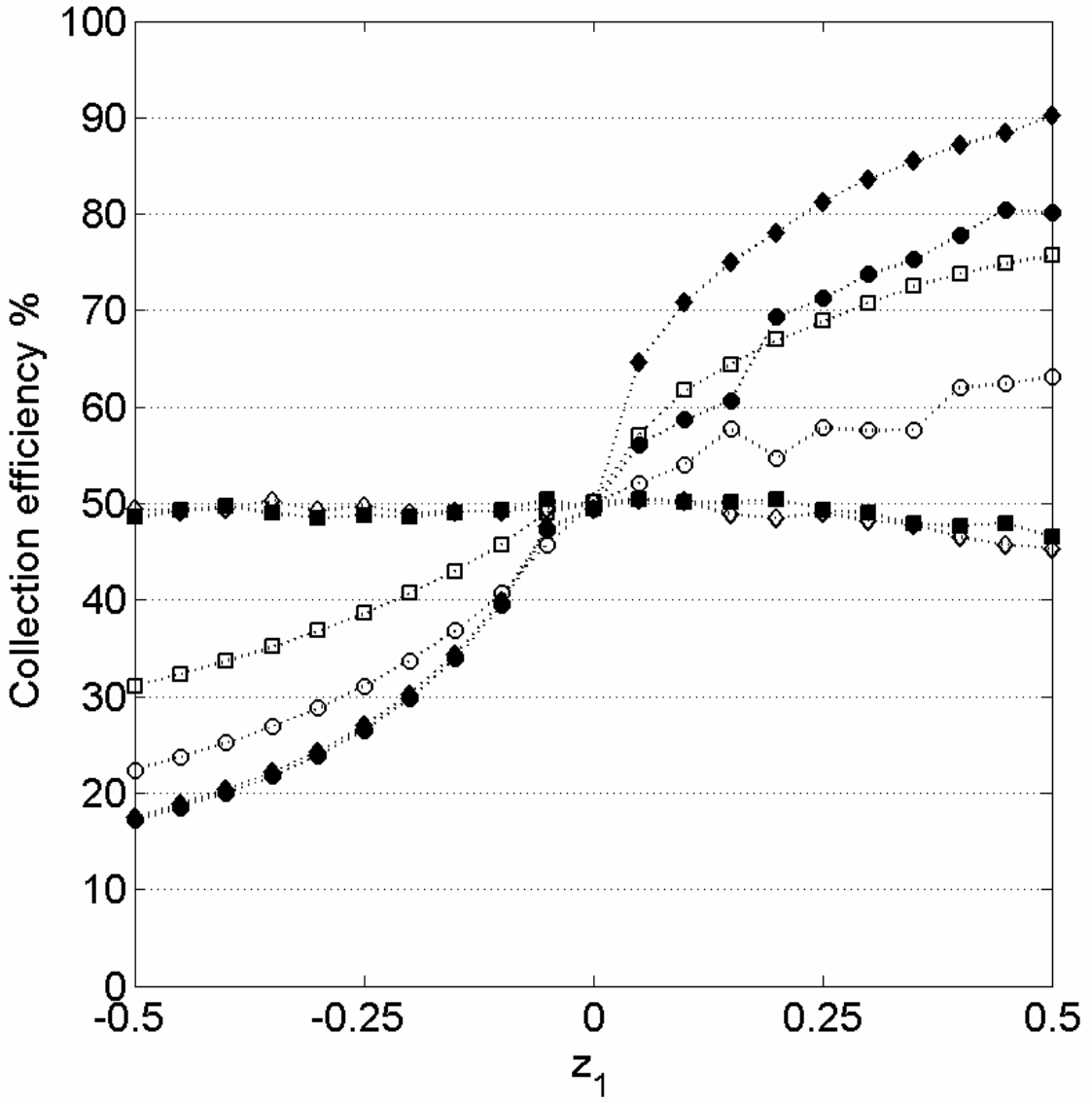

Figure 3.5: Effect of recess or protruding electrodes on the collection efficiency for an electrode with r_1= 25 μm, r_2= 31.2 μm and r_3= 33.7 μm in a 10mM $Ru(NH_3)_6^{3+/2+}$ solution. The height of the protrusion and depth of the recess is described by z_1, which is positive for protrusions and negative for recesses. Disc generating mode (filled marker) and the ring generating mode (empty marker) are simulated. Circles indicate both ring and disc protruding/recessed, squares only the disc and diamonds only the ring protruding/recessed.

In Fig 3.5 when the ring is generating with both ring and disc protruding (empty circle) the CE seems to fluctuate.. Some fluctuations are also observed on the disc generating trace (filled circle) again with ring and disc protruding. We have repeated the simulations for these cases taking intermediate z_1 values, to those shown on the figure and have found that the instability in the collection efficiency is still present.

When the electrodes are protruded the entire protruding surface becomes active electrochemically. The disc is no longer a disc but a solid cylinder and similarly the ring becomes a hollow cylinder. It is we believe the increase in electrode area which is not matched with an increase in current because of the non-ideal mass transport to these new surfaces that leads to the fluctuation observed. Figure 3.6 shows the concentration profile for the ring generating cases when both electrodes are protruding. It highlight the peculiar mass transport to the walls of the protruding electrodes.

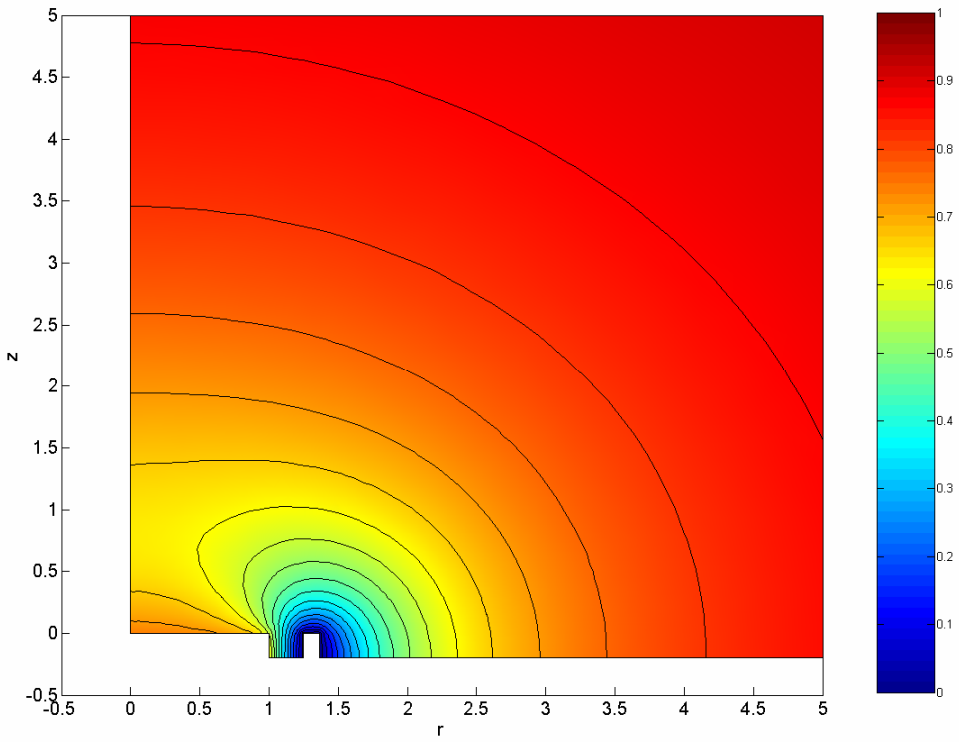

Figure 3.6: Concentration contour plots for ring generating case. Both ring and disc are protruding (Z_1 = 0.2), contour lines show concentration (line spacing c= 0.5).

(c) Varying the flux distribution at the generator electrode

The collection efficiency of a given ring-disc microelectrode describes how much of the species produced at the generator reaches the surface of the collector. Understanding the flux distribution at the generator is therefore important. (122) Aside from electrode geometry there are three parameters that can affect the flux at the surface of an electrode, the voltage applied, the diffusion coefficient and the reaction rate constant of the species.

Theory

We consider a system consisting of a ring-disc microelectrode set in an insulating plane. The model is in cylindrical polar coordinates (r,z) with rotational symmetry about the z axis as described in Fig 3.2a. The solution within the model boundary contains an electro-active species, A, which is assumed to undergo a simple one electron transfer leading to species B (see Eq. 3.5). The model geometry, parameters and equation system were non-dimensionalised with respect to, R_1, the radius of the disc, $C_{A,\infty,}$ the bulk concentration of species A and D the diffusion coefficient (75) (see section 3.2.1a).

For a still solution with high background electrolyte concentrations the mathematical model describing the mass transport of species A and B is given by:

$$\frac{\partial c_B}{\partial \tau} = \nabla^2 c_B \tag{3.13}$$

$$\frac{\partial c_A}{\partial \tau} = \nabla^2 c_A \tag{3.14}$$

In these simulations slow scan cyclic voltammograms (i.e. v =1 mV/s) are being modelled. In this case the reaction occuring at the generator is described by a normal flux in accordance to the Butler-Volmer equation, Eq. 3.15, for which the electron transfer coefficeint,α, is taken equal to 0.5. The boundary condition are summarised in Table 3.4.

$$\nabla_n c_A = \Theta\left(e^{[-\alpha\xi]} c_{A,0} - e^{[(1-\alpha)\xi]} c_{B,0}\right) \tag{3.15}$$

Θ and ξ are respectively a non-dimensional reaction rate and the non-dimensional applied voltage defined as:

$$\Theta = \frac{k_o \times R_1}{D} \qquad \xi = \frac{F \times (E - E_o)}{T \times \Re}$$

Where $\mathbf{k_0}$ is the reaction rate constant, **D** the diffusion coefficient, $\mathbf{R_1}$ the radius of the disc, **F** Faraday's constant, **E** the applied potential, $\mathbf{E_0}$ the formal redox potential, **T** the temperature and $\Re$ the Universal gas constant.

The potential applied to the generator, ξ is swept between ξ_{min} and ξ_{max} with a scan rate v:

$$\xi = \xi_{min} + v\tau \tag{3.16}$$

The non-dimensional normal flux at the electrodes is given by Eq. (3.8).

In these time dependent simulations, the collector is always at the diffusion limiting case and the geometry of the electrode is $r_1 = 1$ $r_2 = 1.25$ $r_3 = 1.35$.

Table 3.4. Initial and boundary conditions for both ring and disc generating cases.

	Disc generating	Ring generating
Initial conditions		
$\tau = 0$	$c_{A,\infty} = 1$; $c_{B,\infty} = 0$	$c_{A,\infty}=1$; $c_{B,\infty}=0$
Boundary conditions		
z=0 $0<r\leq r_1$	Eq 3.14; $\nabla_n c_B = -\nabla_n c_A$	$\nabla_n c_A = -\nabla_n c_B$; $c_B = 0$
z=0 $r_2<r\leq r_3$	$\nabla_n c_A = -\nabla_n c_B$; $c_B = 0$	Eq 3.14; $\nabla_n c_B = -\nabla_n c_A$
z=0 $r_1<r\leq r_2$; $r_3<r\leq r_{max}$	$\nabla_n c_A = \nabla_n c_B = 0$	$\nabla_n c_A = \nabla_n c_B = 0$
r=0 $0<z\leq z_{max}$	axial symmetry	Axial symmetry
$r= r_{max}$ $0<z\leq z_{max}$	$c_A = 1$; $c_B = 0$	$c_A = 1$; $c_B = 0$
$z= z_{max}$ $0<r\leq r_{max}$	$c_A = 1$; $c_B = 0$	$c_A = 1$; $c_B = 0$

Results and discussion

As the voltage applied to the generator goes beyond the formal redox potential, E_o, the electrode begins to act as a source or sink and the radial diffusion to and from the electrode will increase. This has been well described in terms of the edge effect. The change in the diffusion profile at the generator can be detected by the collector providing

the gap between the two electrodes is small. In Fig 3.7 (b,d) the collector does indeed detect this change and the CE is seen to rise as the voltage goes above E_o. Different electrode geometries will increase or decrease this effect. We envision that the change in CE as a result of increasing overpotential could be used as a mechanism to probe different aspects of the mass transport mode being investigated.

To investigate the effects of the diffusion coefficient and reaction rate constants on the collection efficiency different values of Θ (3e4 to 3e-6) were also considered in these simulations. Curves a in Figure 3.7 are representative of dissolved gases reacting at the electrode whilst curves f would represent proteins reacting on the electrode. The effect of varying Θ on the generator's flux is seen in Fig 3.7(a,c). As Θ decreases the amount of overpotential needed to reach the diffusive limiting case increases. The collection efficiency is affected by these changes but eventually reaches the same limiting values. A decrease in the reaction rate constant results in an increase in the level of overpotential needed to reach the maximum collection efficiency. On the other hand an increase in the diffusion coefficient results in an increase in the over potential needed. It is the changes in reaction rate constants that are most relevant, however, because diffusion coefficients in solution only vary by two to three orders of magnitude whereas k_0 can vary by 10 orders of magnitude. The issue of needing more overpotential to reach the same collection efficiency is a problem because most of the time the oxidation and reduction of a species is limited to a specific potential window beyond which other reactions will interfere. As a result it may not be possible to reach the required level of overpotential to drive the reaction fully, in which case the flux at the electrodes and the collection efficiency will be lower and may lead to misinterpretation.

Experimental confirmation of the simulated results are shown in Fig 3.7a and 3.6c. The redox couples used are ($Ru(NH_3)_6^{3+/2+}$), for the line marked Ru, and ($Fe^{2+/3+}$ as $Fe(NH_4)_2(SO_4)_2$), for the line marked Fe. The oxidation of Fe(II) to Fe(III) is shown as a reduction for comparison purposes (line marked Fe). The location of both experimental curves with respect to simulated curves falls within the limit of published data for D and k_o values.(123-126).

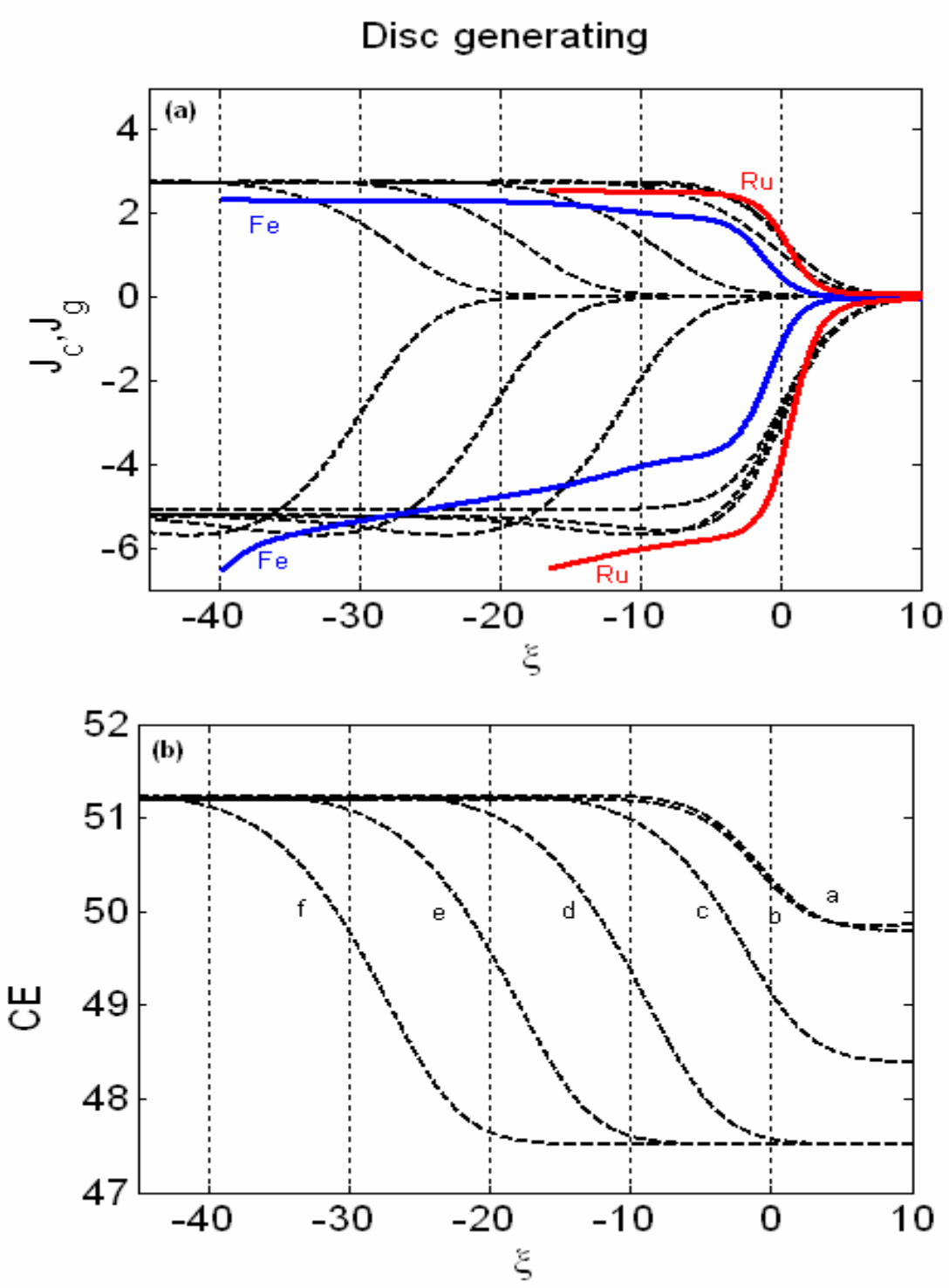
Disc generating
(a)
Ru
Fe
Fe
Ru
J_c, J_g
ξ
(b)
a
b
c
d
e
f
CE
ξ

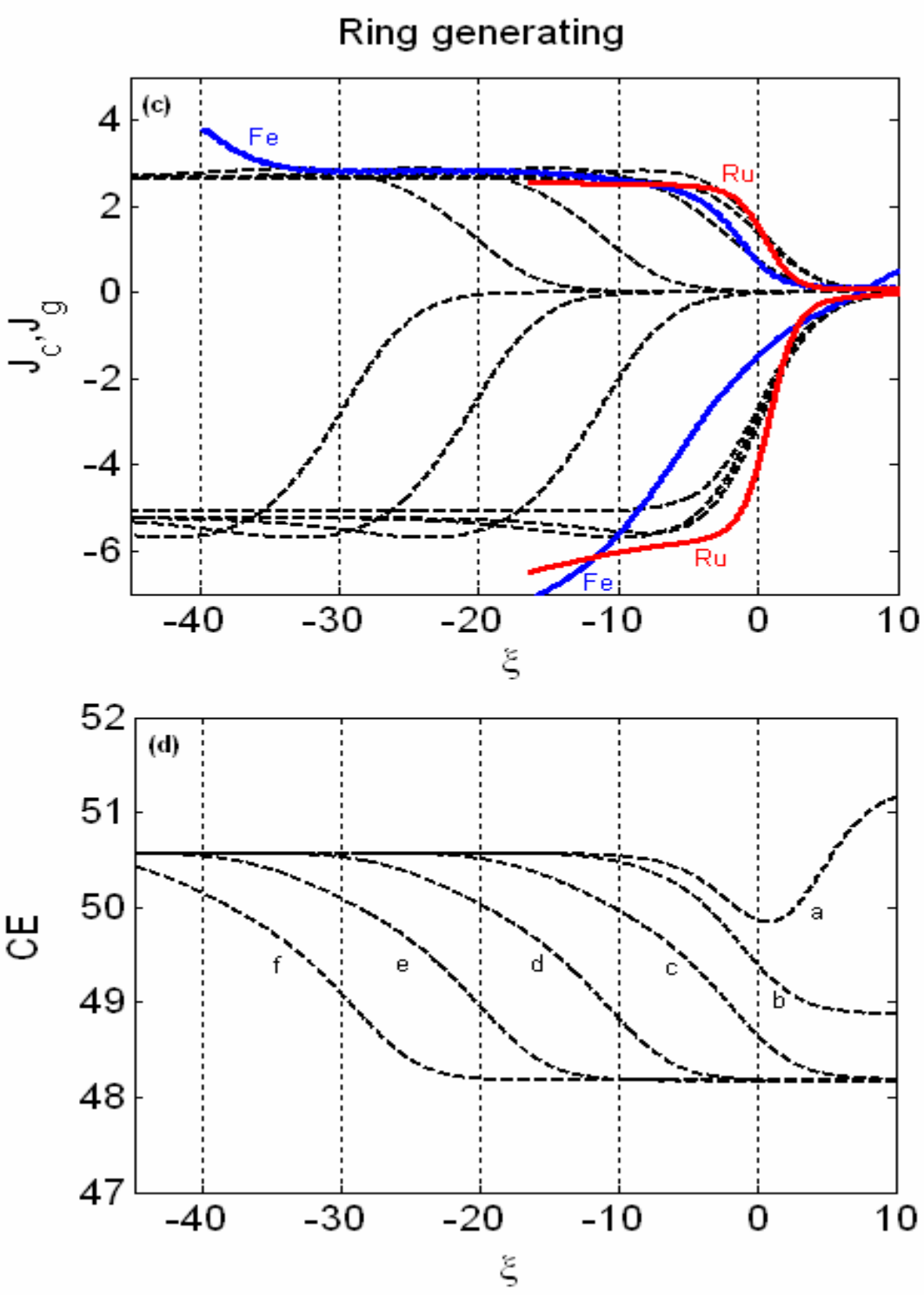

Figure 3.7: Influence of voltage, diffusion coefficient and reaction rates constant on the flux **(a,c)** and collection efficiency **(b,d)** of a ring-disc microelectrode. The dimensions of the electrode used are R_1= 25 µm R_2= 31.2 µm and R_3= 33.7 µm. Curves a, b, c, d, e and f represent simulations for different values of Θ (a =3.16x10^4, b =3.16 x10^2, c =3.16,

d =3.16 x10^{-2}, e =3.16 x10^{-4}, f =3.16 x10^{-6}). In (a) and (c) the modeled fluxes are shown as dotted lines, whilst experimental recordings are solid lines. The collector flux, J_c, is positive and the generator flux, J_g, negative. The experimental curves marked Ru represents the reduction of $Ru(NH_3)_6^{3+/2+}$ and the line marked Fe represents the oxidation of $Fe(NH_4)_2(SO_4)_2$ shown as a reduction for comparison purposes.

Conclusion

The evaluation of collection efficiencies at ring-disc microelectrodes operating as collector-generators was investigated theoretically. The disc diameter, inner ring radius and outer ring radius were varied extensively and their effect on the collection efficiency were simulated. In all cases CE increases as the inner ring radius is decreased. For disc generating cases, CE increases when the outer ring radius is increased whereas for ring generating cases CE decreases as the outer ring radius increases.

The influence of recessed or protruding electrodes on the CE was also investigated and was found to be significant. In general, protrusion of the electrode increases the CE values whereas a recess decreases it. Recess or protrusion of the collector electrode will always be more significant than a recess or protrusion of the generator.

The contribution of electrode voltage, diffusion coefficient and reaction rate constant on the CE values obtained for ring-disc microelectrode was also modelled. All three parameters affect the flux distribution at the generator electrode. The highest collection efficiencies are achieved when the flux at the edges of the generator is at a maximum, which is possible with high overpotentials, fast diffusion and fast kinetics.

Finally experimental measurements of the various cases modelled showed good agreement with simulations.

3.2.2 Transient current response at the ring

When used as a collector-generator, the ring-disc microelectrode is able to detect changes in mass transport in its vicinity. Mass transport in tissue can be divided into two components, a diffusion term and a convection term. Changes in perfusion in tissue mostly reflect changes in convection, the diffusion term is believed to be constant

because the tissue environment is not changing as the measurements are being made. If the sensor is to be used to make measurements in a number of different tissue locations within the same experiment, then the diffusion term cannot be overlooked. In the steady state, differentiating between the contribution from diffusion and the contribution from convection is impossible. During the transient response that proceeds the steady state this may be different. This is because the timescales of diffusion and convection are different. Exploiting this difference should enable us to identify and quantify the contribution of diffusion mass transport. The questions we will be answering are, what influence do the diffusion coefficients of species A and B and the initial concentration of species A have on the transient current response of the sensor. Experimental investigation of the response of the sensor to different tissue types (i.e. fat, smooth muscle, kidney etc.) is presented in Section 6.2.1. Here we consider the numerical simulation of such experiments. The model used is the same as in Section 3.2.1.a except that a time dependant case is considered (i.e. Eq. 33.13, 3.14). Also the diffusion coefficients of species A and B are no longer equal as they are varied independently. Varying the initial concentration of species A is also considered, although it must be said that the effect this will have is more predictable (i.e. vary the current response). The range of diffusion coefficients consider is from 0 to 1 (non dimenalised with respect to the value of D_A in solution) for both species A and B and c_A at time t=0 is varied from 0 to 1 (nondimentionalised with respect to the value of c_A in solution).

Results and discussion

The results in Figure 3.8 show that once a steady state is achieved the value of the diffusion coefficient of species A and B or the concentration of A has no effect on the level of collection efficiency. This was also highlighted is section 3.2.1.c where it was shown that the same steady state collection efficiency values were achieved for different values of $k_0.r/D$. In the transient state varying the concentration and diffusion coefficient of species A (Fig 3.8.a,b) also has little effect on the CE behaviour. The only change seen is a reduction in the current values for the ring and disc because fewer tracer molecules (i.e. species B) are present (see Fig 3.9a,b). This was expected as it follows from the limiting equation at an electrode, which relate the current to the concentration and

diffusion coefficient of a species. Significant changes to the collection efficiency occur, however, when the diffusion coefficient of species B is varied (see Fig 3.8.c). In this case, as the diffusion coefficient increases the time needed to reach a steady state CE value decreases. These changes in the CE are mostly due to changes in the ring current as seen in Fig. 3.9c, the slight changes in the disc current reflect the fact that as D_B changes the reaction at the generator becomes diffusion limited but with respect to the diffusion of species B.

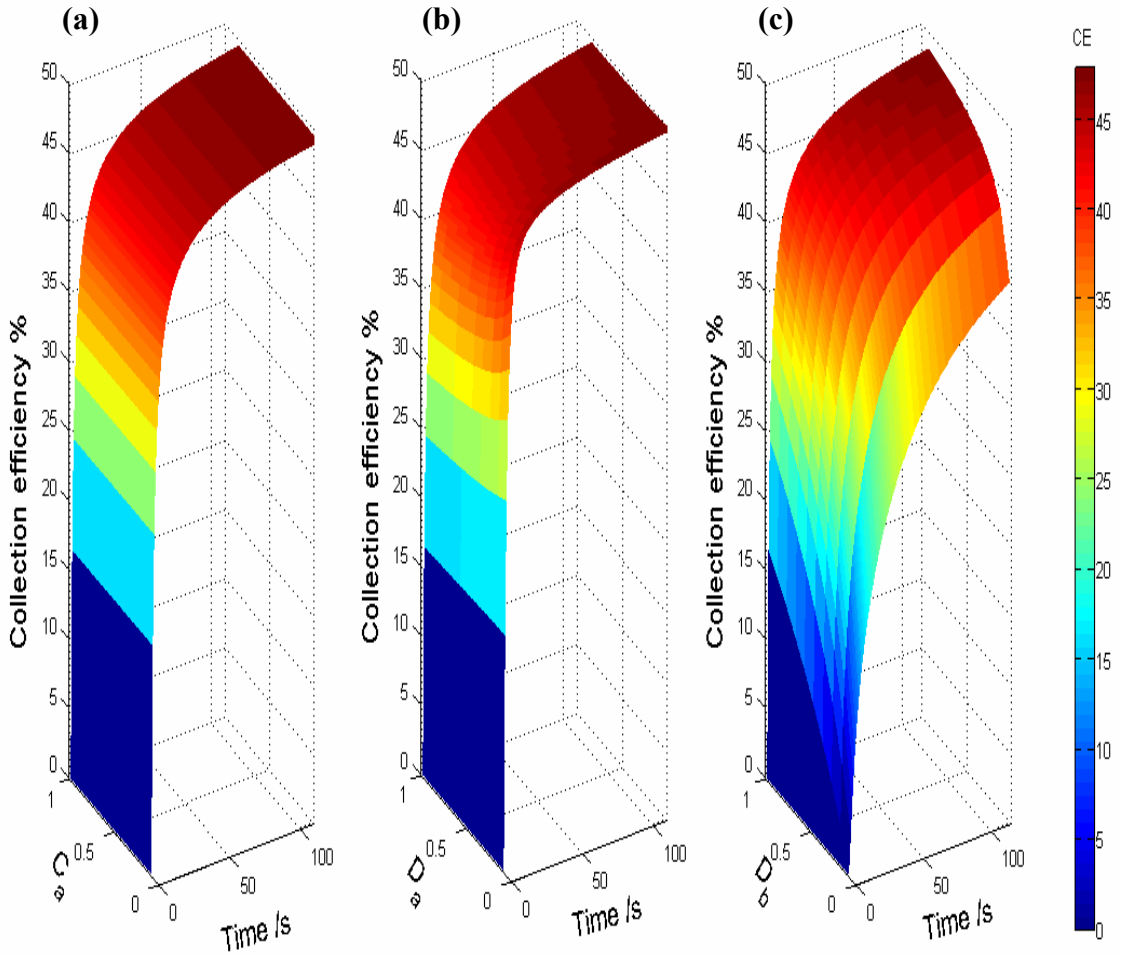

Figure 3.8: Transient variation of the collection efficiency leading to the steady state. **(a)** Concentration of species A is changed from 0-1. **(b)** Diffusion coefficient of species A is varied from 0-1 and **(c)** diffusion coefficient of species B is varied from 0-1. The simulations were run for an electrode with geometry $r_1 = 1$, $r_2 = 1.2$ and $r_3 = 1.4$ and the redox couple used is $Ru(NH_3)_6^{3+/2+}$.

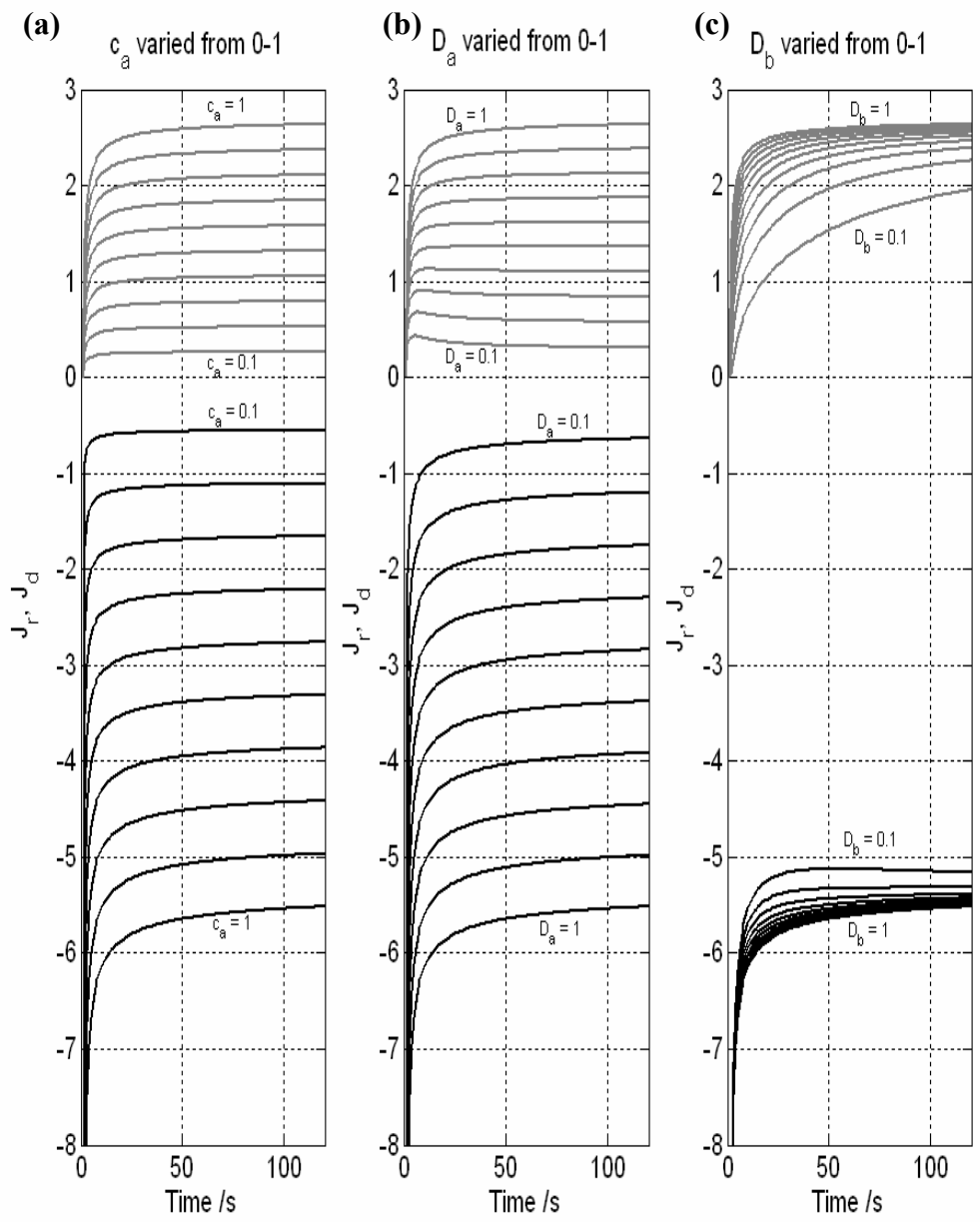

Figure 3.9: Current transients at the disc for **(a)** different value of c_A, **(b)** different value of D_A, **(c)** different values of D_B. The grey lines show the transient flux at the collector i.e. the ring. The black lines show the transient at the generator i.e. the disc. The simulations were run for an electrode with geometry $r_1 = 1$, $r_2 = 1.2$ and $r_3 = 1.4$ and the redox couple used is $Ru(NH_3)_6^{3+/2+}$.

These results support the idea that the ring-disc electrode operating in the collector generator mode is capable of differentiating between the contributions from diffusion and convection mass transport. Such studies have been carried out on band-band microelectrode by Amator et al. and Feldman et al. (127,128), both of which produced similar conclusions. However, these effects have not been reported for ring-disc microelectrode to our knowledge nor has the application of this technique been linked to a way of monitoring changes in tissue type or structure (i.e. fat, muscle, burnt tissue, etc.)

The key findings of this investigation are that if the current at the electrodes decreases it is due to a change in D_A or c_A and if the collection efficiency changes during the transient response it is due to a change in D_B. This becomes very useful when the sensor is placed in tissue, as we will be able to tell what is taking place in the tissue. A steady state shift in the collection efficiency can be attributed to a change in convection. A change in the current values will indicate a change in the concentration or diffusion coefficient of species A (i.e. water). A change in the transient collection efficiency will indicate a change in the diffusion coefficient of species B (i.e. hydrogen). All of these insights give a more complete understanding of what is occurring in tissue.

3.2.3 Investigating the effect of a membrane layer above the sensor

To protect the sensor from fouling when used in-vivo, a gas permeable membrane is often applied on the surface of the electrodes. Numerically this can be modelled by considering a layer above the electrode in which the diffusion coefficient of both species A and B and the concentration of species A are varied. This follows from the idea that both diffusion coefficients and concentration are generally different from their bulk values within a membrane.

Membrane coated electrodes or electrodes covered by a thin film are found in a large number of applications (i.e. fuel cells, enzyme based electrodes, in-vivo sensors). In general the membrane is used either to trap a redox mediator or to act as a selective barrier. Some numerical work is also reported and has focused on assessing the effect of membrane porosity, mass transport and the concentration and diffusion coefficient of the species within the membrane (129-131). Arkoub et al. investigated the effects of such variables on double band microelectrodes operating as collector-generator under a thin

film of Nafion to be used as an artificial nose (132). They were able to relate the current and collection efficiency of the bands to a specific membrane thickness, concentration and diffusion coefficient of the redox couple placed in the membrane. Such an analysis opens the possibility of in situ determination of membrane swelling, of redox concentration and diffusion coefficient, which ultimately improves the measurements accuracy. Such an analysis has not yet been reported for ring-disc electrodes and this motivated our investigation of the problem.

The model used is a steady state model. This model is very similar to the one used in Section 3.2.1, only this time an additional subdomain is present as shown in Fig 3.10. A continuity boundary condition is applied to the internal boundaries of this sub domain. In addition to the extra boundary, this model differs from that in Section 3.2.1.a in that the initial value of c_a and the overall values of D_a and D_b can be varied from 0 to 1 in the membrane. The size of the membrane was also varied from 0 to 1. The simulations were run for an electrode with geometry $r_1 = 1$, $r_2 = 1.2$ and $r_3 = 1.4$. These simulations are steady state simulations.

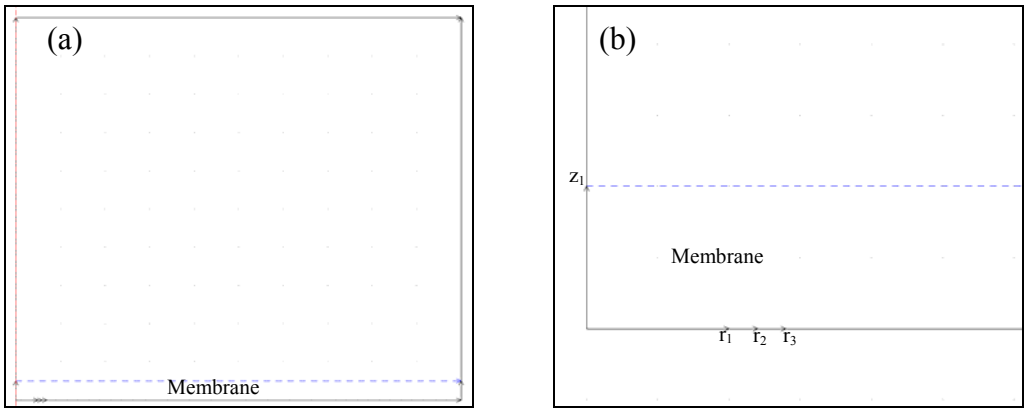

Figure 3.10: Geometrical model of the ring-disc microelectrode with a protective membrane above the electrodes. **(a)** View of the entire model, **(b)** close up of the electrode and membrane (thickness 1).

Results and discussion

The simulated results are shown in Figure 3.11a, 3.11b and 3.11c where the changes in collection efficiency (Z axis) are presented with respect to thickness of the membrane (X axis). In Fig 3.11a the Y axis shows the effect of varying the initial concentration of species A from 0 to 1 in the membrane. In Fig 3.11b the Y axis shows

the variation of D_a, the diffusion coefficient of species A in the membrane is varied from 0 to 1, In Fig 3.11c the Y axis show the variation in D_b, the diffusion coefficient of species B in the membrane is varied from 0 to 1.

From Fig 3.11a it is clear that varying the concentration of species A has no effect on the collection efficiency of the sensor. The electrode current will vary linearly with c_a but the ratio of the current stays the same, so the CE stays unchanged. This is true regardless of the membrane thickness. Similarly varying the diffusion coefficient of species A, Fig 3.11b has no effect on the collection efficiency, despite the current at the electrodes varying linearly with D_a (this follows from the equation describing the current at a microelectrode i.e. $I = 4nFDcr$). It is only when the diffusion coefficient of species B in the membrane is varied that the collection efficiency will be affected Fig 3.11c. In this case a large drop in the collection efficiency occurs as the diffusion coefficient tends towards 0 from its bulk value of 1. It is when the membrane thickness is minimum that the collection efficiency is lowest, as the membrane grows the collection efficiency recovers. Simulations with even larger membrane thicknesses confirm this further (see Fig 3.12).

Physically it is quite likely that D_b will change in the membrane in which case a thicker membrane will be more advantageous, this may however limit the detection capabilities of the sensor, namely its probing volume.

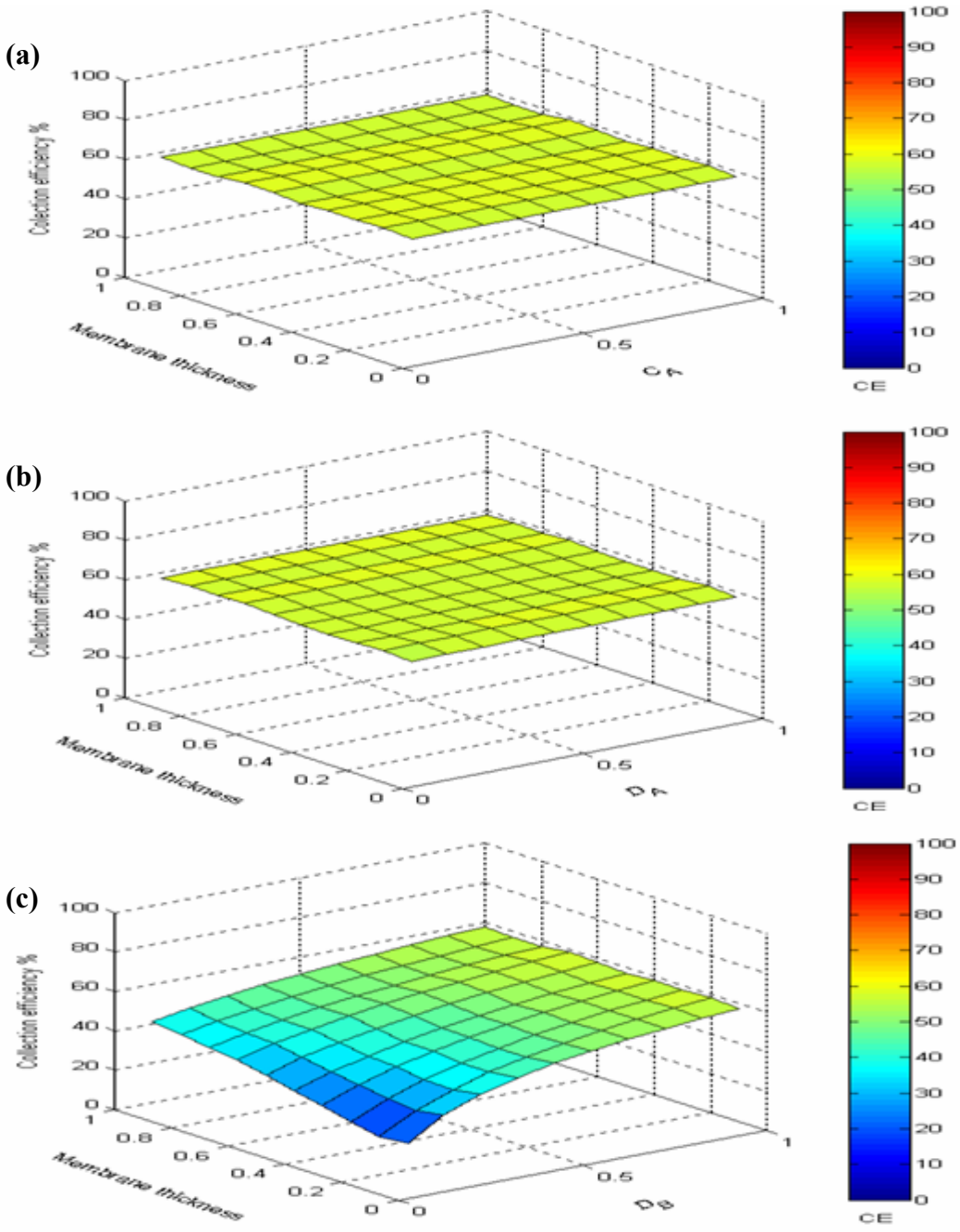

Figure 3.11: Variation in the collection efficiency as a result of a membrane above the sensor, disc generating case. Varying the concentration of species A in the membrane **(a)**. Varying the diffusion coefficient of species A in the membrane **(b)**. Varying the diffusion coefficient of species B in the membrane **(c)**. Electrode geometry is r_1=1 r_2=1.2 r_3=1.4, redox couple used is $Ru(NH_3)_6^{3+/2+}$.

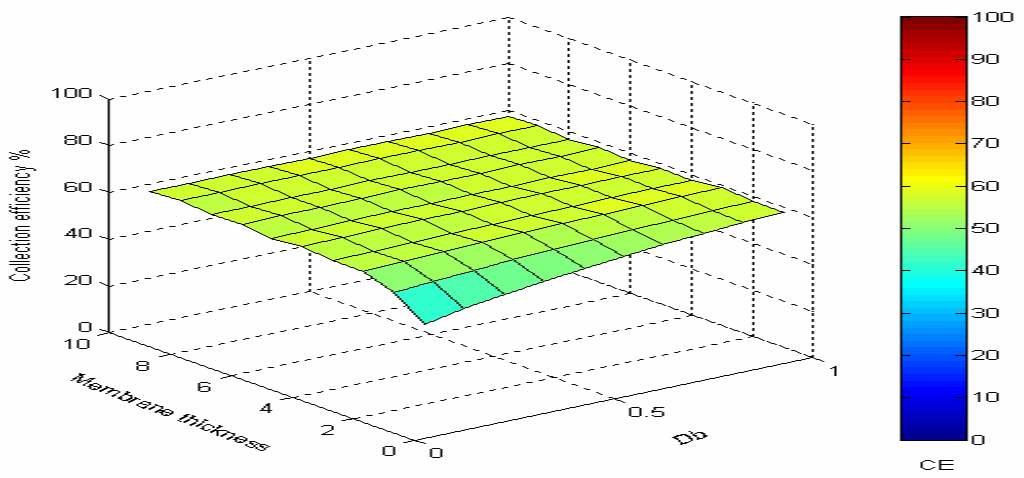

Figure 3.12: Variation in the collection efficiency as a result of a membrane above the sensor, disc generating case. Varying the diffusion coefficient of species B in the membrane. The thickness of the membrane is increase substantially from 0-10. Electrode geometry is r_1=1 r_2=1.2 r_3=1.4, redox couple used is $Ru(NH_3)_6^{3+/2+}$.

3.2.4 Influence of one capillary vessel in the vicinity of the sensor

One of the ways of assessing the influence of the environment on the sensor and the collection efficiency it measures, is to consider a microscopic view of the environment above the sensor. The question asked here is how would the sensor respond to the presence of a single capillary in its vicinity? This simple case was modelled and made more complex by varying the location of the capillary in space.

In these models we cannot use the axial symmetry simplification because of the presence of the capillary (i.e. the model geometry is no longer symmetrical). As a result to obtain quantitative data one has to model in three dimension, this is quite expensive computationally. Useful qualitative information can nevertheless be obtained from a two dimension model and along with the less expensive computation motivated our use of such a model.

Theory

We consider a steady state model in two dimension, which is a section through the ring-disc electrode. The ring and disc electrodes thus become line electrodes set in an insulating plane. The ring consists of two small lines set on either side of a larger line, the disc. Above the electrodes a circle represents the capillary vessel see Fig. 3.13. The solution within the model boundary contains an electro-active species, A, which is assumed to undergo a simple one electron transfer leading to species B (See Eq 3.5).

The forwards reaction occurs at the generator electrode whilst the backwards reaction occurs at the collector. The collection reaction is always assumed to be diffusion limited. Species A and B are assumed to diffuse freely in solution and have equal diffusion coefficients, D. The model geometry, parameters and equation system were non-dimensionalised with respect to, X_1, the radius of the disc, $C_{A,\infty,}$ the bulk concentration of species A and D the diffusion coefficient :

$$c_A = \frac{C_A}{C_{A,\infty}} \qquad c_B = \frac{C_B}{C_{A,\infty}} \qquad x = \frac{X}{X_1} \qquad y = \frac{Y}{X_1}$$

Dimensionless parameters are in lower case, whilst dimensional ones are in upper case. For a still solution with high background electrolyte concentrations the mathematical model describing the mass transport of species A and B is given by:

$$\nabla^2 c_A = 0 \tag{3.17}$$

$$\nabla^2 c_B = 0 \tag{3.18}$$

Where ∇^2 is the Laplacian operator in two dimensions (see Eq. 3.2). Within the model space a capillary vesel is prestent which is modelled as a circle, with diameter similar to that of a large capillary vessel (i.e. 10 μm in diameter). The walls of the capillary are assumed to be a sink for species B so that c_B=0. The boundary conditions used in this model are sumarised in Table 3.5. The flux at the electrodes is given by:

$$J = \int_{\rho_2}^{\rho_1} \nabla_n c_a \, dx \tag{3.19}$$

The integration limits ρ_1 and ρ_2 are respectively $-x_1$ and x_1 for the disc, x_2 and x_3 as well as $-x_2$ and $-x_3$ for the ring.

The model boundaries, x_{max} and y_{max} were twenty times greater than r_3. Simulations with larger limits did not significantly change the flux measured at the electrodes (i.e. <1%). The mesh was refined at the electrodes (minimum element size $0.01x_1$) and allowed to grow towards the boundaries. Doubling the number of mesh elements did not noticeably enhance the solution.

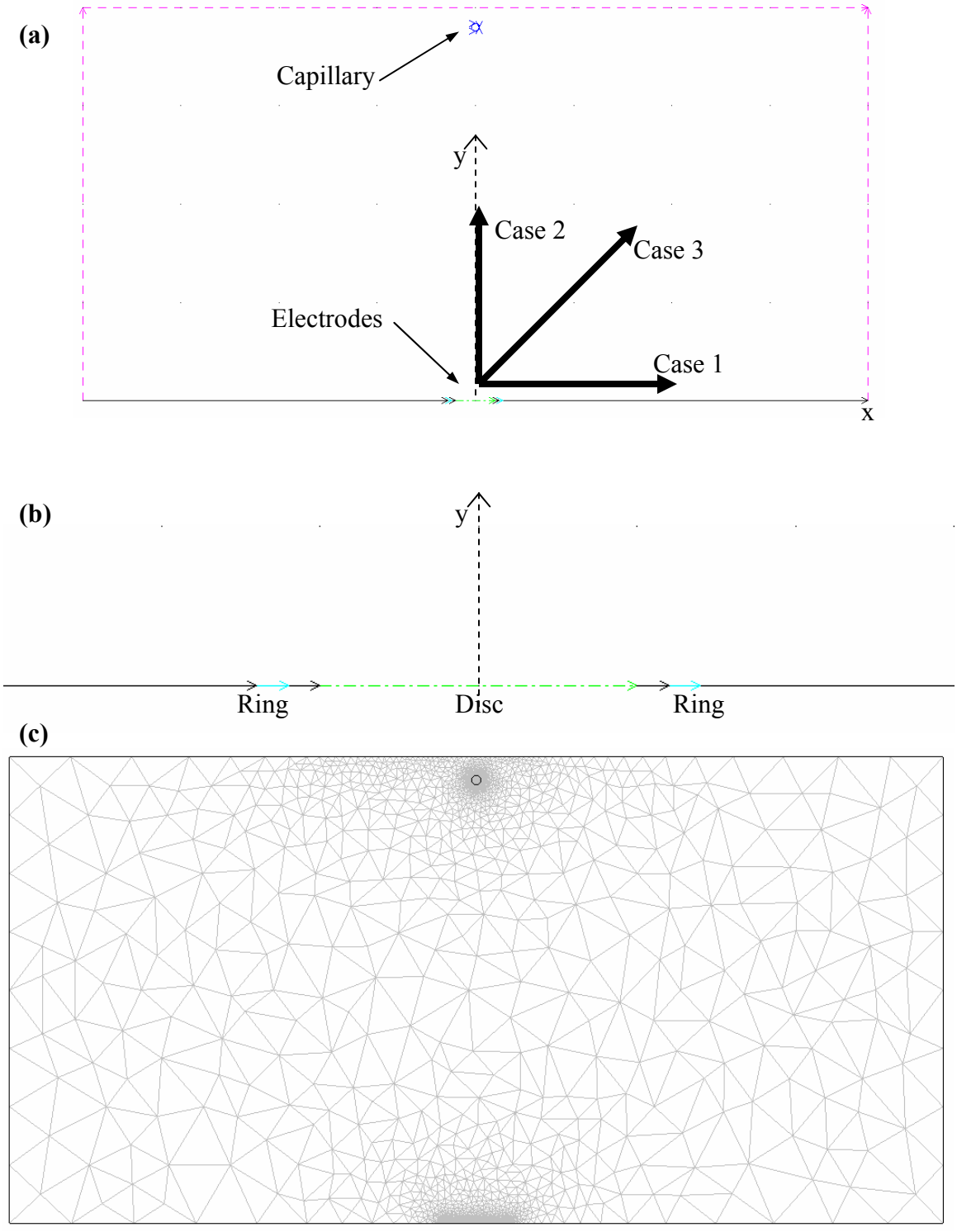

Figure 3.13: (a) Model geometry in two dimensions with a capillary vessel acting as a sink. The three movements of the capillary considered are shown as Case 1, 2 and 3 for respectively a horizontal, vertical and diagonal movement of the capillary. **(b)** Close up of the electrodes. **(c) Shows the model mesh structure.**

Table 3.5. Boundary conditions for disc generating cases.

	Disc generating
Boundary conditions	
y=0 $-x_1<x\leq x_1$	$c_A = 0$; $\nabla_n c_B = -\nabla_n c_A$
y=0 $x_2<x\leq x_3$; $-x_2<x\leq -x_3$	$\nabla_n c_A = -\nabla_n c_B$; $c_B = 0$
y=0 $x_1<x\leq x_2$; $x_3<x\leq x_{max}$; $-x_1<x\leq -x_2$; $-x_3<x\leq -x_{max}$	$\nabla_n c_A = \nabla_n c_B = 0$
$x=x_{max}$ $0<y\leq y_{max}$	$c_A = 1$; $c_B = 0$
$x=-x_{max}$ $0<y\leq y_{max}$	$c_A = 1$; $c_B = 0$
$y= y_{max}$ $-xmin<x\leq x_{max}$	$c_A = 1$; $c_B = 0$
Capillary walls	$c_B = 0$

Results and discussion

The location of the capillary vessel in the vicinity of the sensor will influence the measurement made at the sensor. As the capillary vessel approaches the sensor surface, the collection efficiency drops because the collector is no longer the sole sink for species B see Fig 3.14 (a, b, c). The somewhat unsteady traces observed in this figure are due to the rearranging of the mesh as the location of the capillary is changed. Figure 3.15 show the flux of species B into the capillary as it is moved vertically from the surface of the electrode case B in Fig 3.14. Figure 3.16 shows concentration plots of the capillary at different locations above the sensor.

These results are a clear indication that the sensor is able to detect a single capillary in its vicinity as long as it is no more than 6 radii lengths away from the centre of the disc. It must be said, however, that we have assumed a zero concentration of species B at the surface of the capillary, this may not always be the case. In fact it is more likely that the concentration of species B on the surface is between 0-1. The results in Fig 3.14 are therefore an overestimation of what is likely to occur in tissue. In addition, one must say that there is no apparent way of determining where the capillary is located. The drop in CE indicates that the capillary is close to the sensor but does not indicate where it is located with respect to the sensor. Finally these results are for a two dimensional model and therefore the values obtained are only qualitative.

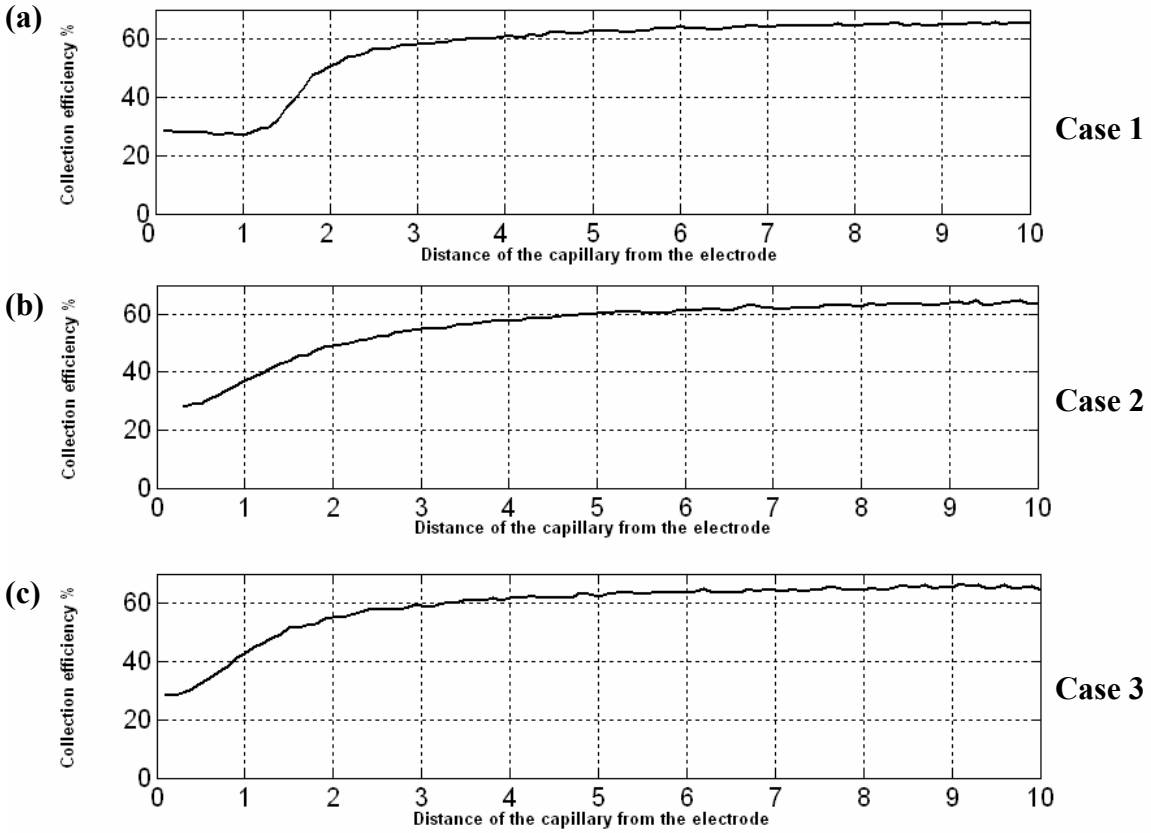

Figure 3.14: Influence of a single capillary vessel on the simulations made by the sensor the sensor and its measurement. Only disc generating cases are considered with an electrode with geometry r_1 = 1, r_2 = 1.2 and r_3 = 1.4, the redox couple used is $Ru(NH_3)_6^{3+/2+}$. Changes in collection efficiency are shown with respect to the location of the capillary, 0 being at the electrode surface and 20 being at the edge of the model. **(a)** The capillary is moved horizontally from above the electrode towards the edge of the model (Case 1). **(b)** The capillary is moved vertically from above the electrode towards the edge of the model (Case 2). **(c)** The capillary is moved diagonally from close to the electrode towards the edge of the model (Case 3).

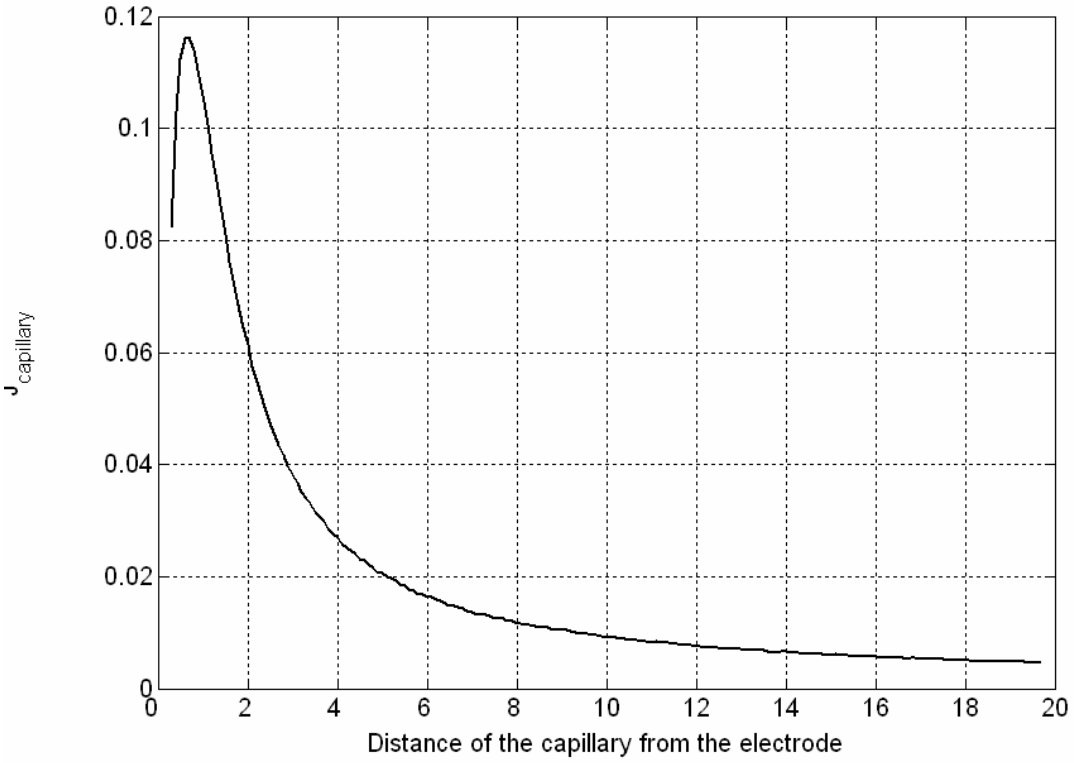

Figure 3.15: Variation of the flux of species B into the capillary as it is moved vertically from the surface of the electrode. ((See Fig 3.14 b for the CE variation)

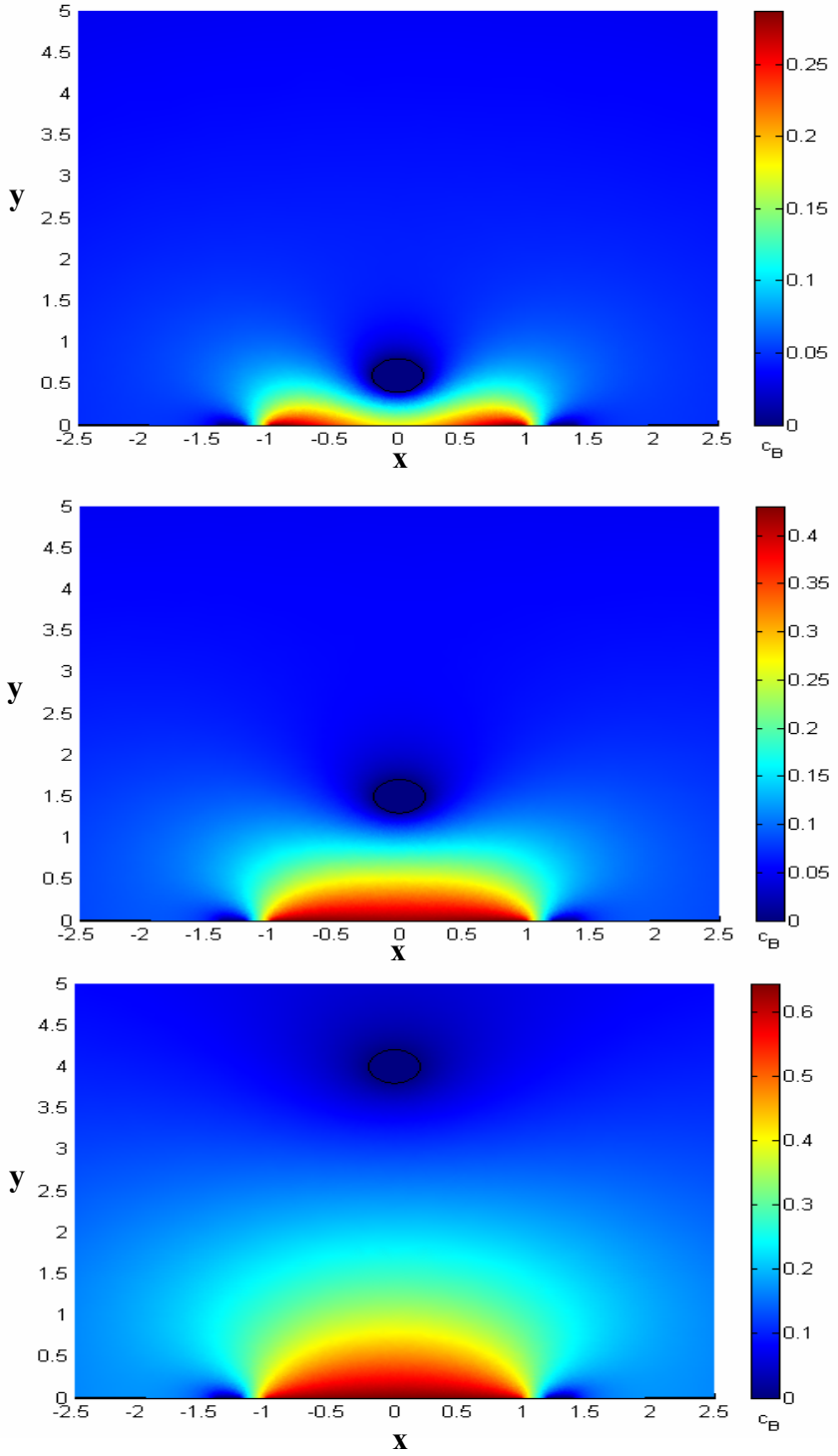

Figure 3.16: Variation in the concentration profile of species B as the capillary height above the sensor changes

3.3 Convection and diffusion

In the following sections convection and diffusion mass transports are considered. As described previously, convection is significant in tissue perfusion. Experimental measurements of convective flow using the ring-disc microelectrode form a considerable portion of this thesis. Numerically the treatment of convection is used as a means of validating sensor characterisation experiments rather than trying to model the types of convective flow that occur in tissue. This is because convection in tissue is very complicated and heterogeneous. Two types of flows were modelled; impinging flow and tube flow. In impinging flow, the sensor is placed at the end of a tube so that the flow over the sensor resembles that of an impinging jet onto a surface. The advantage of this flow environment is that it has been solved analytically, so in the model one can use a predefined flow profile over the sensor. When pipe flow is considered, the sensor is placed perpendicular to the flow direction in a pipe. As a results a boundary layer will form on the surface of the sensor. In this case the velocity profile over the sensor is calculated by solving the Navier-Stokes equations.

3.3.1 Impinging jet flow

lmpinging jets are well established in fluid mechanics, where they are exploited for their enhanced heat and mass transfer characteristics. The flow profile from an impinging jet has been extensively studied and has revealed interesting features and characteristic regions where a particular flow profile is observed. These are the core region, the stagnation point, the wall jet region and the fully developed flow region, these were described analytically by Homann and Frössling (133,134).

In electroanalysis (HPLC, FIA), the use of impinging jets is growing steadily because they provide reproducible and well described mass transport characteristics. In the past achieving well-defined flow profiles over an electrode would have involved the use of a rotating disc electrode (135). However this technique is not suited to microelectrode because of problems in placing the electrode at the centre of the disc. In electrochemistry impinging jets have been used to study reaction mechanisms (136), investigate the effects of mass transport (137) as well as for HPLC end column detection (138,139).

In our application, the flow arrangement used is similar to that used in HPLC where the sensor is placed at the end of a tube. In some respects this is not true jet flow because the movement of the flow is relatively slow and it is limited by the walls of the tube. However the results presented do suggest that the jet flow approximation assumed is valid, therefore the analysis presented should be relevant to more classical jet flows experiments as well.

Theory

A system consisting of a ring-disc microelectrode embedded in an insulating plane is considered (Figure 3.17). The solution present within the model boundary contains an electro-active species, A, which is assumed to undergo a simple one electron transfer leading to species B (Eq. 3.5). The forwards reaction occurs at the generator electrode whilst the backwards reaction occurs at the collector. Both disc and ring generators are considered in the simulations where diffusion and convection mass transfers are taking place. For the steady stat the mathematical model of the mass transport above the electrodes is given by the following system of partial differential equations:

$$D \nabla^2 c_a - u \nabla c_a = 0 \tag{3.20}$$

$$D \nabla^2 c_b - u \nabla c_b = 0 \tag{3.21}$$

Where D is the diffusion coefficient assumed to be equal for species A and B taken as D = 7.6×10^{-10} m^2/s. ∇ is the gradient and ∇^2 is the Laplacian in polar coordinates, c is the concentration and **u** is the local flow velocity (where **u**=(u,v)). The impinging jet flow profiles are computed using Eq. 3.22, 3.23 and 3.24 (173):

$$\Psi = kzr^2 \tag{3.22}$$

$$u = \frac{1}{r}\frac{\partial \Psi}{\partial r} = 2kz \tag{3.23}$$

$$v = -\frac{1}{r}\frac{\partial \Psi}{\partial z} = -kr \tag{3.24}$$

Where Ψ is the axis-symmetric stream function. The stream function is a complete solution that simplifies the expression of the flow velocities. The assumptions associated with the stream function are that the flow is steady, incompressible and axisymmetric about the centre of the jet.

The non-dimensional parameters used in the simulations are:

$$c_A = \frac{C_A}{C_{A,\infty}} \quad c_B = \frac{C_B}{C_{A,\infty}} \quad r = \frac{R}{R_1} \quad z = \frac{Z}{R_1} \quad Pe = \frac{R_1{}^2 k}{D_A}$$

Where Pe is a form of the Peclet number which relates convection to diffusion. The boundary conditions used are found in Table 3.6.

Simulations were carried out using Femlab 3.2's finite element solvers in Matlab. The mesh was refined over the disc and ring (min element size 0.01 x r_1) and expanding towards the model boundaries. A sample code used for the numerical modelling can be found in Appendix 3.

Table 3.6 Initial, sub-domain and boundary conditions or settings for both ring and disc generating cases.

	Disc generating	Ring generating
Sub-domain settings		
v (z component of the velocity) u (r component of the velocity)	-kr 2kz	-kr 2kz
Boundary conditions		
z=0 $0<r\leq r_1$ z=0 $r_2<r\leq r_3$ z=0 $r_1<r\leq r_2$; $r_3<r\leq r_{max}$ r=0 $0<z\leq z_{max}$ r= r_{max} $0<z\leq z_{max}$ z= z_{max} $0<r\leq r_{max}$	$c_A = 0; \nabla_n c_B = -\nabla_n c_A$ $\nabla_n c_A = -\nabla_n c_B$; $c_B = 0$ $\nabla n_A = \nabla n_B = 0$ Axial symmetry $c_A = 1$; $c_B = 0$ Convective flux	$\nabla_n c_A = -\nabla_n c_B$; $c_B = 0$ $c_A = 0$; $\nabla_n c_B = -\nabla_n c_A$ $\nabla n_A = \nabla n_B = 0$ Axial symmetry $c_A = 1$; $c_B = 0$ Convective flux

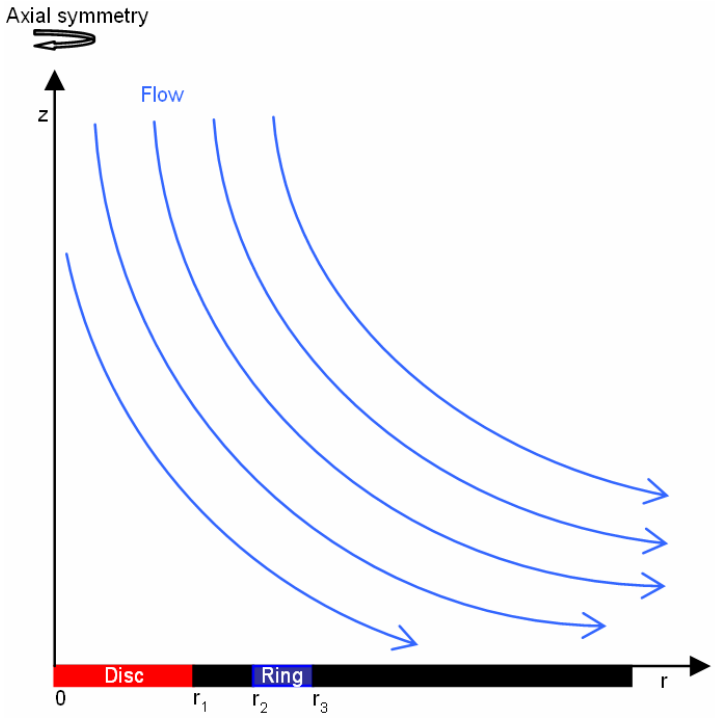

Figure 3.17: Schematic representation of the Ring-Disc electrode and the direction of the flow above the electrode.

Results and discussion

For an electrode with geometry $r_1 = 25$ µm $r_2 = 31.2$ µm $r_3 = 33.7$µm, as the Peclet number increases the collection efficiency decreases. The rate of decrease in CE is more significant when the ring is generating then when the disc is generating (see Fig 3.18). This is mostly due to the geometrical arrangement of the electrodes and the direction of flow. When the flow is reversed for negative Pe values (somewhat unlikely experimentally, but interesting numerically) it is the disc generating mode that sees the highest drop in CE. Which confirms that the geometry of the electrodes and direction of flow play a significant role in the way in which the CE drops with increasing flow rates. The concentration profiles of species B are shown in Fig 3.19, where Fig 3.19a is for a disc generating case and Fig 3.19b is for the ring generating case.

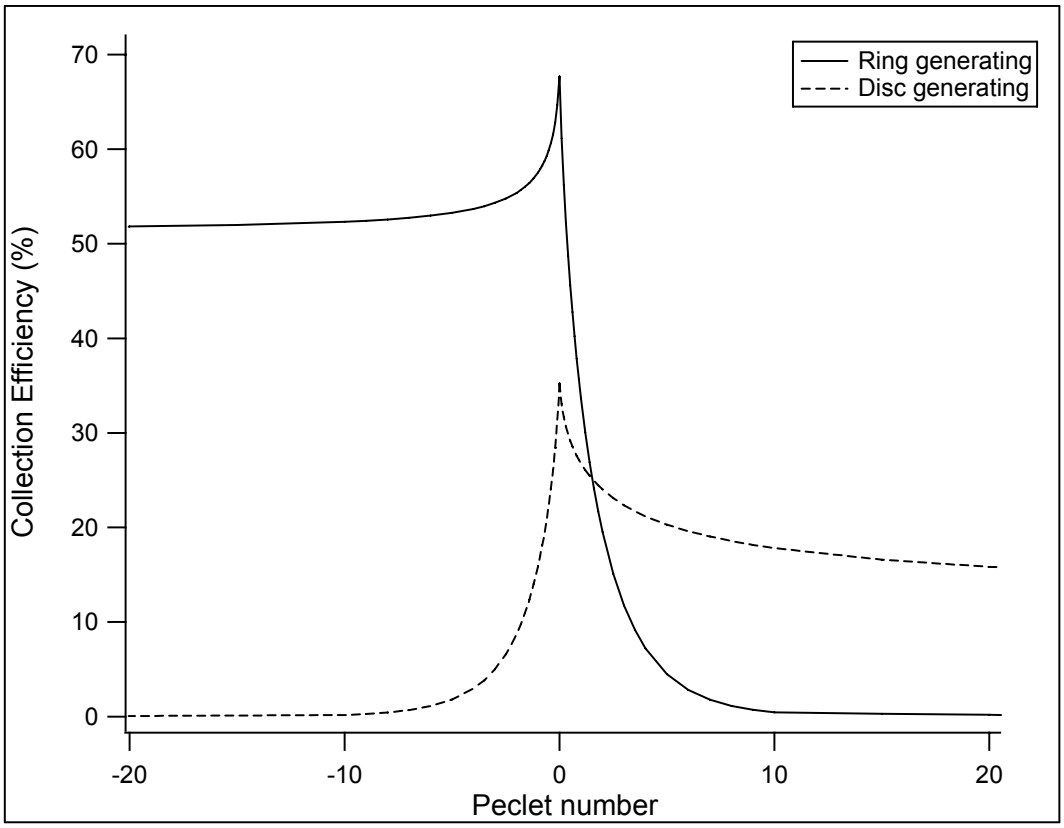

Figure 3.18: Simulated change in collection efficiency with Peclet number. Disc generating case is in dotted line, ring generating case is in solid line. Negative Pe values describe the cases where the flow is reversed.

In Figure 3.18 it can be seen that beyond a certain Peclet number, the collection efficiency no longer drops. The dynamic limit of the sensor has been reached, any changes in the collection efficiency beyond such Peclet numbers will not be due to convection. In some applications operating in this mode is required, for instance where homogeneous chemical reactions in solutions are being investigated (EC type mechanisms) but for flow measurements we want to be below this limit.

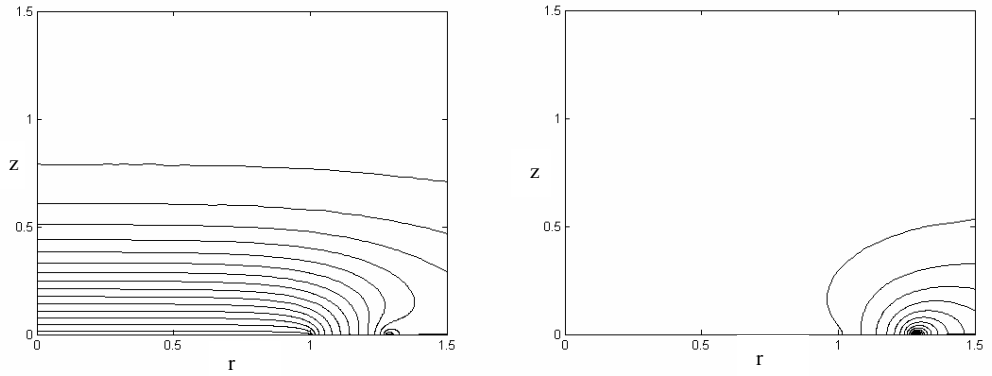

Figure 3.19: Concentration contour plot for species B. **(a)** Disc generating, **(b)** ring generating for a Peclet number of 3. Electrode geometry is r_1 = 25 μm r_2 = 31.2 μm r_3 = 33.7μm and the redox couple used is $Ru(NH_3)_6^{3+/2+}$. Contour lines have equal concentration separation (c = 0.5).

Our application is to detect flow, so the plateau reached by the CE indicates the maximum level of flow that can be detected by the sensor. It is interesting to see that when the ring is generating the dynamic range is lower than when the disc is generating. This would tend to suggest that these detection limits are a function of electrode geometry and size. To investigate this, the size of the sensor was varied extensively. The simulated results are shown in Fig 3.20-21 and clearly show that electrode geometry plays a significant role in the dynamic limit of the sensor. When the disc is generating increasing r_2, the ring-disc separation will decrease the collection efficiency. When r_3 is increased the collection efficiency increases which is consistent with the fact that an electrode of larger area will collect more. When the ring is generating, increasing r_2 also decreases the CE. Increasing r_3 decreases the collection efficiency, because the contribution from the edge effect is becoming less and less significant as the ring area is increased. In section 3.2.1.a it was also shown that thin ring generators will have a higher collection efficiency than large ring generators. For a more detailed description of these effects, we refer the reader to that particular section.

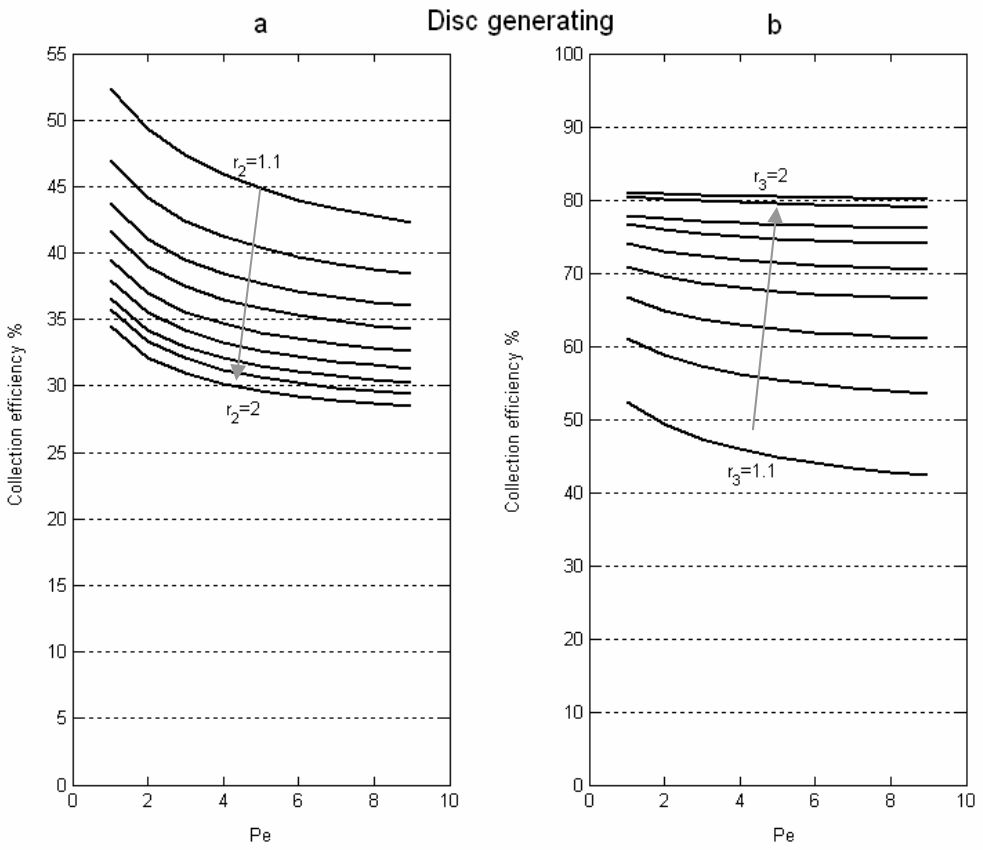

Figure 3.20: Change in collection efficiency with Peclet number for disc generating case. **(a)** Effect of changing r_2. The arrow indicates increasing r_2. **(b)** Effect of changing r_3. The arrow indicates increasing r_3.

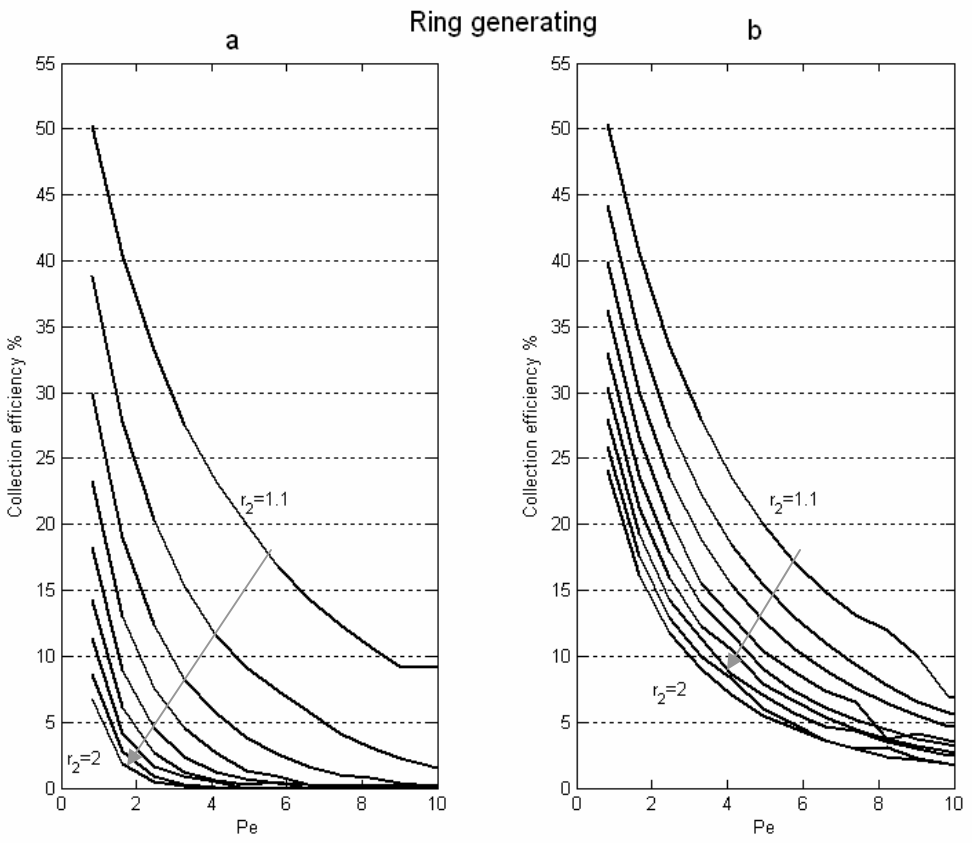

Figure 3.21: Change in collection efficiency with Peclet number for ring generating case. **(a)** Effect of changing r_2. The arrow indicates increasing r_2. **(b)** Effect of changing r_3. The arrow indicates increasing r_3.

Relating the simulations to experimental measurements

The impinging jet simulations described in the previous section consider the effects of convection as a stream function, Ψ. To correlate the simulated results for the collection efficiency with experimental recordings one must relate the stream function and its variable k with the flow rate through the flow cell. This can be done numerically by solving the Navier-Stokes equations for the flow through the flow cell. Once the flow is calculated, the velocity profiles over the sensor can be extracted; this in turn is related to the variable k in the stream function as described in Equations 3.22-3.24.

We consider a circular duct at the end of which a sensor is placed (Fig 3.22). Rotational-symmetry is assumed about r = 0 in order to simplify the model. Real tube

dimensions are used in the model. The equations governing the flow through the duct are the Navier-Stokes equations, which in the steady state are:

$$v\nabla v = -\nabla p + \mu\nabla^2 v \tag{3.25}$$

$$\nabla v = 0 \tag{3.26}$$

Where v and p are the velocity and pressure.

The properties of the solution are taken to be those of water (ρ = 1 kg.m^{-3} μ = 1x10^{-3} kg.m.s^{-1}). The boundary conditions are shown in Fig 3.22, the inlet velocity at the top of the duct (boundary a) is taken as a fully developed Poiseuille flow with a profile defined by:

$$V_r = 2V_m\left(1-\left(\frac{r}{d/2}\right)^2\right) \tag{3.27}$$

Where d is the diameter of the tube (2 mm), r is the radius, and V_m is the mean velocity taken as the volume flow rate divided by the area of the pipe (see Table 3.7). This flow profile is valid because the length of tubing from the pump is over 0.5m long and the flow rates are in the laminar regime with Reynolds numbers of the order of unity.

On boundary c where the flow exits the model, an outflow pressure is assumed, it is taken as atmospheric pressure. All other boundaries have a no slip condition except on the axis of symmetry where continuity is imposed. The mesh was refined around the sensor, inlet and exit area because of the somewhat complex geometry of the model at these boundaries.

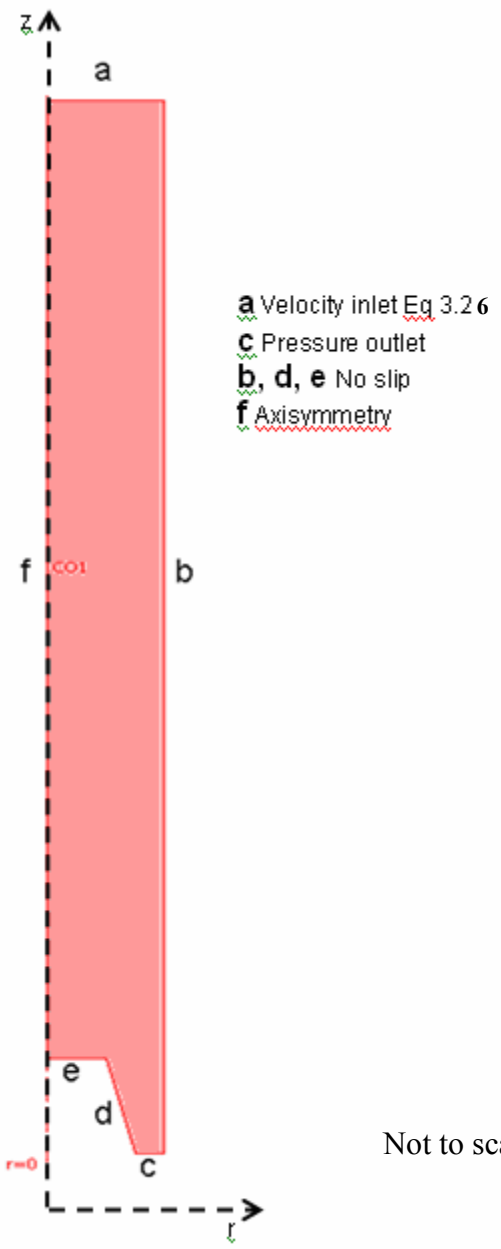

Figure 3.22: Two-dimensional axisymmetric model geometry for the impinging jet flow simulations. The dimensions are real and in millimeters. Flow direction is from top to bottom. The structure at the bottom (boundaries e and d) represents the tip of the sensor.

Table 3.7: Values for the volume flow rate and the mean flow velocity

Volume flow rate ml/min	Volume flow rate m^3/s	Mean flow velocity Vm m/s
0.1	1.67E-09	5.31E-04
0.5	8.33E-09	2.65E-03
1	1.67E-08	5.31E-03
1.5	2.50E-08	7.96E-03
2	3.33E-08	1.06E-02
2.5	4.17E-08	1.33E-02
3	5.00E-08	1.59E-02
3.5	5.83E-08	1.86E-02
4	6.67E-08	2.12E-02
4.5	7.50E-08	2.39E-02
5	8.33E-08	2.65E-02

Figure 3.23 shows the normal and radial flow profiles above the sensor for a flow rate of 5ml/min. The flow profile does not change substantially when different flow rates are considered, only the value of the velocity changes. This is what is predicted by the stream function, Ψ. From these simulations, the velocity in the r and z directions along a given line above the sensor can be plotted; this is shown in Figure 3.24. The linear relationship of flow and distance is an indication that the flow over the sensor is indeed that of a jet impinging onto a surface. The assumption of the stream function used in the diffusion convection model is therefore a good approximation. The slope of these plots enables us to calculate k, this follows from Eq. 3.23-24. Both u and v velocity plots give the same value for k, which again is consistent with theory. Table 3.8 lists the simulated values of k obtained for different flow rates.

Table3.8: Relationship between Peclet number, flow rate and k values

Pe	**k**	**Vm**
	m	**ml/min**
1	1.216	0.405333
2	2.432	0.810667
3	3.648	1.216
4	4.864	1.621333
5	6.08	2.026667
6	7.296	2.432
7	8.512	2.837333
8	9.728	3.242667
9	10.944	3.648
10	12.16	4.053333

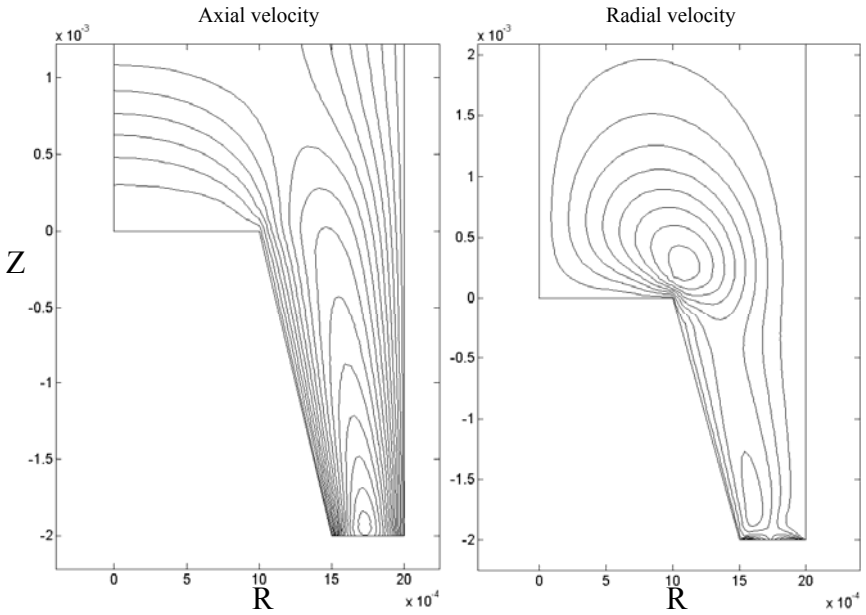

Figure 3.23: (a) Normal and **(b)** radial flow contours over the sensor for a flow rate of 5 ml/min.

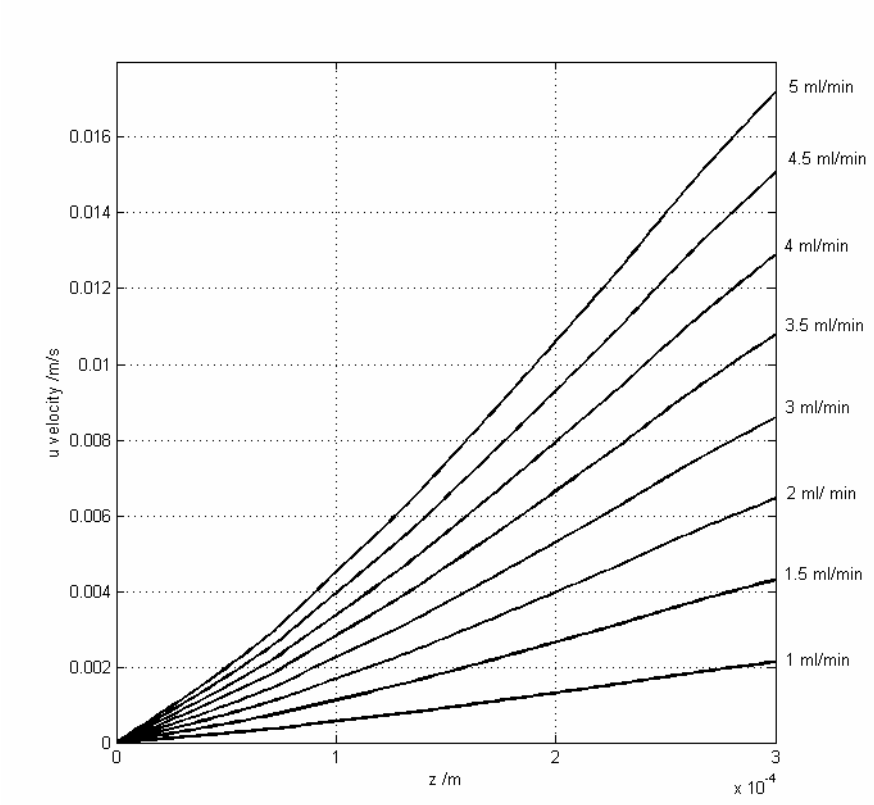

Figure 3.24: Radial component of the velocity above the sensor for different flow rates applied at the entrance of the flow cell. The slope of the lines is used to evaluate k the component of the stream function used in the convection diffusion model.

This analysis enables the direct comparison of the simulated results with the experimental ones. These are shown in Figure 3.25 for a disc generating case and 3.26 for a ring generating case. In the disc generating case the agreement between the experimental curves and the numerical ones is good especially when the flow rate is low. For higher flow rates the agreement is less good this might indicate a deviation from the impinging jet flow profile as the flow rate increases (i.e. possible recirculation, etc.). In the ring generating mode the agreement between numerical and experimental measurements is less good. The reasons for this are unclear our experience would have us think the cause is related to imperfections in the ring electrode (i.e. recess or protrusion). The discrepancies are particularly noticeable for the 50 micron disc electrode (pink trace). These points are further discussed in Section 5.2.2.

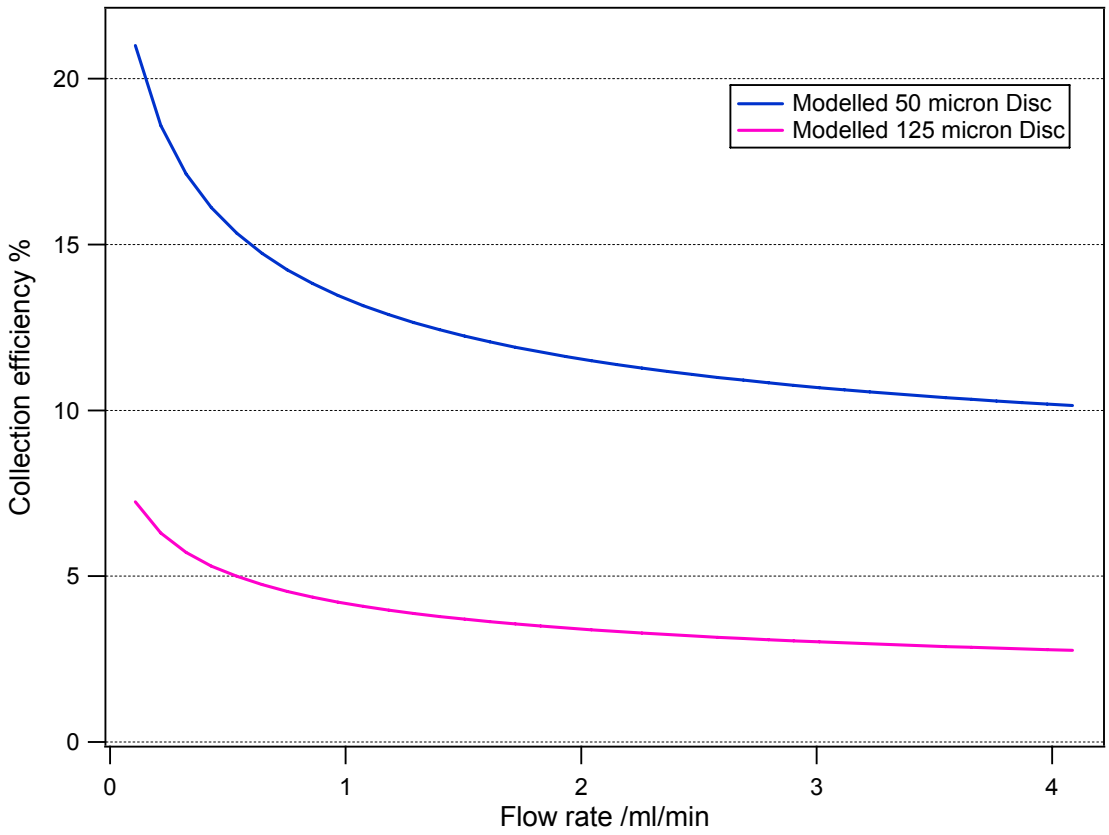

Figure 3.25: Effect of flow on the collection efficiency of a ring-disc microelectrode for disc generating cases. Markers represent average experimental measurement and range (n = 3), solid line represents the simulated results. The sensor used had dimensions of R_1 = 25 µm, R_2 = 31.2 µm, R_3 = 31.3µm (50 Disc) R_1 = 62.5 µm, R_2 = 75 µm, R_3 = 75.5 µm (125 Disc). The redox couple is $Ru(NH_3)_6^{3+/2+}$.

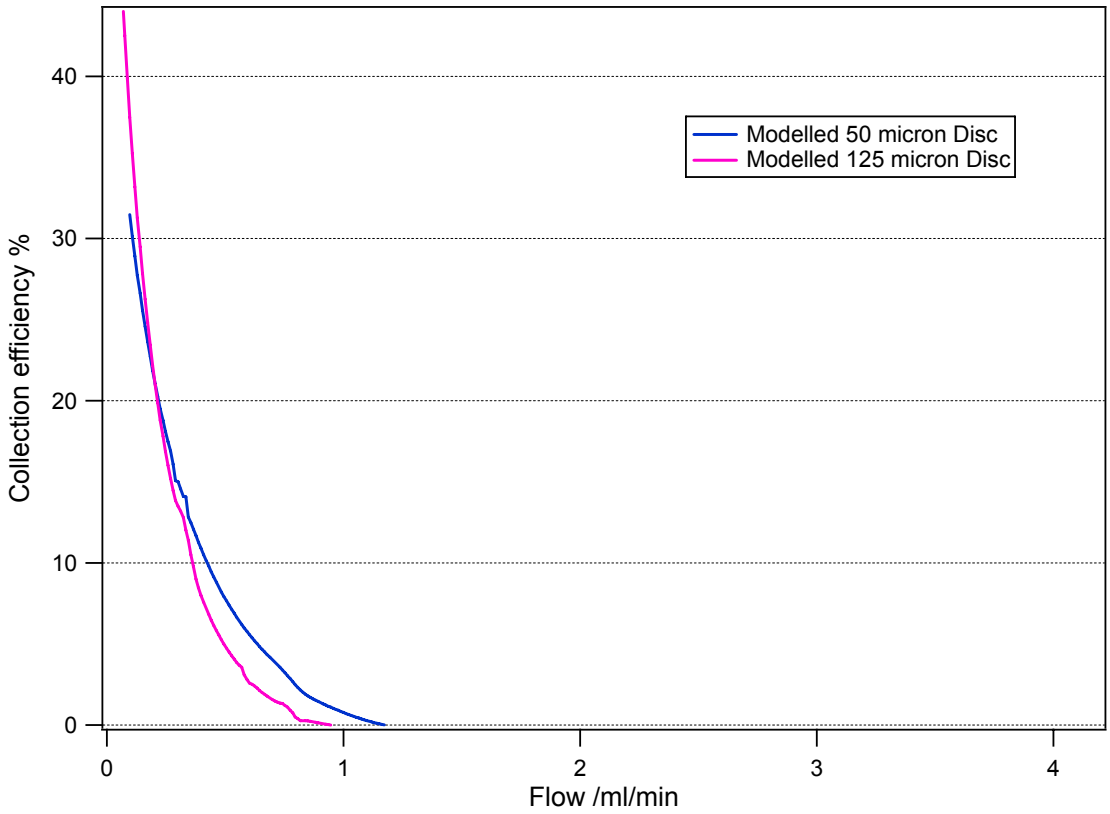

Figure 3.26: Effect of flow on the collection efficiency of a ring-disc microelectrode for ring generating cases. Markers represent average experimental measurements and range (n = 3), solid line represents the simulated results. The sensor used had dimensions of R_1 = 25 µm R_2 = 31.2 µm R_3 = 31.3µm (50 Disc) R_1 = 62.5 µm R_2 = 75 µm R_3 = 75.5 µm (125 Disc). The redox couple is $Ru(NH_3)_6^{3+/2+}$.

3.3.2 Tube flow

Laminar flow through tubes has been widely studied and suitably characterised. Most analytical chemistry and chemical engineering applications involve tubes and channels, the potential for processes monitoring in these ducts is undoubtedly motivating research into electrochemical measurements in tubes. The most common electrode geometries used in tubes are band and tubular electrodes. Both are placed flush with the tube wall and have been used for the detection of food colorants (140), floride (141), glucose and ascorbic acid (142) amongst other things. Amatore and Compton have both contributed significantly to the use of band and tubular electrodes for measurements in ducts. In recent years they have published a number of papers and reviews on the use of

multiple channel electrodes as collector-generators. Compton's work in this area has been more theoretical (143-149), whilst Amatore's work has involved both experimental and numerical studies (59,150-152). A particular mention has to be made for the series of papers published by Amatore et al. on the use of double band electrodes for the *in situ* electrochemical determination of flow profiles in channels (59,150,151). The parallels between these publications and our work are noteworthy.

With regards to the design of a perfusion sensor, tube flow is a good environment to characterise the response of the sensor to flow. Incidentally tube flow is not too dissimilar to the flow of blood through blood vessels. In future our analysis may be useful if the sensor is to be used to measure flow inside a blood vessel.

The numerical flow analysis used here follows a different sequence from the one described in the previous section 3.3.1. In this case we cannot express the flow profile in the convection diffusion model in terms of a predefined function because no such function exists. We therefore have to solve the Navier-Stokes equations first, so as to establish the profile of the flow over the sensor. Subsequently this flow profile is employed in the convection diffusion model used to compute the collection efficiency of the sensor for a given flow rate.

Flow through a tube

The model used in the fluid flow simulations is in three dimensions. It resembles the experimental setup in that a solution flows through a pipe (8 mm diameter) in which a sensor has been inserted. We used real dimension for this model as it was rather particular to our application. The sensors used experimentally were set in epoxy and had a diameter 5 mm (tubular shape), they were inserted so that the electrode surface was at the centre of the pipe. The model used is shown in Figure 3.27. The boundary conditions are Eq. 3.27 for the inlet and a pressure of 1 atm at the outlet, all other boundaries have a no slip condition. The properties of the fluid used are those of water at room termperature (ρ = 1 kg.m^{-3} μ = 1x10^{-3} kg.m.s^{-1}). The equation solved is the Navier Stokes equations (Eq. 3.25).

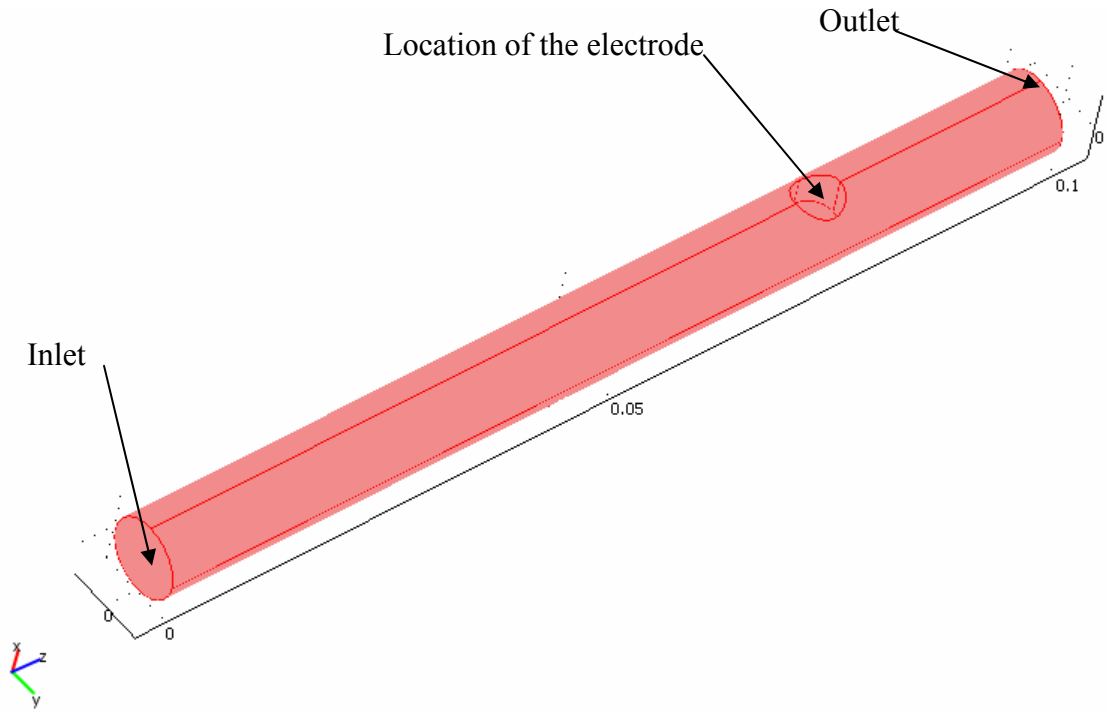

Figure 3.27: Model geometry used to compute the flow profile over the electrode surface.

The inlet velocity profile used is shown in Figure 3.28. Figure 3.29 showns a velocity profile through the tube. The velocity of the fluid below the sensor is seen to increase which is consistent with the fact that we are constricting the area of the tube. On the surface of the electrode a boundary layer is formed, as long as the flow through the tube is stable the thickness of the boundary layer should be stable. We then compute the change in velocity normal to the surface of the sensor. The velocity profile over the sensor surface for different flow rates through the tube are shown in Figure 3.30. These profiles are then used in the convection diffusion model.

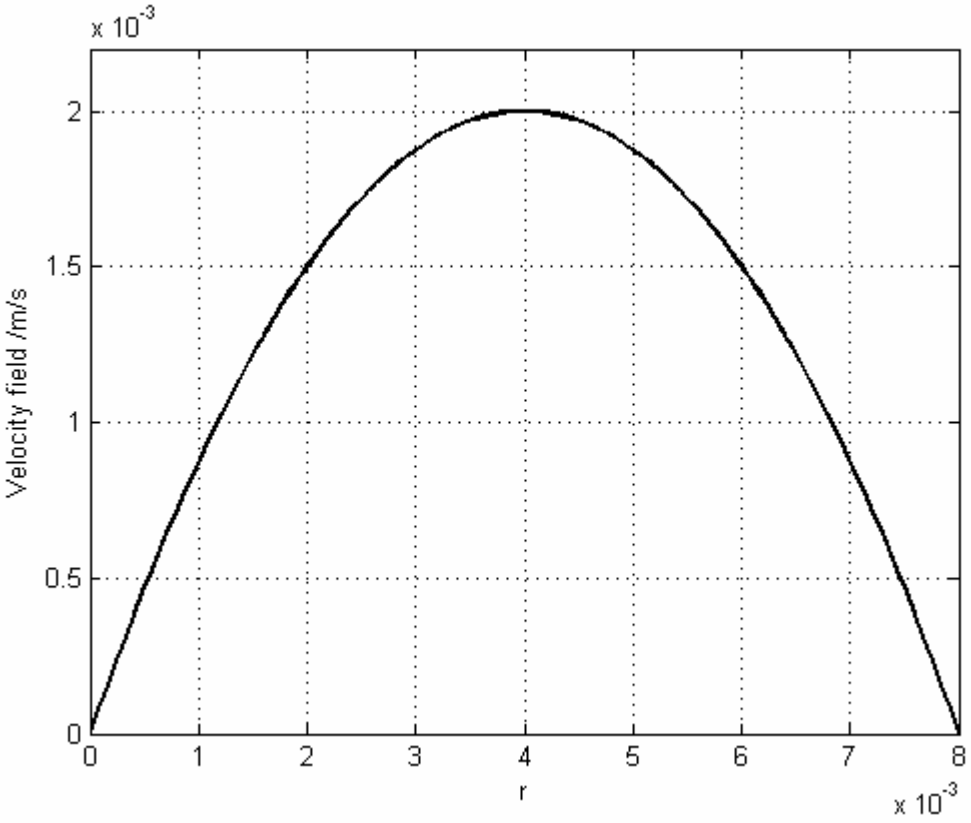

Figure 3.28: Velocity profile applied to the inlet of the tube for a flow rate of 3 ml/min. This follows from the assumption that the flow is fully developed and laminar when it reaches the flow cell. Experimentally this was achieved by separating the pump and the flow cell by 0.5 m of tubing.

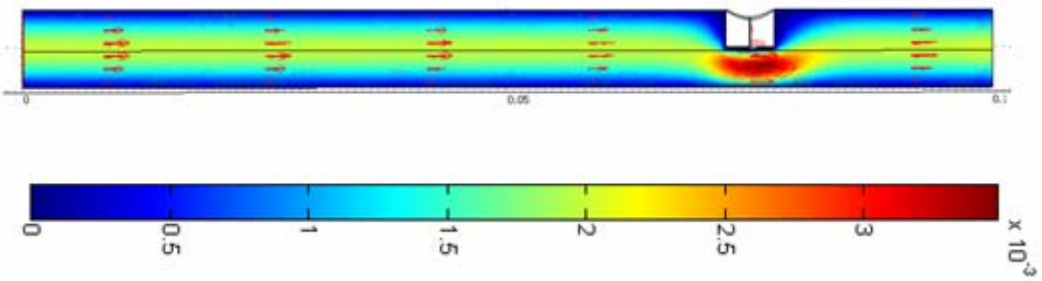

Figure 3.29: Slice plot of the velocity through the centre of the tube for a flow rate of 3 ml/min(i.e. along y = 0). Colour bar indicates the velocity of the fluid in m/s.

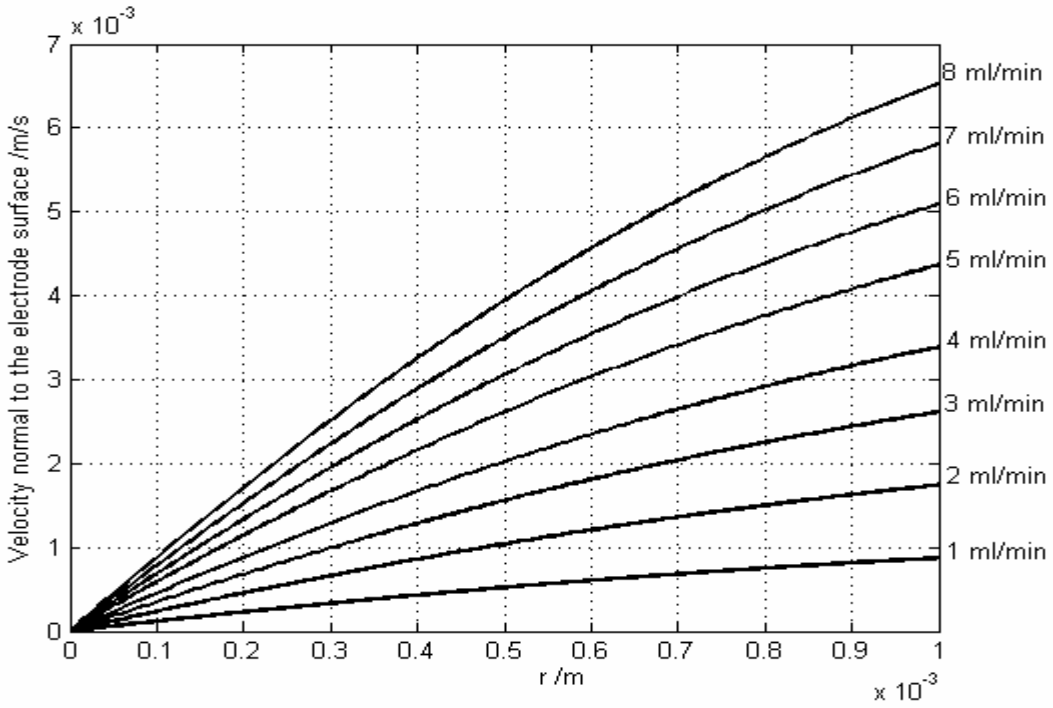

Figure 3.30: Velocity profile directly above the sensor for different flow rates through the pipe.

Convection diffusion model

Having established the flow profile over the surface of the electrode we can now apply it to a diffusion convection model of the sensor, thereby assessing the effect of flow on the collection efficiency.

The diffusion convection model is a two dimensional model. The axial symmetry boundary condition cannot be used here because the flow only acts in one direction. The model used is shown in Figure 3.31, the steady state case is considered and two species are interacting. The equations being solved are the same as in Section 3.31 (Eq. 3.20 and 3.21). The model is non-dimensionalised as in previous sections. The boundary conditions are described in Table 3.9 where a is the slope of the velocity profile taken from Fig. 3.30.

Table 3.9: Boundary conditions

	Disc generating
Sub-domain settings	
u (y component of the velocity)	$-a\times y$
Boundary conditions	
$y=0$ $-x_1<x\leq x_1$	$c_A = 0$; $\nabla_n c_B = -\nabla_n c_A$
$y=0$ $x_2<x\leq x_3$; $-x_2<x\leq -x_3$	$\nabla_n c_A = -\nabla_n c_B$; $c_B = 0$
$y=0$ $x_1<x\leq x_2$; $x_3<x\leq x_{max}$; $-x_1<x\leq -x_2$; $-x_3<x\leq -x_{max}$	$\nabla_n c_A = \nabla_n c_B = 0$
$x=x_{max}$ $0<y\leq y_{max}$	$c_A = 1$; $c_B = 0$
$y= y_{max}$ $-xmin<x\leq x_{max}$	$c_A = 1$; $c_B = 0$
$x=-x_{max}$ $0<y\leq y_{max}$	Convective flux

The influence of flow on the collection efficiency is shown in Figure 3.32. In these simulations the dimensions of the sensor are varied. The left-hand plot shows variations in x_2 and the right-hand plot shows variations in x_3. We see that the collection efficiency drops with increasing flow rate. As the ring-disc separation, x_2, increases the overall level of CE drops. As the ring thickness, x_3, increases the overall level of CE increases.

These simulations are qualitative, to obtaine quantitative simulations of the effect of electrode geometry and flow rates on the collection efficiency three dimensional simulations are required.

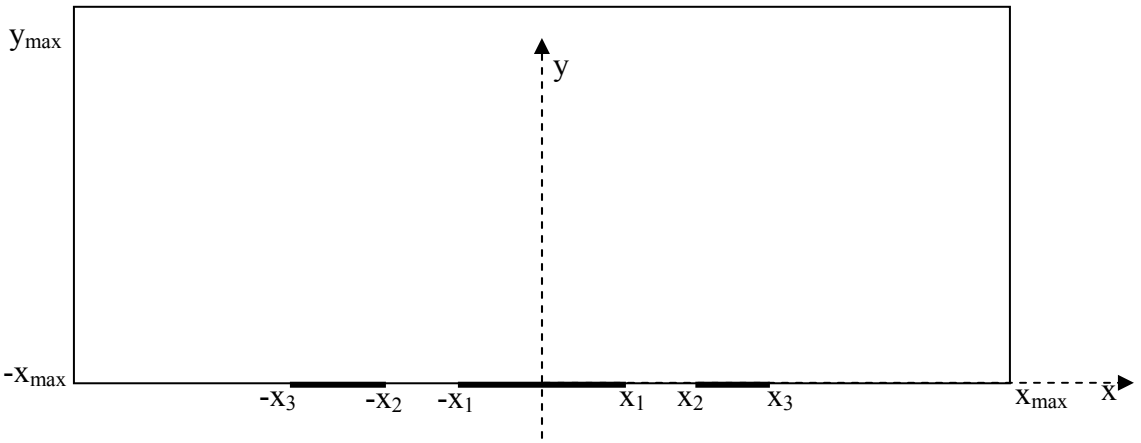

Figure 3.31: Schematic representation of the model used to simulate the effects of flow over the sensor. The model is in two dimensions which leaves the ring split in two bands either side of the disc.

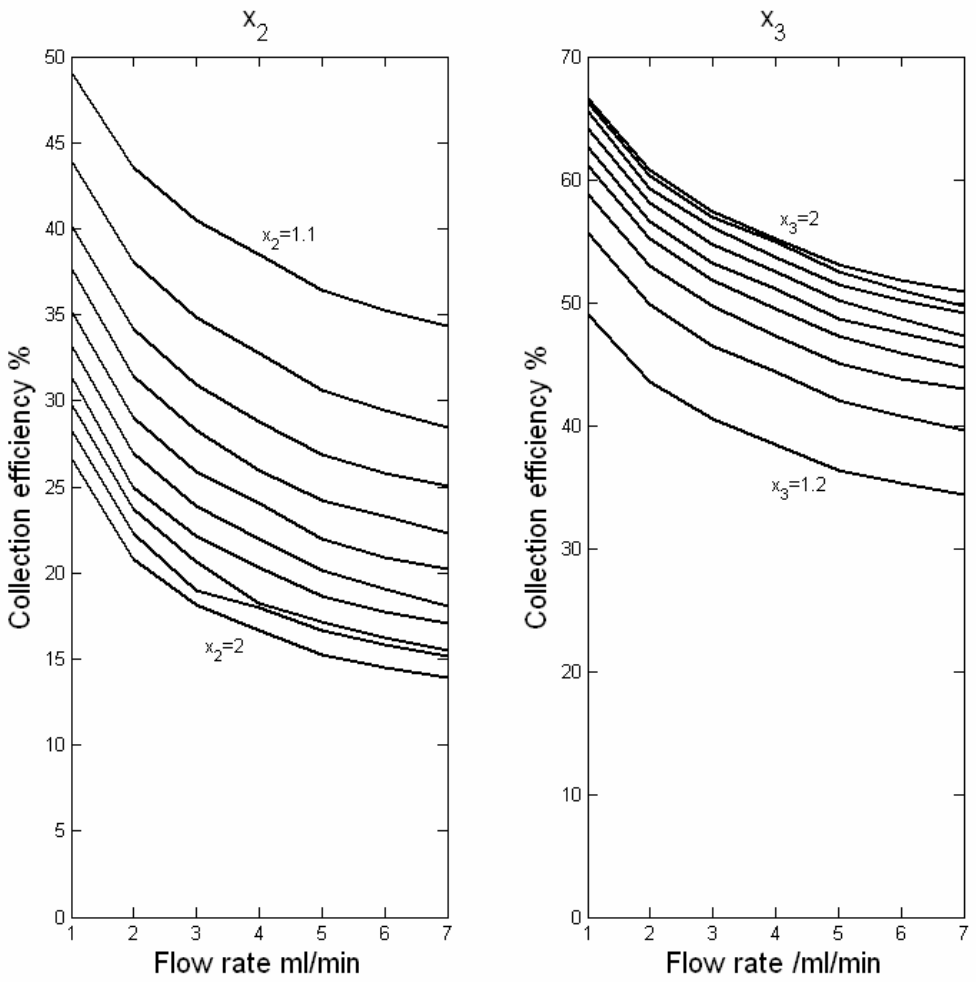

Figure 3.32: Modelled change in collection efficiency with flow rate for different electrode dimensions. The left-hand plot shows variations in x_2 and the right-hand plot shows variations in x_3.

3.4 Conclusion

In this chapter a number of numerical models describing the behaviour of the ring-disc microelectrode under different mass transport modes were presented.

Initially only diffusion mass transport was considered. The effects of varying the size and shape as well as protrusion or recess of the electrodes, the operating mode and the flux distribution were investigated (3.2.1). The effects of coating the electrode with a membrane were also studies (3.2.3). As well as the possibility of using transient electrode responses to gain more information about the medium in which the sensor is evolving (3.2.2).

In the second part convection and diffusion mass transport were considered. Two flow profiles were investigated, impinging jet flow onto the sensor and tube flow over the sensor. Again the effects of varying the electrode size was investigated and revealed that there is a detection limit beyond which a sensor will not be able to detect changes in flow.

Whenever possible the model results were compared to experimental measurements. In general we found good agreement between the two.

Overall the model predictions were useful in highlighting features or limitations of the ring-disc microelectrode. These contributed to the design process as well as providing a fuller understanding of the mechanisms controlling the behaviour of the sensor in its various application modes.

4

Mass transport measurements under diffusion control

Diffusion plays a key role in tissue perfusion as it dominates transport of nutrients and metabolites between the cells and the capillary vessels. Electrochemical sensors and more specifically microelectrodes are particularly sensitive to diffusion. This sensitivity is further enhanced when microelectrodes are used as collector-generators as in our application. In the following section we will describe the basic principle of the sensor, its features and how it is used to detect changes in diffusion.

4.1 Experimental methods

The experiments presented in this and the next two chapters all rely on the same electrochemical protocols. These experimental methods will be discussed here. The way in which the ring-disc microelectrode can be used as a collector-generator to make mass transport measurements will also be presented.

4.1.1 Electrode polishing and cleaning

Polishing and cleaning the electrode was always done prior to using the sensor for measurements. Polishing is done by tracing figures of eight with the tip of the electrode in aqueous slurries of alumina powder (Buehler, Windsor, UK) placed on polishing mats (Buehler, Windsor, UK). Three grades of alumina powder are used: 1, 0.3 and 0.05 μm, the electrode is thoroughly rinsed and sonicating in deionised water between each grade.

To assess the progress of the polishing process, the limiting current of the electrodes and the collection efficiency of the sensor are measured intermittently. Often a sensor displayed good correlation between the electrode currents and electrode size but had low collection efficiency. This is generally caused by slight defects in the sensor surface often located between the ring and the disc. These defects have little effect on the limiting current at both the ring and disc electrodes but they do affect the collection efficiency measurement (because of the coupling and the transport of redox species from one electrode to the other). Polishing of the sensor was done until the current and collection efficiency levels were close to their predicted value. The current levels at the ring and disc electrode were established by the equations of Szabo and Saito (57,58), whilst the level of collection efficiency of the sensor was established by numerical simulations.

After polishing, cleaning the electrodes is done by cycling the potential at the electrodes between -1.5 and 1.5 V vs. Ag/AgCl in 0.5 M H_2SO_4 at a scan rate 2.5 V/s for 15 min. The generation of oxygen and hydrogen at the potential extremes helps dislodge species absorbed onto the electrode surface. Then the electrodes are held at -1.5 V for 15 min, which leaves the surface clean (66). One of the ways used to assess the cleanliness of the electrode surface is by cyclic voltammetry where one can check if the peak to peak

separation of a reversible redox couple such as $Ru(NH_3)_6^{3+/2+}$ is close to 57 mV . If it is substantially different, then the cleaning process has to be prolonged.

4.1.2 Cyclic voltammetry

The characteristics of the redox species that are useful to our investigation are the voltage at which the oxidation and reduction occurs, the current drawn by the oxidation and reduction and the formal redox potential of the reaction. This information is best obtained using cyclic voltammetry (CV). In CV a triangular wave voltage perturbation is applied to the electrode (Fig 4.1a). From the electrode current response the potential at which the oxidation and reduction reactions are taking place as well as the formal redox potential E_0 can be identified. At slow scan rates, the limiting current at a microelectrode is directly related to its radius (56,66). Figure 4.1 shows the information obtained from CV. In our investigation, CV was performed at the start of every experiment to assess the state of the electrode, the solution and the state of the reference and counter electrodes. Through this we identify at which potential the generator and collector are to be held or what current to impose the generator. During the experiments, cyclic voltammograms were often repeated to check that the system had not drifted or changed significantly. Figure 4.1 shows a typical cyclic voltammogram for the redox couple $Ru(NH_3)_6^{3+/2+}$ at intermediate scan rates. When H_2 was used as the redox couple, the same parameters were extracted from the curves although the limiting current was often hard to assess because of bubble formation.

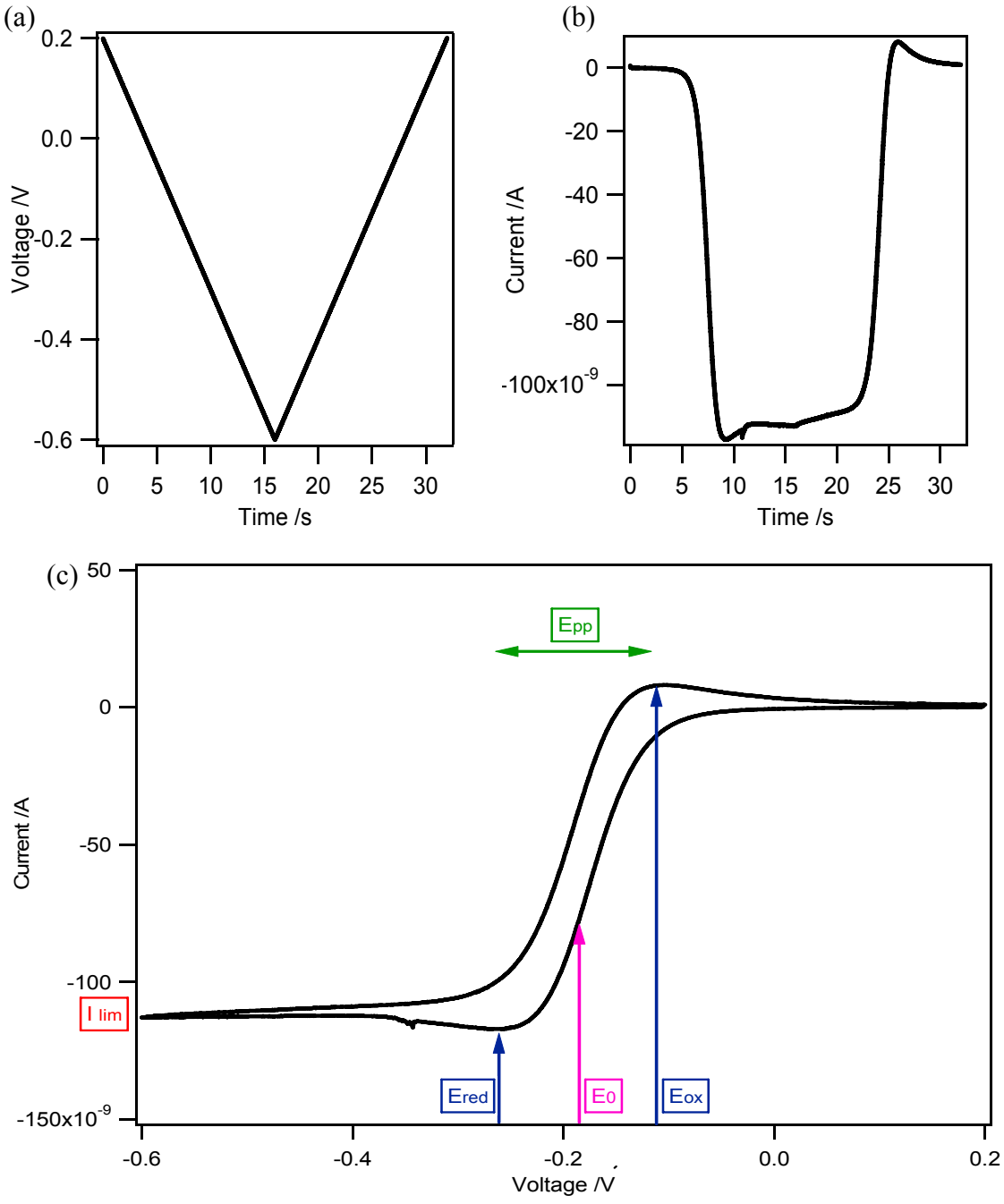

Figure 4.1: (a) The triangular voltage wave-form applied to the electrode. **(b)** Current response at the electrode **(c)** Cyclic voltammogram of a 50 μm Pt disc diameter electrode in 10 mM $Ru(NH_3)_6^{3+/2+}$ in 1 M KCl. E_0 is the formal redox potential, E_{ox} and E_{red} are the potentials at which the oxidation and reduction reactions are taking place, E_{pp} is the peak to peak separation and I_{lim} is the diffusion limiting current.

4.1.3 Collecting mode

In this work constant potential amperometry was always used to collect the redox couple. The reason for collecting the redox couple using this techniques is that it guarantees the right species is collected be it H_2 or $Ru(NH_3)_6^{2+}$. Another advantage is that this technique imposes no limitation on the amount of current that can be drawn by the electrodes. Finally this technique is well suited because it provides high temporal resolution. In our application the concentration of generated species at the surface of the collector changes in response to often rapid changes in mass transport, thus it is essential to be able to continuously detect these changes.

4.1.4 Generation mode

There are two generating modes that can be used to generate the tracer molecule. These are constant current generation and constant voltage generation. Both were used in this thesis, their operation advantages and disadvantages will now be described.

Constant voltage generation

Constant voltage generation is carried out using chronoamperometric techniques operated through a potentiostat. The main reason for using this technique to generate the tracer molecule is that it ensures the right species is generated. Chronoamperometry is an electrochemical technique in which the potential at the electrode is stepped whilst the current is measured and plotted over time. This technique has the advantage of providing good temporal resolution with regards to the events that take place at the electrode (56). A typical chronoamperometric trace is shown in Figure 4.2; Figure 4.2a shows the input signals for the generator and the collector, whilst Fig 4.2b shows the current response at the generator and collector. The collection efficiency is calculated by taking the ratio of collector to generator current.

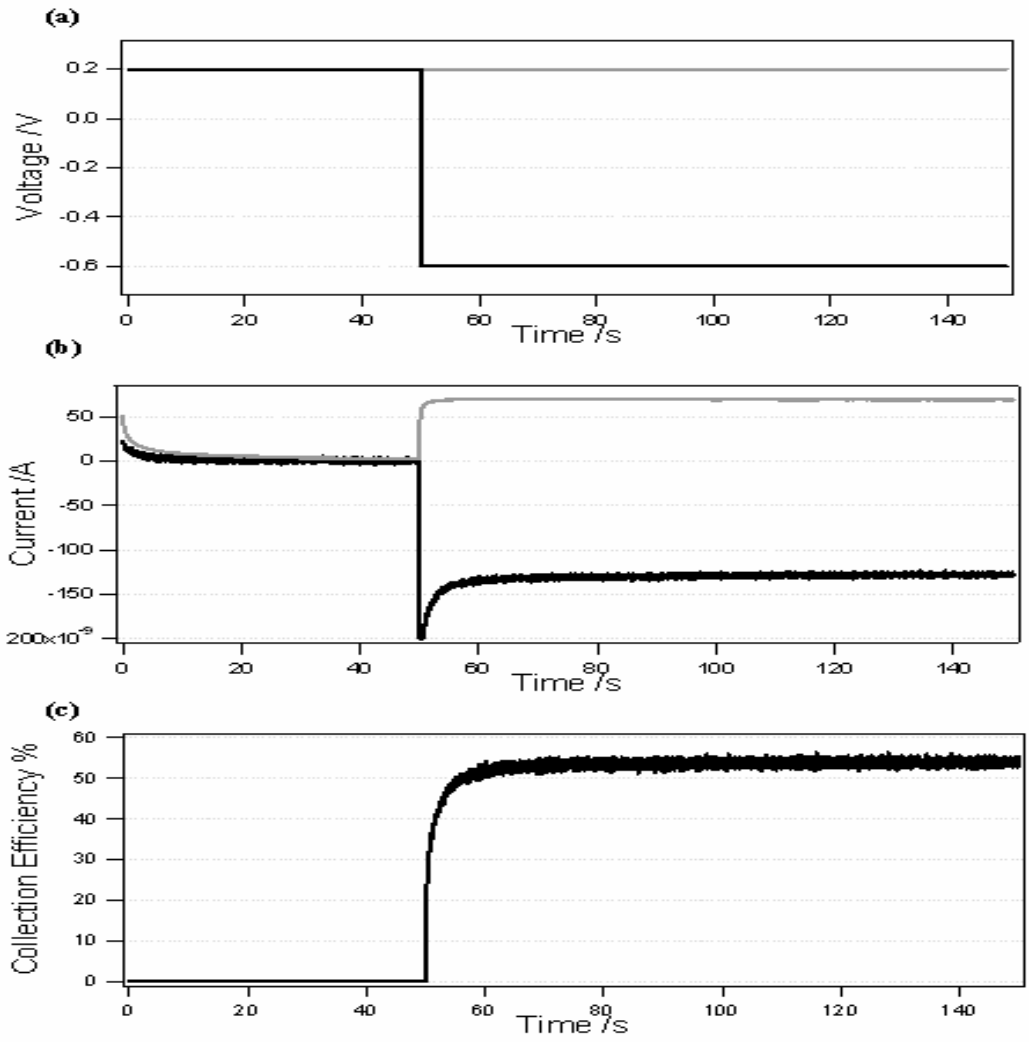

Figure 4.2: (a) Input voltage to the generator (black) and the collector (grey). **(b)** Chronoamperometric trace or current response at the generator (black) and collector (grey) electrodes. **(c)** Collection efficiency evaluated from the ratio of collector current to generator current. The sensor used had a disc diameter of 50 μm and ring thickenss 2.5 μm, the disc generating mode was employed in a 10 mM $Ru(NH_3)_6^{3+/2+}$ in 1 M KCl.

Despite being used throughout this work, chronoamperometry is not our preferred operating mode for the sensor. The reason being that the mass transport we wish to measure at the collector may also affect the generation of the redox couple. This is because chronoamperometry imposes no control on the amount of current passed, thus the amount of species generated can vary. In fact when using chronoamperometry to generate our tracer species changes in reactant concentration, diffusion coefficient and

reaction kinetics will all lead to changes in generator current. The effects of changing the mass transport on the measurement are shown in Figure 4.3. Both the generator and collector are affected by the change in mass transport, the measurement would be simpler if only the collector could detect the mass transport changes. This is disadvantageous as it adds complexity to the measurement of mass transport which is our chief intent. Similarly the influence of reactant concentration on the current measurement at the collector and generator is illustrated in Figure 4.4.

There is one application where constant voltage generation is essential; this is when investigating the transient behaviour at the ring-disc microelectrode. In Section 3.2.2 numerical investigation of transient ring-disc measurements were discussed as a way of probing the nature of the tissue type, the water concentration and variations in H_2 and H_2O diffusion coefficient (experimental investigation of these effects is presented in Section 6.2.1).

The reason we used chronoamperometry to generate the redox couple is that it is a technique that is easily implemented and present on all commercial electrochemical instruments.

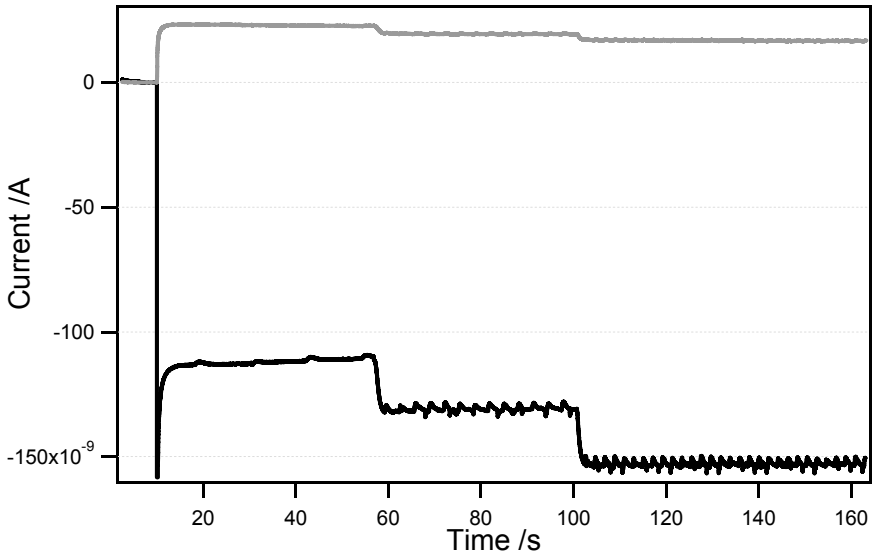

Figure 4.3: Problems arising from the use of chronoamperometry to generate the redox couple. The generator trace is in black and the collector trace is in grey. The steps are induced by the change in pump speed, these changes in mass transport are detected at the generator and the collector. It would be simpler if only the collector detected these changes.

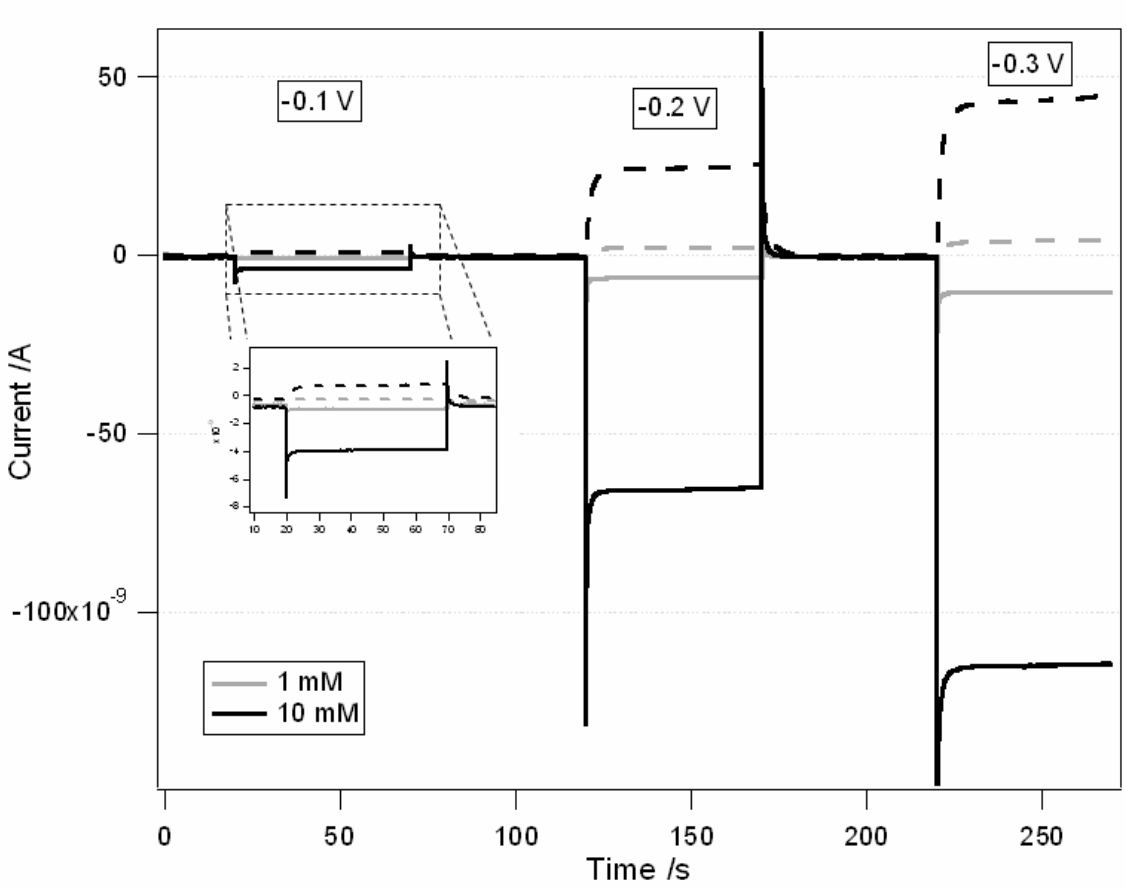

Figure 4.4: Constant voltage step generation at the disc (-0.1, -0.2 and -0.3 V steps), the ring was held at 0.2 V vs. Ag/AgCl. The black trace shows the response when the solution contains 10 mM $Ru(NH_3)_6^{3+2+}$, grey trace is for a solution that contains 1 mM $Ru(NH_3)_6^{3+2+}$.

Constant current generation

Constant current generation is done using a galvanostat and the technique of chronopotentiometry. To establish the level of current that needs to be imposed, cyclic voltammetry can be used. In our application we generally impose currents that are close to the diffusion limiting value although as we will see later, lower current levels may be useful.

Chronopotentiometry is similar to chronoamperometry, only a fixed current is imposed on the electrode rather than a fixed voltage. Chronopotentiometry is popular for electroplating, scanning electrochemical microscopy and electrochemical time of flight

applications (153,154). This technique provides good temporal resolution of the events taking place at the electrode. Imposing a fixed current also means the electrode is not affected by mass transport effects. For our measurements this technique is useful because it will guarantee a constant concentration of generated species, thus making the measurements of tissue perfusion easy to interpret. Figure 4.5 shows a series of traces obtained using chronopotentiometric generation.

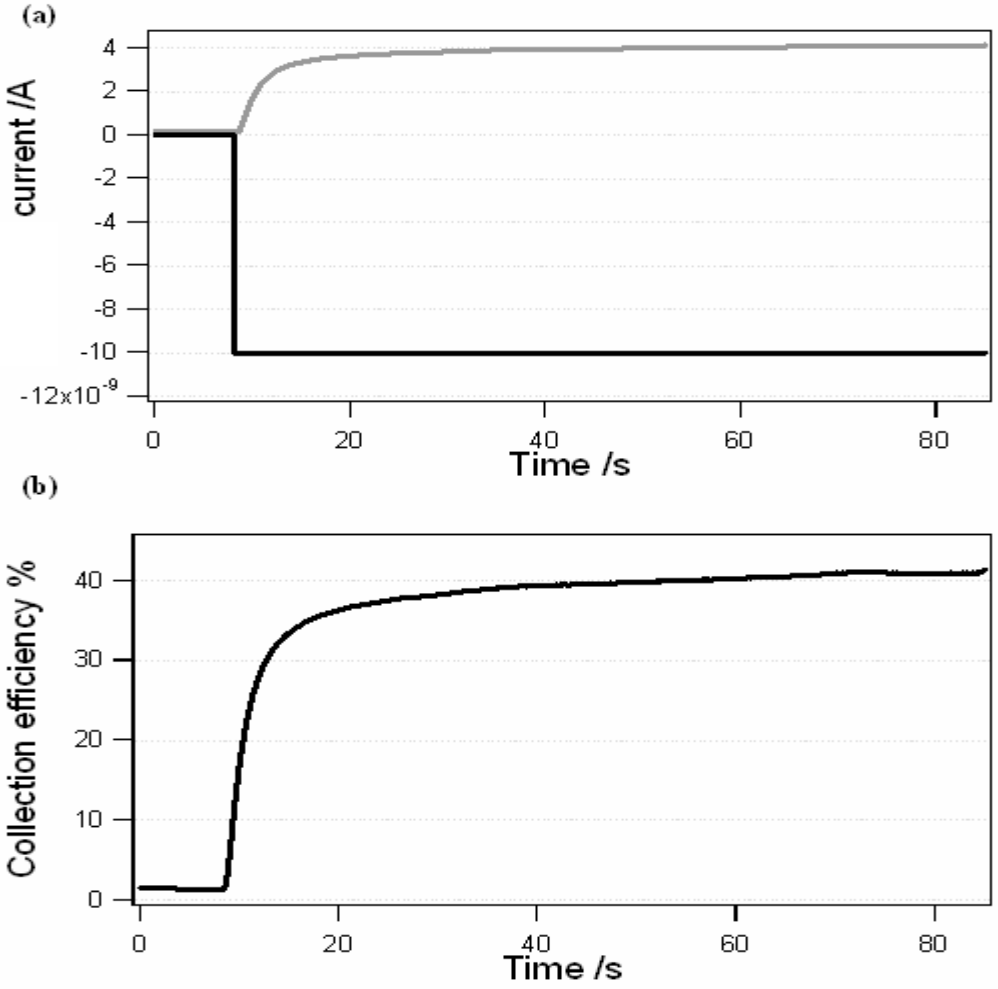

Figure 4.5: (a) Current step imposed at the generator (black) and the current measured at the collector (grey). **(b)** Collection efficiency evaluated as the ratio of collector to generator current.

When imposing currents at an electrode it is a good practice to monitor the voltage at that electrode as this will indicate whether or not the desired reaction is taking place. Sometimes the current imposed is too large which results in additional reactions being drafted in to fulfil the current requirement. This may also occur as a result of changes in concentration, diffusion coefficient or reaction kinetics at the surface of the electrode. The Sand equation describes these effects:

$$\tau^{1/2} = \frac{nFAD^{1/2}\pi^{1/2}c_{bulk}}{2I} \qquad (4.1)$$

Where **τ** is the transition time (i.e. time needed for the concentration of reactant species at the surface to fall to zero), **n** is the number of electrons transferred, **F** Faraday's constant, **A** the area of the electrode, $\mathbf{c_{bulk}}$ is the bulk concentration and **I** the current imposed at the electrode. Fig 4.6 shows what happens to the voltage when too much current is imposed (56). Monitoring the voltage also gives an indication of bubble formation when generating H_2.

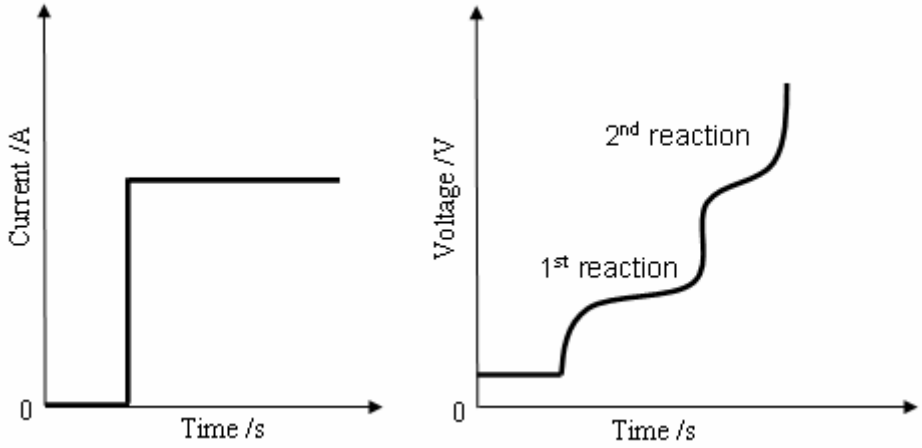

Figure 4.6: (a) Current step imposed at the electrode. **(b)** Voltage response to the current step. The current step is too large so another reaction occurs to fill the current gap. Adapted from Bard and Faulkner (56).

Constant current generation is useful because it simplifies the mass transport measurement made by the ring-disc microelectrode. The reason for the simplification is that when imposing a constant current at the generator, changes in mass transport or reaction kinetics as well as changes in reactant concentration and diffusion coefficient will have little effect on the measurement made. This means that only the collector will detect the changes in mass transport. Variation in concentration of reactant and mass transport near the generator are the most likely changes in our application. To illustrate the advantage of using constant current generation to limit the effects of changing reactant concentration, collector-generator measurements were made in two solutions with different $Ru(NH_3)_6^{3+/2+}$ concentrations (see Fig 4.7). We see that for different current steps at the generator (5,10 nA) the level collected is roughly the same. With constant voltage generation we see a ten fold difference in current (Fig. 4.4).

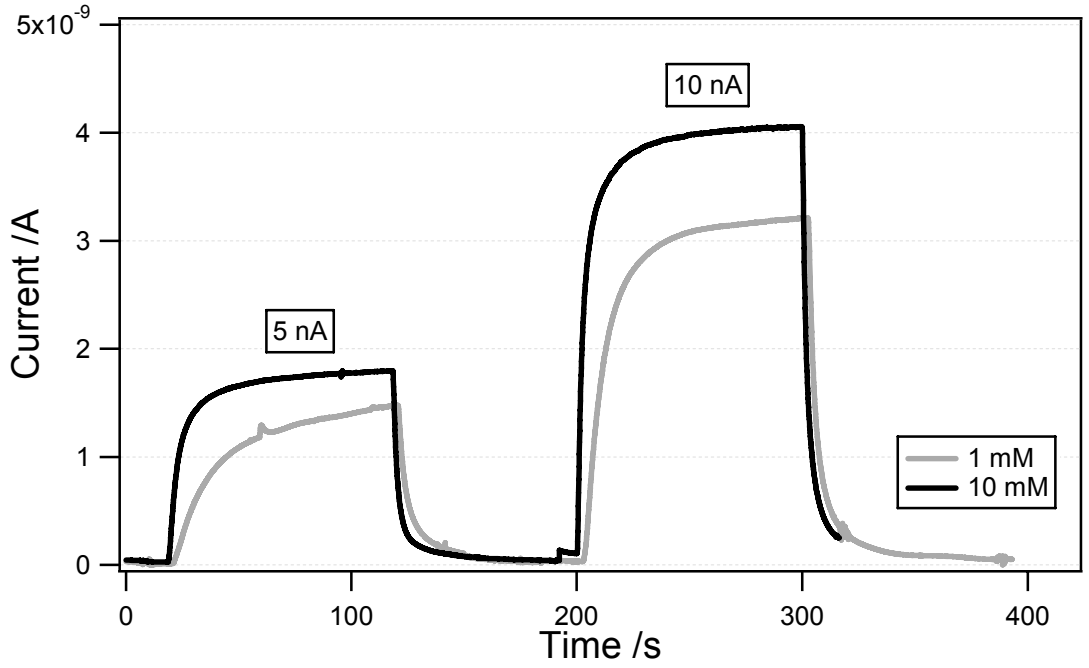

Figure 4.7: Current response at the ring following a constant current generation at the disc. Black trace represents a solution with a 10 mM concentration of $Ru(NH_3)_6^{3+2+}$, grey trace 1 mM concentration. Steps represent successive generation of 5 and 10 nA. Collector was held at 0.2 V vs. Ag/AgCl, the electrode had a disc diameter of 50 μm.

4.2 Features of the ring-disc electrode

4.2.1 Feedback, shielding factor

The spatial arrangement of the ring-disc microelectrode means there are two electrodes in close proximity at which electrochemical reactions are taking places. If the electrodes are too close to each other, their diffusional fields may overlap. This can have a positive or negative influence on the current levels at the electrodes (135). When both electrodes are inducing the same reaction, for instance a reduction, the overlapping of diffusional fields will have a negative effect by lowering the current at both electrodes. This effect is called shielding and happens because both electrodes are competing for the same species. When the two electrodes are performing the reverse reactions such as an oxidation and reduction or a generation and collection, an overlap of the diffusion fields will have a positive effect. This is called feedback and results in an increase in the current at both electrodes. In feedback the product of the reaction at one electrode is the reactant for the reaction at the other electrode. An illustration of feedback and shielding is shown in Figure 4.8. In Fig 4.8 (c) we can see that the current at the disc generator electrode drops by more than 50 % as a result of shielding. Under feedback mode the increase in current is just below 25 %.

In our application the sensor is by default used in the feedback mode. By making the electrode spacing small the current response at both electrodes is thus often enhanced. This serves to improve the measurement resolution and the signal to noise ratios.

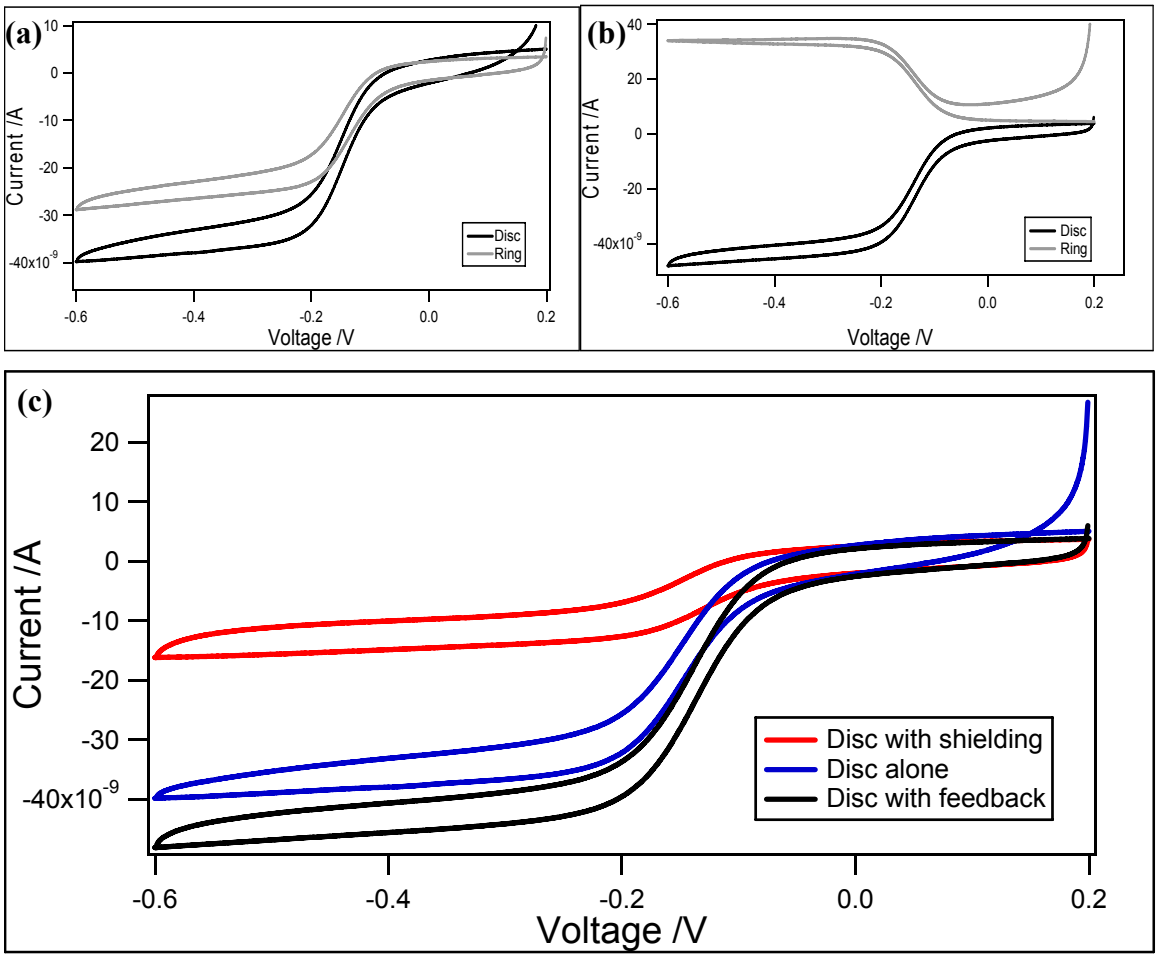

Figure 4.8: (a) Cyclic voltammogram of the ring and disc, each electrode was scanned separately. **(b)** Typical feedback trace, where the disc is generating $Ru(NH_3)_6^{3+}$ and the ring is collecting $Ru(NH_3)_6^{2+}$. The potential at the disc is scanned from 0.2 to -0.6 at 0.05 mV/s, whilst the ring is held at 0.2 V. **(c)** Difference in generator current responses for different operating modes. Black curves represent the generator electrode response with feedback from the ring, blue curves are for the disc scanned alone and the red curves are for a disc shielded by the ring.

4.2.2 Difference between ring and disc generating modes

The significant difference in size and shape between the ring and disc electrodes is a notable advantage of the ring-disc microelectrode. This difference has repercussions on the current levels at the electrodes as well as the collection efficiency measured when they are coupled. These differences are seen in Figures 4.9, 4.10 and 4.11 where both disc

and ring generators are considered. In these experiments the voltage at the generator starts at 0.2 V and then is stepped in increments of 0.05 V from -0.1 to -0.3 V. The current density of the ring electrodes is always higher than that of the disc electrodes because of the larger contribution of radial diffusion at the rings. This radial diffusion also means that the collection efficiency when the ring is generating may be higher than when the disc is generating. This is the case in Fig 4.10 (c) and 4.11 (c), despite the fact that the generating current at these rings is less than the generating current at the discs. These differences are useful as they may provide ways of probing different aspects of the mass transport in tissue or be used to extend the dynamic range of a particular sensor.

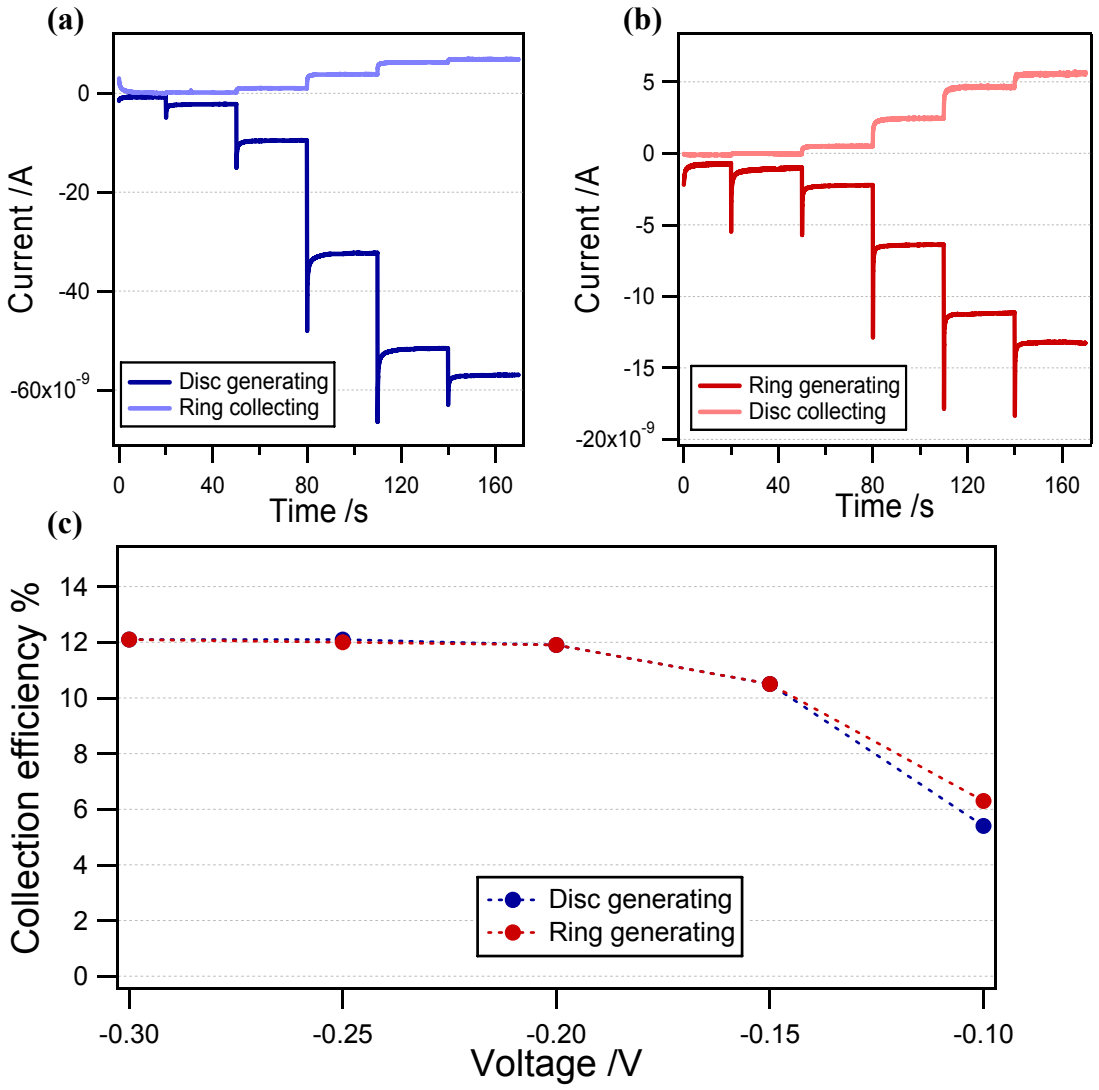

Figure 4.9: Current response at a 25 µm disc diameter sensor under various operating modes. The generator and collector currents response are shown for different voltage steps applied to the generator (0.2, -0.1, -0.15, -0.2, -0.25, -0.3 V). The collector was always held at 0.2 V vs Ag/AgCl. The solution was 10 mM $Ru(NH_3)_6^{3+/2+}$ in 1 M KCl. **(a)** Disc generating mode, dark blue indicate the disc generator, light blue indicates the ring collector. **(b)** Ring generating mode, dark red indicates the ring generator, light red indicates the disc collector. **(c)** Resultant collection efficiency for the disc and ring generating mode. Note the CE traces for ring and disc generating overlap which is a coincidence due to the size of the electrode.

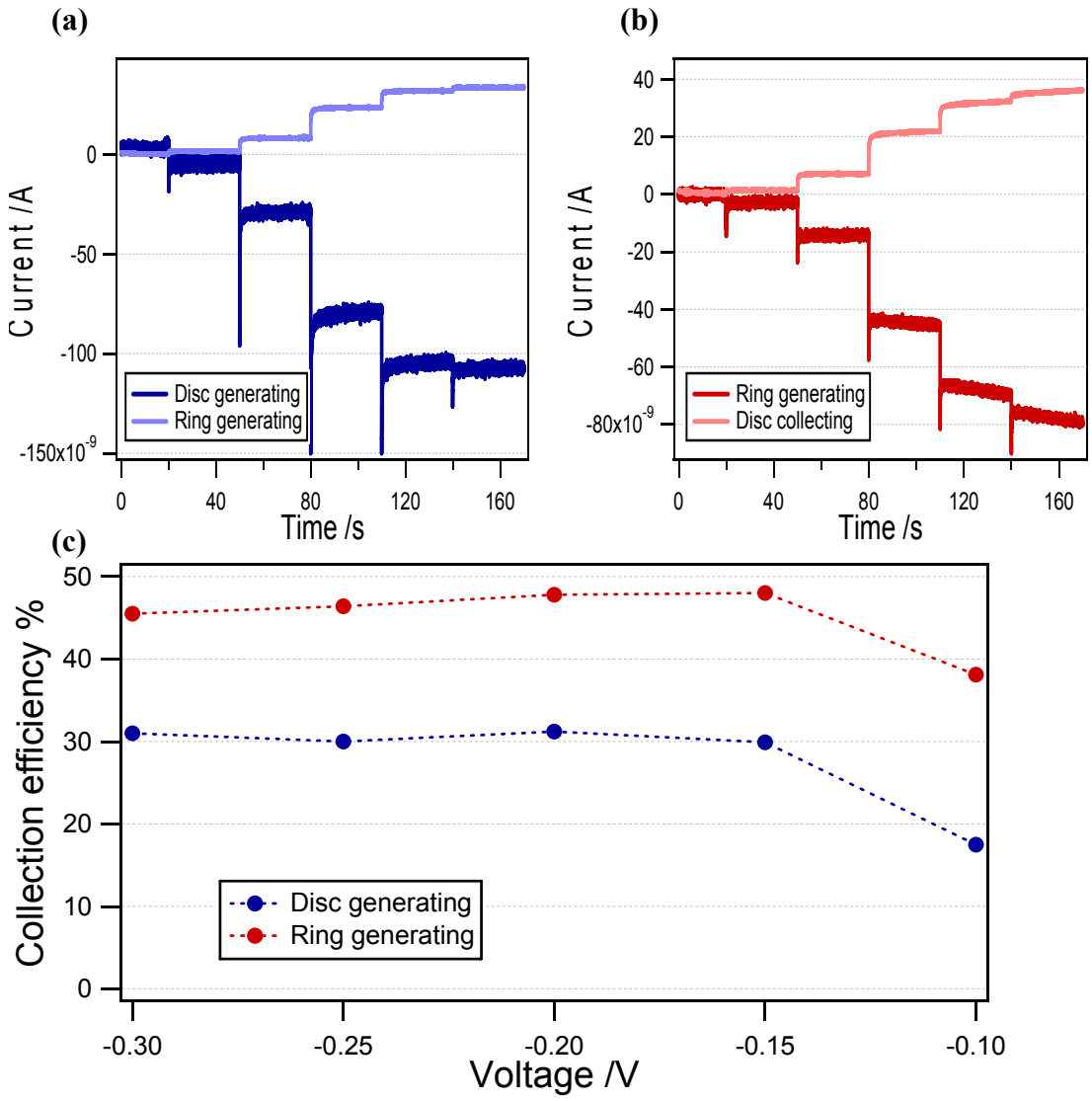

Figure 4.10: Current response at a 50 µm disc diameter sensor under various operating modes. The generator and collector currents response are shown for different voltage steps applied to the generator (0.2, -0.1, -0.15, -0.2, -0.25, -0.3 V). The collector was always held at 0.2 V vs Ag/AgCl. The solution was 10 mM $Ru(NH_3)_6^{3+/2+}$ in 1 M KCl. **(a)** Disc generating mode, dark blue indicate the disc generator, light blue indicates the ring collector. **(b)** Ring generating mode, dark red indicates the ring generator, light red indicates the disc collector. **(c)** Resultant collection efficiency for the disc and ring generating mode (blue and red respectively).

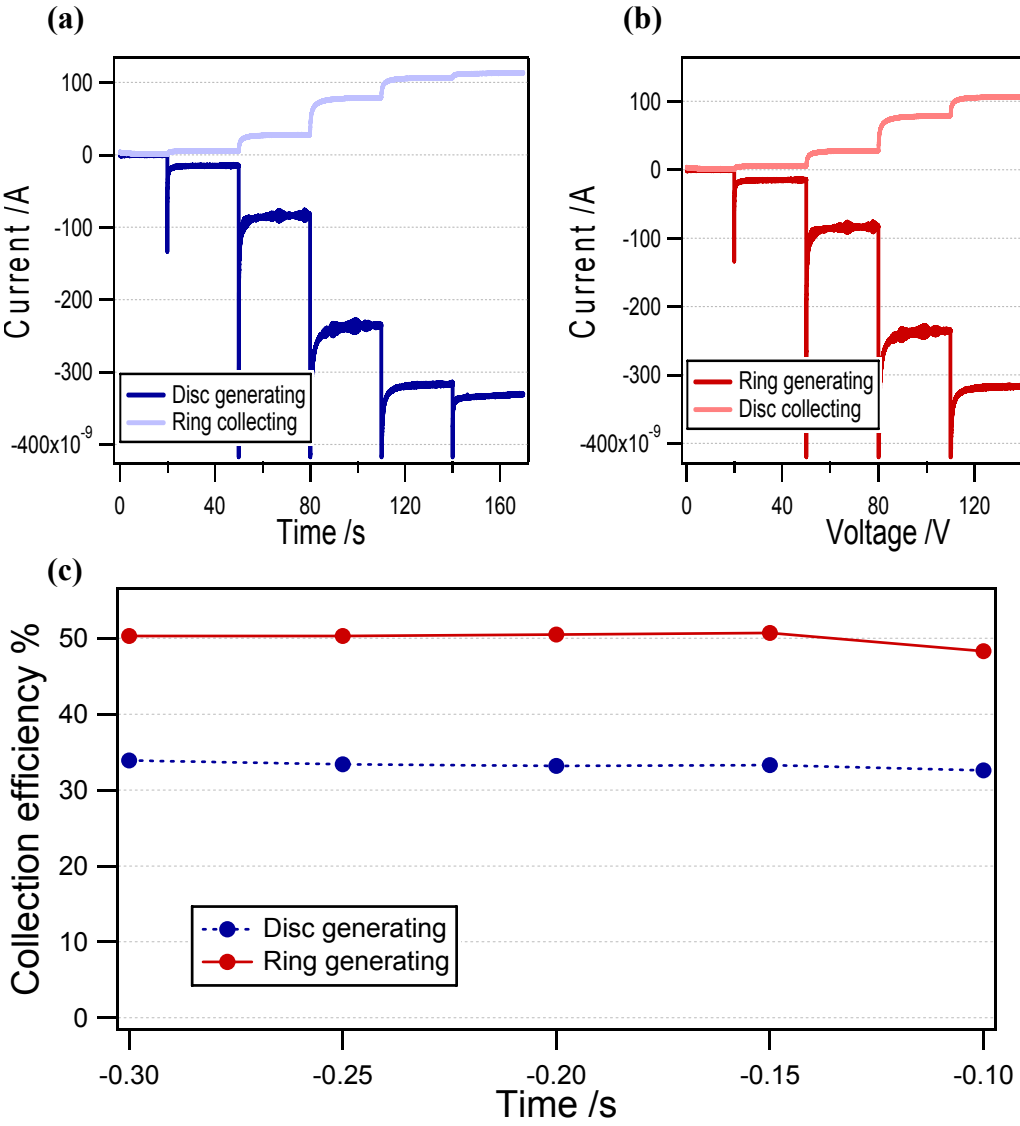

Figure 4.11: Current response at a 125 μm disc diameter sensor under various operating modes. The generator and collector currents response are shown for different voltage steps applied to the generator (0.2, -0.1, -0.15, -0.2, -0.25, -0.3 V). The collector was always held at 0.2 V vs Ag/AgCl. The solution was 10 mM $Ru(NH_3)_6^{3+/2+}$ in 1 M KCl. **(a)** Disc generating mode, dark blue indicate the disc generator, light blue indicates the ring collector. **(b)** Ring generating mode, dark red indicates the ring generator, light red indicates the disc collector. **(c)** Resultant collection efficiency for the disc and ring generating mode (blue and red respectively).

4.3 Conclusion

Throughout this chapter we have investigated the behaviour of the collector-generators under the influence of diffusion mass transport. The experimental techniques used to probe mass transports with the ring-disc microelectrodes were also introduced.

Some of the special features of the ring-disc microelectrode are presented; these include the shielding and feedback effects, both of which influence the level of current measured at the ring and disc electrodes. Feedback occurs in our measurements and we show how it is used to enhance the signal strength.

Constant current and constant voltage generation modes are discussed and their differences highlighted. For our application the constant current generation is shown to be generally superior to constant voltage generation because the generator signal is independent of mass transport, concentration and diffusion coefficient changes. This greatly simplifies the measurement of mass transport.

5

Mass transport measurements under convection and diffusion control

Tissue perfusion involves both diffusion and convection mass transport. In this chapter we expose the ring-disc microelectrode to a number of situations in which controlled convective mass transport is taking place in the vicinity of the sensor. The effects of varying the electrode size, operating mode and flux at the generator are studied under jet impinging and tube flow. The sensor is also used to measure flow rates in tissue mimicking materials and pulsatile flows. The measurements made confirms that the ring-disc microelectrode is capable of monitoring changes in mass transport at the micron level.

5.1 Introduction

Measuring flow using electrochemical methods is a well established principle. Levich has written a seminal book on the subject (155), the content of which has been made somewhat more accessible by others (56,156). The field of microfluidics is where most current applications of electrochemical flow measurements are found.

There are two ways of performing electrochemical flow measurements. The simplest method involves placing an electrode in a flowing solution containing an electroactive species. A sufficient amount of over-potential is applied to the electrode so that the reaction at the surface becomes mass transport limited. As the flow rate changes over the electrode, the movement of the electroactive species to and from the electrode will change. This leads to a change in the current observed at the electrode. In general an increase in current reflects an increase in the flow rate above the electrode (improved mass transport), whilst a decrease reflects a decrease in the flow rate (impaired mass transport). The changes in mass transport represent changes in the fluid boundary layer above the electrode surface. For thin boundary layers (i.e. fast flow) the mass transport due to convection is more significant than that due to diffusion thus the current increases. For thicker boundary layers diffusion is more significant and the current is lower. This method of measuring flow is simple as only one electrode is used. It has been used in a large number of applications such as turbulence measurements (157), microfluidics (158) or physiological flows (159,160). The main disadvantage with this method is that the measurements are very general in that all the changes in the system will affect the measurement. As a result, extracting flow parameters becomes difficult. For instance, changes in temperature will be perceived as changes in flow. In addition this technique only works if an electroactive species is present in solution, which in general means adding it to the solution. This is not always possible either because the volume of flow is too large or because the electroactive species would interfere (i.e. chemical processes). Some authors have circumvented this problem by monitoring dissolved oxygen in solution, although this has its limitations (i.e. changing concentrations will affect the currents, detecting oxygen can be tricky). Another disadvantage is that the measurement resolution achieved is rather poor. The only way to improve it is by having a number of different sized electrodes.

Using a single electrode to monitor flow is effective but a far better way is to use an electrode couple operating as collector-generators. In this technique the electroactive species is generated at one electrode and transported to the other by the prevailing mass transport mechanism in solution. As the mass transport changes the collector will collect more or less of the generated species so its current will increase or decrease. The collector-generator method is not affected by other changes in the system because the recording from both electrodes will be considered thus cancelling any baseline shifting such as temperature. The detection range is also much wider as small changes in flow will have much more effect on the transport of the tracer from the generator to the collector. There has been extensive use of collector-generators to measure flow. Currently the most popular electrode geometry is the dual band microelectrode because it is easily integrated into microfluidic applications and is easy to make. Other geometries such as disc arrays, the dual disc and ring-disc have also been used (56). The combined work of R.G. Compton (122,143-145,148,149,161-166) and C. Amatore (59,127,150-152,167) on dual band microelectrode for flow measurements has significantly advanced the subject, although other contributions are noteworthy (126,168). A special mention has to be made regarding the series of articles by Amatore et al. on the *in situ* monitoring of the velocity profile in microfluidic channels using dual band microelectrodes (59,150,151). These describe how any flow profile can be derived from the measurements at the electrode couple, provided the electrode and channel dimensions are known. Comparable investigations will be presented in this chapter in which a number of flow environments were considered. The aim was to investigate the response of the sensor to a broad range of convective mass transport so as to improve its design for measuring tissue perfusion.

The flow environments studied were tube flows, impinging jet flows and flow through porous media. Two redox couples were used in these experiments $Ru(NH_3)_6^{3+/2+}$ and $H_2^{/+}$. These studies demonstrated the versatile and remarkable flow detection capabilities of the ring-disc microelectrodes. In addition the design of the electrodes was improved by identifying the dynamic range of the sensor as well as the relationship between the sensor size and the flow detection capacities.

5.2 Impinging jet flow

Impinging jets are well established in fluid mechanics, where they are exploited for their enhanced heat and mass transfer characteristics. These reasons have also motivated electrochemists to use them, although at significantly lower flow rates. It was pointed out in Section 3.3.1 that previously achieving well defined flow profiles over an electrode would have involved the use of a rotating disc or ring-disc electrode (56). However this technique is not suited to microelectrodes because of problems in placing the electrode at the centre of the disc. The main uses for impinging jets have been to study reaction mechanisms(169), investigate the effects of mass transport (76,121,170), for high performance liquid chromatography (HPLC) end column detection, flow injection analysis and capillary electrophoresis (90,171,172). In our application the flow arrangement used is similar to the kind used in HPLC where the sensor is placed at the end of a tube. The small size of the electrodes with respect to the size of the jet means that our arrangement is that of a micro-jet rather than a wall-jet, where the electrode area is larger than the jet impinging area.

5.2.1 Material and methods

Flow cell

A polydimethylsiloxane (PDMS) cast was made to serve as a flow cell for this study. The basic design of the cast consisted of a 2 mm diameter glass capillary with two smaller sections of glass capillary branching off in succession. The branches were parallel to one another and formed a right angle with the main tube. This cast was placed in a shallow box into which PDMS was poured. The resultant flow cell is shown in Fig 5.1.

The PDMS (silicone elastomer, SYLGARD 184, Dow Corning) was prepared following the manufacturer's instructions by thoroughly mixing one part of curing agent with ten parts of the base (by volume). The mixture was then degassed to remove bubbles for 10-20 min. It was then slowly poured into a suitable box containing the mould. If bubbles were generated during the pouring, the mixture was again degassed. The entire assembly was then cured for 2 hours at 70 °C. Ethanol was often used to detach the PDMS flow cell from the supporting box and also to remove the glass capillary tubing.

The flow cell was connected to the end of the HPLC column (reciprocating pump 1050 series, Hewlett-Packard) with standard tubing and connectors. The reference and counter electrodes were placed upstream of the sensor which was inserted into the end of the flow cell. Usually the sensor was inserted 2-3 mm into the flow cell. For these experiments the sensor was encased in a pulled glass capillaries 1.5 mm in diameter. The sensor was held in the flow cell by micromanipulators, which enabled the sensor tip to be moved in all three dimensions (see Figure 5.1).

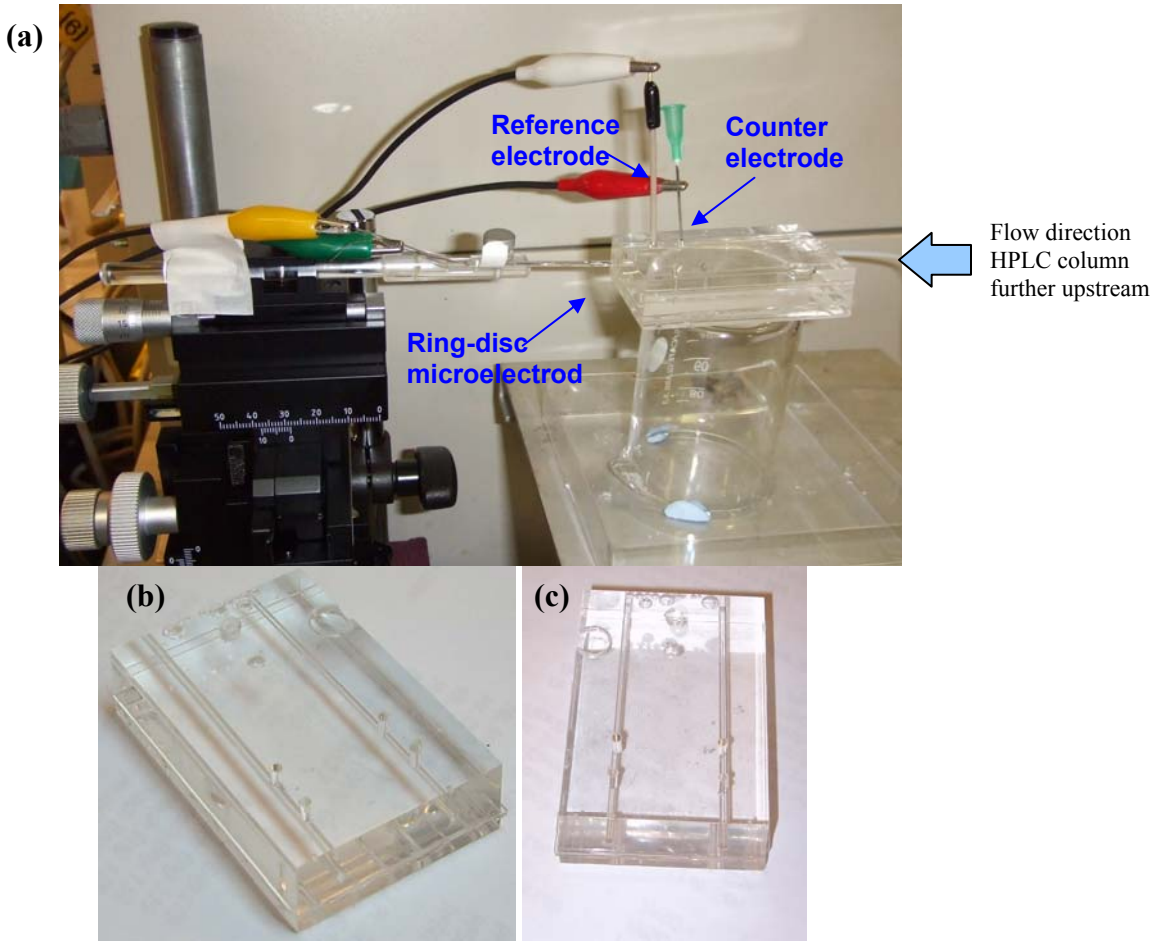

Figure 5.1: (a) Impinging jet experimental set up with the sensor placed at the end of a PDMS flow cell also containing a Ag/AgCl reference electrode and a stainless steel counter electrode. The sensor positioning at the end of the pipe is controlled by an micromanipulator. **(b)** and **(c)** Close up of the flow cell, which contains two tubes with different diameters (1.5 and 2 mm)

Instrumentation

An eight channel potentiostat CHI 1030 (CH Instruments Inc. Texas) was used to control the voltage at the ring-disc microelectrodes. The flow cell also contained a Ag|AgCl (3 mol dm^{-3} KCl) reference and stainless steel counter electrodes.

Chemical Reagents

Chemical reagents $Ru(NH_3)_6Cl_3$ and KCl, (Aldrich) were used to make a solution of 10mM $Ru(NH_3)_6Cl_3$ in 1M KCl. The solutions were deoxygenated by bubbling with nitrogen for 20 min prior to use. Demineralised and filtered water was taken from a Purite Select system (resistivity of ≥14 MΩ cm).

5.2.2 Results and discussion

In these experiments the redox couple used is $Ru(NH_3)_6^{3+/2+}$, the generator electrode reduces $Ru(NH_3)_6^{3+}$ to $Ru(NH_3)_6^{2+}$, the collector performs the reverse reaction some distance away by oxidising the ruthenium (II) complex. The potentials at which the diffusion limiting reduction and oxidation happen are respectively -0.6 and 0.2 V vs Ag/AgCl. Both disc and ring generating modes were considered. A number of sensors of different dimensions were used in these experiments. Before the effect of flow rate could be investigated, the sensor had to be placed in the centre of the flow stream to ensure that the resultant impinging jet would be centred onto the electrode tip. Placing the sensor in the centre of the tube was not always sufficient to ensure that the sensor tip was at the centre of the flow profile because the sensor tip was not always at the centre of the pulled capillary.

To centre the sensor tip, the disc and ring potentials were set to their respective values for generation and collection. The flow through the cell was set to a constant value, usually 1 ml/min. By moving the location of the sensor up and down and side to side it was possible to locate the point at which the collection efficiency was lowest. This in turn represents the location of the stagnation point, which in laminar tube flow occurs at the centre of the flow profile. When the sensor is placed anywhere but at the centre of the tube, the collection efficiency will be higher. Figure 5.2 illustrates the relative position of the sensor tip and the flow profile in the tube and how this can affect the

collection efficiency. Figure 5.3 shows a typical collection efficiency trace during the centring process. The centre was found iteratively by finding the horizontal then the vertical centre and then checking each direction to be certain of the accuracy.

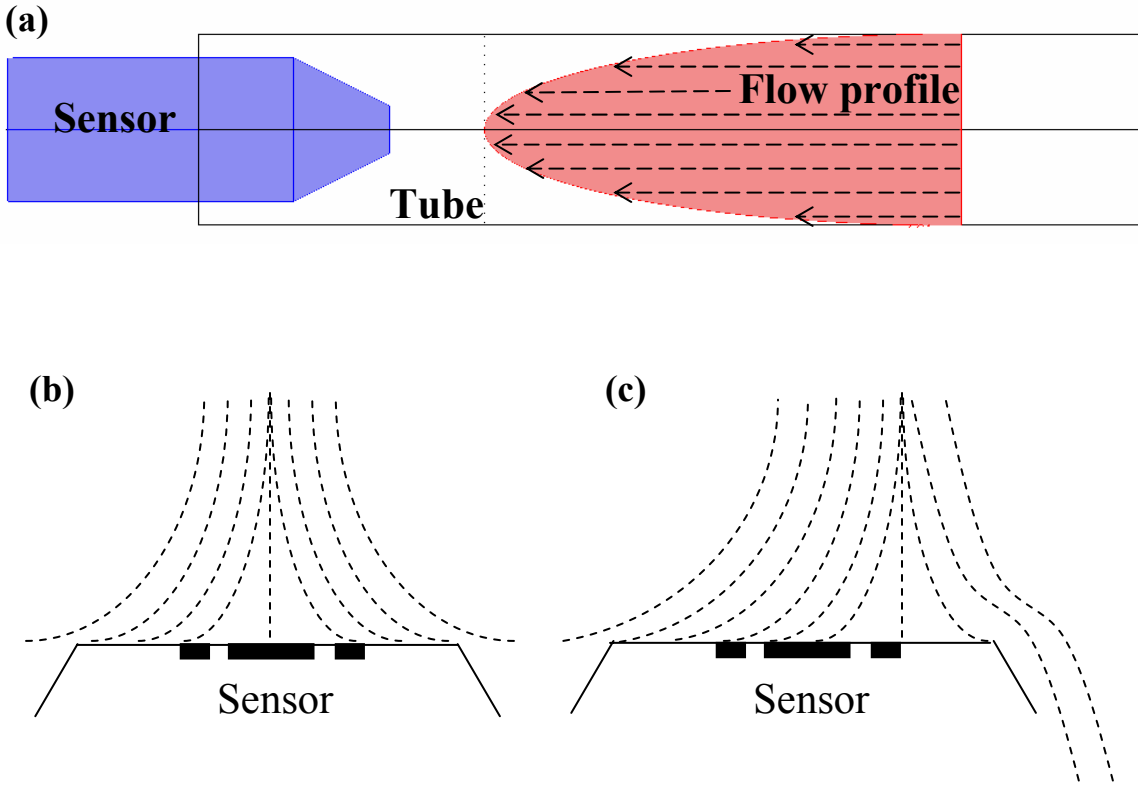

Figure 5.2 : (a) Schematic representation of the sensor in the flow cell. Sensor is in blue, the flow profile in the tube is represented in pink. The sensor is moved vertically or horizontally in the tube in order to have the sensor tip positioned at the point where the velocity is maximum. **(b)** Schematic representation of the sensor tip and the impinging jet flow onto it for a sensor that is well centred in the tube and **(c)** for a sensor that is eccentric.

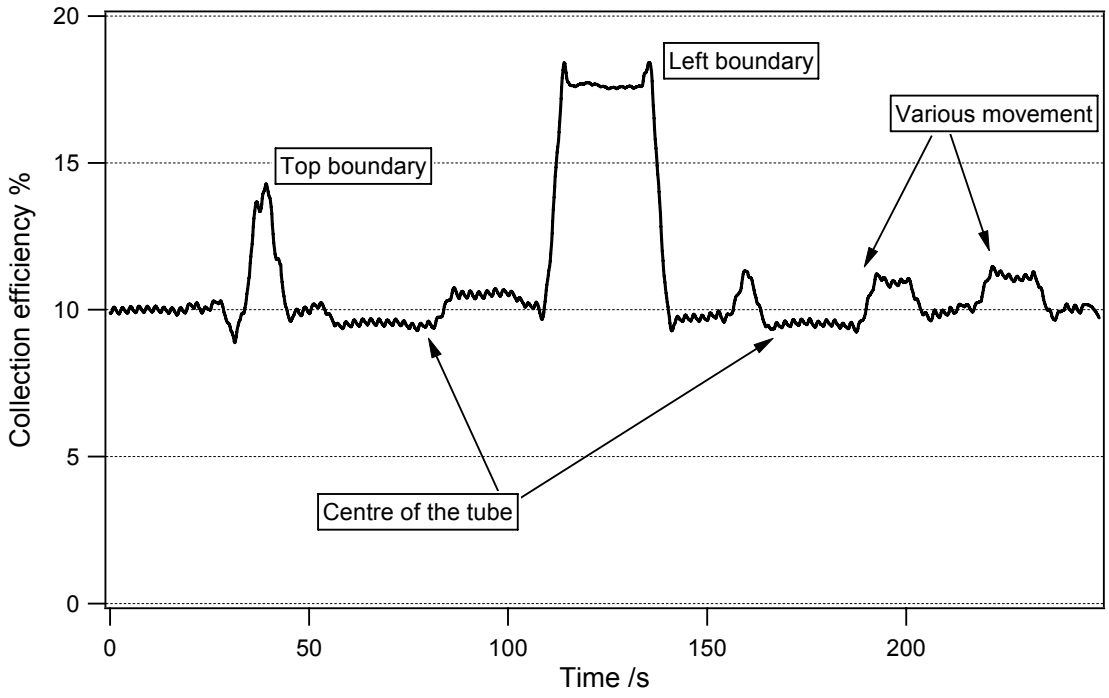

Figure 5.3: Change in collection efficiency as the sensor tip is moved in the tube. The lowest CE value is reached when the tip is in line with the flow profile. The highest values occur when the tip is close to the tube wall. Since the sensor is extremely sensitive to movement, this method proved a very satisfactory way of aligning the sensor. Ripples in the trace are due to pulsatility of the flow.

Once the sensor tip has been centred, the investigation of the effects of flow on the collection efficiency were carried out. Figure 5.4 shows some typical raw data, where the collection efficiency is seen to drop every time the flow is increased in 1ml/min step increments. Beyond 4-5 ml/min the CE does not change significantly, the sensor has effectively reach its detection limit. The flow was then decreased in increments back to the starting flow rate of 0.1 ml/min. The ripples in the collection efficiency are the result of small variations in flow caused by the pump.

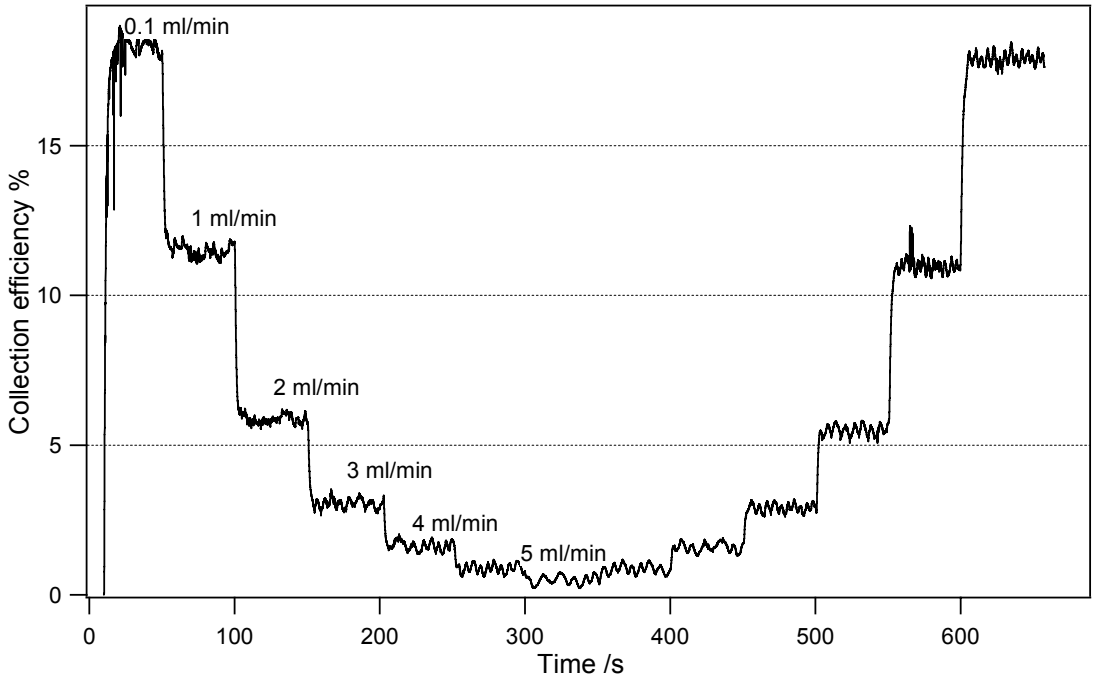

Figure 5.4: Change in collection efficiency with flow rate for a disc generating case. Flow is increased from 0.1 to 5 ml/min then decreased again in 1 ml/min step increments. The redox couple used is $Ru(NH_3)_6^{3+/2+}$ in 10 mM concentrations. The sensor has dimensions r_1 = 62.5 μm, r_2 = 75 μm and r_3 = 76 μm.

Figure 5.5, 5.6 and 5.7 further show the relationship between collection efficiency and flow rate for the disc generating and the ring generating cases respectively. The response of three sensors of different dimensions is shown. One can clearly see that the dimensions of the sensor influence the range of flow rates that can be detected. The influential dimensions are the collector size and how far it is from the generator, a thorough investigation of these variables is presented in Section 3.3.1. For each sensor used these dimensions are somewhat different, which explains the different flow detecting capacities.

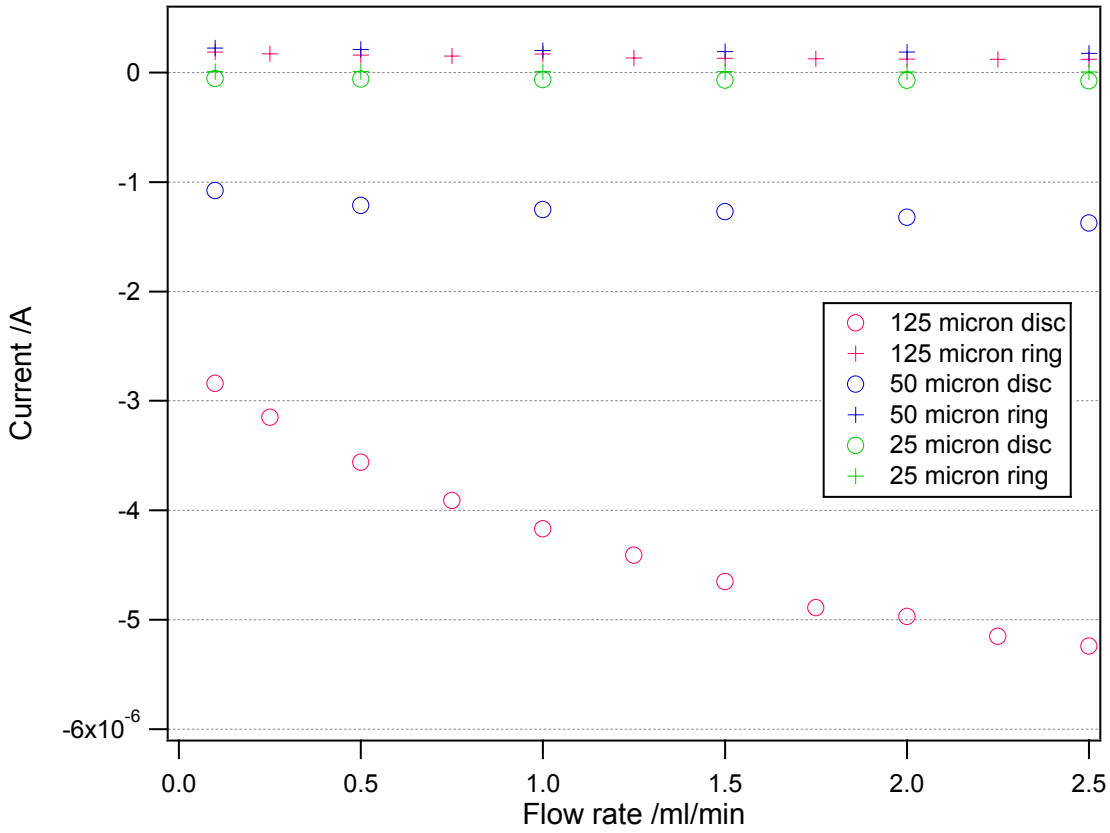

Figure 5.5: Effect of flow rate on the current at the disc and ring. Disc generating, ring collecting mode for three electrodes with disc diameter 25, 50 and 125 μm. Ring current are represented by crosses, disc current are represented by circles. The redox couple used is $Ru(NH_3)_6^{3+/2+}$ in 10 mM concentrations.

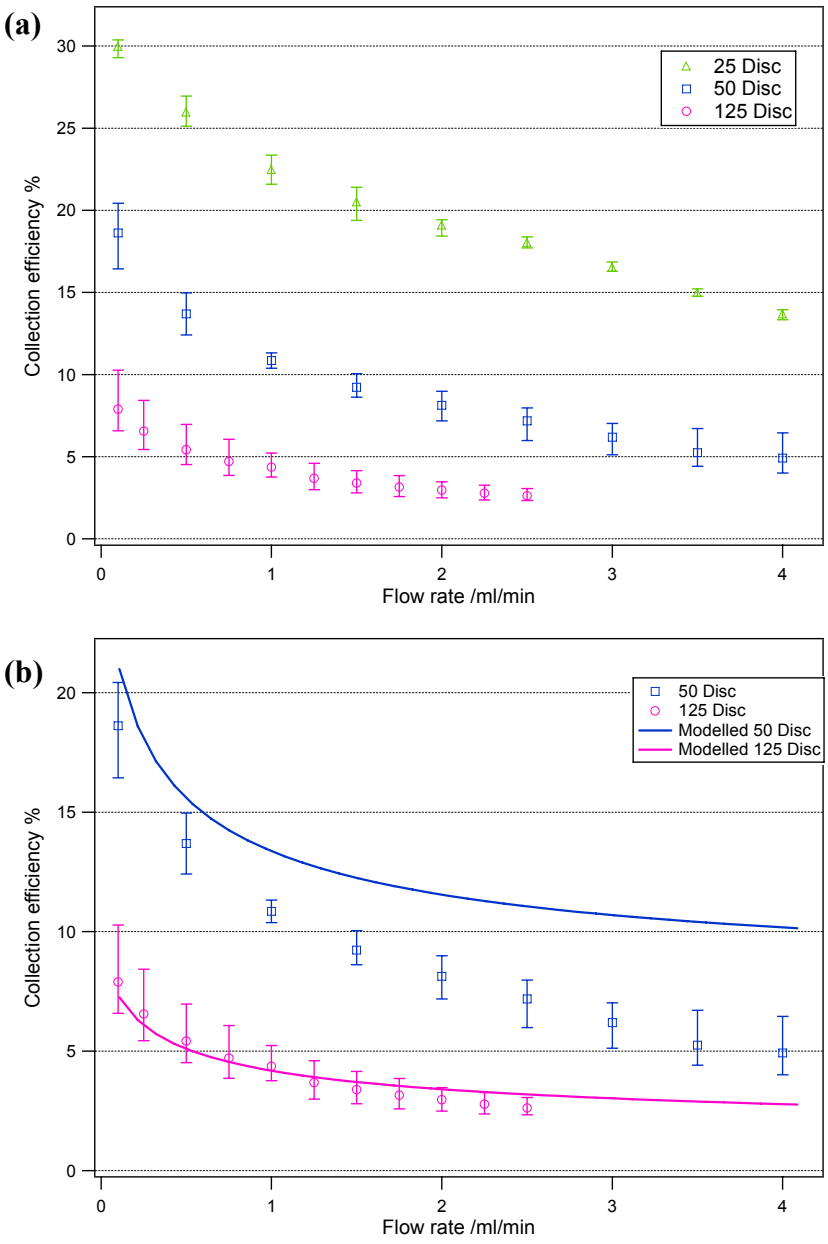

Figure 5.6: Change in collection efficiency with flow for a disc generating case. **(a)** Three sensors are used each of which has different dimensions. The electrode named **25 Disc** has dimensions r_1=12.5 µm, r_2=17.5 µm and r_3= 17.7 µm, **50 Disc** r_1=25 µm, r_2=32.5 µm and r_3= 32.7 µm, **125 Disc** r_1=62.5 µm, r_2=75 µm and r_3= 75.2 µm. The average and range of three trials are represented by the markers. **(b)** The solid lines represent the numerical simulations.

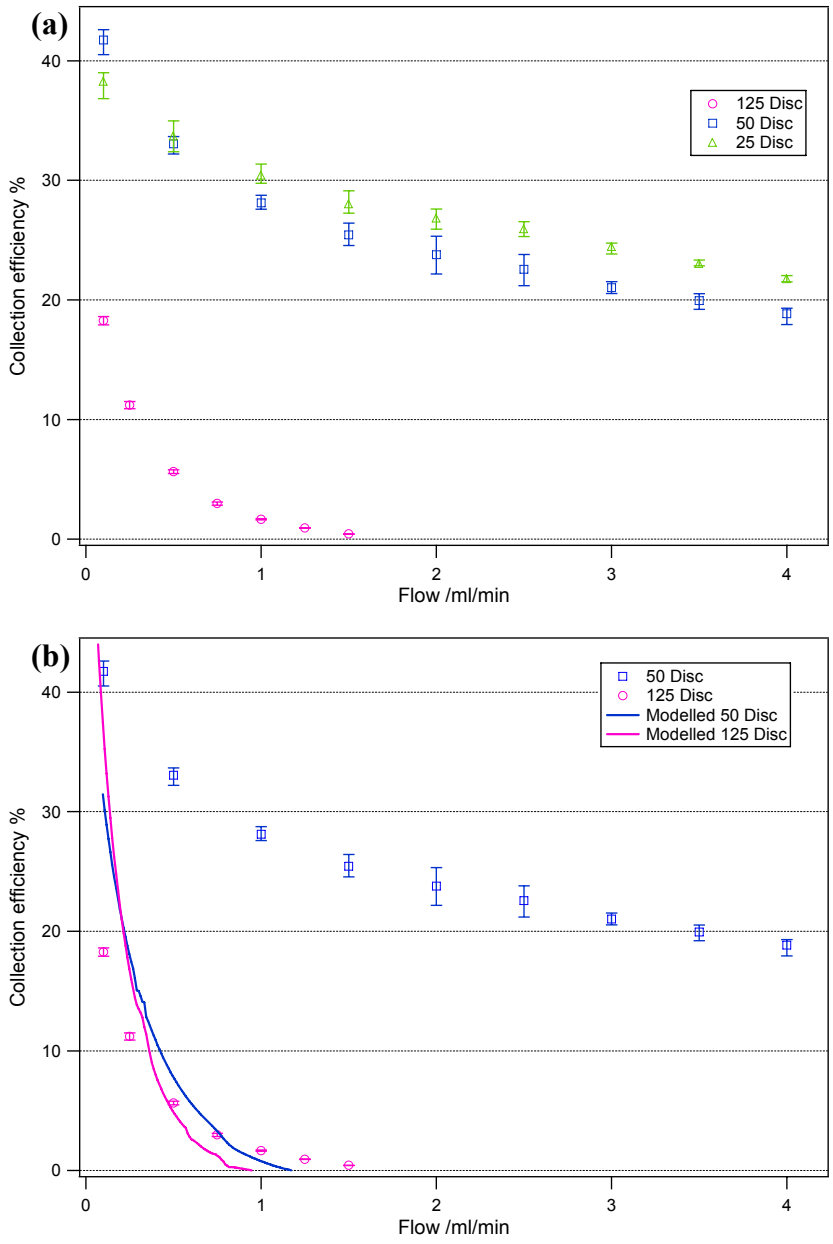

Figure 5.7: Change in collection efficiency with flow for a ring generating case. **(a)** Three sensors are used each of which has different dimensions. . The electrode named **25 Disc** has dimensions r_1=12.5 µm, r_2=17.5 µm and r_3= 17.7 µm, **50 Disc** r_1=25 µm, r_2=32.5 µm and r_3= 32.7 µm, **125 Disc** r_1=62.5 µm, r_2=75 µm and r_3= 75.2 µm. The average and range of three trials are represented by the markers. **(b)** The solid lines represent the numerical simulations.

The measurements shown in Figure 5.7 are for ring generating cases. In Section 3.3.1 we presented numerical models of such cases (shown in Fig 5.7b), which predict that the collection efficiency of these sensors should drop significantly as the flow increases and that they should have difficulty in detecting flow beyond 2 ml/min (i.e. their CE is too close to 0%). This is not the case experimentally for the 25 and 50 m Disc sensors. The 125 Disc sensor exhibits the expected response (i.e. that predicted by the simulations Section 3.3.1) but not the other two. It is hard to pin point the reason for such a discrepancy, especially when for the disc generating case the numerical and experimental traces are in very good agreement. We believe the reason could be uneven electrode surfaces, which would shield regions between the ring and the disc in which the redox cycling could occur without being disrupted by the flow. Such issues have been reported by others working with thin rings and impinging jets (76). Further polishing of the electrodes was undertaken to try to eradicate the problem without much success.

5.2.3 Conclusion

We have investigated the behaviour of the sensor under controlled hydrodynamic conditions, through the use of jet flows impinging on the surface of the sensor. The collection efficiency of the sensor is seen to decrease as the flow rate increases. Sensors with different dimensions exhibit different responses to the same flow rates. This introduces the idea that each sensor has a particular flow detection range or dynamic range. By using the disc or ring as generator it is possible to have two very distinctive dynamic ranges owing to the significant difference in the shape of these two electrodes. Numerical work presented in section 3.3.1 indicates that the experimental results obtained for the ring generating cases are not as predicted. Sensors with 25 and 50 μm disc diameter did not exhibit the expected sharp decrease in collection efficiency with flow rate. The reasons for this discrepancies was not established although we believe the uneven surface of the electrode is to blame.

5.3 Tube flow measurements

Laminar flow through tubes is well characterised and has been studied exhaustively (173,174). Tube flow is also easy to set up experimentally and is incidentally a fairly good approximation of flow in very small blood vessels. Tube flow therefore presented itself as an ideal test rig in which to investigate the flow measurement capacities of the sensor.

Flow studies in tubes are also widespread in electrochemistry. Many collector-generator type studies have been reported, most of which make use of tubular band microelectrodes. Flow injection analysis, capillary electrophoresis and high performance liquid chromatography are the techniques in which tubular flow measurements are being used. Work done with these electrodes is very similar to that done with dual band microelectrodes in channel flow. Numerical and experimental investigation of the effect of electrode dimensions and electrode flux on the flow detection capacities of these electrodes has been presented (141,147,175-177).

5.3.1 Material and methods

Flow cells

A number of PDMS flow cells were made to serve as flow cells for this study. The basic design of the flow cell consists of a tube with three smaller tubes branching off in succession. All of the branches are parallel to one another and form a right angle with the main tube (see Fig 5.8). Different tube diameters were tested ranging from 2 mm to 2 cm. The flow cell that was used predominantly, however, had a tube diameter of 8 mm.

To make the cast, sections of plastic tubing were used. It was found that when all sections of the cast were held together, the flow cell were less likely to fail. In most cases the pieces of tubing were stuck together with glue (glue gun) before being placed in a small shallow box. PDMS was then poured into the box and cured as described in the previous section (Section 5.2.1).

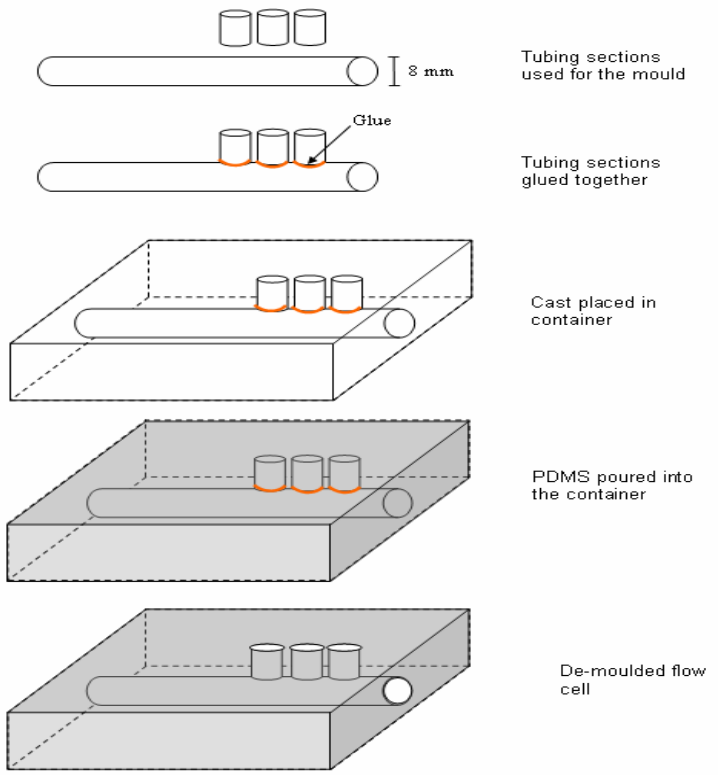

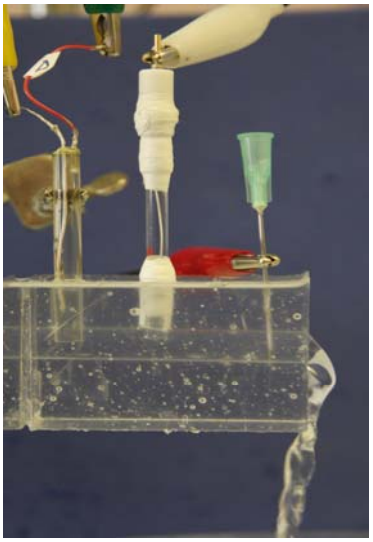

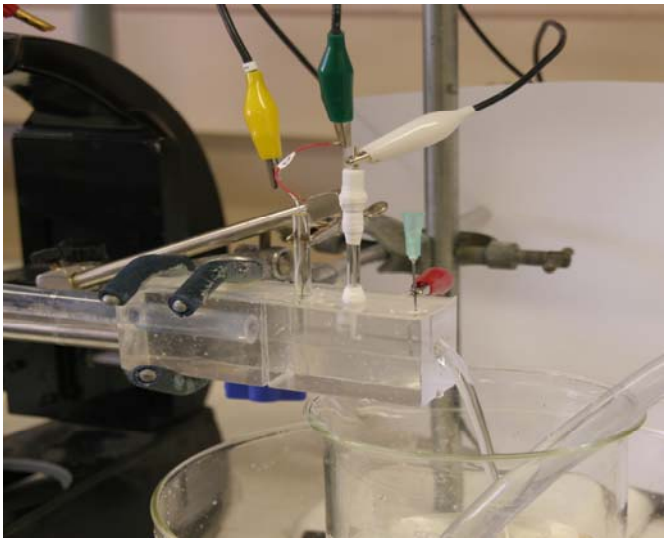

Figure 5.8: Schematic representation of the steps involved in making the flow cells and pictures of the flow cells made. Reference (Ag/AgCl) and counter (stainless steel) electrodes were always placed downstream of the sensor in the flow cell with the reference closest to the sensor.

Flow rig

Two types of arrangements were used to force the fluid through the flow cell, hydrostatic pressure head or an HPLC pump.

For the hydrostatic pressure head arrangement, a 5 L tank of KCl buffer was connected to the flow cell by 2 m length tubing, 0.5 m of which were kept straight just upstream of the flow cell to allows the flow to develop Calculation of the Reynolds number in the tube and entry length required shows that in the most extreme case the flow becomes fully developed after 0.1 m (Re ranges from 10 to 80 depending on the flow rate). The buffer was collected after the flow cell and pumped back into the 5 L tank using a peristaltic pump (200HC, HR flow inducer, Watson Marlow Limited). The flow rate was changed by varying the valve opening of the 5 L tank.

When an HPLC pump (1050 series**,** Hewlett-Packard) was used the length of connecting tubing used was shorter but the 0.5 m of straight tubing upstream of the flow cell was retained for the reasons outlined above.

Flow rate measurements were made for each experiment with volumetric beakers and a stop watch and compared to the flow rate indicated by the pump.

The sensor was held in place in the flow cell with a micromanipulator, this enabled a controlled positioning of the sensor in the tube. The convection term above the sensor can then be described in terms of the boundary layer that has formed on the surface of the sensor. Figure 5.9 illustrates the different setups used.

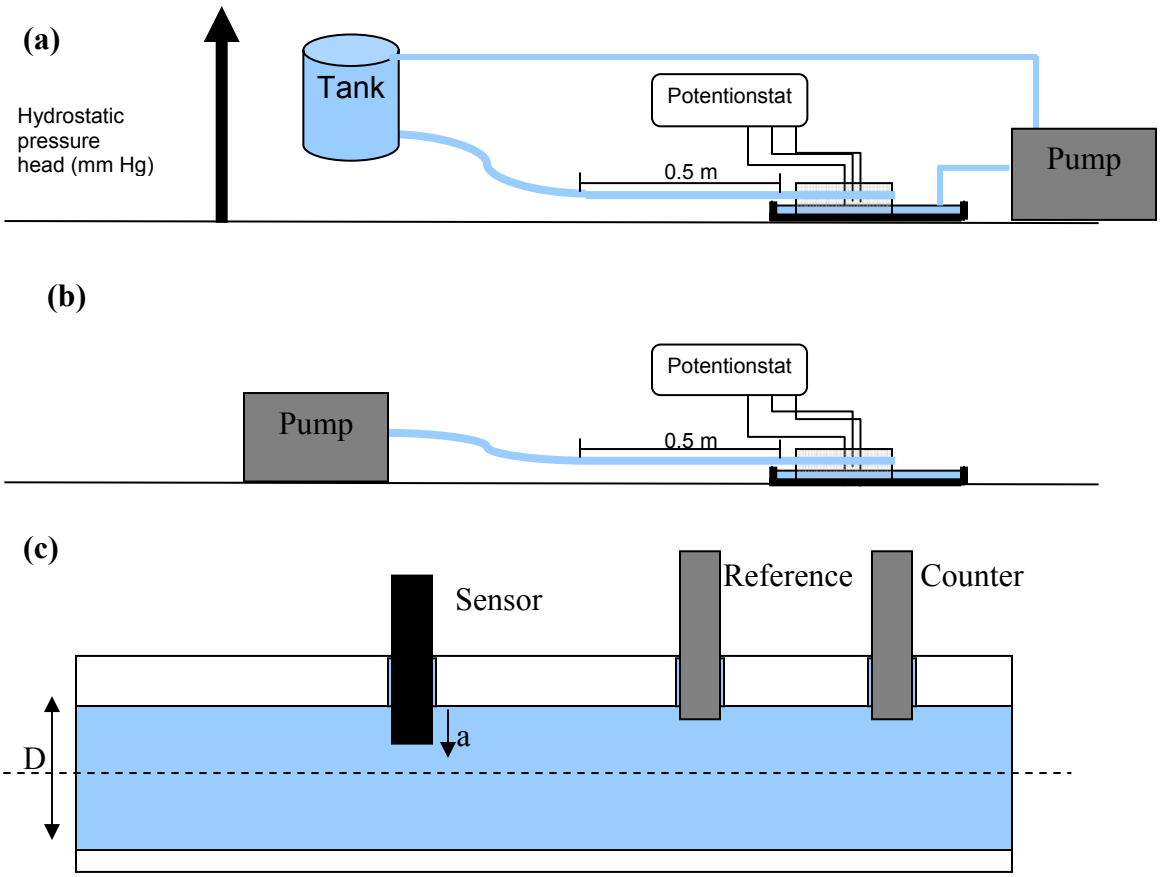

Figure 5.9: Schematic representation of the flow rig used. **(a)** Shows the setup when a HPLC pump is used to drive the flow through the flow cell. **(b)** Shows the setup when a hydrostatic pressure head is used to drive the flow. **(c)** Shows a schematic of the flow cell and the location of the sensor, reference and counter electrode. **D** is the diameter of the tube, **a** is the depth to which the sensor has been lowered in the tube. At the wall a = 0.

Instrumentation

An eight channel potentiostat CHI 1030 (CH Instruments Inc. Texas) was used to control the voltage at the ring and disc microelectrodes. The flow cell also contained a Ag|AgCl (3 mol dm^{-3} KCl) reference and stainless steel counter electrodes.

Measurements

With the sensor placed half way into the tube a/D = 0.5, the generator potential is set between -1 and -1.5 V and collector electrode potentials are set to 0.2 V vs. Ag/AgCl.

At these potentials hydrogen is being generated and collected respectivly. Only disc generating cases were considered in these experiments, this is because the disc generating case is less susceptible to electrode polishing problems. Recordings of collection efficiency were then made in a continuous fashion whilst the flow rate was being changed in step increments from 0 to 8 ml/min.

5.3.2 Results and discussion

Usually the recordings took 10 to 20 s to reach to their steady state value when the flow rate was altered as shown in Fig 5.10. As the flow rate was increased the collection efficiency decreased, owing mainly to a decrease in the collector current. Figure 5.11 summarises the results obtained for a disc generating case. The two traces represent measurements made with sensors of different dimensions, a 50 μm and a 125 μm disc diameter sensor. The measurements of collection efficiency were taken from averages of the steady state curves. The drop in collection efficiency with increasing flow rate describes how the H_2 concentration profile around the collector changes. With increasing flow more H_2 is washed away before it can reach the collector. When comparing the measurements made by the two sensors, it becomes clear that beyond a certain flow rate their collection efficiency no longer drops. This limit varies with the size of the ring-disc electrodes and effectively describes the dynamic range of the sensors. We observed these effects in the previous section with impinging jet flow. A number of authors using dual band collector-generators in channel and tube flow have also reported different dynamic limits for different sensor sizes (145,178). This indicates that the sensor dimensions can be specifically chosen to suit a given range of flow rates. This was investigated numerically in Section 3.3.2

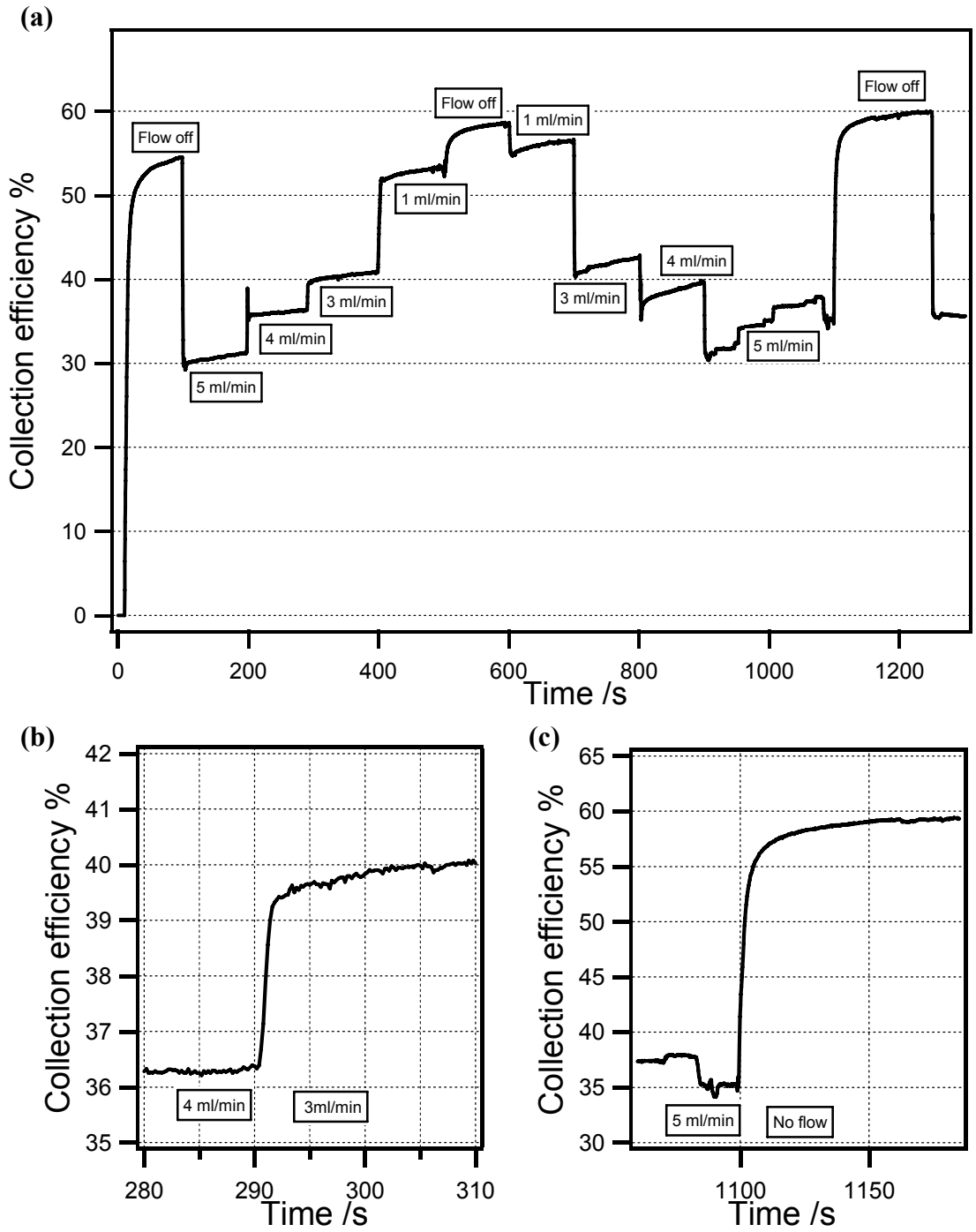

Figure 5.10: Changes in collection efficiency as the flow is varied. **(a)**The sensor is placed perpendicular to the flow direction. H_2 is the redox couple used with a sensor with disc diameter 50 μm. **(b)** and **(c)** show the transient to the steady state value after the flow rate has been changed. The sensor used had a 50 μm disc diameter located at a/D=0.5.

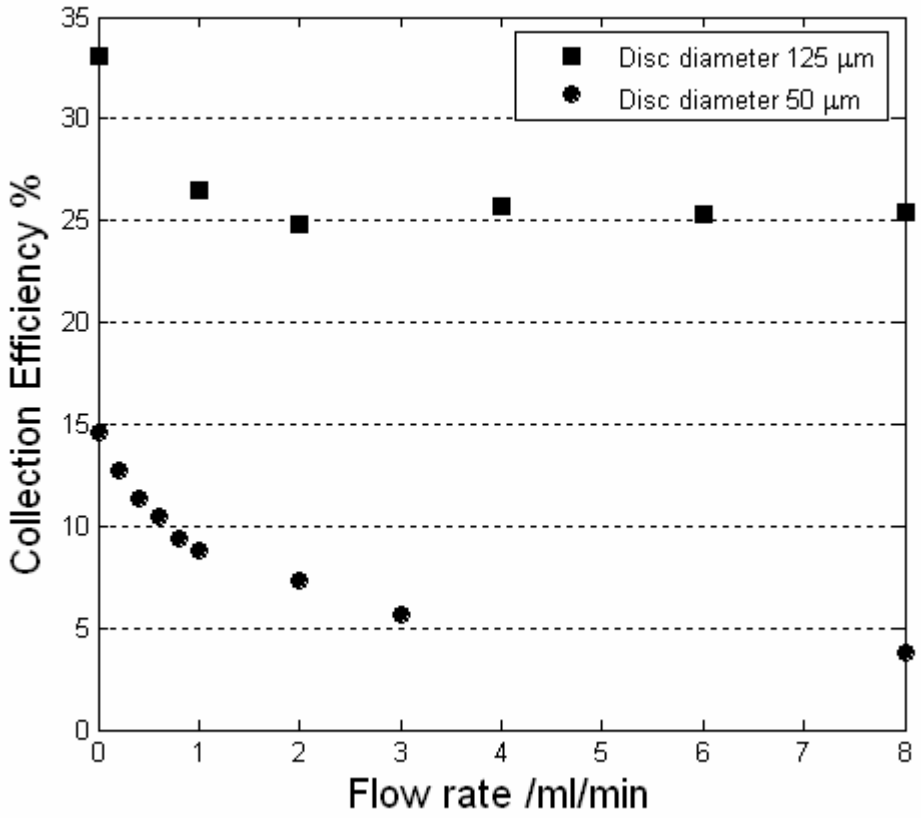

Figure 5.11: Change in collection efficiency with flow for two sensors of different dimensions (50 and 125 µm disc diameter). Only disc generating cases are considered and the redox couple used is H_2. The difference in detection range for each sensor is clearly seen. The electrodes were positioned at a/D=0.5.

In the following section we return to using $Ru(NH_3)_6^{3+/2+}$ as the redox couple. This is done in order to show how different levels of generator applied voltage or current will influence the measurements of flow. Such an analysis could be done with H_2, of course, but because of the formation of bubbles at high generator potentials the interpretations of the results would be more complicated. Also $Ru(NH_3)_6^{3+/2+}$ undergoes a simple one electron transfer from the outer sphere, making it well suited to such investigations. The experimental setup is the same as described in the previous paragraphs.

It is well established and has been highlighted throughout this thesis that the level of flux at the generator electrode will influence the collection efficiency. In the diffusion limit, the flux at a microelectrode will have a significant radial component described as the edge effect. When the reaction is rate limiting, the flux is predominantly normal to the surface of the electrode. Because of the coupling between the generator and the collector, any change in the direction of the flux will influence the collection efficiency. To investigate this, we applied different potentials to the generator (-0.1, -0.2 and -0.3 V) whilst maintaining the collector at the diffusion limiting potential (0.2 V vs Ag/AgCl). Note that the formal redox potential of $Ru(NH_3)_6^{3+/2+}$ is -0.19 V vs Ag/AgCl. Subsequently different currents were applied to the generator (-1, -5, -10, -50 nA) and the collector was again at the diffusion limit (i.e. applied potential 0.2 V). The relationship between current and voltage is shown in Figure 5.12 and shows how applying different voltages or currents will influence the flux at the electrode.

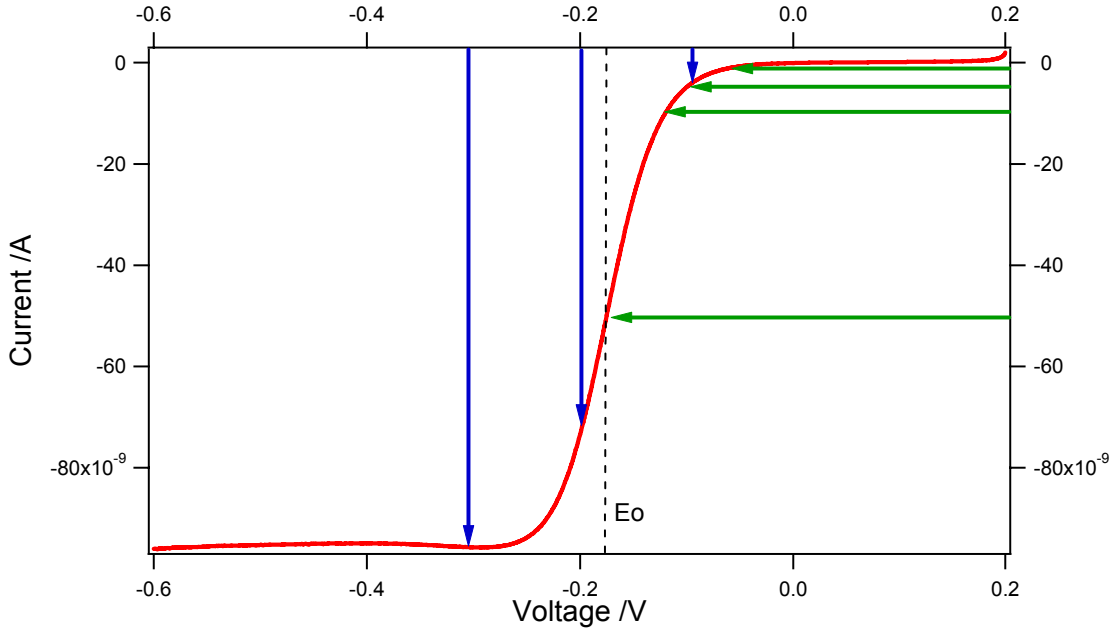

Figure 5.12: Current voltage characteristics of a 50 µm disc electrode in 10 mM $Ru(NH_3)_6^{3+/2+}$. The blue arrows show the voltage applied to the disc (-0.1, -0.2, -0.3 V) and the resultant current it yields. Green arrows show the current applied to the disc (-1, -5, -10, -50 nA) and the corresponding voltage.

Figure 5.13 shows how the collection efficiency changes with flow for different applied potentials and Figure 5.14 is for different generator applied current. The overall response of the sensor to flow seems independent of applied voltage or current. However the level of collection efficiency increases as the reaction goes from being rate limiting to diffusion limiting, this occurs for applied potentials that are beyond -0.19 V, the formal redox potential. When applying a fixed current to the generator, we expected to see more spread between the curves, for instance applying 5 or 10 nA should be well below the diffusion limit and the collection efficiency should reflect this, but it did not. At low flow rates an increase in collection efficiency was observed which was not expected. The increase could be due to the generated species being gently forced onto the collector. Alternatively the generator may have been recessed slightly, a small amount of convection may be improving the mass transport within the recess.

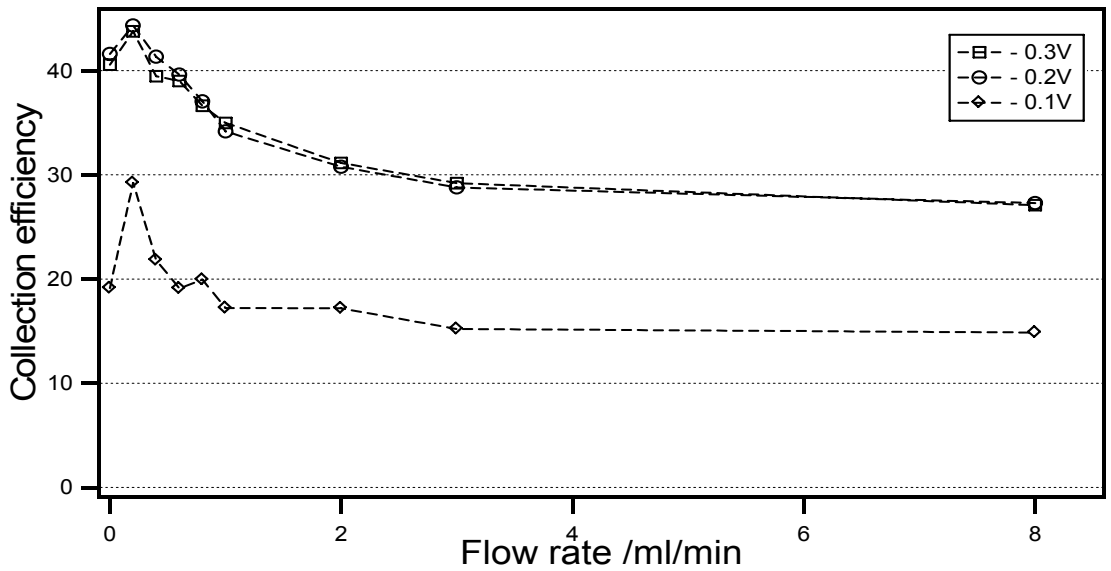

Figure 5.13: Change in collection efficiency with flow for different applied voltages at the disc generator. The collector is always held at the diffusion limiting case of 0.2 V. $Ru(NH_3)_6^{3+/2+}$ was used as redox couple (10 mM in 1M KCl), it has a formal oxidation potential of - 0.19 V.

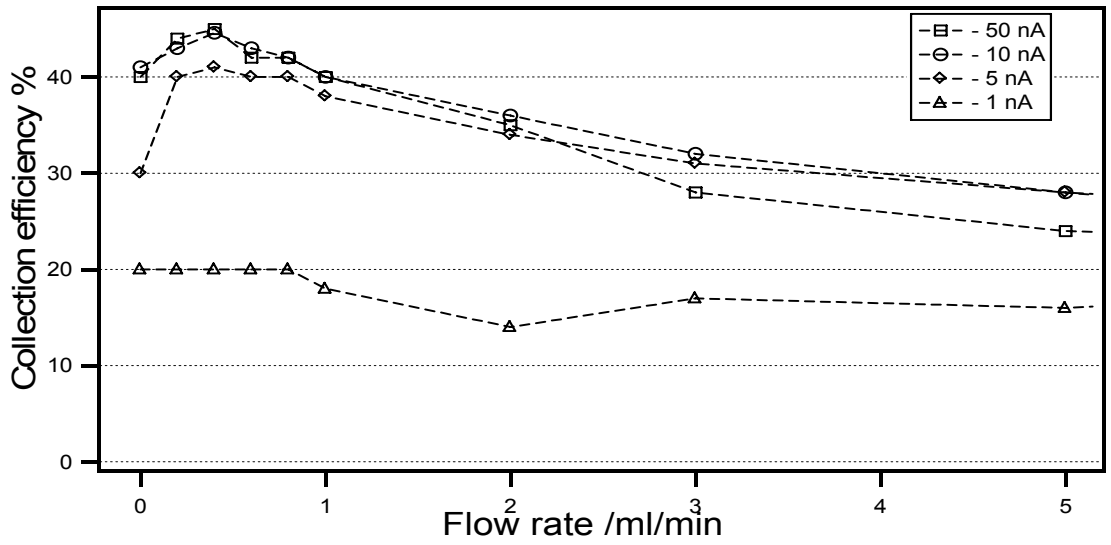

Figure 5.14: Change in collection efficiency with flow for different applied currents at the disc generator. The collector is always held at the diffusion limiting case of 0.2 V. $Ru(NH_3)_6^{3+/2+}$ was used as redox couple (10 mM in 1M KCl), it has a formal oxidation potential of - 0.19 V.

We now return to experiments where H_2/H^+ is used as redox couple. Having established that the sensor is capable of distinguishing between large flow variations (i.e. on the order 1 ml/min), it was essential to test the flow resolution that was achievable at lower flow rates. To do this we attempted to measure changes in flow rate across the diameter of the tube by changing the depth of the sensor in the tube. The change in flow due to the velocity profile in the tube should be detectable with sufficient measurement resolution. The experimental results are shown in Figure 5.15 and highlight the versatile measurement capacities of the sensor. The collection efficiency does indeed drop as the sensor is advanced into the tube. Being able to monitor small changes in flow will be especially useful when flow measurements are made in damaged tissue where the flow is predominantly slow.

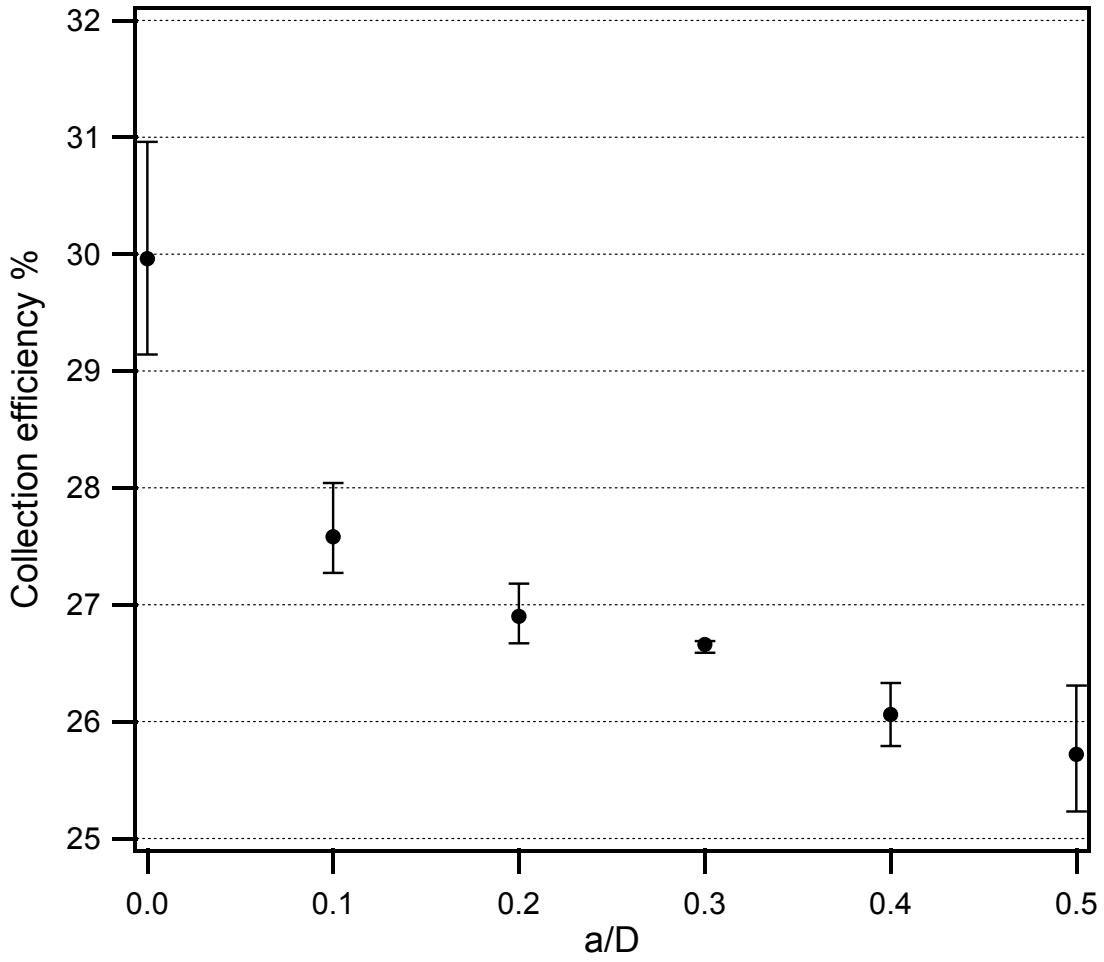

Figure 5.15: Experimental measurement of the change in collection efficiency as the sensor is advanced into the tube. The averages and range of three trials are shown The sensor used had a disc diameter of 50 μm, the flow rate was held at 1 ml/min.

In Figure 5.16 the sensor depth was further advanced into the tube until it reached the opposite wall. When this is done we see that the collection efficiency decreases, stabilised then decreases even further. What is happening is that the sensor is effectively disrupting the flow by constricting the area through which the fluid can flow and thus increasing the velocity locally. This is detected by the sensor as a drop in the collection efficiency. The flow through the tube in these conditions is undoubtedly more complicated as a result this experiment was only undertaken as an illustration of the

behaviour of the sensor rather than as a proper characterisation and to highlight that care must be taken not to constrict the flow cell.

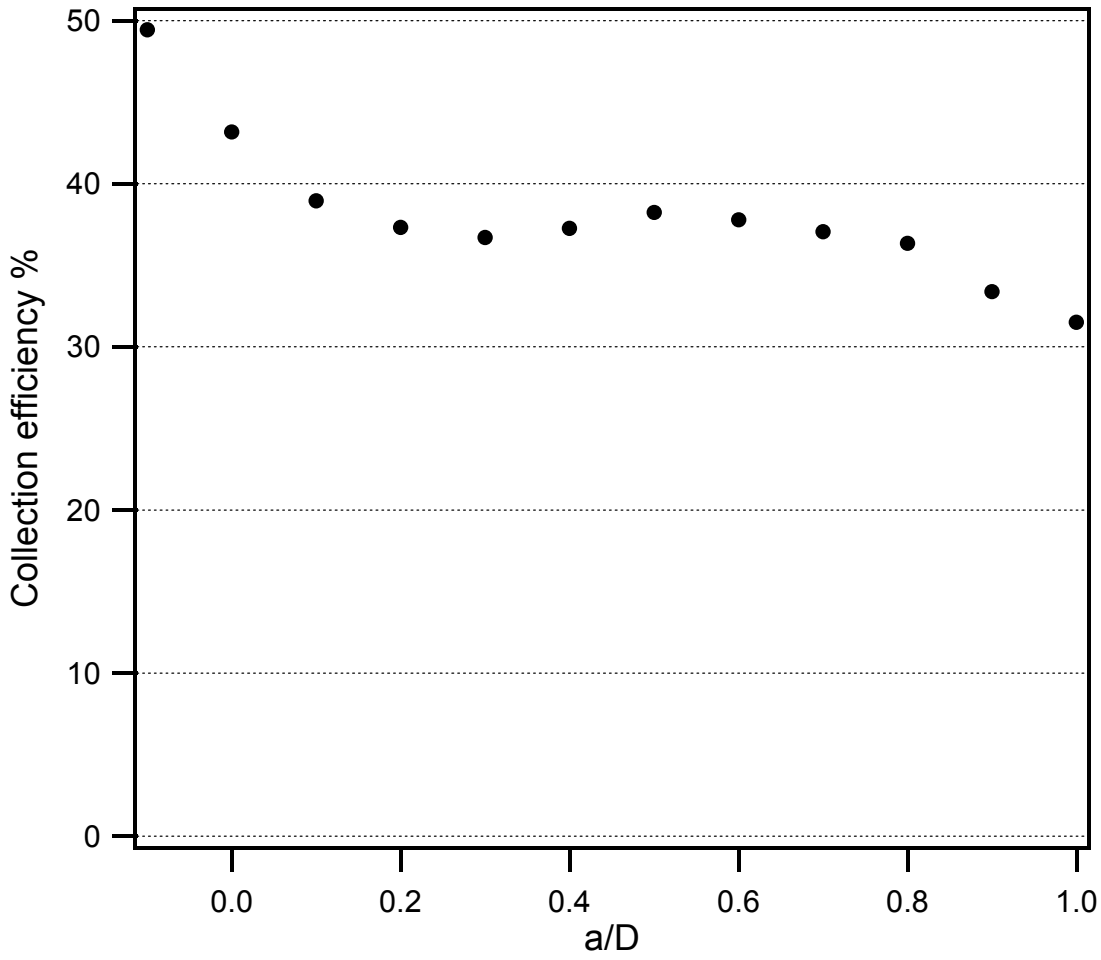

Figure 5.16: Variation in the collection efficiency as the sensor is advanced through the tube. The sensor starts outside the tube and is advanced all the way to the opposite wall (i.e. a/D = 1). The flow rate is maintained at 1 ml/min and the sensor used has a disc diameter of 125 μm. The tube had diameter of 8 mm and the electrode had an outer diameter of 5 mm.

It is important to note that having the sensor perpendicular to the flow is probably not the best way to use the ring-disc microelectrode for flow detection. This is because portions of the sensor will not be used. Far better assemblies are the band-band, disc-disc or tubular electrodes which can be placed inline with the flow. If we consider the case

when the disc is generating as in these experiments, when convection is significant the portion of the ring that is upstream from the disc will have trouble collecting the H_2, whilst the portion of the ring downstream from the disc will have the advantage of having H_2 advected onto it. As the flow rate increases the portion of the ring upstream that will not be collecting H_2 increases. Figure 5.17 illustrates this effect.

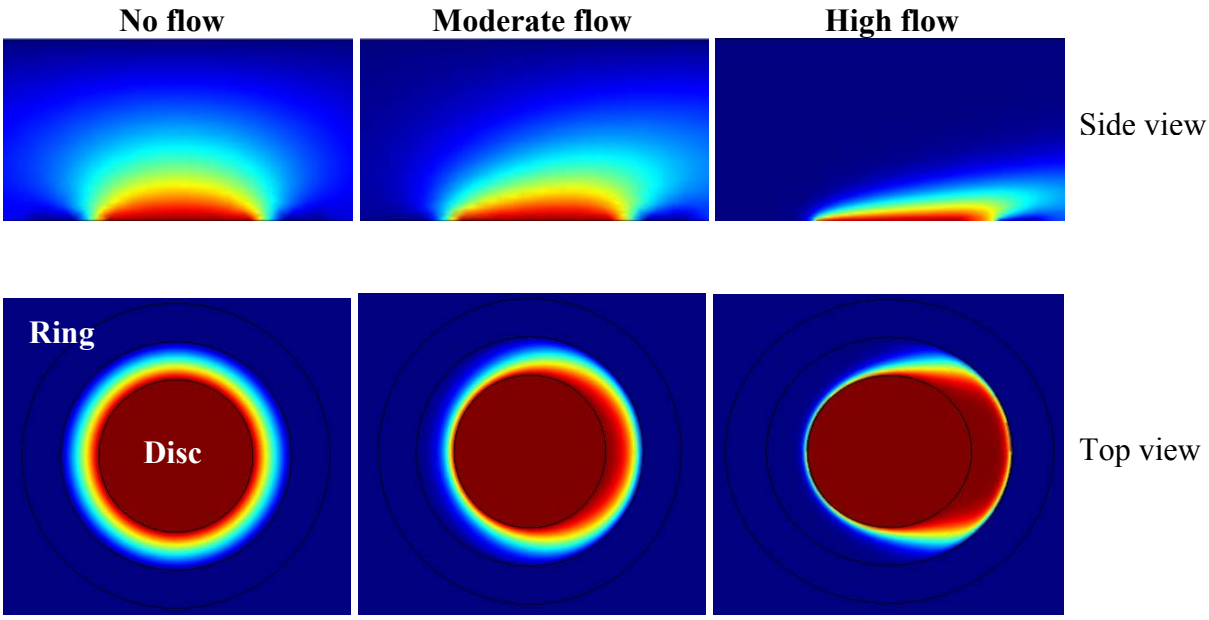

Figure 5.17: Schematic representation of the concentration profile over the ring-disc electrodes under different flow conditions when the disc is generating. Flow direction is from left to right. Colours indicate concentration of H_2, dark red indicates maximum concentration blue indicates minimum concentration.

5.3.3 Conclusion

We are able to measure overall changes in flow rate within tubes. Measurements show that the collection efficiency drops with increasing flow rate. The response of the sensor to changes in flow is rapid, on average the steady state is reached 20 seconds after the flow rate has been changed. Sensors with different dimensions have different flow detection limits.

The effects of generator current density on the measurements were also investigated, we found no significant change in the response to flow or detection range

for different electrode fluxes. However the collection efficiency reaches higher levels at the diffusion limiting case than at the rate limiting case.

Finally the sensor was used to measure the changes in flow velocity across the radius of the tube, demonstrating that the sensor is capable of detecting small changes in flow, although the effect of blockage of the flow can affect the results.

5.4 Measuring pulsatile flow

Blood flow is pulsatile in nature, as the blood reaches the extremities of the body and the vessels get smaller the pulse is damped but still must be considered. The sensor was able to detect pulsating flow coming from the pumps (see Figure 5.18). This was the case even when very accurate "pulse free" pumps were used such as those found on HPLC systems (dual-headed reciprocating pistons with large amounts of control optimization of the pressure and flow rate). Looking in detail at these measurements we realised that the measurement sensitivity of the sensor could be used to measure pulses of different frequencies. This highlights the fact that the sensor has a good temporal and flow resolution.

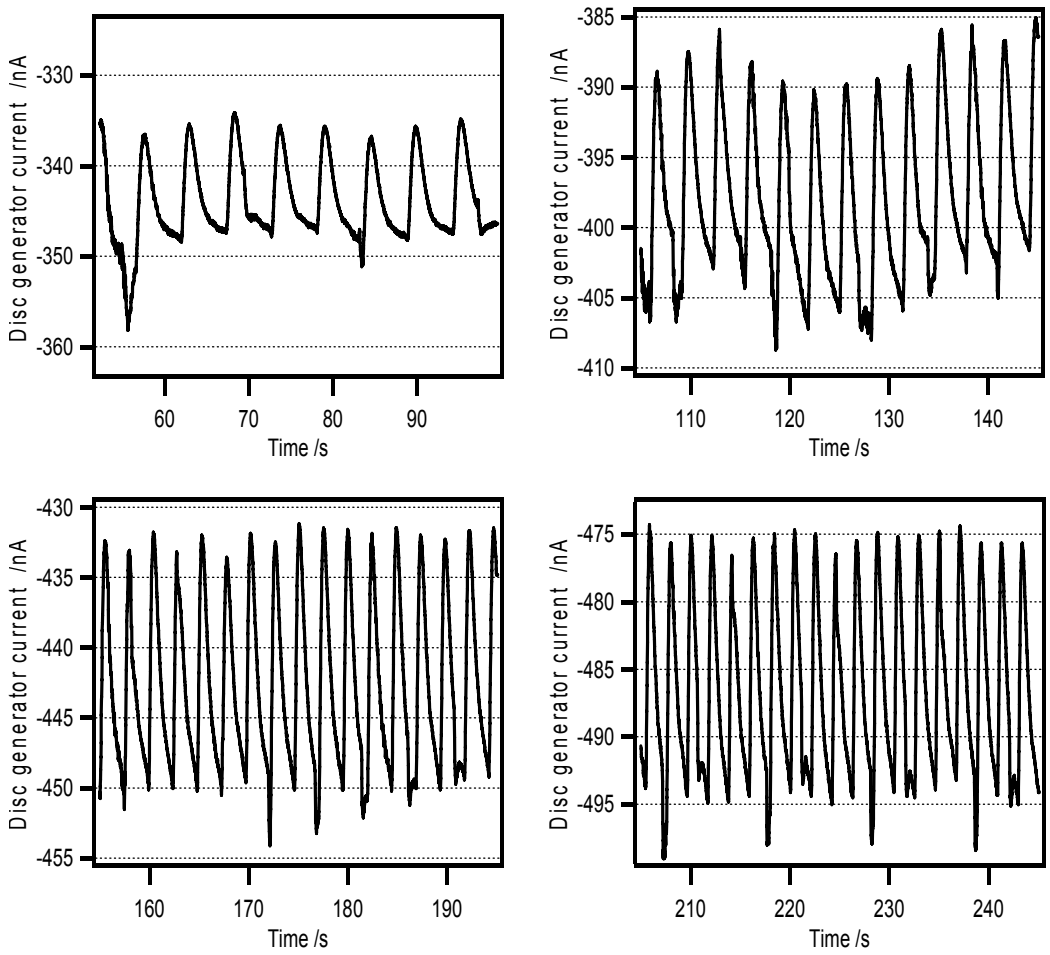

Figure 5.18: Sensors measurements of the pulse produced by the pump. Disc generator currents are shown. The pulse frequency increases with increasing flow rate, only small amplitude changes are seen.

These fortuitous measurements of pulses motivated a more thorough investigation, which was carried out with pumps that have very accurate pulsatile settings specially designed to mimic the activity of the heart. A sensor was placed in one of the branches of a model circulatory system so that the surface of the sensor was perpendicular to the flow. Disc generating ring collecting cases were considered exclusively. The recordings for different pulse frequencies are shown in Fig 5.19. It seems that using the collection efficiency trace to identify the pulse may be too complicated. This is because both the generator and collector currents are affected by the pulse. The collector current "picks up" two components of the pulse. The first is at the

generator, where the generation of hydrogen is subject to the pulse. The second comes from the interval between the generator and the collector, in which time the hydrogen in solution will have been affected by the pulse. The second contribution makes the current response at the collector slightly out of phase with that at the generator. As a result, when the collection efficiency is considered the results appear more complex than when only the generator current is considered. In some ways a single electrode would be more useful for the measurements of pulses than an electrode couple.

Moreover, numerical simulations of the flow above the electrode would have to be considered to obtain a quantitative understanding of the pulse, this was unfortunately beyond the scope of this thesis.

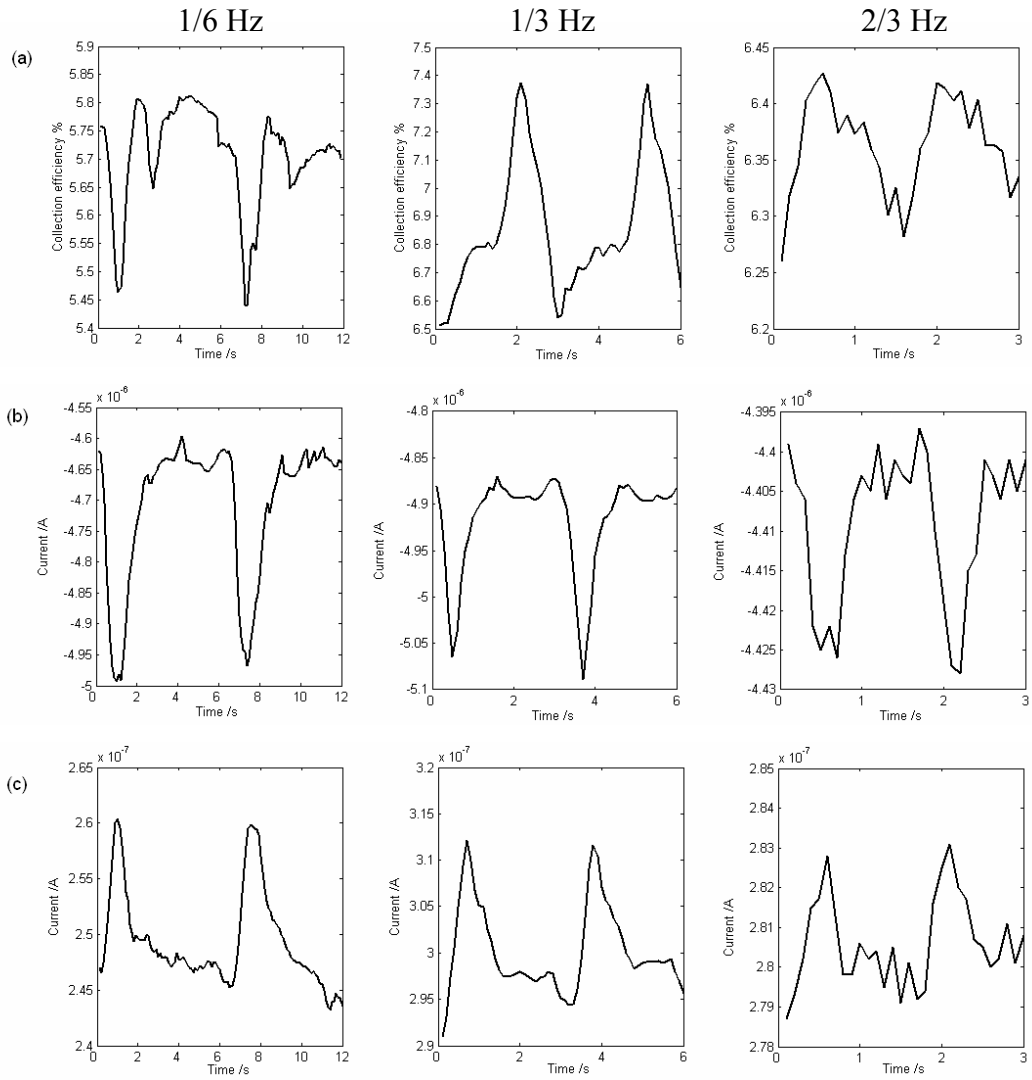

Figure 5.19: (a) Effect of pulse on the collection efficiency for a sensor with a disc diameter of 50 μm. The measurements of three frequencies are shown. In the first column the pulse has a frequency of 1/6 Hz, in the second column the frequency is 1/3 Hz, and 2/3 Hz for the third column. **(b)** Shows the current at the generator (disc) for the three frequencies considered and **(c)** shows the current at collector (ring).

5.5 Flow through tissue mimicking materials; porous media gels and tissue scaffolds.

Flow through tissue is complex and intricate due to the random like arrangement of capillaries, larger vessels, and extracellular tissue. An experimental way of modelling such flows is to consider a porous media with a network of interconnecting pores.

Many porous materials have been developed as biomaterials for application within the human body (i.e. bone grafts, tissue scaffolds, artificial organs etc.)(179,180). These materials are designed to mimic human tissue and as a result their properties (porosity, gas diffusion coefficients, water content etc.) are similar to those of tissue, which make them ideal for carrying out control tests for the sensor.

The measurement of flow through porous medium has been notoriously hard to achieve. MRI (181-183), ultrasound (184), and to an extent laser Doppler (185) and classical electrochemical techniques (159) are currently used to provide overall measurements. Small scale or localized measurements are harder to achieve with such methods because their resolution or penetration is limited. Incidentally, these are the same reasons why these techniques are not well suited to monitor perfusion on the cellular level.

In this section we have investigated the flow measurement capacities of the ring-disc microelectrodes embedded in different tissue mimicking materials. Not knowing how the sensor would perform we investigated a wide range of materials from gels to foams in order to correlate our measurements with key material properties which we believe will be encountered in tissue (i.e. the influence of gas diffusion coefficients, porosity etc.).

5.5.1 Gels

Materials and methods

Two different gels were used in these experiments:

- Gelatin
- Agar

The reason for choosing these gels is that they form structures that are similar to tissue along with the fact that they create dense hydrated media. They have also been used extensively as tissue phantoms in MRI and ultrasound characterisations (159,186,187).

Collagen is the most widely used tissue derived polymer. It is present in almost all mammalian tissues (i.e. skin, bone, cartilage, tendon etc.). Gelatin is derived from collagen. Gelatin gel is formed simply by changing the temperature of the solution containing it. To make the gel 15-30% gelatin powder (Sigma) was dissolved into 1M KCl solutions (mixtures by weight).

Agar gel is a type of marine algal polysaccharide, which forms thermally reversible gels (188). The physical structure of the gel can be controlled by using a range of agarose concentrations, which result in various pore sizes. To make the 1-10 % gel agarose (99.99% Sigma) was dissolved in 1M KCl solutions and heated to simmering temperatures, then left to cool in the fridge (mixtures by weight). The gel forms upon cooling.

Once the gels were formed circular sections were excised and placed in the hole of the flow cell in which the sensor is inserted. The sensor was then placed above the gel and was pushed down so that the lower face of the gel layer was flush with the tube wall. A description of the assembly is shown in Figure 5.20. Initially it had been hoped that the gel could be placed within the tube, so as to have flow through the gel. It was also envisaged that small size tubes could be cast into the gels, again to allow flow through the gel. Unfortunately neither option worked out in practice as the gels decomposed under the direct influence of flow, even at low flow rates.

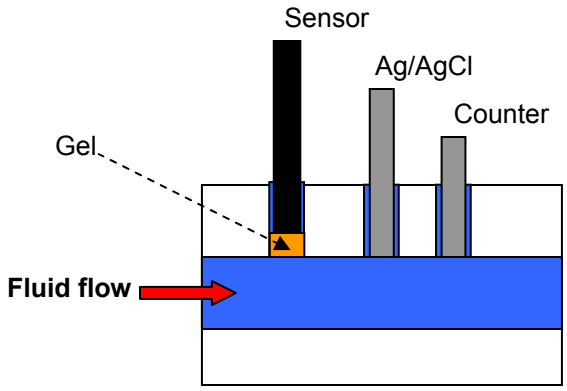

Figure 5.20: Schematic representation of the flow cell with a layer of gel or porous material placed below the sensor.

Results and discussion

Working with the gels in flowing solutions was somewhat tricky as they often dissolved, especially when low concentrations were used. It also soon became clear that the sensor was not capable of detecting changes in flow when a layer of gel was placed beneath it. We tried different thicknesses of gel, 2, 1 and 0.5 mm. However none were thin enough to enable the detection of flow. Thinner films were achieved but they would disintegrate in the flow. A larger electrode (2 mm disc diameter Pt) was then used to assess if it was indeed a probing volume issue. This time the solution flowing through the flow cell was saturated with H_2, the macroelectrode was simply collecting hydrogen from the solution through the gel. In this case H_2 could be detected when the thickness of the gel was below 1.5 mm. This means that the gel layer limited the detection of H_2 to 1-1.5 times the radius of the electrode. with our sensor this would have meant producing a layer of gel that was between 25 and 50 μm thick. Detecting flow beyond the practically achievable gel layer thicknesses is therefore not possible with the sensors used. Larger sensors with larger probing volumes would have to be made but this fall outside the aim of the project. So our investigation of gels as tissue mimicking materials was abandoned.

5.5.2 Porous media and tissue scaffolds

Materials and methods

Three types of porous materials were used in this study

- Polyurethane foams
- Melonin
- Dialysis tubing

Pure polyurethane reactive foams of different concentrations were donated to us by The Regenerative Medicines and Nanotechnologies group at Imperial College (Dr Stevens) see Fig 5.21.

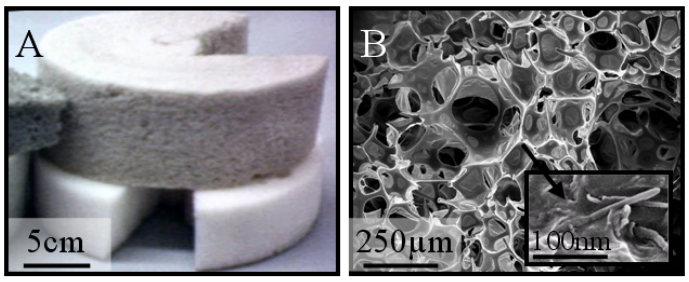

Figure 5.21: (A) Photographic and SEM imaging of direct reactive polyurethane foams. **(B)**. The porous structure is observed more closely using SEM. The imaging reveals that the nanocomposite scaffold had an interconnective porous structure (mean pore size = 151µm ± 3.6 µm)

Melolin consists of a highly absorbent cotton and polyester fibers. Melolin is used in wound dressings to absorb the exudate released by the wound. When wet this material is quite dense as a result of the fibers swelling and obstructing the pores. The use of this material in wound care was the main motivation for working with it.

Dialysis tubing is a type of semi or partially permeable membrane tubing made from regenerated cellulose or cellophane. They are used to monitor the chemistry of the extracellular space in living tissue. They are designed to mimic a “blood capillary” in that they absorb components of the extracellular fluids as a result of concentration gradients

(189). Bundles of tubes all oriented perpendicular to the flow were used in these experiments, they provided a complex matrix of pores and permeable membranes through which solutions could flow.

In these experiments the tissue mimicking material could be placed directly in the flow field without being displaced or damaged. A schematic of the flow cell is shown in Figure 5.22.

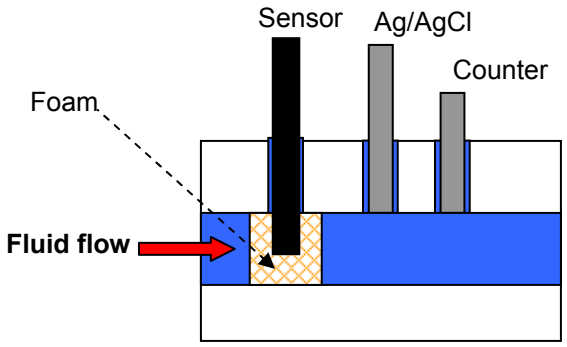

Figure 5.22: Schematic representation of the flow cell with a layer of porous material placed below the sensor.

The sensor was placed a quarter of the way down the tube so it was surrounded from all sides by foam. The sensor is therefore probing the flow within the material. A pump drives the solution through the flow cell which also contains a reference and counter electrode placed in the fluid downstream of the sensor.

Results and discussion

Figure 5.23 show the effect of increasing the flow rate on the collection efficiency for different materials. As the flow increases the CE decreases, however the relative value of the CE for different materials is different. The CE is low in porous materials because most of the H_2 is being washed away and therefore less is being collected. In less porous materials, the H_2 is less mobile and more is being collected which increases the CE. Figure 5.24 further highlights this point by showing the response of the sensor in two polyurethane foams of different porosity. The effect of flow is clear and the different CE level as a result of material porosity is relatively constant for different flow rates.

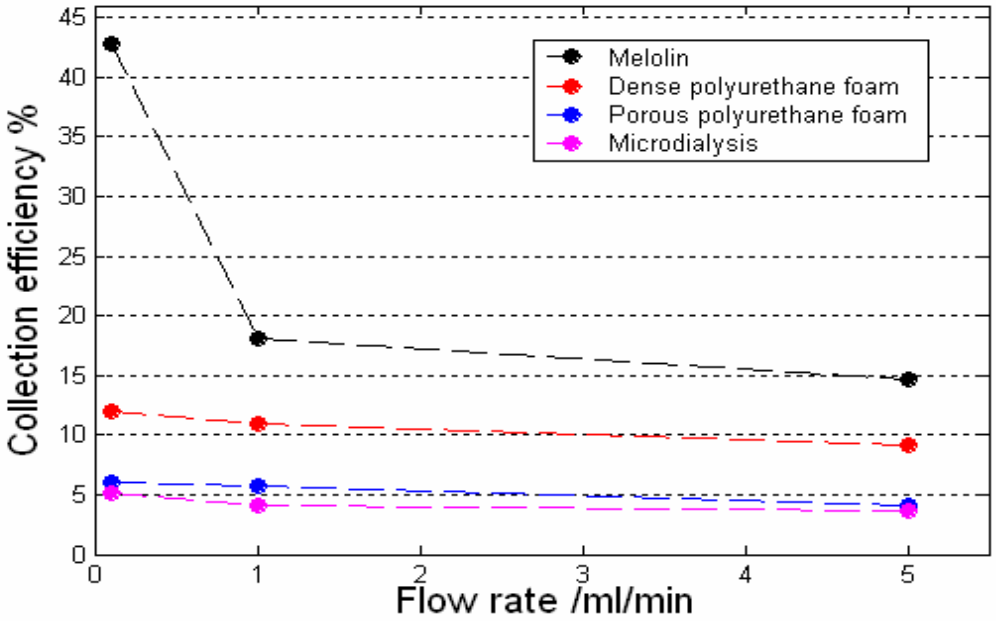

Figure 5.23: Change in collection efficiency with flow for a sensor placed in materials of different porosity. The sensor used is a 50 μm diameter operating is the disc generating mode.

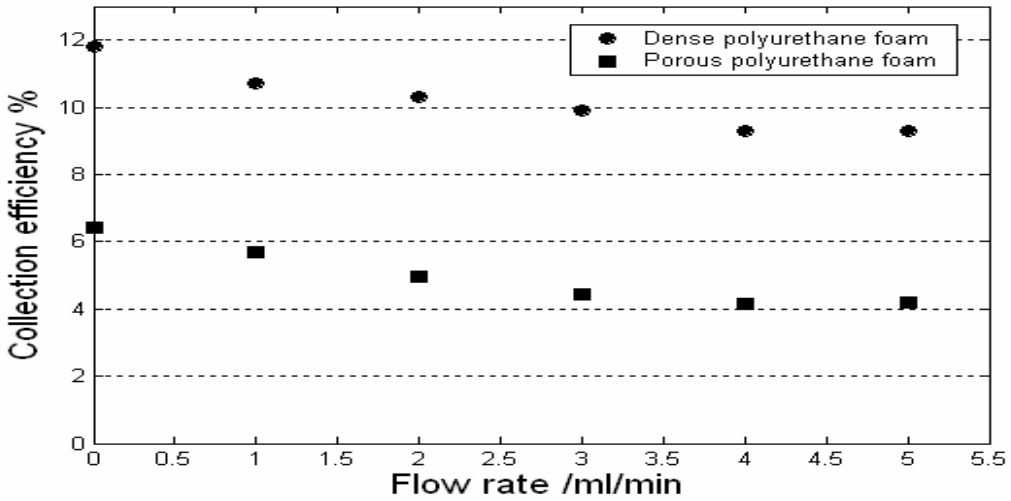

Figure 5.24: Change in collection efficiency with flow for a sensor placed in two polyurethane foams of different porosity. The sensor used is a 50 μm diameter operating is the disc generating mode.

5.5.3 Conclusion

Tissue mimicking materials were used in this section to investigate the response of the sensor in an environment that is close to what we expect to encounter in tissue.

Gels were not suited to this investigation because they were too dense and decomposed under the effects of flow. Larger sensors would have been capable of detecting flow beyond the practically achievable gel thickness, however using larger sensors is not the aim of this thesis.

Flow measurements in foams and porous media were achieved. A large range of flow rates were measured in different porous materials. From these measurements we find that the collection efficiency is low in porous materials whilst in less denser materials the collection efficiency is higher.

This investigation presents the potential of the sensor in monitoring flow in complex structures something which is currently beyond the reach of more classical techniques such as MRI and ultrasound.

5.6 The hydrogen wash in / out technique

The hydrogen wash in/out technique is a well established tissue perfusion measurement technique also referred to as the hydrogen clearance technique. It was first established in 1964 by Aucland et al (190) although earlier work by Kety and Schmidt in 1945 had pioneered the idea of introducing an inert gas (i.e. nitrous oxide) into the brain to monitor blood flow (36). Since then the hydrogen wash in/out technique has been used extensively and has significantly contributed to our understanding of microscopic blood flow. Young has written a good review of the technique and its numerous applications (191). This technique has mostly been used on animal models but can be used in humans if properly setup.

The basic concept of the technique is to polarographically monitor the arrival and departure of a bolus of hydrogen through tissue. To do this, a platinum electrode is placed in the tissue of interest. Hydrogen is then introduced into the breathing air of the animal or dissolved H_2 is injected intravenously. The potential of the electrode is set sufficiently positive to oxidise all the H_2 that comes into contact with its surface (i.e. 0.2 vs Ag/AgCl). As the H_2 arrives in the tissue, the electrode current will rise; this is the wash

in curve. When the current at the electrode reaches a steady state the hydrogen supply is turned off and the current drops; this is the wash out curve.

Because of the similarity of this well established technique with the one we have developed, we are able to use the same sensor to preform both our measurements and the H_2 clearance measurement. Only the disc electrode is used for the hydrogen wash in method. As the sensor is not changed, one measurement can be made after the other, thus the location of the measurement is the same and the comparison is very accurate.

5.6.1 Materials and methods

The experimental setup is the same as in the previous section, the electrode arrangement in the flow cell is shown in Figure 5.22 The only notable addition to the experimental protocol is the preparation of H_2 saturated solutions. Initially this was done electrochemically by passing a substantial current through a large Pt mesh working electrode to an equally large Pt counter electrode. This was done in a cell with two barrels separated by a frit, which was used to limit the mixing of the solutions and the gases. In practice however this did not work well and mixing of the solutions took place. In addition due to the high currents used and the KCl present in solution chlorine gas was being produced at the anode.

Better results were achieved by bubbling H_2 gas through KCl solutions using a gas collection jar. Different bubbling times were investigated, 30 min being the most effective. Despite thorough sealing of the collection jar, the concentration of H_2 in solution was variable and the solutions had to be used soon after the bubbling.

5.6.2 Results and discussion

H_2 wash in/out technique is characterised by a wash in period followed by a wash out period. In the wash in section the current rises sharply then plateaus as a result of H_2 arriving then saturating the tissue in which the electrode is placed. During the wash out section the current drops back to zero because the supply of H_2 has been shut. Figure 5.25 shows a typical hydrogen wash in and the subsequent wash out curve for the arrival and departure of hydrogen from a tissue mimicking material. Two flow rates were investigated: 5 and 1 ml/min (see label on the graph). One can see the influence of flow

rate on the amplitude of the current as well as its influence on the steepness of the wash in and wash out curves. With increasing flow rate the current amplitude increases, which indicates that more H_2 is reaching the electrode. The shape of the wash in and wash out curve also helps to describe the effect of flow rate. A slower wash in and wash out is characteristic of slow flow rates whist a faster one is characteristic of high flow rates. We have to note however that the curve shown in Figure 5.25 never reaches a steady state. We find that the current rises then drops rather than reaching a plateau, we believe this is due to the H_2 diffusing out of the solution.

Quantifying the level of flow from these curves is possible and can be done in a number of theoretical ways (39). Greenbaum provides one of the most experimentally relevant methods (192). It relies on the method of moments to quantitatively describe the wash in curve and does not require a steady state to be achieved. This decreases the time needed for each experiment but also it makes possible measurements of perfusion in very ischemic tissue where achieving a steady state H_2 current is notoriously difficult.

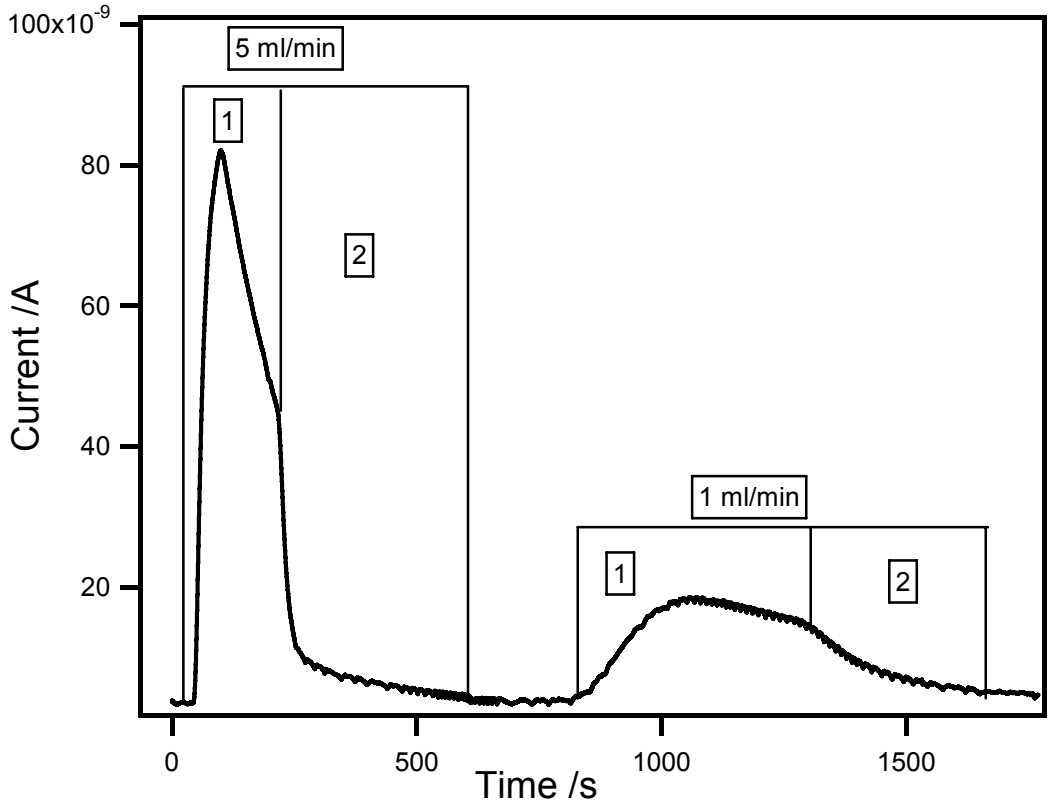

Figure 5.25: Typical hydrogen wash in/out curve for a Pt electrode placed in a polyurethane foam. The peak on the left is for a flow rate of 5 ml/min, whilst the peak on the right is for a flow rate of 1ml/min. Each peak can be broken down into two parts **(1)** the wash in period during which the H_2 is introduced into the system, this section of the curve is characterised by a rise then a steady state current plateau. **(2)** The supply of hydrogen is turned off and the wash out curve is observed, during which the H_2 is removed from the vicinity of the sensor. The sensor used had a disc diameter of 50 μm.

In Figure 5.26 the influence of material porosity on the H_2 wash in measurement is investigated with two polyurethane foams of different densities. As with our sensor we expect this method to be able to distinguish between materials of different porosity because the porosity of the material would influence the mass transport within it. This is the case, for a porous material the amplitude of the wash in curve is high and the rise is steep. Whereas for a less porous material the maximum current reached is lower and the rate of wash in and wash out is much slower. This technique is therefore also capable of detecting differences in material porosity. The tissue analogy of a porous material is one

where many blood vessels are carrying blood and the transport of nutrients and metabolites is fast. A less porous material would represent a tissue where blood flow is impaired.

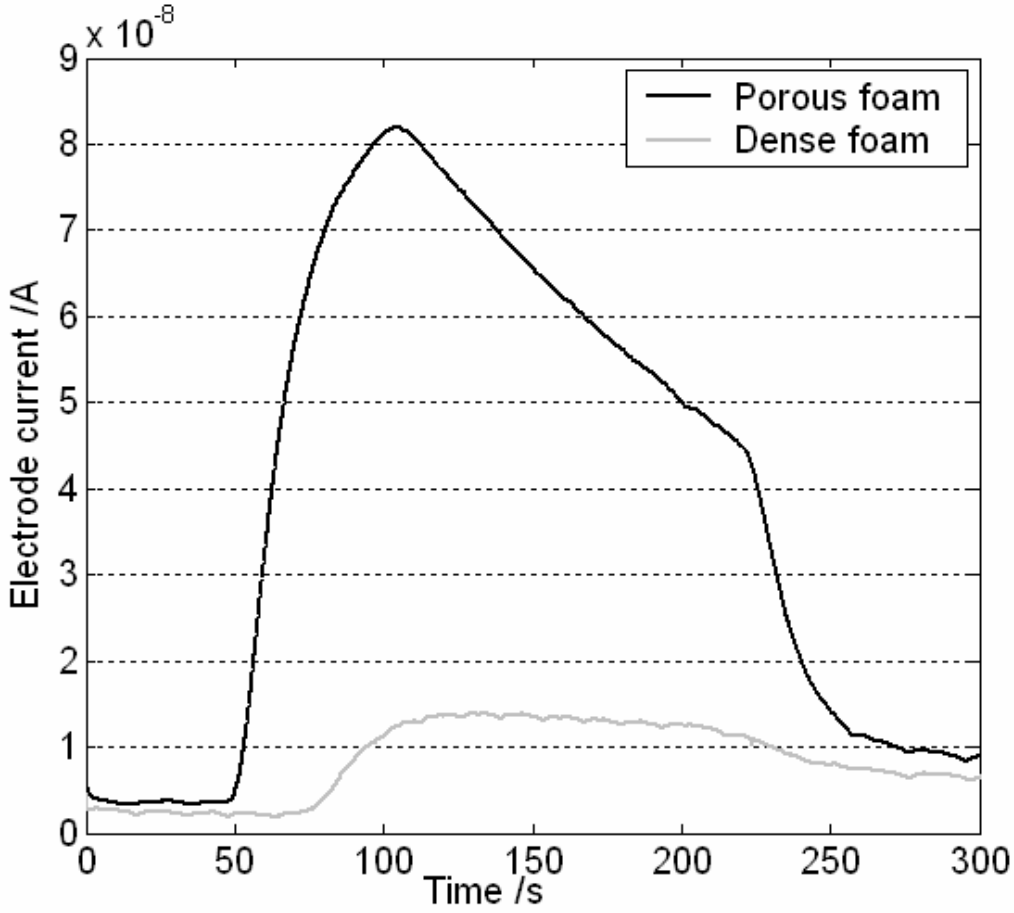

Figure 5.26: Hydrogen wash in/out curves for two foams of different density. The flow rate was 5ml/min and the sensor used had a disc diameter of 50 μm.

It must be said, however, that the hydrogen wash in/out technique has some notable disadvantages when compared to the method we have developed. These are:

- Temporal resolution
- Introducing hydrogen into the system.
- Quantifying the measurements

The poor temporal resolution of the hydrogen wash in/out technique is its main drawback. Figure 5.25 shows this very clearly, one can see it takes 1500 s for two measurements to be made, this sort of time scale is well beyond the biological response timeframe and as a result key events are not seen when this technique is used to monitor perfusion.

The delivery of hydrogen into the tissue is another problem. Firstly because of the risks associated with handling large quantities of the gas. Secondly the arrival of blood is impaired in poorly perfused tissue and as a result the arrival of hydrogen will also be impaired. Reaching a steady state current value is also affected by the delivery of hydrogen as seen in both Figure 5.25 and 5.26. In some cases measurements are not possible because H_2 never makes it to the electrode. It is precisely in these tissues that measurements of perfusion would be most informative.

Quantifying the measurements made in terms of blood flow is somewhat contentious using the hydrogen wash in/out technique. The approximations used to estimate blood flow from the wash out curves are not always true. Namely the assumption that arterial H_2 concentration is zero and that the wash out is exponential when it is often polyexponential. As a result misleading data are sometimes reported (192).

5.7 Conclusion

Characterisation of the ring-disc microelectrode under controlled convective mass transport have been carried out in this chapter. A number of different flows were investigated, namely: impinging jet flow, pipe flow, pulsatile flow and flow through porous media.

In all flow regimes the collection efficiency of the sensor is seen to decrease as the flow rate increases. This is because less of the generated species is able to reach the collector since it is being washed away.

The dimensions of a sensor will influence its response to flow. Each sensor has a dynamic range beyond which changes in flow are indiscernible. By carefully choosing the dimensions of a sensor, it is possible to maximise a detection range of the sensor. In addition by using the ring or the disc as generator, it is also possible to study different aspects of the flow regime. This makes efficient use of the intrinsic differences in shape between the two electrodes that make up the sensor.

The response of the sensor to changes in flow is rapid, on average the steady state is reached 20 seconds after the flow rate has been changed. The effects of current density on the measurements were also investigated. We found no significant change in the response to flow or detection range for different electrode fluxes. However the collection efficiency reaches higher levels when in the diffusion limiting case than in the rate limiting case.

The response of the sensor to porous materials, a model for tissue, is good. Materials of different porosity can be differentiated by the sensor in the form of changes in the collection efficiency.

Finally we attempted to compare some of the measurements made with the ring-disc microelectrode with another perfusion measurement technique; the hydrogen wash in/out technique. We found that this technique is able to perform similar flow measurements to the ones made with our sensor. However some significant limitations exist with the method (poor temporal resolution and safety). Such limitations are not encountered with the ring-disc microelectrode and therefore help to emphasise its potential.

6

Mass transport measurements in vitro

The work described in this chapter pertains to the use of the sensor *in vitro*. In the first part the work done to prepare the sensor for use *in vitro* is describe. The tissue response to the sensor as well as the response of the sensor to the tissue is considered. In the second part we present measurements made in rat, rabbit and human tissue as well as a short study of tissue perfusion using the perfused rabbit ear model. These measurements are used as a proof of principle of the sensor and the tissue perfusion measurement technique developed throughout this thesis.

6.1 Preparing the sensor for use *in vitro*

6.1.1 Biocompatibility and fouling

The tissue perfusion sensor developed is an invasive sensor, in that it has to be inserted into the tissue of interest to perform the measurements. This has a number of consequences, one has to consider the effect the sensor has on the tissue as well as the effect the tissue has on the sensor. We start by considering the influence the sensor may have on the tissue.

When an object is inserted into tissue it will have to displace or slice through cells, blood vessels and connective tissue (see Fig 6.1). This can result in damage to the tissue, which in turn can lead to a forced or unnatural cellular response (193). The measurements made following this are stimulated and are not representative of physiological circumstances. In practice after a sensor is introduced into tissue it is left to sit before any measurements are made, this is referred to as equilibrating the tissue to the sensor (194). If the sensor is too large, the tissue surrounding it may never behave normally. Research in this field has focused on the damage caused by stab wounds (195) or needles wounds (196,197). More recently, the effects of placing electrodes or microdialisis tubing into tissue have been studied and were shown to cause oedema and disruption to the microcirculation (198-200). The work of Adrian Michael provides a good overview of the subject and further highlights how inserting a sensor into tissue can lead to erroneous measurements (201). For our application, there are two key findings in this body of research. The first is that if the object is smaller than 200 μm then the damage to tissue is restricted to the cells directly adjacent to the sensor. The other important finding is that if the object has a sharp tip, the damage is far greater than if it has a rounded tip.

The sensors we have produced have diameters well below 200 μm, thus alone they should cause limited damage when inserted into tissue. However, manipulating a sensor of the order of 25 μm is not an easy task and as a result the sensors have to be encased in a stronger and unfortunately larger housing. Usually electrochemical probes of this size are encased in glass capillaries, with the wire either left protruding from the glass tip or polished flat. However, for the versatile applications for which the sensor is currently being used, this arrangement would not be rugged enough. We have found that

the most suitable housing for the sensor is a hypodermic needle, which is familiar to medical personnel and patients. The manufacturing process described in Chapter 2 remains the same only the sensor wire has to be insulated to prevent it from being short circuited by contact with the needle. Figure 6.2 shows a sensor encapsulated into a hypodermic needle. The use of needle sensors will cause damage to the tissue. However if the needle has a rounded tip and is inserted delicately the damage can be minimised as highlighted in Fig 6.1.

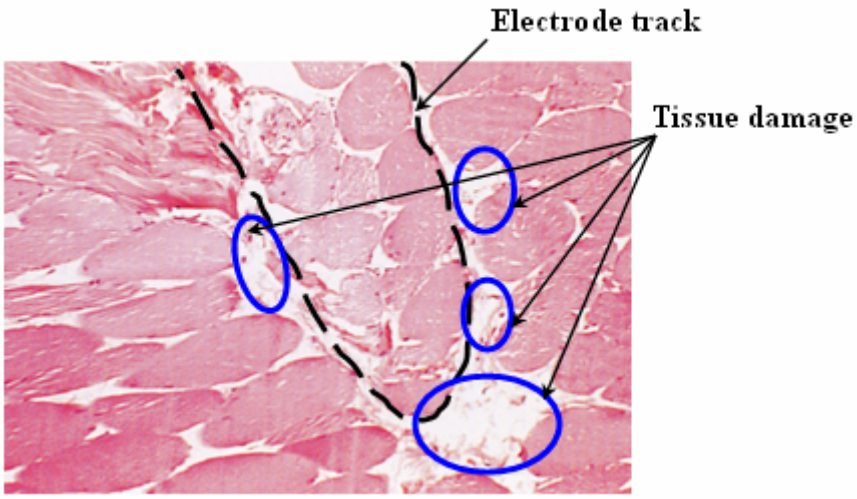

Figure 6.1: A transverse section of tibialis anterior muscle stained with haematoxylin and eosin at 100 magnification. The track of the electrode in the centre of the field is surrounded by minimal cell damage. There is slight distortion and extravasation of blood cells around the electrode (192). The electrode was placed in a 23 gauge needle.

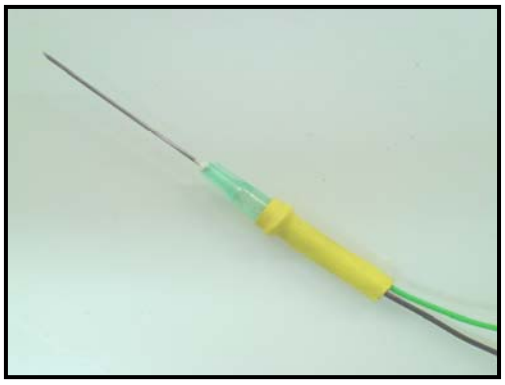

Figure 6.2: Sensor encased in a hypodermic needle.

We now consider how the tissue may damage the sensor. When inserted into tissue the sensor will face two types of cellular response; biocompatibility and fouling. Both have negative consequences on the measurements and should be addressed. The subject of sensor interactions with tissue has been well reviewed by Frost and Meyerhoff (202) as well as Wilson and Gifford (203).

Biocompatibility refers to the defence mechanism our body has developed to protect itself from foreign bodies. When a foreign object enters the body it is rapidly surrounded by albumin and fibrinogen (204). These will form a small semi permeable barrier but also signal the presence of the foreign object. Immunogenic cells will then gather around the object to try and break it down chemically. If this does not succeed, they signal for a collagen encapsulation to take place. This has the effect of chemically and physically isolating the object from the surrounding cells. Eventually blood vessels will form around the encapsulation to maintaining the encapsulation indefinitely (see Fig 6.3). For our measurements, such an outcome would limit our perfusion measurement capabilities because the volume probed would encompass the fibrous encapsulation (i.e. fibrous layer are typically 20 µm thick after 3 weeks (205)).

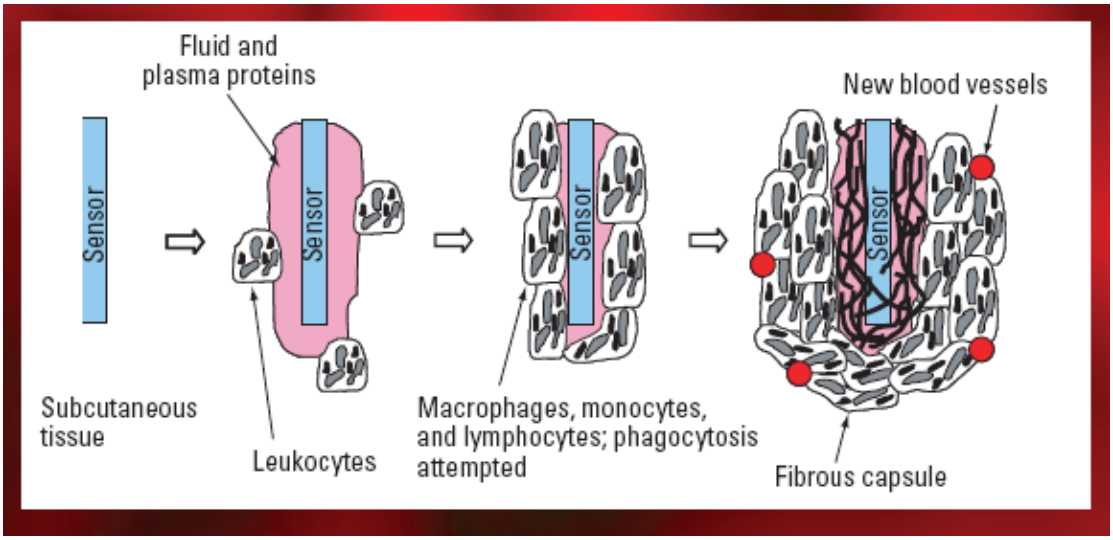

Figure 6.3: Steps that lead to the encapsulation of a sensor as a result of the response of the tissue to foreign objects. Leukocytes appear on the sensor within hours and are soon followed by phagocytosis events, fibrous encapsulation and new blood vessels appear within a week. Taken from ref (202)

Fouling is a phenomenon that is particular to electrochemical sensors as it relates to the blocking of the electrode surface by protein and lipids or their absorption onto the surface (206-208). The main effect of fouling is to reduce signal strength. The factors that influence fouling are electrode material, electrode geometry, applied electric field and the surrounding environment (209). Despite extensive studies of the subject not all the aspects of fouling are understood (202,203,210). What is clear, though, is that eventually a sensor will foul, it is important therefore to be able to delay this inevitability.

Biocompatibility and fouling may have up to three effects on the response of the sensor (i) altering the diffusion coefficient of species reacting at the surface, (ii) influence the conductivity of the electrode and (iii) change the electrocatalysis properties of the sensor.

To investigate these effects the sensors were subjected to albumin (bovine serum) as a surrogate for tissue. Methods of protecting the sensor from the biological environment were also investigated.

The fouling of the electrode surface by albumin

Electrode surface chemistry is recognised to play a central role in fouling. Throughout this thesis we have systematically acid cleaned our electrodes by potential cycling from 1.5 to -1.5 V in 0.5M H_2SO_4 for 15 min, followed by 15 min at -1.5 V. The end result of this process is to leave the electrode surface clean (211).

To investigate the effect of the cleaning process and the protection it could provide against fouling, sensors were scanned in 1M PBS solution with 4% albumin. This involved cyclic voltammograms for 1 hour between the generation and collection potentials of hydrogen (i.e. -1.5 and 0.3 V). Albumin is the main protein of blood plasma and provides a suitable alternative to blood for testing the fouling of sensors. The cyclic voltammograms for a 125 μm disc in albumin solution is shown in Figure 6.4a. where the current level is seen to drops with time. There are three reasons that could explain the drop in current:

- A shift in the reference electrode
- Impaired mass transport
- Slowing down of the surface kinetics

Since we do not drive the H_2 reaction to mass transport limiting levels, we cannot tell from the data in Fig 6.4a which is the source of the shift.

To investigate the causes of the drop in current seen in Fig 6.4a, we ran cyclic voltammograms with the sensor in albumin solution which contained either 10 mM $Ru(NH_3)_6^{3+/2+}$ or 10 mM $Fe(CN)_6^{4-/3-}$. If the drop in current is due to the shifting of the reference electrode, then a shift in E_0 should be seen. If it is a mass transport issue, then the limiting current of both species should drop. If it is a kinetic issue, then the peak separation should change. The results are shown in Figure 6.4.b for $Fe(CN)_6^{4-/3-}$ and 6.4.c for $Ru(NH_3)_6^{3+/2+}$.

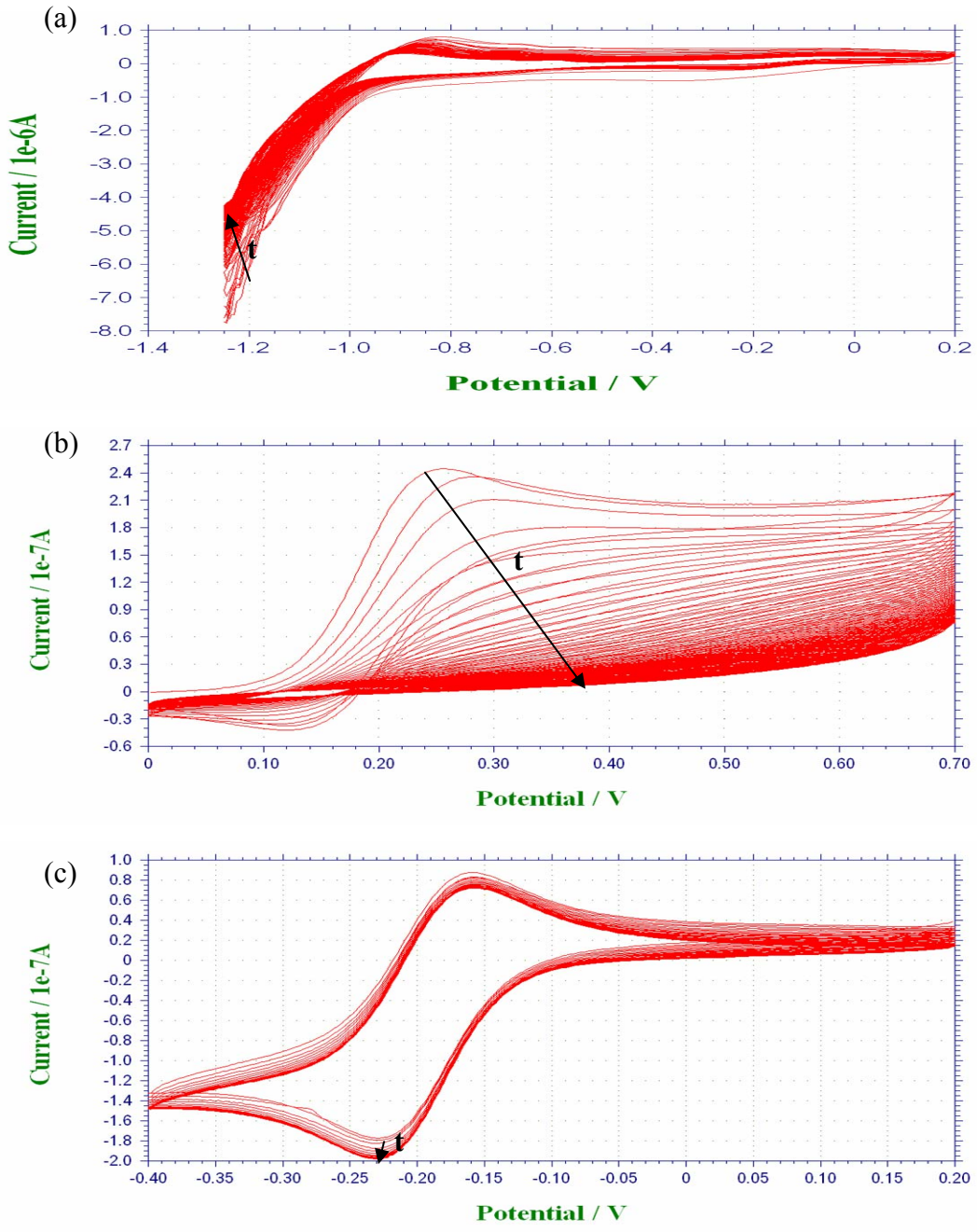

Figure 6.4: Repeated cyclic voltammograms in solutions containing 4 % albumin in 1 M PBS. Scan rate was 0.05 V/s and the sensor had a disc diameter of 125 µm. **(a)** Hydrogen is being generated. For plots **(b)** the solution also contains 10 mM $Fe(CN)_6^{4-/3-}$, **(c)** the solution contains 10 mM $Ru(NH_3)_6^{3+/2+}$. Black arrow shows the shift in the peak current with successive cyclic voltammograms.

From Fig 6.4 one can deduce that the decrease in current observed is not due to the voltage at the reference electrode drifting to more positive value. This is established by monitoring the formal redox potential which does not change significantly when either $Ru(NH_3)_6^{3+/2+}$ or $Fe(CN)_6^{4-/3+}$ is used. Scans in $Fe(CN)_6^{4-/3-}$ show a clear decrease in current Fig 6.4 b. With successive CVs, the peak to peak separation is increasing and therefore the kinetics of the reaction are becoming more sluggish. When $Ru(NH_3)_6^{3+/2+}$ is used as the redox couple, the diffusion limiting current increases slightly and the peak separation does not change. Mass transport can therefore be rule out as the cause for the decrease in the current at the electrodes. The cause therefore appears to be kinetic. From the work of Guo et al. it is know that albumin binds irreversibly to Pt to form a uniform monolayer (212). They also suggest that the absorption of albumin is enhanced by positive potentials. Our investigation would tend to suggest that the redox species and its binding site on platinum are also important considerations. This helps explain why fouling is observed when generating H_2 but not when using $Ru(NH_3)_6^{3+/2+}$.

Further investigation into the effects of albumin on the sensor is presented in Figure 6.5 In this experiment, cyclic voltammograms were performed on the electrode for 12 hours in a solution containing 4 % albumin with 10 mM $Ru(NH_3)_6^{3+/2+}$ in 1M KCl. Monitoring the current at the start, middle and end of the cycling shows that initially the current drops but eventually stabilises. This is the case for both $Ru(NH_3)_6^{3+/2+}$ and H_2 generation currents. It seems that the initial two hours of the immersion in albumin are most detrimental to the current response. However beyond this the electrode current is stable for hours (tested up to 16 hours). With this in mind it is possible to design an experiment in such a way that the sensor can be acclimatised to the tissue environment before any measurements are made, thus limiting the effects of fouling.

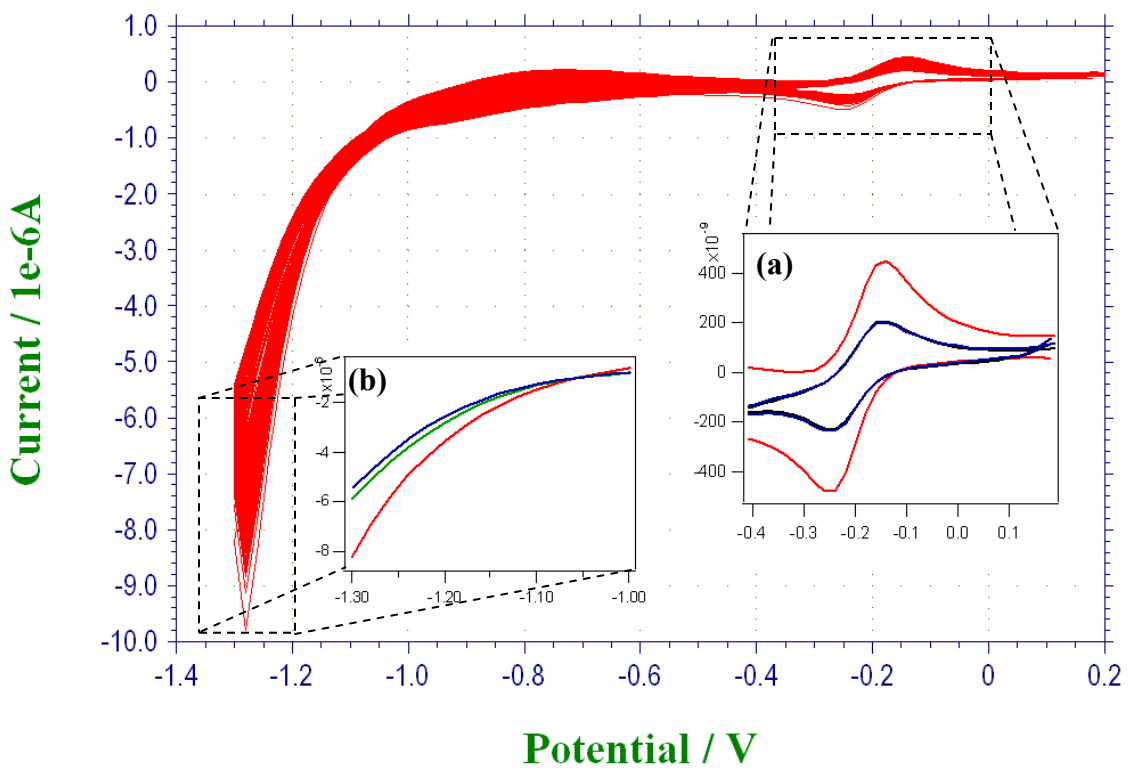

Figure 6.5: Effect of albumin on the current voltage response of a 50 µm disc electrode cycled for 12 hours at a scan rate of 0.1 V/s. The solution consisted of 10 mM $Ru(NH_3)_6^{3+/2+}$ in 1M KCl with 4 % albumin. **(a)** Close up of the $Ru(NH_3)_6^{3+/2+}$ current voltage response at different times, red trace is the first scan, green trace is after 6 hours and blue trace is after 12 hours (blue and green trace overlap). **(b)** Close up of the hydrogen generation current with time.

The results presented above provide a simple way of dealing with albumin. However when placed in living tissue or in contact with blood for significant length of time (i.e. hours) the sensor will be faced with a multitude of other foreign body responses. These have been shown to significantly deteriorate electrode current responses, it is therefore most likely that the sensor will have to be actively protected. There are many methods used to overcome electrode biocompatibility and fouling issue, namely surface modification, local drug delivery or membrane coating. In our case the most suitable method is to coat the sensor with a semi-permeable membrane. These have been shown to prevent protein absorption and favour positive cellular responses (i.e. cell growth), whilst allowing smaller molecules (i.e. H_2) to reach the electrode surface. As

well as improving the selectivity of analytes, membranes can also be engineered to improve biocompatibility. To this effect four coating materials were studied:

- Polyvinyl-chloride
- Nafion
- Poly(sodium 4-styrenesulfonate) poly-L-lysine
- Poly-ethylene-glycol

These coating material were selected because of their reported success in dealing with fouling (213-228). The outcome of this investigation is not presented in this thesis because the results drawn were conflicting and difficult to interpret. It was found that adding a membrane to the electrode resulted in a drop in current and a drop in collection efficiency. When the coated sensors were subjected to albumin the current and collection efficiency increased. The increase in current and CE when subject to albumin is hard to interpret as it suggests that the mass transport of the species involved in the reactions has improved as a result of the albumin. Membrane thickness and geometry was also hard to quantify and therefore reproduce. Unfortunately not enough experiments were carried out to assess the reproducibility of these measurement, and draw adequate conclusions.

For the initial application of the sensor, membrane coatings would be useful but not crucial. It has been shown that the sensor can cope with the presence of proteins for hours as long as the sensor is "acclimatised". The biocompatibility and fouling mechanism present in tissue is strongly dependent on the foreign body response, this however only occurs in intact organisms. The initial applications of the sensor are in excised tissue and organs through which buffer not blood is being pumped. As a result it is likely measurements with the sensor will be possible for hours before the current responses begin to decrease significantly.

Potentiostats and galvanostat

As well as considering how the sensor should be packaged and protected from the tissue, the potentiostats and galvanostat needed for the measurement should also be suitable for use in medical application. The biggest risk is passing a high current through the patient. Thankfully the low currents involved in electrochemical measurements mean this is not really a consideration, nevertheless to stay on the safe side the potentiostats and

galvanostat are designed with a floating ground, which can be connected to an insulated trolleys. The instruments is connected to a laptop PC via an analogue to digital converter. The manufacturing of the potentiostats and galvanostat was done by GBE designs Ltd.(UK) according to our specifications (see Fig 6.6).

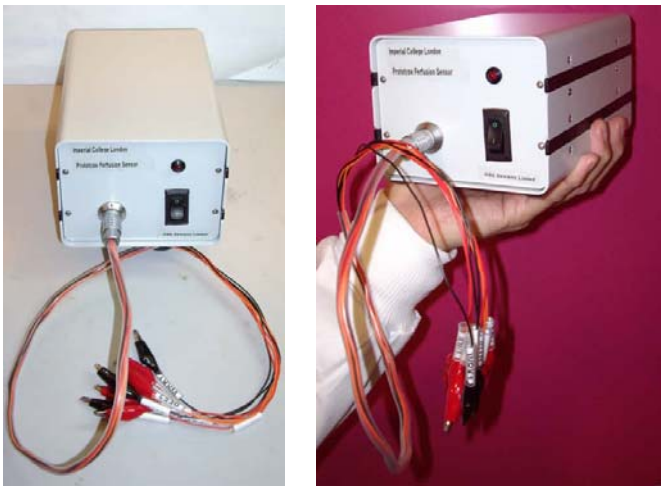

Figure 6.6: Picture of the first prototype of the two potentiostats and galvanostat.

Hydrogen reaction

The sensor relies on the electro-generation and collection of hydrogen gas to operate. The mechanisms involved in this process were described in Chapter 1. In this section we revisit these with particular focus on the consequences of inducing such reactions in tissue.

Variations in water concentrations around the sensor would influence the generation of hydrogen; low concentrations being most problematic as they result in low signal levels. Fortunately, despite changes in water concentrations in tissue the levels never drop below molar concentrations. At such concentrations, generating hydrogen is not limited by water concentration but more commonly by bubble formation. We can be confident that water concentration is not a concern. With regards bubble formation, the hydrogen generation is limited to levels that fall below the onset of bubbles. Bubbles are clearly noticeable on cyclic voltammograms traces as high amplitude current fluctuations. Usually this occurs beyond -1.5 V on the disc and a bit earlier on the ring.

An important consideration with regards to the reactions occurring at the electrodes is to assess how they may change the pH of the tissue. This happens because

of the production of OH^- molecules at the generator. Of course the collector reverses this reaction but does not collect all the product, thus there is a net increase in OH^- around the sensor, which will increase the pH. At the generator's counter electrode oxidation reactions are taking place, their exact nature cannot be accurately described but the most likely products are oxygen, chlorine and protons. If the two electrodes are close together the production of H^+ ions at the counter should balance the OH^- products from the generator. Placing the working and counter electrodes in close proximity may not always be feasible however.

Equally as important to consider is the pH levels in tissue and the effect this may have on the generation. At low pH the excess presence of H^+ ions means H_2 can be formed without splitting water. At high pH, water has to be split. The governing reactions at low pH are:

$$2H^+ + 2e^- \rightleftharpoons H_2$$

Or

$$2\ H_3O^+ + 2e^- \rightleftharpoons H_2 + 2H_2O$$

whilst in neutral and basic solutions the following reaction prevails:

$$2H_2O + 2\ e^- \rightleftharpoons H_2 + 2OH^-$$

The normal physiological pH value in tissue is 7.4, in ischemic situations tissue pH can drop (pH 6). The drop in pH is mainly caused by carbon dioxide build up, which is metabolised as carbonic acid. It is likely that our sensor will be used in tissue that is ischemic as well as in healthy tissue. Changes in pH are therefore likely to occur in the vicinity of our sensor. The effect of changing the pH near the sensor was investigated by measuring the collection efficiency in solutions of different pH. Figure 6.7 shows how the collection efficiency changes when pH changes. The potential applied to the electrode was constant -1.1 V. As the pH goes from 5 to 8 the collection efficiency drops by 5%. The transition from one reaction to the other is clearly seen. We believe the change in collection efficiency is due to the difference in diffusion coefficient of water and

hydrogen ion. Changes in pH in tissue occur more slowly than changes in blood flow, thus it may be possible to overlook the effects of a change in pH which would appear as a shift in the baseline CE value. Also large changes in pH occur only in extreme cases of tissue trauma. Still, this issue is worth bearing in mind.

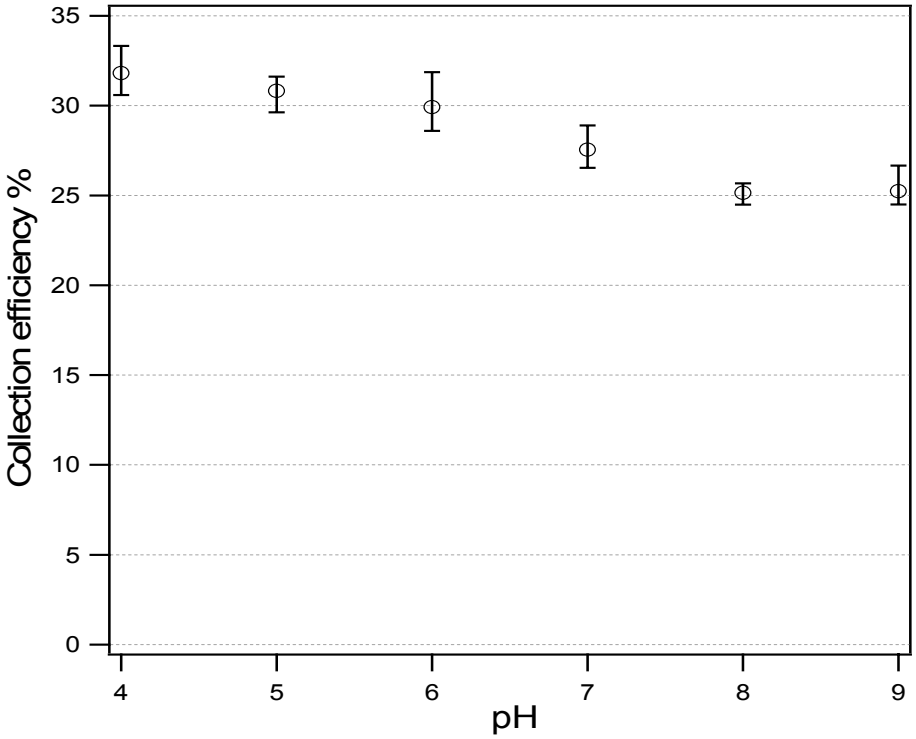

Figure 6.7: Change in collection efficiency with solution pH for a fixed applied potential of -1.1 V. Sensor used has a disc diameter of 125 μm. The trace shows averages and range n=3.

6.1.2 Conclusion

The work done to prepare the sensor for use *in vitro* has been presented. This has involved investigating the effects the sensor will have on the tissue and the effects the tissue will have on the sensor, the so called fouling and biocompatibility issues.

When the sensor is left in an environment containing albumin it will eventually succumb to fouling. However, after being subject to albumin for two hours the drop in current is limited and remains stable for up to sixteen hours.

We have also shown how the sensor and instrumentation are packaged in order to limit the influence of the measurement on the tissue and patient.

6.2 *In vitro* experiments

The following sections describe the application of the ring-disc microelectrode in biological tissue for monitoring tissue perfusion. These experiments showed that the sensor is capable of measuring cellular level perfusion in a continuous fashion. The experiments also highlighted some of the unique features of the sensor discussed throughout this thesis.

Two types of experiments are presented; the first shows the sensor response to different types of tissue, the second shows the sensor being used to monitor perfusion in perfused rabbit ears.

Krebs buffer

All experiments with tissue used Krebs buffer to maintain the tissue and cells alive. To make a litre of Krebs buffer the following chemicals were combined into a volumetric flask:

6.84 g NaCl

0.35 g KCl

0.3675 g $CaCl_2.2H_2O$

0.144 g $MgCl_2$

0.166 g NaH_2PO4H_2O

2 g Sodium carbonate

2 g Glucose

The solution made was then continuously bubbled with 95 % O_2 and 5 % CO_2.

6.2.1 Rat, rabbit and human tissue

In this section we present the measurements of mass transport made with the sensor in different tissue types. Rat, rabbit and human tissue were tested and showed good response. In these experiments no convection is present; instead the sensor is

measuring diffusion of H_2 through the tissue. These experiments serve two purposes; first they prove the sensor can work in different tissues and secondly they provide measurements of collection efficiency in a large variety of tissues. The level of collection efficiency measured in these unperfused tissues is the maximum value expected for that particular tissue. Once convection is present in the tissue, the measured CE will be lower. A database of CE values is thus being compiled, it will serve as guidance for subsequent experiments where the tissue is perfused.

Rat and rabbit tissue

The rat and rabbit tissue were acquired from Imperial College animal house, the organs and tissue samples required were delivered in oxygenated Krebs buffer. In general the organs (liver, lung, heart and kidney) were cut into sections and the tissue samples (fat, muscle, connective, epithelial etc.) were placed in a large Petri dish containing Krebs buffer which was continuously bubbled with 95% O_2 and 5% CO_2. The buffer covered ¾ of the samples. Needle sensors were used in these experiments along with an Ag/AgCl wire reference electrode (separated from the solution by an agar seal) and a stainless steel needle counter electrode. All the electrodes could thus be inserted into the tissue. It was found that the reference electrode needed to be quite close to the working electrode (within 1 cm) to limit resistance artefacts.

Potential steps were used to measure collection efficiencies in the different tissues. In these experiments only disc generating cases were considered, the ring collector potential was always at 0.2 V. The generator potential followed a sequence of 50 s at 0.2 V then 50 s at -1.5 V, this sequence was repeated for 3-5 cycles. So for 50 s no H_2 was generated followed by 50 s when it was.

The collection efficiency for a sensor placed in rabbits heart muscle and fat is shown in Figure 6.8 (a). The current response at the collector is shown in (b) and that of both collector and generator are seen in (c). In different tissues the collection efficiency response is different although the final or steady state level is similar. Measurements in the buffer reach a steady state fastest followed by, the heart muscle tissues and then the fat. The time needed to reach steady state is dependent on the diffusion of H_2, slower diffusion coefficients will lead to a slower CE steady state response. The current

responses shown in Fig 6.8(b) and (c) also provide some useful information about the environment in which the sensor is placed. In the buffer the level of current at the generator and collector are highest. They are lower in the muscle tissues and are at their lowest in the fat. This current level is directly related to the water concentration in the tissue and contributes further to our understanding of the tissue environment. These results also correlate with the model prediction discussed in Section 3.2.2.

Experiments in rat tissue exhibited comparable and reproducible results in terms of collection efficiency and current levels. Unfortunately only a single rat was available for the experiments, so we cannot comment about the consistency of these trends in rat tissue.

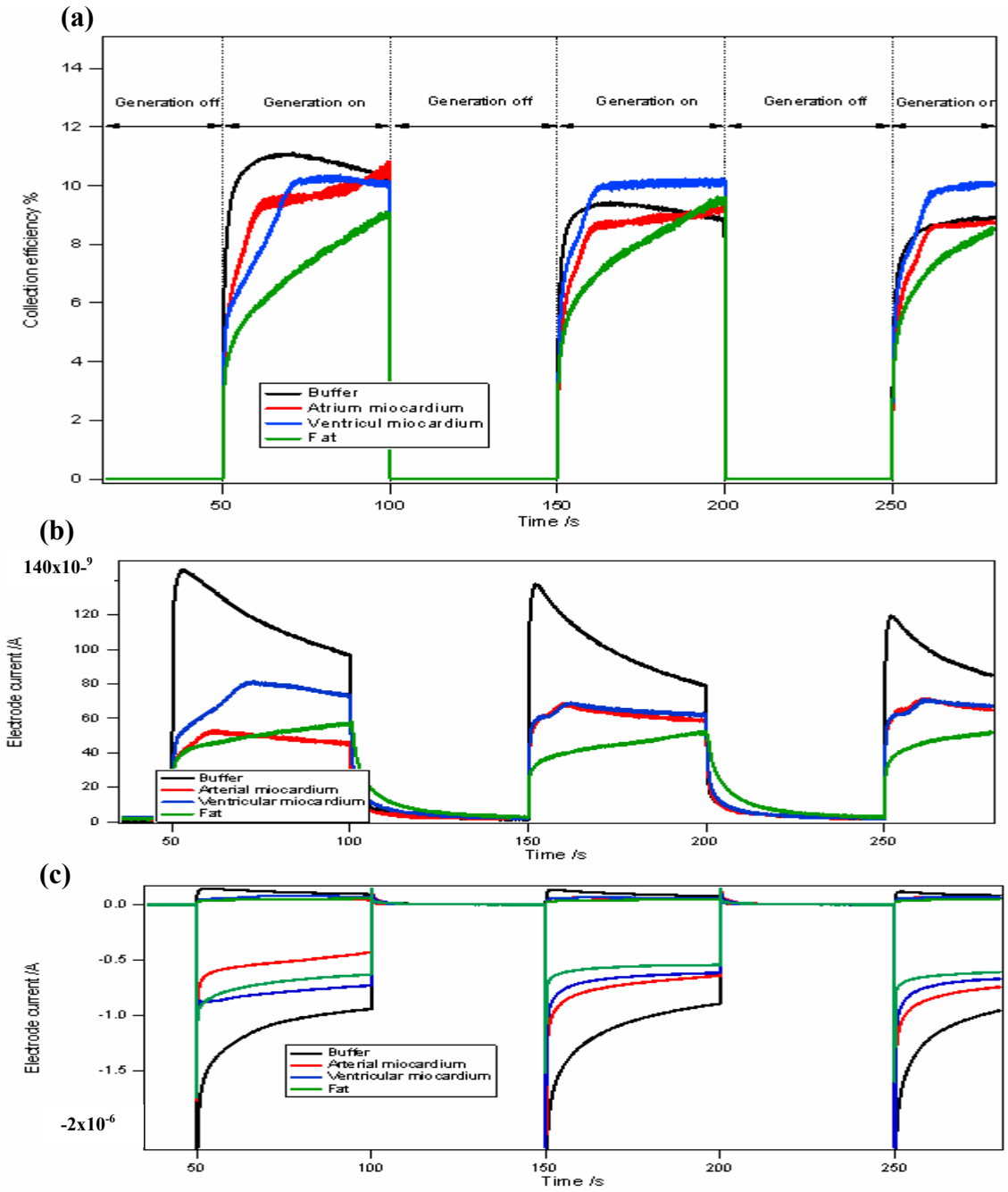

Figure 6.8: **(a)** Transient change in collection efficiency for different rabbit tissues. The sensor used had a disc diameter of 125 μm. **(b)** Transient change in collector current (ring) for different rabbit tissues. **(c)** Transient change in collector and generator currents for different rabbit tissues.

Human tissue

Tests in human tissue were performed in the Blond McIndoe Institute, East Grinstead,UK, which specialises in wound care. The tissue was supplied post-operatively and was less than a day old. Sections of viable tissue were selected and consisted of the epidermis, dermis and sometimes the fat layer (see Fig 6.9). To keep the cells alive, the tissue was bathed in Krebs buffered . Measurements of perfusion were made by placing a sensor firmly onto the surface of the tissue. An Ag/AgCl reference electrode and a platinum mesh counter electrode were placed in the vicinity of the sensor as sketched in Figure 6.9.

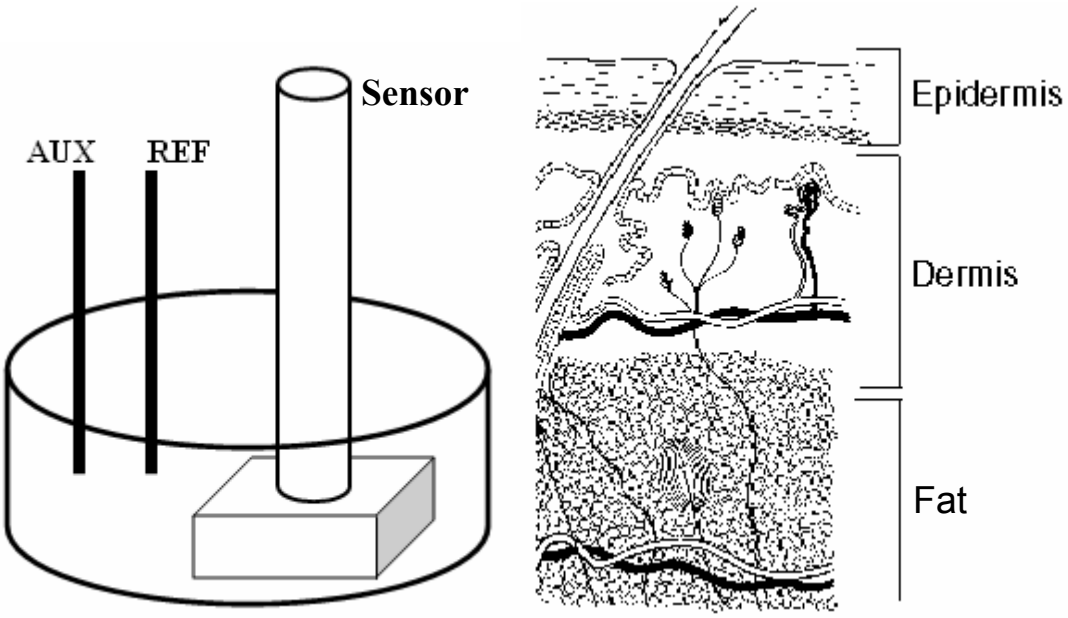

Figure 6.9: Left hand diagram shows the experimental setup, with the tissue sample placed in Krebs. The sensor was firmly positioned onto the surface of the skin layer being investigated, Ag/AgCl and platinum mesh counter were placed in the solution. Right hand diagram shows a schematic representation of the different layers of human tissue, the epidermis, dermis and the fat.

Before starting the measurements in tissue, cyclic voltammograms were preformed to assess if the buffer interfered with the recordings. We found no indication of electro-activity at the potentials at which the collector and generator were set.

The collection efficiency values obtained for different skin layers are shown in Figure 6.10 (a). On the epidermis the CE is high, significantly higher than in solution.

Taken alone this measurement indicated that hydrogen is not diffusing easily in this tissue. Measurements in the fat / dermis layer, on the other hand, display CE values that are a few percentages higher than those obtained in the buffer. This indicated that hydrogen diffuses readily in these tissues; almost as well as in aqueous solution.

Figure 6.10 (b) shows the currents obtained at the collector and generator electrodes when the sensor was placed either on the epidermis or the dermis / fat layer. We can clearly see that when measurements are made in the buffer, the current values are high. These then drop both for the dermis and the epidermis. The currents are particularly low for the epidermis layer. These low currents indicate lower water concentrations in the tissue, despite the skin being submerged in buffer.

Not only do we see that the different layers of skin alter the way in which H_2 diffuses, we find that the water content of the different layers changes and is much lower than in the buffer. In the animal tissue experiments, we showed there were differences in electrode currents between the tissues and the buffer, but not to the extent that we see with the human epidermis and to a degree the fat /dermis layer. The lack of freshness or the impermeable nature of the skin may be to blame.

(a)

(b)

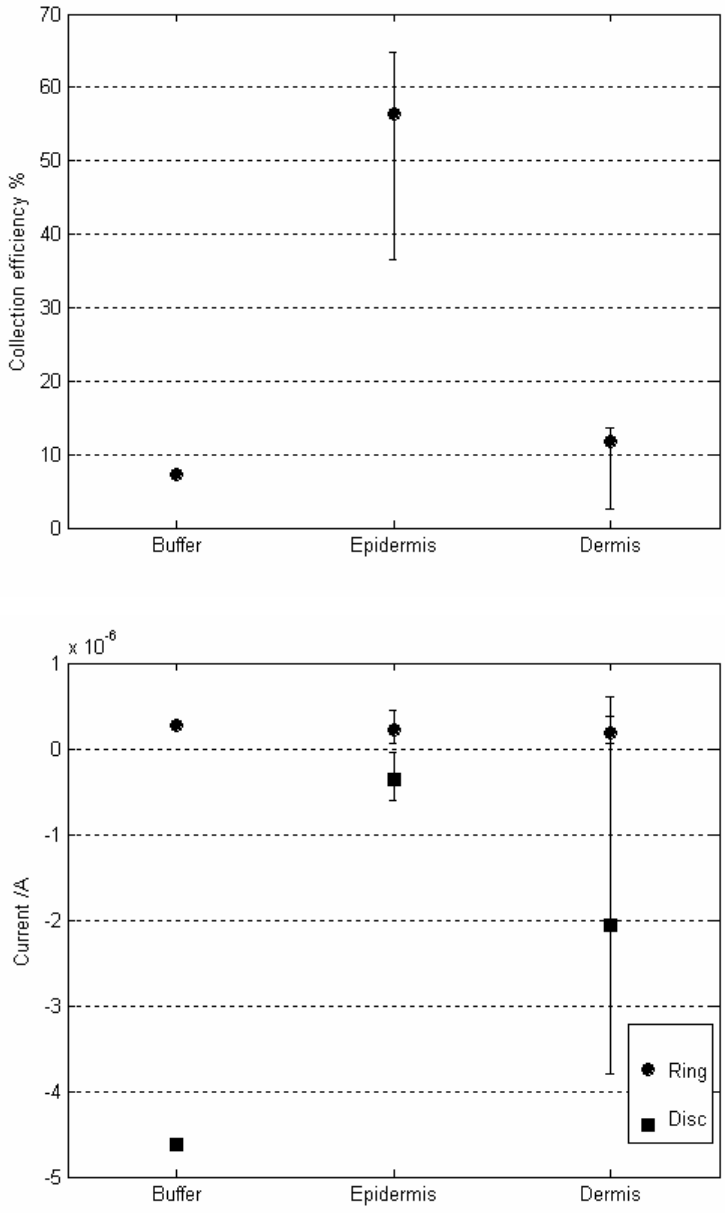

Figure 6.10: (a) Collection efficiencies measurements for different layers of human skin. The sensor was a 50 μm disc diameter sensor. Disc generating mode. **(b)** Variation in electrode current in the different layers of human skin. Measurements were made with a 50 μm disc electrode. Note absolute electrode current are plotted. Error bars shows the range of five trials.

The Blonde McIndoe Institute specialises in burns and their treatment. We therefore investigated the effects of scalding the tissue on the collection efficiency

measurements. The scalding was done by dipping bits of tissue into boiling water, usually for no longer than ten seconds. The measurements of collection efficiency in scald and un-scaled tissue are shown in Figure 6.11. We see that once the tissue is scald the collection efficiency drops both for the epidermis and the dermis layer. The current values for both collector and generator are seen to rise after the scalding (see Fig 6.11). These measurements indicate that after scalding the tissue H_2 and water can diffuse more easily. We believe this is because the proteins and structure of the tissue have been denatured by the scalding, the barriers to motion are therefore less important and the H_2 and water can move around more freely.

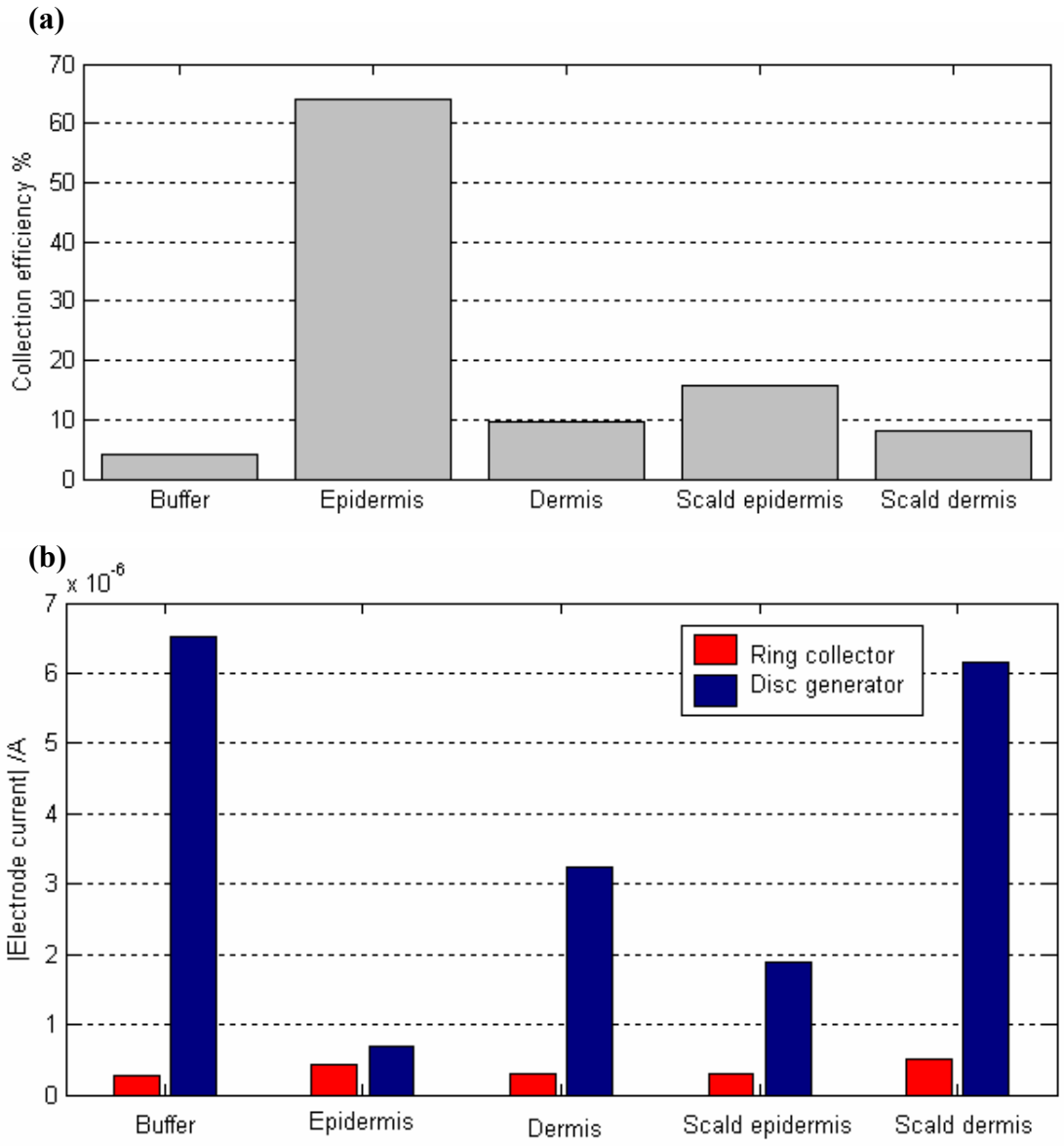

Figure 6.11: **(a)** Variation in collection efficiency for the different layers of tissue and the effect scalding the tissue has on the measurement. **(b)** Collector (ring) and generator (disc) current in different scald and un-scald tissues. The sensor used had a disc diameter of 50 µm. Note absolute electrode current is plotted.

6.2.2 Perfused rabbit ear

The perfused rabbit ear is a model that is often used to study perfusion and the microcirculation (229-234). The rabbit ears is a good model because the vasculature of the ear consists of a large artery that runs along the centre of the ear before bifurcating to

smaller vessels and eventually dense network of capillaries that cover the ear. The presence of large and small scale blood vessels means complex blood flow conditions can be studied using the ear (i.e. pharmacology, vasodialation/constriction, ischema, perfusion etc. (229,230,233,234)). Figure 6.12 shows a schematic of the rabbit ear vasculature and close up pictures of the capillary beds.

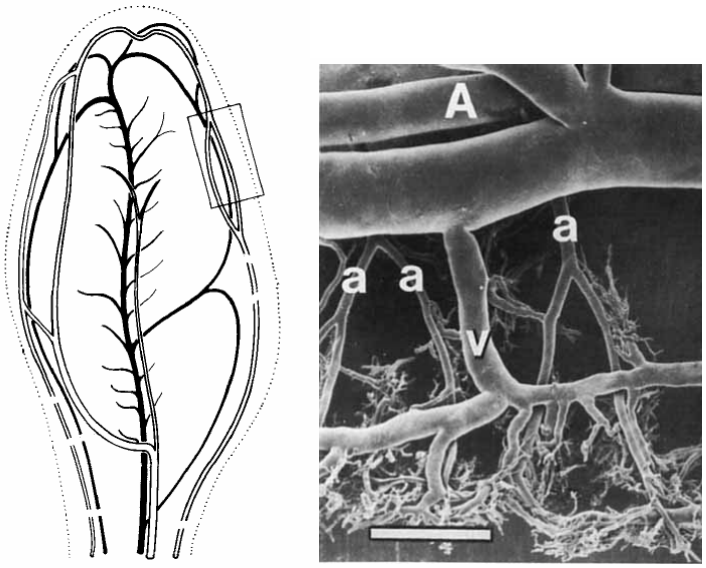

Figure 6.12: (a) Drawing of main features the rabbit ear vasculature, dorsal view. Black solid vessels represent arteries, veins are in white. Rectangle on the right indicates the area in which fig 6.12(b) was taken. **(b)** Cast of the vasculature in the ear of an adult rabbit. A refers to arteries, V to veins, the scale bar represents 100 μm (taken from (235)).

The ears were removed from five dead New Zealand white rabbit of varying ages (the rabbits were being killed for other experiments). Once removed, the main artery was cannulated so that Krebs buffer could be pumped through the ear. Krebs was flushed through the ear as soon as possible to prevent coagulation of the blood and blocking of the vessels. When the Krebs was first flushed through the ear, the displacement of the blood was clearly seen and served as a good visualisation of state of the vasculature. Figure 6.13 shows pictures of the experimental arrangement and details of the location of the sensor in the ear.

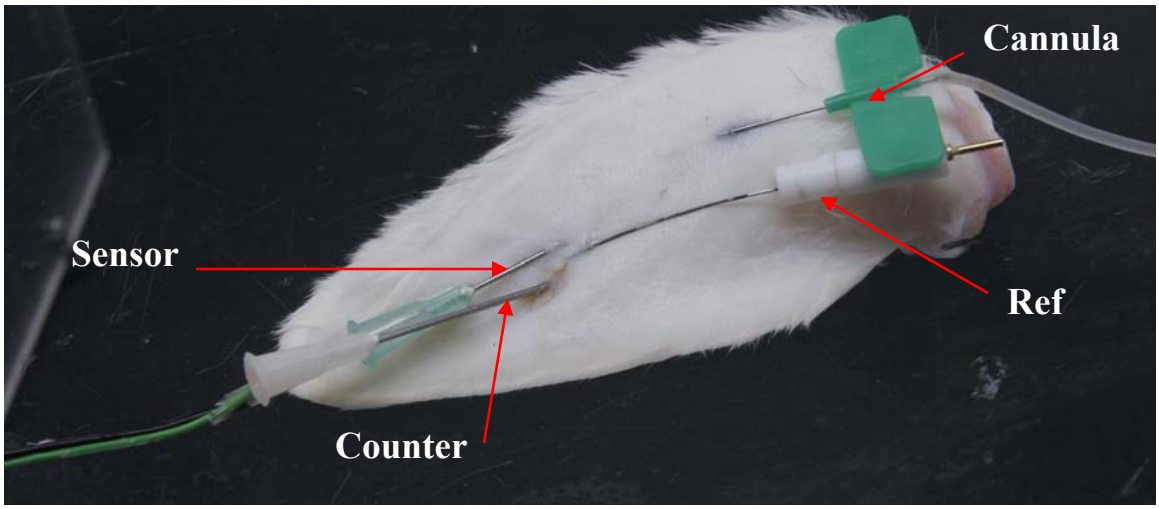

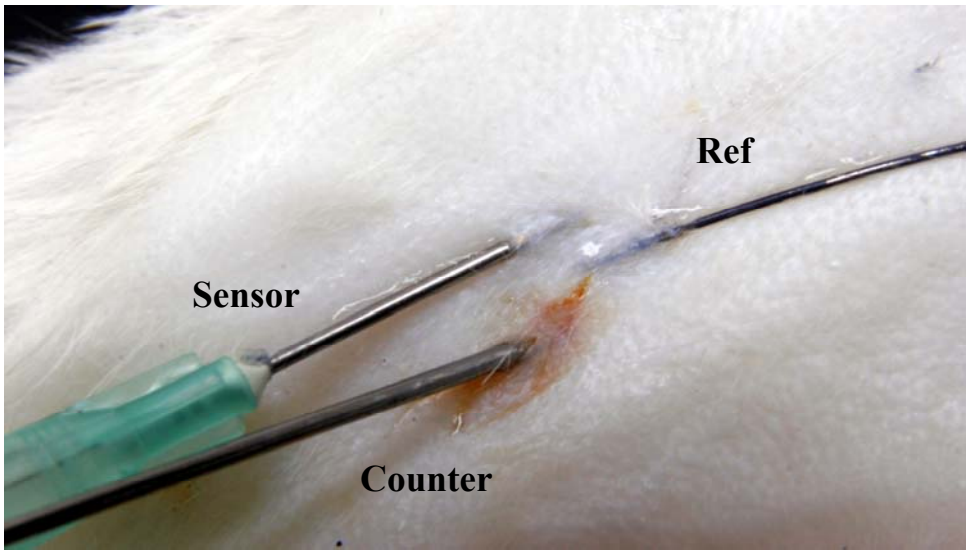

Figure 6.13: Pictures of the rabbit ear in the experimental setup. The location of the sensor, reference, counter electrodes and cannula are highlighted.

Hydrostatic pressure was used to force the buffer through the vasculature of the ear rather than a pump, as it was easier to maintain an accurate pressure. A 1 L flask was placed at predefined heights. The Krebs buffer in the flask was bubbled with 95% O_2 5% CO_2. A 2 mm diameter tubing was used to connect the flask to the cannula. A long section of this tubing was submerged in a heating bath upstream of the ear, so that the solution entering the ear was close to 37 °C. The small diameter of the tubing was useful as it meant there was only a relatively small volume of fluid between the flask and the ear. Two three-way valves were also placed at different locations in the flow rig, to allow more flexible access to the tube (i.e. for removing bubbles in the tubing, injecting solutions etc.)

The experiment consisted of measuring the change in collection efficiency with changes in the pressure head of the perfusate. Hydrogen wash in/out curves were also collected using the disc electrode at the same location in the ear (the sensor was not moved). The range of pressure heads was from 150 to 22 mm Hg, systolic and diastolic pressures in the rabbit ear are reported as 110/80 mmHg (236).

Collection efficiency measurements were relatively easy to make, and changes in pressure were easily detected. Figure 6.14 shows a typical collection efficiency trace, where the effects of changing the perfusate pressures are clearly seen. As we have come to expect, the collection efficiency drops with increasing pressure. In Figure 6.14.a the pressure is increased then decreased in steps. Each time the pressure is changed, the CE responds accordingly. The time scale of the response is worth considering. This response is not a sensor response, which occurs over milliseconds. The delayed response to a change in pressure is caused by the latency in the ear vasculature. The measurements were made in capillary beds, at the extremity of the vascular tree. It takes time for pressure changes in the main artery to be reflected in the capillaries and longer still for tissue perfusion to change beyond the capillaries. Other physiological events may also contribute to the delay such as vasodilatation or contraction. This is because the tissue is living, the ear cannot therefore, be considered as a passive network of vessels. Figure 6.14.b shows this response in more detail. It takes around 60 s for the majority of the change in CE to occur when the pressure is changed from 70 to 22 mm Hg. The ripples

observed in the trace could be electrical noise, or they could be due to small scale mass transport variations in the vicinity of the sensor.

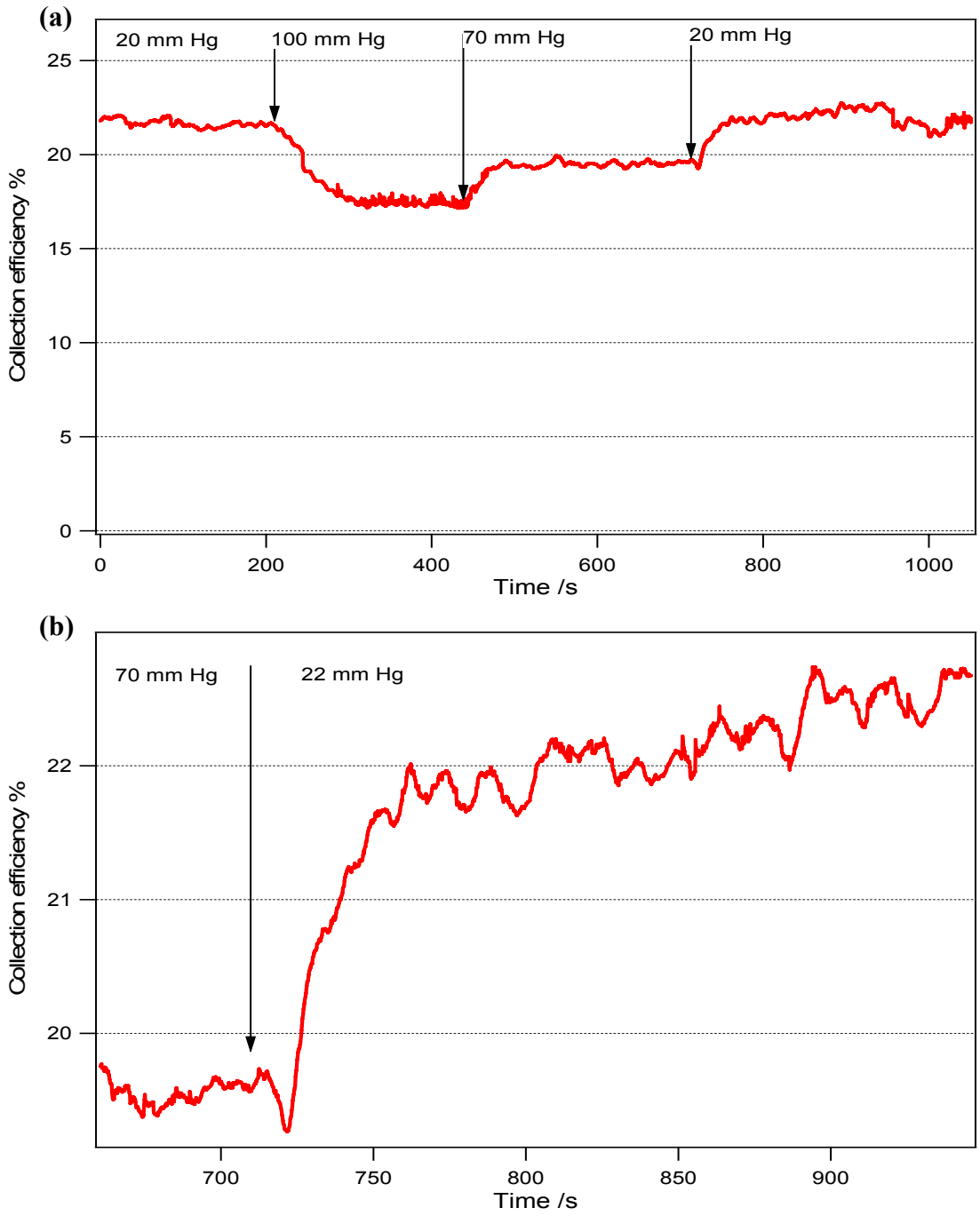

Figure 6.14: (a) Changes in collection efficiency due to changes in perfusate pressure. Measurements are made in a perfused rabbit ear with a sensor with a 50 µm disc diameter. **(b)** Close up of the change in collection efficiency when the perfusate pressure is decreased from 70 to 20 mm Hg.

The effects of turning the flow on and off (Figure 6.15) were also investigated. When the flow is on, the collection efficiency drops, rising again once the flow is switched off. There is some drift in the signal, the cause of this is yet unclear. The time response is again very interesting. A slow recovery to high CE values is observed once the flow has been turned off. This response then gets faster with successive on/off transients. The slow recovery when the flow is turned off is representative of a diffusive mass transport. The on transient is faster because of convection.

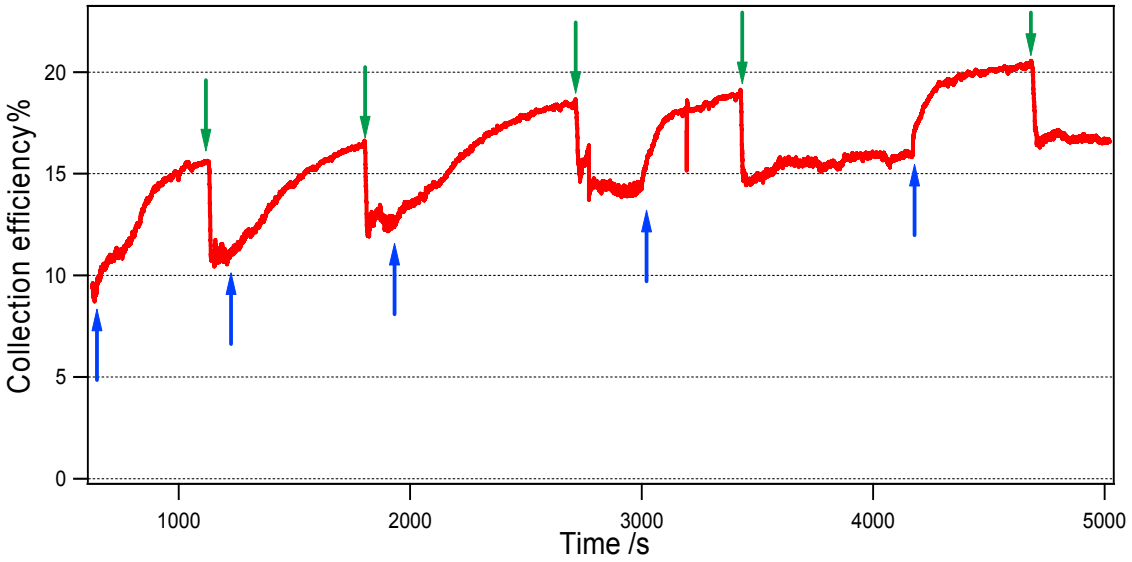

Figure 6.15: Change in collection efficiency as the flow into the ear is turned on and off. Green arrows indicate the moment when the flow was turned on, blue arrows when the flow was turned off. The sensor had a 50 µm disc diameter.

We also perfused the muscle at the base of the rabbit ear. To do this a catheter containing Krebs solution was inserted directly into the muscle, which subsequently swelled as it filled with buffer. This type of experiment can only be done once as it is very hard to force the solution out of the muscle once it is in. Figure 6.16 shows the response obtained. The response is slow and progressive.

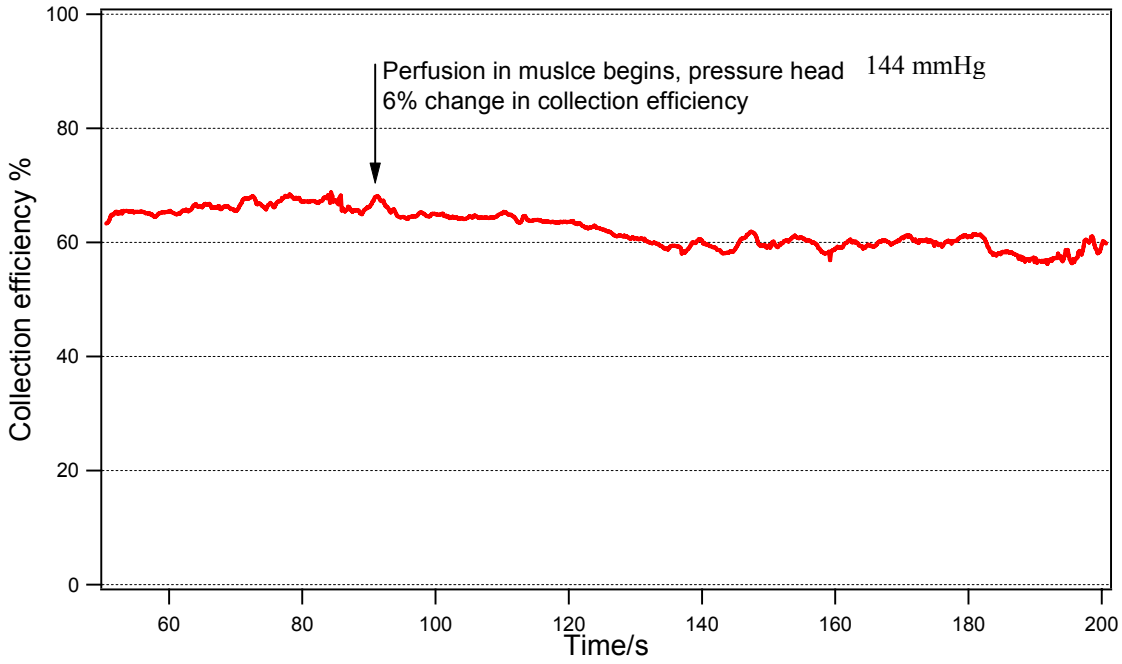

Figure 6.16: Decrease in collection efficiency following the perfusion of muscle tissue. The sensor has a 50 μm disc diameter, the pressure head was 144 mm Hg.

In addition to the collection efficiency experiments, hydrogen wash in measurements was performed. This was done to validate the measurement made with the collector generator technique and to compare it with a well established tissue perfusion measurement technique. The hydrogen clearance experiments were a little trickier to do. The main problems were the changing concentration of the saturated hydrogen solution and the non-physiological way in which the hydrogen is introduced into the tissue.

As discussed in Section 5.6.1 the concentration of hydrogen in the saturated solution changes even when placed in a sealed glass container. This complicated the experiments. The first injections of solution had high hydrogen content but subsequent injections had far less. This meant the signals were often low and noisy.

Another problem encountered relates to the way the hydrogen solution is administered to the ear. Using hydrostatic pressure to deliver the H_2 solution was taking too long to reach the sensor in the tissue. One had to resorte to injecting the solution directly into the ear through the cannula. The injection was done slowly but the pressure and flow rate are probably higher than physiological values. As a result, the wash in curve cannot be used. Typically 2 ml volume of solution were injected. Once the

injection is complete, the hydrostatically driven flow to the ear is resumed. The resultant wash out curve is therefore at physiological levels of pressure and can be used to compare with the collection efficiency measurements. Figure 6.17 shows H_2 wash out curves for two different driving pressures. For high hydrostatic pressures the wash out occurs over

60-70 s. For low pressure the wash out curve is much more drawn out as it takes longer for the hydrogen to leave the region surrounding the sensor (i.e. >200 s). These measurements confirm the collection efficiency results. We have to note, however, that the current levels in the H_2 wash out method are rather low and that the temporal resolution is poor.

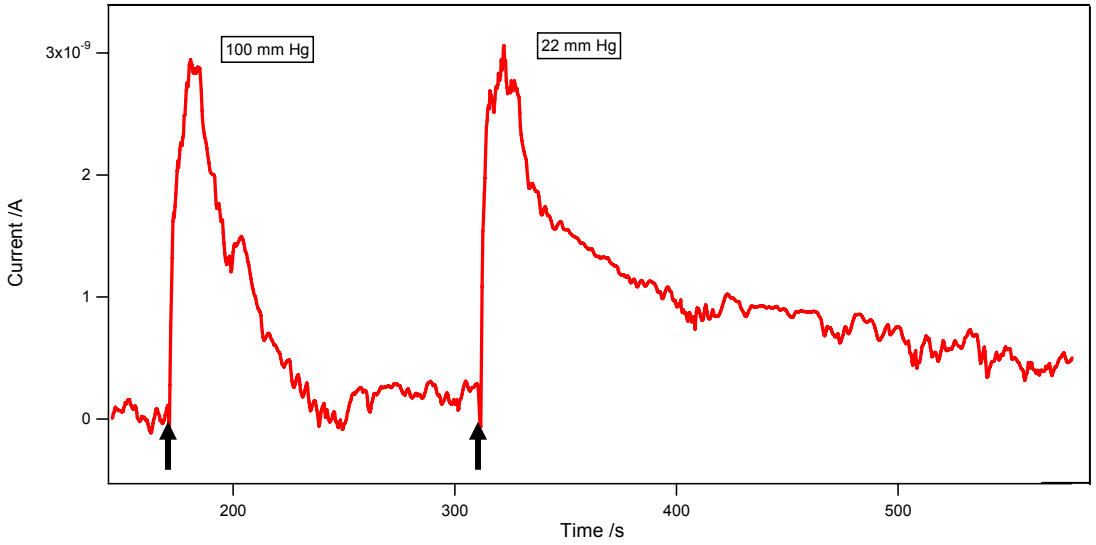

Figure 6.17: Hydrogen wash out curves for different prefusate pressures in the rabbit ear. Arrows indicate the time at which H_2 was introduced into the ear by injecting H_2 saturated solution through a cannula into the main artery. Measurements were made with a 50 μm disc electrode placed in of the ear capillary bed.

6.3 Conclusion

In the first part of this chapter, the work done to prepare the sensor for use *in vitro* was presented. The influence the sensor may have on tissue, the damage it may cause as well as the influence the tissue may have on the sensor were discussed (i.e. biocompatibility and fouling). The steps taken to limit the damage to the sensor and the tissue were also investigated. These include packaging the sensor and subjecting the sensor to albumin for 2 hours prior to testing.

In the second part of the chapter, we applied the sensor to biological tissues. initially in conditions with no convection. It was found that the sensor is capable of detecting differences in tissue water concentration as well as differences in hydrogen diffusion. These differences were most noticeable between scald and un-scald human tissues. Subsequently the sensor was tested in perfused rabbit ears. In this model, convection is present and the sensor was placed in capillary beds where it was able to detect a range of changes in perfusate pressure.

These measurements show that the sensor is capable of detecting changes in tissue perfusion in a continuous fashion while simultaneously supplying additional information about the state of the tissue.

7

Conclusion and future work

The focus of this thesis has been the development of an electrochemical tissue perfusion sensor. Tissue perfusion describes the movement of respiratory gases, nutrients and metabolites within tissue. It is a mass transport mechanism that occurs on the cellular level. Poor tissue perfusion is associated with a large number of serious health problems, yet our understanding of poor perfusion is limited, mainly because current measurement techniques do not provide sufficient resolution.

In this work a novel approach to measuring tissue perfusion was proposed and developed. It relies on the electrochemical generation and collection of hydrogen gas within tissue. This technique is superior to existing tissue perfusion measurement techniques for three reasons: (i) continuous measurement capabilities, (ii) measurements on the cellular level and (iii) the use of a diffusible and inert tracer as a marker of perfusion. The pair of microelectrodes used to generate and collect H_2 are made of platinum and have a ring-disc shape with an outer diameter below 150 μm.

The work presented in this thesis can be divided into four parts, the achievements in each part having significantly contributed to the outcome of the work:

To make these ring-disc microelectrodes a **novel fabrication technique** was developed. This method is based on an inverted cylindrical sputter coater. The machine built produced extensive length of "ring-disc" wire which then only needed to be cut to the desired length, connected and insulated. The thickness of the coating applied to the wire was dense, uniform and accurately controlled. The electrodes produced displayed good electrochemical behaviour. Overall this fabrication method is a significant improvement on the current techniques used to make ring-disc microelectrodes and the possibilities that emerge from this process are noteworthy.

A number of **numerical models** of the ring-disc microelectrode under diffusion and convection mass transport modes were presented. These models were mainly used to inform the design of the electrodes and to probe the behaviour of the sensor under various operating conditions. In general experimental measurement shows good agreement with the numerical predictions.

Extensive **experimental testing** of the ring-disc microelectrode was carried out under diffusion and convection mass transport modes. These experiments were designed to investigate the mass transport measurement limits of the sensor under conditions that

are likely to be present in tissue. It was shown that detailed and precise mass transport measurement were possible under a variety of circumstances. The measurement limits were shown to be strongly dependent on the size of the electrodes and the way in which the sensor is operated (disc or ring generating, level of overpotential use to generate H_2 etc.).

Finally a selection of **in-vitro experiments** were undertaken, these were used as a proof of concept. Overall these experiments showed that continuous and cellular level measurements of tissue perfusion are possible using the method developed, which was the aim of this work. The potential use of the sensor to distinguish between tissue types is also a significant outcome of this work. The sensor was able to measure changes in tissue perfusion within the capillary beds of perfused rabbit ears. A number of measurements in animal and human tissues were also undertaken and showed that the sensor was able to provide detailed information about mass transport in these tissues as well as a way of differentiating between the tissues.

This work has shown that the ring-disc microelectrode is well suited to monitoring tissue perfusion on the cellular level. It now remains to be tested more extensively on animal or human models. This is now being undertaken as part of the commercialisation partnership with IPSO BIO Ltd.

The design process undertaken in this thesis does suggest that each application will require a specific sensor geometry and operation to yield optimum measurements. For long term implantation application the coating of the sensor is essential, the work alluded to in Chapter 6 regarding the coating of the sensor will have to be extended in order to guarantee stability of the sensor in such applications. Finally the interpretation of the measurement made with the sensor will also have to be investigated as the formal relationship between collection efficiency and capillary blood flow rate was not proposed in this work. I envision that the standard blood flow measurement unit ml/g/min, may prove too general to describe the type of measurement made by the sensor; instead the rate of mass transport may provide a more suitable measure of tissue perfusion.

References

(1) A Krogh: The anatomy and physiology of capillaries, Yale University press, New Haven, 1922.

(2) FE Curry, JC Mason, CC Michel: Development of a Method of Measuring Filtration Coefficient of Individually Perfused Frog Mesenteric Capillaries. Journal of Physiology-London 234 (1973) P26-P27.

(3) JR Levick, CC Michel: Effects of Position and Skin Temperature on Capillary Pressures in Fingers and Toes. Journal of Physiology-London 274 (1978) 97-&.

(4) CC Michel: Transport of macromolecules through microvascular walls. Cardiovascular Research 32 (1996) 644-53.

(5) CC Michel: Microvascular permeability, ultrafiltration, and restricted diffusion. American Journal of Physiology-Heart and Circulatory Physiology 287 (2004) H1887-H88.

(6) CC Michel: Fluid exchange in the microcirculation. Journal of Physiology-London 557 (2004) 701-02.

(7) JR Levick: Flow through Interstitium and Other Fibrous Matrices. Quarterly Journal of Experimental Physiology and Cognate Medical Sciences 72 (1987) 409-38.

(8) W Wang, CP Winlove, CC Michel: Oxygen partial pressure in outer layers of skin of human finger nail folds. Journal of Physiology-London 549 (2003) 855-63.

(9) FE Curry, CC Michel: Microvascular Permeability. Physiological Reviews 79 (1999) 703.

(10) MP Wiedeman, RF Tuma, HN Mayrovitz: An Introduction to Microcirculation, Academic Press, US, 1981.

(11) SE Charm, GS Kurland: Blood Flow and Microcirculation, John Wiley and Sons, London, 1974.

(12) DL Carden, DN Granger: Pathophysiology of ischaemia-reperfusion injury. Journal of Pathology 190 (2000) 255-66.

(13) P Martin: Wound healing - Aiming for perfect skin regeneration. Science 276 (1997) 75-81.

(14) L Pascarella, GWS Schonbein, JJ Bergan: Microcirculation and venous ulcers: A review. Annals of Vascular Surgery 19 (2005) 921-27.

(15) AJ Singer, RAF Clark: Mechanisms of disease - Cutaneous wound healing. New England Journal of Medicine 341 (1999) 738-46.

(16) GM Tozer, C Kanthou, BC Baguley: Disrupting tumour blood vessels. Nature Reviews Cancer 5 (2005) 423-35.

(17) O Parodi, R Demaria, L Oltrona, R Testa, G Sambuceti, A Roghi, M Merli, L Belingheri, R Accinni, F Spinelli, A Pellegrini, G Baroldi: Myocardial Blood-Flow Distribution in Patients with Ischemic-Heart-Disease or Dilated Cardiomyopathy Undergoing Heart-Transplantation. Circulation 88 (1993) 509-22.

(18) TM Nork, CBY Kim, D Shanmuganayagam, MS Van Lysel, JN Ver Hoeve, JD Folts: Measurement of regional choroidal blood flow in rabbits and monkeys using fluorescent microspheres. Archives of Ophthalmology 124 (2006) 860-68.

(19) H Anetzberger, E Thein, M Maier, C Birkenmaier, K Messmer: Fluorescent microspheres are reliable for serial bone blood flow measurements. Clinical Orthopaedics and Related Research (2004) 241-48.

(20) I McCarthy: The physiology of bone blood flow: A review. Journal of Bone and Joint Surgery-American Volume 88A (2006) 4-9.

(21) DS Fluck, PJE Etherington, D O'Hare, CP Winlove, DJ Sheridan: Myocardial tissue perfusion determined by particulate and diffusible tracers during ischaemia: what is measured? Cardiovascular Research 32 (1996) 869-78.

(22) E Monnet, D Pelsue, C MacPhail: Evaluation of laser doppler flowmetry for measurement of capillary blood flow in the stomach wall of dogs during gastric dilatation-volvulus. Veterinary Surgery 35 (2006) 198-205.

(23) GS Lausten, T Kiaer, B Dahl: Laser-Doppler Flowmetry for Estimation of Bone Blood-Flow - Studies of Reproducibility and Correlation with Microsphere Technique. Journal of Orthopaedic Research 11 (1993) 573-80.

(24) K Wardell, GE Nilsson: Duplex laser Doppler perfusion imaging. Microvascular Research 52 (1996) 171-82.

(25) AMA Schabauer, TW Rooke: Cutaneous Laser-Doppler Flowmetry - Applications and Findings. Mayo Clinic Proceedings 69 (1994) 564-74.

(26) KU Frerichs, GZ Feuerstein: Laser-Doppler Flowmetry - a Review of Its Application for Measuring Cerebral and Spinal-Cord Blood-Flow. Molecular and Chemical Neuropathology 12 (1990) 55-70.

(27) AN Obeid, NJ Barnett, G Dougherty, G Ward: A Critical-Review of Laser Doppler Flowmetry. Journal of Medical Engineering & Technology 14 (1990) 178-81.

(28) JS Chatterjee: A critical evaluation of the clinimetrics of laser Doppler as a method of burn assessment in clinical practice. Journal of Burn Care & Research 27 (2006) 123-30.

(29) EJ Droog, W Steenbergen, F Sjoberg: Measurement of depth of burns by laser Doppler perfusion imaging. Burns 27 (2001) 561-68.

(30) RC Bray, KR Forrester, J Reed, C Leonard, J Tulip: Endoscopic laser speckle imaging of tissue blood flow: Applications in the human knee. Journal of Orthopaedic Research 24 (2006) 1650-59.

(31) WJ Thomson: Heat clearance method of estimating peripheral blood flow? Brithish Journal of Anaesthetics 38 (1966) 572.

(32) P Vajkoczy, H Roth, P Horn, T Lucke, C Thome, U Hubner, GT Martin, C Zappletal, E Klar, L Schilling, P Schmiedek: Continuous monitoring of regional cerebral blood flow: experimental and clinical validation of a novel thermal diffusion microprobe. Journal of Neurosurgery 93 (2000) 265-74.

(33) M Nitzan, Y Mahler: Theoretical-Analysis of the Transient Thermal Clearance Method for Regional Blood-Flow Measurement. Medical & Biological Engineering & Computing 24 (1986) 597-601.

(34) W Mullerschauenburg, H Apfel, H Benzing, E Betz: Quantitative Measurement of Local Blood-Flow with Heat Clearance. Basic Research in Cardiology 70 (1975) 547-67.

(35) H Kamiya, G Watanabe, T Saito, T Doi, S Tomita, H Ohtake, T Kanamori: Real-time and continuous monitoring of myocardial blood flow using a thermal diffusion method. European Journal of Cardio-Thoracic Surgery 21 (2002) 748-52.

(36) K Aukland, BF Bowe, RW Berliner: Measurement of local blood flow with hydrogen gas. Circulation reserach 14 (1964) 164-87.

(37) E Lenigerfollert, DW Lubbers, J Huber, R Wodick: Measurements of Microflow by Local Hydrogen Clearance. Arzneimittel-Forschung/Drug Research 25 (1975) 983-83.

(38) K Stosseck, DW Lubbers, N Cottin: Determination of Local Blood-Flow (Microflow) by Electrochemically Generated Hydrogen - Construction and Application of Measuring Probe. Pflugers Archiv-European Journal of Physiology 348 (1974) 225-38.

(39) W Young: H-2 Clearance Measurement of Blood-Flow - a Review of Technique and Polarographic Principles. Stroke 11 (1980) 552-64.

(40) DK Harrison, M Kessler: Local Hydrogen Clearance as a Method for the Measurement of Capillary Blood-Flow. Physics in Medicine and Biology 34 (1989) 1413-28.

(41) M Kawasuji, F Kawajiri, T Iwa: Measurement of Regional Myocardial Blood-Flow - Application of the Electrolytic Hydrogen Clearance Method in Man. Journal of Thoracic and Cardiovascular Surgery 96 (1988) 775-81.

(42) DS Fluck, PJE Etherington, DJ Sheridan, CP Winlove: Solute exchange in the rabbit myocardium: Ischaemia, reflow, and myocardial necrosis. Basic Research in Cardiology 93 (1998) 354-60.

(43) K Sas, K Csete, Z Vezekenyi, L Sztriha, L Vecsei, J Papp: Effects of citalopram and fluoxetine on the corticocerebral blood flow in conscious rabbits. Acta Physiologica Hungarica 94 (2007) 167-77.

(44) K Csete, Z Vezekenyi, T Doczi, JG Papp, M Bodosi, P Barzo: Comparison of regional vasomotor responses to acetazolamide and CO2 in rabbit cerebrum and cerebellum, measured by a hydrogen clearance method. Acta Physiologica Scandinavica 182 (2004) 287-94.

(45) AE Fray, RJ Forsyth, MG Boutelle, M Fillenz: The mechanisms controlling physiologically stimulated changes in rat brain glucose and lactate: A microdialysis study. Journal of Physiology-London 496 (1996) 49-57.

(46) GS Pell, MD King, E Proctor, DL Thomas, MF Lythgoe, DG Gadian, RJ Ordidge: Comparative study of the FAIR technique of perfusion quantification with the hydrogen clearance method. Journal of Cerebral Blood Flow and Metabolism 23 (2003) 689-99.

(47) JF Cusick, J Myklebust: Continuous Quantitative Local Cerebral Blood-Flow Measurement - Calibration of Thermal-Conductivity Measurements by the Hydrogen Clearance Method. Stroke 11 (1980) 661-64.

(48) GR Diresta, JW Kiel, GL Riedel, P Kaplan, AP Shepherd: Hybrid Blood-Flow Probe for Simultaneous H-2 Clearance and Laser-Doppler Velocimetry. American Journal of Physiology 253 (1987) G573-G81.

(49) R Uranishi, H Nakase, T Sakaki, OS Kempski: Evaluation of absolute cerebral blood flow by laser-Doppler scanning - Comparison with hydrogen clearance. Journal of Vascular Research 36 (1999) 100-05.

(50) TJ Day, TD Lagerlund, PA Low: Analysis of H2 Clearance Curves Used to Measure Blood-Flow in Rat Sciatic-Nerve. Journal of Physiology-London 414 (1989) 35-54.

(51) LK Fellows, MG Boutelle: Rapid Changes in Extracellular Glucose-Levels and Blood-Flow in the Striatum of the Freely Moving Rat. Brain Research 604 (1993) 225-31.

(52) MR Urban, JCT Fairbank, PJ Etherington, L Loh, CP Winlove, JPG Urban: Electrochemical measurement of transport into scoliotic intervertebral discs in vivo using nitrous oxide as a tracer. Spine 26 (2001) 984-90.

(53) DJ Barron, PJE Etherington, CP Winlove, JR Pepper: Regional perfusion and oxygenation in the pedicled latissimus dorsi muscle flap: the effect of mobilisation and electrical stimulation. British Journal of Plastic Surgery 50 (1997) 435-42.

(54) DJ Barron, PJ Etherington, JR Pepper, PC Winlove: Simultaneous measurement of tissue pO(2) and perfusion during muscular contraction of the latissimus dorsi. Basic and Applied Myology 8 (1998) 67-74.

(55) RM Penner, MJ Heben, TL Longin, NS Lewis: Fabrication and Use of Nanometer-Sized Electrodes in Electrochemistry. Science 250 (1990) 1118-21.

(56) AJ Bard, LR Faulkner: Electrochemical Methods, Weiley, New York, 201.

(57) Y Saito: Rev Polarogr 15 (1968) 177.

(58) A Szabo: Theory of the Current at Microelectrodes - Application to Ring Electrodes. Journal of Physical Chemistry 91 (1987) 3108-11.

(59) C Amatore, M Belotti, Y Chen, E Roy, C Sella, L Thouin: Using electrochemical coupling between parallel microbands for in situ monitoring of flow rates in microfluidic channels. Journal of Electroanalytical Chemistry 573 (2004) 333-43.

(60) C Amatore, C Sella, L Thouin: Effects of chemical environment on diffusivities within thin Nafion(R) films as monitored from chronoamperometric responses of generator-collector double microband assemblies. Journal of Electroanalytical Chemistry 547 (2003) 151-61.

(61) JE Baur, PN Motsegood: Diffusional interactions at dual disk microelectrodes: comparison of experiment with three-dimensional random walk simulations. Journal of Electroanalytical Chemistry 572 (2004) 29-40.

(62) H Rajantie, DE Williams: Potentiometric titrations using dual microband electrodes. Analyst 126 (2001) 1882-87.

(63) P Tomcik, S Jursa, S Mesaros, D Bustin: Titration of As(III) with electrogenerated iodine in the diffusion layer of an interdigitated microelectrode array. Journal of Electroanalytical Chemistry 423 (1997) 115-18.

(64) Southampton, electrochemistry, group: Instrumental methods in electrochemistry, Ellis Horwood Limited, Chichester, 1985.

(65) B Hibbert: Introduction to electrochemistry, The Macmillan press Ltd., Basingstoke, UK, 1993.

(66) RN Adams: Electrochemistry at Solid Electrodes, Marcel Dekker, New York, 1969.

(67) LI Krishtalik: Advances in Electrochemistry and Electrochemical Engineering, New York, 1972.

(68) S Trasatti: Work Function, Electronegativity, and Electrochemical Behavior of Metals .3. Electrolytic Hydrogen Evolution in Acid Solutions. Journal of Electroanalytical Chemistry 39 (1972) 163-&.

(69) M Volmer, A weber: Nucleus formation in supersaturated systems. Z. Phisik Chemie 119 (1926) 277.

(70) SF Jones, GM Evans, KP Galvin: Bubble nucleation from gas cavities - a review. Advances in Coloid and Interface Science 80 (1999) 27-50.

(71) JV Macpherson, PR Unwin: Determination of the Diffusion Coefficient of Hydrogen in Aqueous Solution Using Single and Double Potential Step Chronoamperometry at a Disk Ultramicroelectrode. Anal. Chem. 69 (1997) 2063-69.

(72) SW Feldberg: Model for current reversal chronopotentiometry with secon-order kinetic complications. Analytical Chemistry 36 (1964) 1051-55.

(73) SW Feldberg: Computers in chemistry and instrumentation, Marcel Dekker, New York, 1972.

(74) SW Feldberg: Electroanalytical chemistry, Marcel Dekker, New York, 1969.

(75) D Britz: Digital simulation in electrochemistry, Springer-Verlag, 1988.

(76) E Bitziou, NC Rudd, PR Unwin: Microjet ring electrode (MJRE): Development, modelling and experimental characterisation. Journal of Electroanalytical Chemistry 602 (2007) 263-74.

(77) P Liljeroth, C Johans, CJ Slevin, BM Quinn, K Kontturi: Disk-generation/ring-collection scanning electrochemical microscopy: Theory and application. Analytical Chemistry 74 (2002) 1972-78.

(78) CA Anastassiou, KH Parker, D O'Hare: Determination of kinetic and thermodynamic parameters of surface confined species through ac voltammetry and a nonstationary signal processing technique: The Hilbert transform. Analytical Chemistry 77 (2005) 3357-64.

(79) LM Zhao, D Schaefer, HX Xu, SJ Modi, WR LaCourse, MR Marten: Elastic properties of the cell wall of Aspergillus nidulans studied with atomic force microscopy. Biotechnology Progress 21 (2005) 292-99.

(80) K Smistrup, O Hansen, H Bruus, MF Hansen: Magnetic separation in microfluidic systems using microfabricated electromagnets-experiments and simulations. Journal of Magnetism and Magnetic Materials 293 (2005) 597-604.

(81) B Chen, SL Thomsen, RJ Thomas, AJ Welch: Modeling thermal damage in skin from 2000-nm laser irradiation. Journal of Biomedical Optics 11 (2006).

(82) AJ Bard, MV Mirkin: Scannning Electrochemical Microscopy, New York, 1994.

(83) RM Wightman, DO Wipf: Electroanalytical Chemistry, New York, 1989.

(84) HJ Levinson: Principles of lithography, Spie Press, 2005.

(85) P Rai-Choudhury: Handbook of microlithography, micromachining and microfabrication, London, 1997.

(86) Y Chen, A Pepin: Nanofabrication: Conventional and nonconventional methods. Electrophoresis 22 (2001) 187-207.

(87) R Ferrigno, PF Brevet, HH Girault: Finite element simulation of the amperometric response of recessed and protruding microband electrodes in flow channels. Journal of Electroanalytical Chemistry 430 (1997) 235-42.

(88) AM Bond, D Luscombe, KB Oldham, CG Zoski: A Comparison of the Chronoamperometric Response at Inlaid and Recessed Disk Microelectrodes. Journal of Electroanalytical Chemistry 249 (1988) 1-14.

(89) Z Liu, O Niwa, R Kurita, T Horiuchi: Carbon Film-Based Interdigitated Array Microelectrode Used in Capillary Electrophoresis with Electrochemical Detection. Anal. Chem. 72 (2000) 1315-21.

(90) O Niwa, M Morita, BP Solomon, PT Kissinger: Carbon film based ring-disk and split-disk dual electrodes as detectors for microbore liquid chromatography. Electroanalysis 8 (1996) 427-33.

(91) N Mano, A Heller: Detection of glucose at 2 fM concentration. Analytical Chemistry 77 (2005) 729-32.

(92) F Rosebury: Handbook of electron tube and vacuum techniques, Addison-Welsley, Reading, Massachusetts, 1965.

(93) B Ilic, D Czaplewski, P Neuzil, T Stanczyk, J Blough, GJ Maclay: Preparation and characterization of platinum black electrodes. Journal of Materials Science 35 (2000) 3447-57.

(94) J Millar, CWA Pelling: Improved methods for construction of carbon fibre electrodes for extracellular spike recording. Journal of Neuroscience Methods 110 (2001) 1-8.

(95) JV Macpherson, PR Unwin: Radial flow microring electrode: Development and characterization. Analytical Chemistry 70 (1998) 2914-21.

(96) SM Rossnagel: Thin film deposition with physical vapor deposition and related technologies. Journal of Vacuum Science & Technology A 21 (2003) S74-S87.

(97) S Swann: Magnetron Sputtering. Physics in Technology 19 (1988) 67-75.

(98) A Roth: Vacuum Technology, North Holland, 1991.

(99) G Zhao, DM Giolando, JR Kirchhoff: Chemical-Vapor-Deposition Fabrication and Characterization of Silica-Coated Carbon-Fiber Ultramicroelectrodes. Analytical Chemistry 67 (1995) 2592-98.

(100) G Zhao, DM Giolando, JR Kirchhoff: Carbon Ring Disk Ultramicroelectrodes. Analytical Chemistry 67 (1995) 1491-95.

(101) M Zhong, JX Zhou, SM Lunte, G Zhao, DM Giolando, JR Kirchhoff: Dual-electrode detection for capillary electrophoresis electrochemistry. Analytical Chemistry 68 (1996) 203-07.

(102) KD Kovalcik, JR Kirchhoff, DA Giolando, JP Bozon: Copper ring-disk microelectrodes: fabrication, characterization, and application as an amperometric detector for capillary columns. Analytica Chimica Acta 507 (2004) 237-45.

(103) P Liljeroth, C Johans, CJ Slevin, BM Quinn, K Kontturi: Micro ring-disk electrode probes for scanning electrochemical microscopy. Electrochemistry Communications 4 (2002) 67-71.

(104) W Kern: Thin film processes, Academic Press, New York, 1978.

(105) ZH Wang, SA Cohen: Hollow cathode magnetron. Journal of Vacuum Science & Technology A 17 (1999) 77-82.

(106) JA Thornton: Magnetron sputtering: basic physics and application to cylindrical magnetrons. Journal of Vacuum Science and Technology 15 (1978) 171-77.

(107) T Kaneko, O Nittono: Improved design of inverted magnetrons used for deposition of thin films on wires. Surface and Coatings Technology 90 (1997) 268-74.

(108) M Amberg, J Geerk, M Keller, A Fischer: Design, characterisation and operation of an inverted cylindrical magnetron for metal deposition. Plasma Devices and Operations 12 (2004) 175-86.

(109) DM Mattox: Handbook of Physical Vapor Deposition (PVD) Processing., Noyes, 1998.

(110) ML Escrivao, PJS Pereira, MH Cabral, CMR Teixeira, MJP Maneira: Current-pressure-voltage characteristics in a planar magnetron discharge. Journal of Vacuum Science & Technology A 21 (2003) 375-80.

(111) SM Rossnagel: Gas-Density Reduction Effects in Magnetrons. Journal of Vacuum Science & Technology a-Vacuum Surfaces and Films 6 (1988) 19-24.

(112) SLR Harvey, KH Parker, D O'Hare: Theoretical evaluation of the collection efficiency at ring-disc microelectrodes. Journal of Electroanalytical Chemistry 610 (2007) 122-30.

(113) CG Phillips, HA Stone: Theoretical calculation of collection efficiencies for collector-generator microelectrode systems. Journal of Electroanalytical Chemistry 437 (1997) 157-65.

(114) D O'Hare, KH Parker, CP Winlove: Metal-metal oxide pH sensors for physiological application. Medical Engineering & Physics 28 (2006) 982-88.

(115) Finite element methods: fifty years of the Courant method, Marcel Dekker Inc., New York, 1994.

(116) MJ Turner, RW Clough, HC Martin, LC Topp: Stiffness and Deflection Analysis of Complex Structures. Journal of the Aeronautical Science 23 (1956) 805-24.

(117) JN Ye, XW Zhao, YZ Fang, RP Baldwin: Parallel and serial dual electrode detectors for capillary electrophoresis. Chinese Journal of Chemistry 16 (1998) 226-33.

(118) J Galceran, SL Taylor, PN Bartlett: Steady-state currents at inlaid and recessed microdisc electrodes for first-order EC ' reactions. Journal of Electroanalytical Chemistry 476 (1999) 132-47.

(119) K Harriman, DJ Gavaghan, P Houston, E Suli: Adaptative finite element simulation of currents at microelectrodes to a guaranteed accuracy. First-order EC ' mechanism at inlaid and recessed discs. Electrochemistry Communications 2 (2000) 163-70.

(120) PN Bartlett, SL Taylor: An accurate microdisc simulation model for recessed microdisc electrodes. Journal of Electroanalytical Chemistry 453 (1998) 49-60.

(121) MA Ghanem, M Thompson, RG Compton, BA Coles, S Harvey, KH Parker, D O'Hare, F Marken: Microwave induced jet boiling investigated via voltammetry at ring-disk microelectrodes. Journal of Physical Chemistry B 110 (2006) 17589-94.

(122) IB Svir, AI Oleinick, RG Compton: Dual microband electrodes: current distributions and diffusion layer 'titrations'. Implications for electroanalytical measurements. Journal of Electroanalytical Chemistry 560 (2003) 117-26.

(123) C Beriet, D Pletcher: A Further Microelectrode Study of the Influence of Electrolyte Concentration on the Kinetics of Redox Couples. Journal of Electroanalytical Chemistry 375 (1994) 213-18.

(124) AF Gil, L Galicia, I Gonzalez: Diffusion coefficients and electrode kinetic parameters of different Fe(III)-sulfate complexes. Journal of Electroanalytical Chemistry 417 (1996) 129-34.

(125) J Weber, Z Samec, V Marecek: Effect of Anion Adsorption on Kinetics of Fe3+-Fe2+ Reaction on Pt and Au Electrodes in Hclo4. Journal of Electroanalytical Chemistry 89 (1978) 271-88.

(126) E Sahlin, A ter Halle, K Schaefer, J Horn, M Then, SG Weber: Miniaturized electrochemical flow cells. Analytical Chemistry 75 (2003) 1031-36.

(127) C Amatore, C Sella, L Thouin: Electrochemical time-of-flight responses at double-band generator-collector devices under pulsed conditions. Journal of Electroanalytical Chemistry 593 (2006) 194-202.

(128) BJ Feldman, SW Feldberg, RW Murray: An Electrochemical Time-of-Flight Experiment. Journal of Physical Chemistry 91 (1987) 6558-60.

(129) ZM Rong, S Rashid, P Vadgama: A bipartite expression for the transient amperometric current at a membrane covered planar electrode to characterize solute diffusion through the membrane. Electroanalysis 18 (2006) 1703-09.

(130) S Um, CY Wang: Three-dimensional analysis of transport and electrochemical reactions in polymer electrolyte fuel cells. Journal of Power Sources 125 (2004) 40-51.

(131) DM Bernardi, MW Verbrugge: A Mathematical-Model of the Solid-Polymer-Electrolyte Fuel-Cell. Journal of the Electrochemical Society 139 (1992) 2477-91.

(132) IA Arkoub, C Amatore, C Sella, L Thouin, JS Warkocz: Diffusion at double microband electrodes operated within a thin film coating. Theory and experimental illustration. Journal of Physical Chemistry B 105 (2001) 8694-703.

(133) Z Homann: Z. Angew. Math. Mech (1936).

(134) N Frossling: Lunds Universitest Arsskrift N. F avd. 36 (1940).

(135) WJ Albery, ML Hitchman: Ring Disc Electrodes, Oxford University Press, 1971.

(136) CMA Brett, A Brett, RG Compton, AC Fisher, GP Tyley: The Wall-Jet Ring-Disk Electrode - the Measurement of Homogeneous Rate Constants from Steady-State Ring Currents. Electroanalysis 3 (1991) 631-36.

(137) RG Compton, AC Fisher, MH Latham, RG Wellington, CMA Brett, A Brett: Wall-Jet Electrodes - the Importance of Radial Diffusion. Journal of Applied Electrochemistry 23 (1993) 98-102.

(138) DG Swartzfager: Amperometric and Differential Pulse Voltammetric Detection in High-Performance Liquid-Chromatography. Analytical Chemistry 48 (1976) 2189-92.

(139) S Cannan, PR Unwin: Characterization and assessment of the microjet electrode as a detector for HPLC. Electroanalysis 16 (2004) 712-18.

(140) MLS Silva, MBQ Garcia, J Lima, E Barrado: Voltammetric determination of food colorants using a polyallylamine modified tubular electrode in a multicommutated flow system. Talanta 72 (2007) 282-88.

(141) JR Santos, RAS Lapa, J Lima: Development of a tubular fluoride potentiometric detector for flow analysis - Evaluation and analytical applications. Analytica Chimica Acta 583 (2007) 429-36.

(142) T Paixao, RC Matos, M Bertotti: Development of a dual-band amperometric detector for determination of ascorbic acid and glucose. Electroanalysis 15 (2003) 1884-89.

(143) JA Cooper, RG Compton: Channel electrodes - A review. Electroanalysis 10 (1998) 141-55.

(144) RG Compton, BA Coles, AC Fisher: Chronoamperometry at Channel Electrodes - Theory of Double Electrodes. Journal of Physical Chemistry 98 (1994) 2441-45.

(145) RG Compton, BA Coles, JJ Gooding, AC Fisher, TI Cox: Chronoamperometry at Channel Electrodes. Experimental Applications of Double Electrodes. J. Phys. Chem. 98 (1994) 2446-51.

(146) M Thompson, RG Compton: Voltammetric monitoring of transient hydrodynamic flow profiles in microfluidic flow cells. Analytical Chemistry 79 (2007) 626-31.

(147) M Thompson, RG Compton: Theory of collection efficiencies in the double tubular hydrodynamic electrode. Journal of Electroanalytical Chemistry 583 (2005) 318-26.

(148) JA Alden, RG Compton: Hydrodynamic voltammetry with channel microband electrodes: Axial diffusion effects. Journal of Electroanalytical Chemistry 404 (1996) 27-35.

(149) RG Compton, AC Fisher, RG Wellington, PJ Dobson, PA Leigh: Hydrodynamic Voltammetry with Microelectrodes - Channel Microband Electrodes - Theory and Experiment. Journal of Physical Chemistry 97 (1993) 10410-15.

(150) C Amatore, A Oleinick, OV Klymenko, I Svir: In situ and online monitoring of hydrodynamic flow profiles in microfluidic channels based upon microelectrochemistry: Concept, theory, and validation. Chemphyschem 6 (2005) 1581-89.

(151) C Amatore, Y Chen, C Sella, L Thouin: The direct, in situ, measurement of the flow velocity inside microfluidic devices via electrochemical coupling between two parallel microband electrodes. Houille Blanche-Revue Internationale De L Eau (2006) 60-64.

(152) C Amatore, A Oleinick, I Svir: Simulation of diffusion-convection processes in microfluidic channels equipped with double band microelectrode assemblies: approach through quasi-conformal mapping. Electrochemistry Communications 6 (2004) 1123-30.

(153) MV Mirkin, BR Horrocks: Electroanalytical measurements using the scanning electrochemical microscope. Analytica Chimica Acta 406 (2000) 119-46.

(154) K Slowinska, SW Feldberg, M Majda: An electrochemical time-of-flight technique with galvanostatic generation and potentiometric sensing. Journal of Electroanalytical Chemistry 554 (2003) 61-69.

(155) VGB Levich: Physicochemical Hydrodynamics, Pretice-Hall, Englewood Cliffs, NJ, 1962.

(156) PMs Monk: Fundamentals of electroanalytical chemistry, Wiley, Kent UK, 2001.

(157) JE Mitchell, TJ Hanratty: A study of turbulence at a wall using an electrochemical wall shear-stress meter. Journal of Fluid Mechanics 26 (1966) 199-221.

(158) E Kjeang, B Roesch, J McKechnie, DA Harrington, N Djilali, D Sinton: Integrated electrochemical velocimetry for microfluidic devices. Microfluidics and Nanofluidics 3 (2007) 403-16.

(159) JV Macpherson, MA Beeston, PR Unwin, NP Hughes, D Littlewood: Scanning Electrochemical Microscopy as a Probe of Local Fluid-Flow through Porous Solids - Application to the Measurement of Convective Rates through a Single Dentinal Tubule. Journal of the Chemical Society-Faraday Transactions 91 (1995) 1407-10.

(160) DR Prytherch, MJA Smith, B Williams: The measurement of cerebrospinal fluid flow. Physcs in Medicine and Biology 24 (1979) 1196-208.

(161) JA Alden, RG Compton: A comparison of finite difference algorithms for the simulation of microband electrode problems with and without convective flow. Journal of Electroanalytical Chemistry 402 (1996) 1-10.

(162) MJ Bidwell, JA Alden, RG Compton: Electroanalysis in flowing systems - The propagation of depletion effects downstream of a channel micro-band electrode. Electroanalysis 9 (1997) 383-89.

(163) BA Coles, RAW Dryfe, NV Rees, RG Compton, SG Davies, TD McCarthy: Voltammetry under high mass transport conditions. The application of the high speed channel electrode to the reduction of pentafluoronitrobenzene. Journal of Electroanalytical Chemistry 411 (1996) 121-27.

(164) RG Compton, MBG Pilkington, GM Stearn: Mass-Transport in Channel Electrodes - the Application of the Backwards Implicit Method to Electrode-Reactions (Ec, Ece and Disp) Involving Coupled Homogeneous Kinetics. Journal of the Chemical Society-Faraday Transactions I 84 (1988) 2155-71.

(165) RG Compton, RAW Dryfe, JA Alden, NV Rees, PJ Dobson, PA Leigh: Hydrodynamic Voltammetry with Channel Microband Electrodes - Potential Step Transients. Journal of Physical Chemistry 98 (1994) 1270-75.

(166) M Thompson, OV Klymenko, RG Compton: Modelling homogeneous kinetics in the double channel electrode. Journal of Electroanalytical Chemistry 576 (2005) 333-38.

(167) P Pastore, F Magno, I Lavagnini, C Amatore: Digital-Simulation Via the Hopscotch Algorithm of a Microelectrode-Based Channel Flow-through Amperometric Detector. Journal of Electroanalytical Chemistry 301 (1991) 1-13.

(168) T Paixao, RC Matos, M Bertotti: Design and characterisation of a thin-layered dual-band electrochemical cell. Electrochimica Acta 48 (2003) 691-98.

(169) JV Macpherson, N Simjee, PR Unwin: Hydrodynamic ultramicroelectrodes: kinetic and analytical applications. Electrochimica Acta 47 (2001) 29-45.

(170) Julie V. Macpherson: Recent Advances in Hydrodynamic Modulation Voltammetry. Electroanalysis 12 (2000) 1001-11.

(171) PRU Susan Cannan: Characterization and Assessment of the Microjet Electrode as a Detector for HPLC. Electroanalysis 16 (2004) 712-18.

(172) ZM Liu, O Niwa, R Kurita, T Horiuchi: Miniaturized thin-layer radial flow cell with interdigitated ring-shaped microarray electrode used as amperometric detector for capillary electrophoresis. Journal of Chromatography A 891 (2000) 149-56.

(173) FM White: Fluid mechnics, McGraw-Hill, 2003.

(174) BS Massey: Mechanics of fluids, Taylor and Francis, 2006.

(175) M Thompson, OV Klymenko, RG Compton: Mass transport limited currents at the tubular electrode. Journal of Electroanalytical Chemistry 575 (2005) 329-37.

(176) I Streeter, M Thompson, RG Compton: Linear sweep voltammetry at the tubular electrode: Theory of EC2 mechanisms. Journal of Electroanalytical Chemistry 591 (2006) 133-40.

(177) JR Santos, J Lima, MB Quinaz, JA Rodriguez, E Barrado: Construction and evaluation of a gold tubular electrode for flow analysis: Application to speciation of antimony in water samples. Electroanalysis 19 (2007) 723-30.

(178) C Amatore, OV Klymenko, A Oleinick, I Svir: In situ and on-line monitoring of hydrodynamic flow profiles in microfluidic channels based on microelectrochemistry: Optimization of channel geometrical parameters for best performance of flow profile reconstruction. Chemphyschem 8 (2007) 1870-74.

(179) BD Ratner, SJ Bryant: Biomaterials: Where we have been and where we are going. Annual Review of Biomedical Engineering 6 (2004) 41-75.

(180) SF Yang, KF Leong, ZH Du, CK Chua: The design of scaffolds for use in tissue engineering. Part 1. Traditional factors. Tissue Engineering 7 (2001) 679-89.

(181) H Van As, D van Dusschoten: NMR methods for imaging of transport processes in micro-porous systems. Geoderma NMR in Soil Science 80 (1997) 389-403.

(182) JD Seymour, PT Callaghan: Generalized approach to NMR analysis of flow and dispersion in porous media. Aiche Journal 43 (1997) 2096-111.

(183) T Baumann, R Petsch, G Fesl, R Niessner: Flow and diffusion measurements in natural porous media using magnetic resonance imaging. Journal of Environmental Quality 31 (2002) 470-76.

(184) C Manes, D Pokrajac, I McEwan, V Nikora, L Campbell: Application of UVP within porous beds. Journal of Hydraulic Engineering-Asce 132 (2006) 983-86.

(185) AP Yarlagadda, AP Yoganathan: Experimental Studies of Model Porous-Media Fluid-Dynamics. Experiments in Fluids 8 (1989) 59-71.

(186) JC Blechinger, EL Madsen, GR Frank: Tissue-Mimicking Gelatin Agar Gels for Use in Magnetic-Resonance Imaging Phantoms. Medical Physics 15 (1988) 629-36.

(187) R Mathurdevre, R Grimee, F Parmentier, J Binet: The Use of Agar-Gel as a Basic Reference Material for Calibrating Relaxation-Times and Imaging Parameters. Magnetic Resonance in Medicine 2 (1985) 176-79.

(188) KY Lee, DJ Mooney: Hydrogels for tissue engineering. Chemical Reviews 101 (2001) 1869-79.

(189) A Atala, DJ Mooney: In Synthetic biodegradable polymer scaffolds, Birkhauser, Boston, 1997.

(190) JT Daugridas, PG Blake, TS Ing: Handbook of dialysis, Lippincott Williams and Wilkins, London, 2001.

(191) SS Kety, CF Schmidt: The determination of cerebral blood flow in man by the use of nitrous oxide in low concentrations. American Journal of Physiology 143 (1945) 53.

(192) AR Greenbaum, PJE Etherington, S Manek, D Ohare, KH Parker, CJ Green, JR Pepper, CP Winlove: Measurements of oxygenation and perfusion in skeletal

muscle using multiple microelectrodes. Journal of Muscle Research and Cell Motility 18 (1997) 149-59.

(193) M Santiago, BHC Westerink: Characterization of the Invivo Release of Dopamine as Recorded by Different Types of Intracerebral Microdialysis Probes. Naunyn-Schmiedebergs Archives of Pharmacology 342 (1990) 407-14.

(194) P DeBoer, ED Abercrombie: Physiological release of striatal acetylcholine in vivo: Modulation by D1 and D2 dopamine receptor subtypes. Journal of Pharmacology and Experimental Therapeutics 277 (1996) 775-83.

(195) AJ Mathewson, M Berry: Observations on the Astrocyte Response to a Cerebral Stab Wound in Adult-Rats. Brain Research 327 (1985) 61-69.

(196) JB Cavanagh: Proliferation of Astrocytes around a Needle Wound in Rat Brain. Journal of Anatomy 106 (1970) 471-&.

(197) D Selander, KG Dhuner, G Lundborg: Peripheral-Nerve Injury Due to Injection Needles Used for Regional Anesthesia - Experimental-Study of Acute Effects of Needle Point Trauma. Acta Anaesthesiologica Scandinavica 21 (1977) 182-88.

(198) H Benveniste, NH Diemer: Cellular Reactions to Implantation of a Microdialysis Tube in the Rat Hippocampus. Acta Neuropathologica 74 (1987) 234-38.

(199) H Benveniste, J Drejer, A Schousboe, NH Diemer: Regional Cerebral Glucose Phosphorylation and Blood-Flow after Insertion of a Microdialysis Fiber through the Dorsal Hippocampus in the Rat. Journal of Neurochemistry 49 (1987) 729-34.

(200) AM Planas, C Justicia, S Sole, B Friguls, J Cervera, A Adell, A Chamorro: Certain forms of matrix metalloproteinase-9 accumulate in the extracellular space after microdialysis probe implantation and middle cerebral artery occlusion/reperfusion. Journal of Cerebral Blood Flow and Metabolism 22 (2002) 918-25.

(201) AS Khan, AC Michael: Invasive consequences of using micro-electrodes and microdialysis probes in the brain. Trac-Trends in Analytical Chemistry 22 (2003) 503-08.

(202) M Frost, ME Meyerhoff: In vivo chemical sensors: Tackling biocompatibility. Analytical Chemistry 78 (2006) 7370-77.

(203) GS Wilson, R Gifford: Biosensors for real-time in vivo measurements. Biosensors & Bioelectronics 20 (2005) 2388-403.

(204) K Rebrin, U Fischer, H Hahn von Dorsche, T von Woetke, P Abel, E Brunstein: Subcutaneous glucose monitoring by means of electrochemical sensors: fiction or reality? Journal of Biomedical Engineering 14 (1992) 33-40.

(205) H Clark, TA Barbari, K Stump, G Rao: Histologic evaluation of the inflammatory response around implanted hollow fiber membranes. Journal of Biomedical Materials Research 52 (2000) 183-92.

(206) N Wisniewski, B Klitzman, B Miller, WM Reichert: Decreased analyte transport through implanted membranes: Differentiation of biofouling from tissue effects. Journal of Biomedical Materials Research 57 (2001) 513-21.

(207) N Wisniewski, F Moussy, WM Reichert: Characterization of implantable biosensor membrane biofouling. Fresenius Journal of Analytical Chemistry 366 (2000) 611-21.

(208) M Gerritsen, JA Jansen, JA Lutterman: Performance of subcutaneously implanted glucose sensors for continuous monitoring. Netherlands Journal of Medicine 54 (1999) 167-79.

(209) F Moussy, WM Reichert: Boimaterials community examines biosensor biocompatibility. diabetes Tchnology and theraputics 2 (2000) 473.

(210) RB Beard, BN Hung, R Schmukler: Biocompatibility Considerations at Stimulating Electrode Interfaces. Annals of Biomedical Engineering 20 (1992) 395-410.

(211) N Wisniewski, M Reichert: Methods for reducing biosensor membrane biofouling. Colloids and Surfaces B-Biointerfaces 18 (2000) 197-219.

(212) B Guo, J Anzai, T Osa: Adsorption behavior of serum albumin on electrode surfaces and the effects of electrode potential. Chemical & Pharmaceutical Bulletin 44 (1996) 800-03.

(213) YN Zhang, YB Hu, GS Wilson, D Moattisirat, V Poitout, G Reach: Elimination of the Acetaminophen Interference in an Implantable Glucose Sensor. Analytical Chemistry 66 (1994) 1183-88.

(214) F Moussy, S Jakeway, DJ Harrison, RV Rajotte: In-Vitro and in-Vivo Performance and Lifetime of Perfluorinated Ionomer-Coated Glucose Sensors after High-Temperature Curing. Analytical Chemistry 66 (1994) 3882-88.

(215) F Moussy, DJ Harrison, RV Rajotte: A Miniaturized Nafion-Based Glucose Sensor - in-Vitro and in-Vivo Evaluation in Dogs. International Journal of Artificial Organs 17 (1994) 88-94.

(216) F Moussy, DJ Harrison: Prevention of the Rapid Degradation of Subcutaneously Implanted Ag/Agcl Reference Electrodes Using Polymer-Coatings. Analytical Chemistry 66 (1994) 674-79.

(217) BZ Yu, Y Moussy, F Moussy: Lifetime improvement of glucose biosensor by epoxy-enhanced PVC membrane. Electroanalysis 17 (2005) 1771-79.

(218) GA Gerhardt, AF Oke, G Nagy, B Moghaddam, RN Adams: Nafion-Coated Electrodes with High Selectivity for Cns Electrochemistry. Brain Research 290 (1984) 390-95.

(219) B Hoyer, M Loftager: Suppression of the Chloride Interference Effect on Solid-State Cupric Ion-Selective Electrodes by Polymer Coating. Analytical Chemistry 60 (1988) 1235-37.

(220) RFB Turner, DJ Harrison, RV Rajotte, HP Baltes: A Biocompatible Enzyme Electrode for Continuous Invivo Glucose Monitoring in Whole-Blood. Sensors and Actuators B-Chemical 1 (1990) 561-64.

(221) DJ Harrison, RFB Turner, HP Baltes: Characterization of Perfluorosulfonic Acid Polymer Coated Enzyme Electrodes and a Miniaturized Integrated Potentiostat for Glucose Analysis in Whole-Blood. Analytical Chemistry 60 (1988) 2002-07.

(222) C Lim, S Slack, S Ufer, E Lindner: Protein adsorption to planar electrochemical sensors and sensor materials. Pure and Applied Chemistry 76 (2004) 753-64.

(223) M Kyrolainen, SM Reddy, PM Vadgama: Blood compatibility and extended linearity of lactate enzyme electrode using poly(vinyl chloride) outer membranes. Analytica Chimica Acta 353 (1997) 281-89.

(224) K Kamei, M Mie, Y Yanagida, M Aizawa, E Kobatake: Construction and use of an electrochemical NO sensor in a cell-based assessing system. Sensors and Actuators B-Chemical 99 (2004) 106-12.

(225) K Kamei, T Haruyama, M Mie, Y Yanagida, M Aizawa, E Kobatake: Development of immune cellular biosensing system for assessing chemicals on inducible nitric oxide synthase signaling activator. Analytical Biochemistry 320 (2003) 75-81.

(226) K Kamei, T Haruyama, M Mie, Y Yanagida, E Kobatake, M Aizawa: Cellular biosensing system for assessing immunomodulating effects on the inducible nitric oxide synthase (iNOS) cascade. Biotechnology Letters 25 (2003) 321-25.

(227) K-i Kamei, T Haruyama, M Mie, Y Yanagida, M Aizawa, E Kobatake: The construction of endothelial cellular biosensing system for the control of blood pressure drugs. Biosensors and Bioelectronics 19 (2004) 1121-24.

(228) K Kamei, T Haruyama, M Mie, Y Yanagida, M Aizawa, E Kobatake: The construction of endothelial cellular biosensing system for the control of blood pressure drugs. Biosensors & Bioelectronics 19 (2004) 1121-24.

(229) CH Lin, FC Wei, S Mardini, SF Ma: Microcirculation study of rabbit ear arterial and venous flow-through flaps using a window chamber model. Journal of Trauma-Injury Infection and Critical Care 56 (2004) 894-900.

(230) WF Taylor, SE Dicarlo, VS Bishop: Neurogenic Vasodilator Control of Rabbit Ear Blood-Flow. American Journal of Physiology 262 (1992) R766-R70.

(231) RD Macpherson, LJ McLeod, RL Rasiah: Myogenic Response of Isolated Pressurized Rabbit Ear Artery Is Independent of Endothelium. American Journal of Physiology 260 (1991) H779-H84.

(232) MF Roberts, AC Zygmunt: Reflex and Local Thermal Control of Rabbit Ear Blood-Flow. American Journal of Physiology 246 (1984) R979-R84.

(233) WR Hume: Effect of Eugenol on Constrictor Responses in Blood-Vessels of the Rabbit Ear. Journal of Dental Research 62 (1983) 1013-15.

(234) G Droogmans, L Raeymaekers, R Casteels: Electromechanical and Pharmaco-Mechanical Coupling in Smooth-Muscle Cells of Rabbit Ear Artery. Journal of General Physiology 70 (1977) 129-48.

(235) H Ninomiya: The vascular bed in the rabbit ear: Microangiography and scanning electron microscopy of vascular corrosion casts. Anatomia Histologia Embryologia-Journal of Veterinary Medicine Series C 29 (2000) 301-05.

(236) SH Weisbroth: The biology of the laboratory rabbit, Academic Pr, 1974.

Appendix 1: Additional component drawing used when building the coater

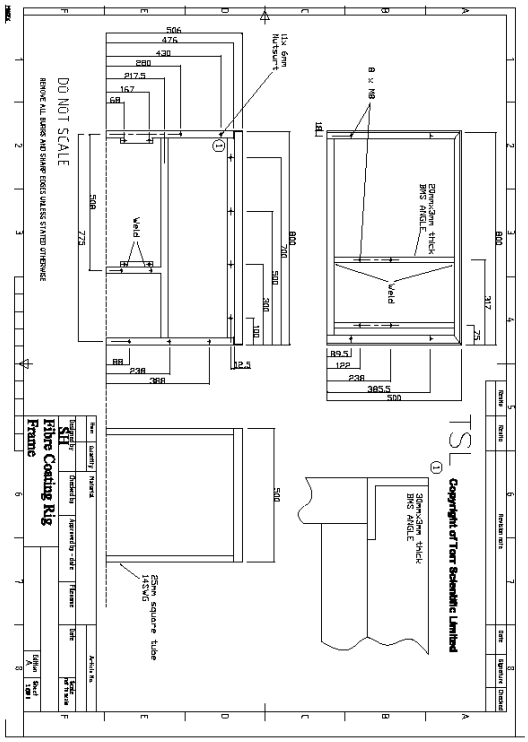

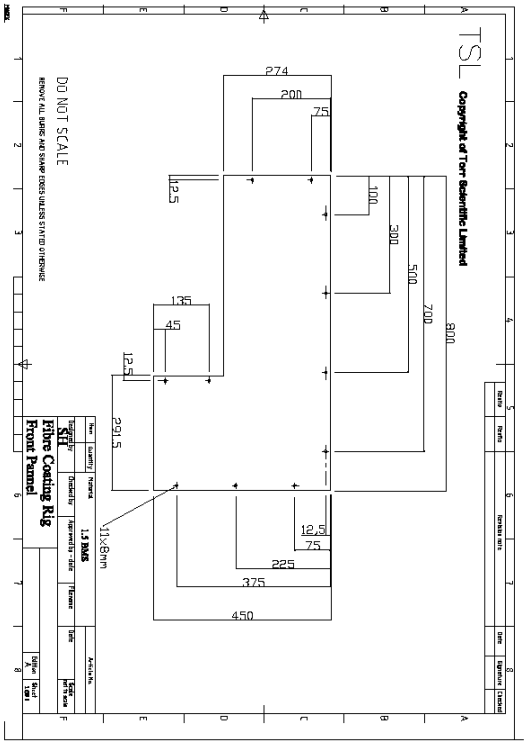

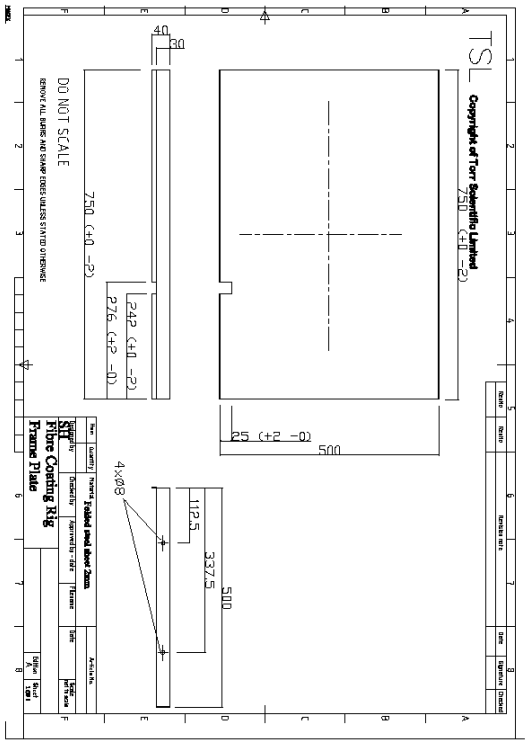

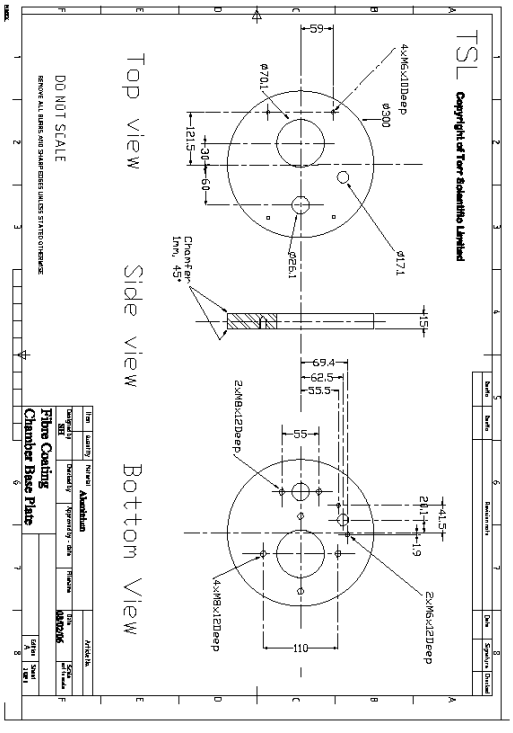

Appendix 2: Additional picture of the ring-disc electrodes

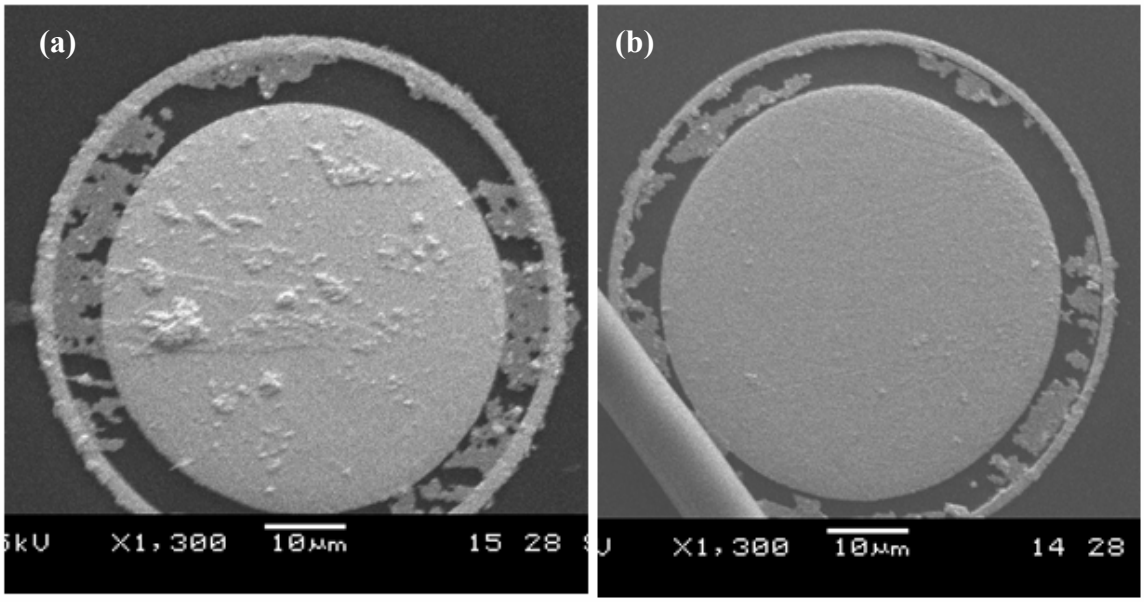

Figure 1: SEM pictures of the different ring-disc electrodes. Both have 50 µm disc diameter and 7.5 µm ring-disc spacing, the ring is larger in **(a)** than it is in **(b)**. Particles on the electrode are bits of gold, which were initially deposited to perform the imaging. The gold had to be removed and replaced by carbon because it was too thick, unfortunately it was not entirely removed

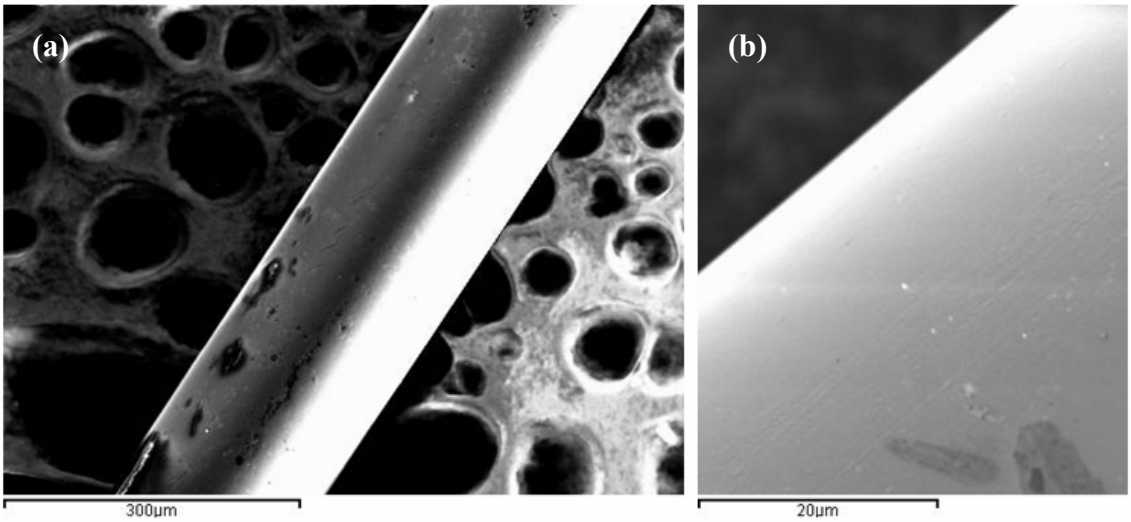

Figure 2: SEM picture of the coated wire. **(a)** In the lower left hand corner the insulator seems to have burnt off. **(b)** Close up of the coated Pt wire, the integrity of the Pt film is seen to be good.

Appendix 3: Sample code used in the numerical modelling of the ring-disc electrode. (Jet impinjing, disc generating, varying r_2 and the Pe number)

```
clear

c=1

while c<10
a=1+c/10
b=a+0.1
marcel=1
while marcel<10

% COMSOL version
clear vrsn
vrsn.name = 'COMSOL 3.2';
vrsn.ext = '';
vrsn.major = 0;
vrsn.build = 222;
vrsn.rcs = '$Name:  $';
vrsn.date = '$Date: 2005/09/01 18:02:30 $';
fem.version = vrsn;

% Geometry
carr={curve2([0,1],[0,0],[1,1]), ...
  curve2([1,a],[0,0],[1,1]), ...
  curve2([a,b],[0,0],[1,1]), ...
  curve2([b,20],[0,0],[1,1]), ...
  curve2([20,20],[0,20],[1,1]), ...
  curve2([20,0],[20,20],[1,1]), ...
  curve2([0,0],[20,0],[1,1])};
g1=geomcoerce('solid',carr);

fem.const = {'xref','25e-6', ...
  'tref','0.8224', ...
  'Dm','Dt*tref/(xref^2)', ...
  'Da','7.6e-10', ...
  'Dt','Da*exp((Ea/R)*(1/293-1/T))', ...
  'T','293', ...
  'Ea','13000', ...
  'R','8.3145', ...
  'Pe',marcel, ...
  'k','Pe*Dt/xref^2'};

% Geometry
clear s
s.objs={g1};
s.name={'CO1'};
s.tags={'g1'};

fem.draw=struct('s',s);
fem.geom=geomcsg(fem);

% Initialize mesh
fem.mesh=meshinit(fem);
```

```
% Initialize mesh
fem.mesh=meshinit(fem, ...
                'hmaxedg',[2,0.005,4,0.005,5,0.005]);

% Application mode 1
clear appl
appl.mode.class = 'FlConvDiff';
appl.mode.type = 'axi';
appl.assignsuffix = '_cd';
clear bnd
bnd.type = {'N0','Nc','C','C'};
bnd.c0 = {0,0,0,1};
bnd.ind = [1,4,3,1,3,1,2];
appl.bnd = bnd;
clear equ
equ.D = 'Dm';
equ.v = '-2*k*z';
equ.u = 'k*r';
equ.ind = [1];
appl.equ = equ;
fem.appl{1} = appl;
fem.sdim = {'r','z'};
fem.border = 1;
fem.outform = 'general';
fem.units = 'SI';

% Multiphysics
fem=multiphysics(fem);

% Extend mesh
fem.xmesh=meshextend(fem);

% Solve problem
fem.sol=femlin(fem, ...
              'solcomp',{'c'}, ...
              'outcomp',{'c'});

% Save current fem structure for restart purposes
fem0=fem;

%intergrate
Idisc(marcel,c)=postint(fem,'2*pi*r*(ntflux_c_cd)', ...
          'dl',[2], ...
          'edim',1);


% Integrate
Iring(marcel,c)=postint(fem,'2*pi*r*(ntflux_c_cd)', ...
          'dl',[5], ...
          'edim',1);


      CE(marcel,c)=-(Iring(marcel,c)/Idisc(marcel,c))*100

     marcel=marcel+1
```

```
  end
  c=c+1
end


DgenPe_1to10_R2_1to2_CE=CE
DgenPe_1to10_R2_1to2_Idisc=Idisc
DgenPe_1to10_R2_1to2_Iring=Iring

save('DgenPe_1to10_R2_1to2_CE','DgenPe_1to10_R2_1to2_CE')
save('DgenPe_1to10_R2_1to2_Idisc','DgenPe_1to10_R2_1to2_Idisc')
save('DgenPe_1to10_R2_1to2_Iring','DgenPe_1to10_R2_1to2_Iring')
```